CHARGE TRANSFER IN VERY SLOW H^+ + D(1*s*) HALF COLLISIONS

by

ERIC D. WELLS

B.A., Hastings College, 1994

A DISSERTATION

submitted in partial fulfillment of the
requirements for the degree

DOCTOR OF PHILOSOPHY

Department of Physics
College of Arts and Sciences

KANSAS STATE UNIVERSITY
Manhattan, Kansas

2000

Approved by:

Major Professor
Itzhak Ben-Itzhak

ABSTRACT

Single ionization of hydrogen molecules leads predominantly to the creation of vibrationally bound molecular ions. A small percentage of the transitions, however, may end in the vibrational continuum of the electronic ground state, resulting in the dissociation of the transient H_2^+ molecular ion into a proton and an H(1*s*) atom. We use the deuterium hydride (HD) isotope to study a H^+ + D(1*s*) "half" collision via this ground state dissociation (GSD) process. The kinetic energy release upon dissociation of the $HD^+(1s\sigma)$ molecular ion is typically less than 0.5 eV, producing very slow collision energies for the "half" collision process. Using this natural particle accelerator, we study charge exchange and elastic scattering in the H^+ + D(1s) "half" collision system. The measured difference in the relative probability of producing H^+ and D^+ fragments from the GSD process demonstrates that the isotopic effect leading to the breakdown of the Born-Oppenheimer approximation for HD^+ leads to the localization of the electron around the deuteron not only for vibrationally bound states near the dissociation limit, but also in the vibrational continuum. We have designed and constructed an apparatus to measure the energy of the slow H^+ and D^+ fragments by imaging their momentum in three dimensions. Measurements of the transition probability, as a function of kinetic energy release, from the lower $1s\sigma$ to the upper $2p\sigma$ state have been conducted at collision energies which are an order of magnitude lower than previously reported. Our results are compared to a simple model based on the analytic Meyerhof formula and to quantum mechanical coupled channels calculations. The general trends of the data agree with the calculations for charge transfer and elastic scattering.

TABLE OF CONTENTS

Table of Contents.....i

List of Figures.....iv

List of Tables……...……..x

Acknowledgements.....…xi

1 Introduction 1

2 Previous Theoretical and Experimental Work 5

2.1 The Homonuclear System: H^+ + H(1*s*).....…5

2.1.1 Homonuclear Potentials.....……..6

2.1.2 Scattering Theory for H^+ + H(1*s*) Collisions…….…….8

2.2 The Heteronuclear System: H+ + D(1s)……..10

2.2.1 Potential Energy Curves of HD^+……...……11

2.2.2 Scattering Theory for H^+ + D(1*s*) Collisions…...…….15

2.3 Previous Experimental Work……...…22

2.3.1 Limit of the Merged-Beams Technique……24

3 Ground State Dissociation 28

3.1 Ground State Dissociation.....28

3.2 The Molecule as an Accelerator…….35

3.3 Charge Transfer in Half Collisions…….38

4 Applications to Other Fields 51

4.1 Aeronomy…….....51

4.2 Astrophysics and Cosmology.....….....52

5 Experimental Method **61**

5.1 Single Ionization and Competing Processes……...62

5.2 General Experimental Considerations…….…….……...67

5.3 Time-of-Flight Method…….……...73

5.4 Momentum Imaging Method…….……..79

6 Results and Discussion **90**

6.1 Integrated Measurements of the GSD Fractions…….91

6.2 Differential Measurements of the GSD Fractions……..98

7 Conclusions and Future Directions **115**

Bibliography 122

Appendix A. Bunched Beam Operation **135**

Appendix B. Analysis of the H_2 Contamination **153**

B.1 Time-of-Flight Technique…….……...……..155

B.2 Momentum Imaging Technique…….……...….158

Appendix C. Recoil Ion Detectors **166**

C.1 Timing Detector……...…170

C.2 Resistive Anode Detector…….171

C.3 Ensuring Uniform Detection Efficiency…….....180

Appendix D. Electronics and Signal Processing **183**

D.1 Time-of-Flight Signals……...……..…183

D.2 Position Signals……....189

Appendix E. Spectrometers **195**

Appendix F. Effusive Jet **207**

Appendix G. Resolution and Error Analysis **213**

Appendix H. Beamline L2 **221**

Appendix I. Data Analysis Code **228**

LIST OF FIGURES

2.1 Adiabatic H_2^+ potential energy curves

2.2 H^+ + H(1*s*) scattering calculations of Hunter and Kuriyan.

2.3 Adiabatic potential energy curves for HD^+

2.4 The Jacobi coordinate set used by Esry and Sadeghpour

2.5 Charge transfer cross sections calculated by Hunter and Kuriyan for H^+ + D(1*s*) and H^+ + H(1*s*) collisions

2.6 Comparison of different calculations for the $H^+ + D(1s) \rightarrow H(1s) + D^+$ reaction

2.7 Charge transfer cross sections for the HD^+ system

2.8 Elastic scattering for the HD^+ system

2.9 Schematic picture of a merged-beams apparatus

2.10 Uncertainty in the center-of-mass energy in a H^+ + H(1*s*) merged-beams experiment

3.1 Ground State Dissociation of HD^+

3.2 Bound-free and bound-bound transition probabilities for HD^+ Ground State Dissociation

3.3 Comparison of measured and calculated GSD fractions for D_2

3.4 $E(R)$ and $-\frac{dE}{dR}$ for HD^+

3.5 Schematic picture of the apparatus used by Carrington *et al*.

3.6 Experimental results of Carrington *et al*.

3.7 The transition probability, $w(E_D)$, predicted by the Meyerhof model

3.8 The transition probability, $w(E_D)$, predicted by coupled channel calculations

3.9 An illustration of a shape resonance for $l = 4$

3.10 An illustration of a Feshbach resonance for $l = 0$

3.11 Coupled channels calculation of the probability for charge transfer and elastic scattering for $l = 0$ and $l = 2$.

4.1 The production of light elements according to a big bang nucleosynthesis model

4.2 A comparison between equation 4.7 and the fit used by Galli and Palla

4.3 Relative fractional abundance of light chemical species according to the standard model

5.1 The ratios of double- to single-ionization and ionization-excitation to single ionization of hydrogen molecules as a function of projectile charge

5.2 The ratio of ionization-excitation to single-ionization of hydrogen molecules by fast proton impact.

5.3 The ratio of double- to single-ionization of hydrogen molecules by fast proton impact.

5.4 Fragment yield from hydrogen molecules as a function of kinetic energy release for various dissociative processes

5.5 The ratio of $\frac{He^{2+}}{He^{+}}$ as a function of constant fraction lower level discriminator setting

5.6 Time-of-flight spectra for a HD target and background

5.7 The measured increase in the H_2 and D_2 contaminations in a HD bottle over time

5.8 A schematic picture of the time-of-flight spectrometer

5.9 Recoil ion trajectories for weak and strong extraction fields

5.10 Baseline fitting for the $m/q = 2$ peak

5.11 A typical COLTRIMS experimental setup

5.12 Conceptual figure of the momentum imaging apparatus

5.13 Cryo-pump with the gas cell mounted on the cold head

5.14 SIMION simulation showing the spectrometer space focusing

6.1 Coordinate system used in this dissertation

6.2 Measured $\frac{H^+}{HD^+}$ ratio using time-of-flight method

6.3 A comparison of the transition probability, $w(E_D)$, predicted by the Meyerhof model and by coupled channels calculations

6.4 The measured energy distribution of the HD+ molecular ion fitted with the sum of two Maxwell-Boltzmann distributions.

6.5 P_z vs. P_y for HD^+ molecular ions.

6.6 P_z vs. P_y for H_2^+ molecular ions and the D^+ fragments from GSD

6.7 Measured energy distributions for the three different molecular ions present in our spectra.

6.8 Measured *w(Ek)* for $0 \leq E_k \leq 1100$ meV

6.9 Measured *w(Ek)* for $0 \leq E_k \leq 150$ meV

6.10 The measured and calculated probabilities for elastic scattering

6.11 The measured and calculated probabilities for elastic scattering in the region around the H(1*s*) threshold.

6.12 A comparison between the calculated ratio of bound-free and total transitions and the results of our measurement

A.1 A schematic picture of the deflector assembly

A.2 A schematic picture of the prebuncher

A.3 The prebuncher field-shaping cones

A.4 The flight regions between the prebuncher and the bunching diagnostics

A.5 A comparison of several prebuncher waveforms

A.6 The structure in arrival times of ideal ions

A.7 Derivative of the prebuncher waveform

A.8 A HD^+ TOF peak measured with a 780 V/cm extraction field

B.1 Typical time-of-flight spectrum of an HD target measured with a weak extraction field

B.2 $P(E_k)$ for H_2^+ and D^+ GSD fragments at 30K

B.3 Measured momentum distributions of HD^+ ions and the momentum distribution of ion with $m/q = 2$

B.4 Comparison of slices of P_y for HD^+ and D_2^+

B.5 Estimating the H_2 contamination

C.1 A micro-channel plate

C.2 MCPs in a chevron configuration

C.3 The shape of the resistive anode

C.4 A ring embedded in the electric field lines of an infinite medium

C.5 Assembly drawing of the resistive anode detector

C.6 The electrical connections of the resistive anode detector

C.7 Image of the mask used to test the position sensitive detector

C.8 A slice across a mask slot and its derivative

C.9 $\frac{He^{2+}}{He^{+}}$ vs. LLD setting for 20 MeV C^{3+} impact

C.10 $\frac{H^{+}}{H_2O^{+}}$ as a function of detector voltage

C.11 $\frac{Ne^{q+}}{Ne^{+}}$ vs. LLD setting for 19 MeV F^{4+} impact

D.1 Block diagram of the TDC time-of-flight electronics

D.2 Block diagram of FTSS time-of-flight electronics

D.3 Time ordering of the four TDC signals

D.4 Block diagram of the electronics used for time-of-flight and position signals

E.1 The time-of-flight Spectrometer

E.2 Side view of momentum-imaging spectrometer

E.3 End view of momentum-imaging spectrometer

E.4 Equi-potential lines of our spectrometer under focusing conditions

E.5 Recoil-ion trajectories under uniform field conditions

E.6 SIMION simulation showing the spectrometer three-dimensional focusing

E.7 The equi-potential lines of the momentum-imaging spectrometer near the pusher plate

E.8 SIMION simulation of P_x as a function of time-of-flight

F.1 $j(\theta)$ for several values of β

G.1 δE vs. E

H.1 Overview of JRM floor plan showing the location of L2

H.2 Block diagram of L2 in its CTOF configuration

H.3 Block diagram of L2 configured for momentum-imaging measurements

H.4 Side view of the momentum-imaging experimental chamber

H.5 End view of L2

H.6 L2 viewed from the northwest

LIST OF TABLES

2.1 Comparison of Feshbach resonance locations and widths

3.1 GSD fractions for H_2, HD, and D_2

3.2 The value of $\frac{H^+}{HD^+}$ and $\frac{D^+}{HD^+}$ predicted using the Meyerhof model

4.1 Branching ratio of dissociative recombination of H_2D^+

4.2 Predicted branching ratio for GSD of HD^+

5.1 Extraction voltages and corresponding maximum E_k collected

6.1 Measured and Calculated HD GSD fractions

A.1 Lengths of the regions between the prebuncher and the bunching diagnostics located before LCM1

E.1 Momentum-imaging spectrometer regions and lengths

G.1 Summary of the factors influencing experimental resolution

ACKNOWLEDGEMENT

Many people have assisted me over the years, and it would be difficult to even mention them all, let alone adequately express my gratitude to them in this limited space, but a few deserve special mention. I owe many thanks to my advisor, Professor Itzik Ben-Itzhak. Itzik is an excellent teacher *and* scientist, and I have come to realize that having an advisor with that combination is a rare privilege. His remarkable enthusiasm for the scientific process is a great example to me. The other permanent member of our group, Professor Kevin Carnes, was an invaluable part of this research, not only because of his considerable technical skills, but also because he always remained calm when Itzik's enthusiasm was making my head hurt.

Professor Brett Esry provided calculations to support our experiment throughout the course of this project. One of the strengths of this work is the close collaboration between experiment and theory, and without Brett's work and that of Dr. Hossein Sadeghpour, we would not have been able to accomplish nearly as much. I enjoyed the short time Dr. Vidhya Krishnamurthi and I were both working on this project at Kansas State University. Professor Larry Weaver's role as a "devil's advocate" helped us to carefully examine our results. Larry's work with the "Research Experience for Undergraduates" program is what drew me to Kansas State University the first time, and I would like to thank him and Professor John Giese for an enjoyable summer.

Dr. Allen Landers and Professor Lew Cocke gave helpful hints about the experimental technique. Professor Martin Stöckli provided advice about mechanical designs. I would also like to acknowledge the discussions we had with Dr. Joe Macek, Dr. Helge Knudsen, Dr. Hiroyuki Tawara, and the faculty, staff, and students at the

Macdonald Laboratory. The superb technical staff at JRM helped in many ways. At various times, Mike Wells, Al Rankin, Bob Geering, Tracy Tipping, Dave Hill, Bob Krause, Steve Kelly, Ron Jackson, Paul Gibson, Dr. Charles Fehrenbach and Vince Needham were all called upon to fix a problem or offer advice, and they were always patient and helpful.

Professors Pat Richard, Kenneth Klaubunde and Mohammad Hosni joined Professors Ben-Itzhak, Cocke, Carnes, and Weaver on my committee. Professor Richard was kind enough to replace Professor Cocke for my final defense, as Professor Cocke was on sabbatical leave. I would like to thank everyone for serving on my committee.

My undergraduate education at Hastings College was largely the result of three teachers: Professors Clyde Sachtleben, Carl Throckmorten, and David Cooke. I thank them for providing me the necessary background to attend a large research university.

On a more personal note, I must thank my entire family for their love and support. Among the lessons I learned from my father was that almost anything is interesting if you investigate is closely enough–a lesson that has served me well. My mother deserves special thanks because she is my mother. I am blessed to have Rachel and Nathan as siblings. I am indebted to the following people for their friendship and encouragement: Denny, Cheryl, and Guy Busick, Dave, Pat, Jennifer, Ben, and Becky Kindschuh, Allen and Denise Landers, Gayln Lind, Bryce Lund, Mike Peterson, Todd Prater, and Matt Smith.

Most importantly, I must thank my wife for her love and care. Beth has made a lot of sacrifices while I went to graduate school, and I thank her for that and too many other things to name.

Chapter 1

The most fundamental system to study charge transfer between an ion and an atomic target is a proton and a hydrogen atom. The transfer of charge (an electron) in the H^+ + H(*1s*) system is a resonant process involving the two lowest electronic states of the transient H_2^+ molecular ion formed during the collision. Experimental determination of the electron transfer cross section is not difficult if the collision energy is in the keV range. As the collision energy is reduced, however, the experimental difficulty increases and there are relatively few measurements for collision energies below 10 eV [1.1]. While the experimental difficulties mount with decreasing collision energies, quantum mechanical effects become more important, making the system more interesting from a theoretical perspective.

The H^+ + D(*1s*) or D^+ + H(*1s*) collision system is similar to the homonuclear system discussed above. In the heteronuclear system, however, electron transfer is only a near resonant process involving the same two lowest energy electronic states of the transient HD^+ molecular ion formed during the collision. The energy gap between the

ground $1s\sigma$ and first excited $2p\sigma$ molecular states is 3.7 meV at the separate atom limit. As in the homonuclear system, experimental determination of electron capture cross sections is difficult at low energies. Furthermore, the presence of the deuterium nuclei makes this system an interesting candidate for study due to the astrophysical interest in deuterium [1.2].

This thesis will explore charge transfer in the H^+ + D(*1s*) system in the energy range below 1 eV by utilizing a process we call "Ground State Dissociation" (GSD) of the HD^+ molecular ion. GSD is the process in which a HD^+ ion in the vibrational continuum dissociates with a kinetic energy release of (typically) below 300 meV. The dissociation allows the study of collisions that start at the internuclear distance, R, of the HD molecule and continue outward to infinity. This is, in effect, half a collision, and these collisions are frequently referred to as "half" or "single pass" collisions. The term "half collision" is the one preferred by researchers studying dissociation of molecules using short pulse lasers [1.3]. Whatever the name, the collision differs from a typical "full" collision in that the range of internuclear distances is traversed only once. As will be discussed later, this has the effect of removing the interference in a "full" collision between charge transfer as R decreases and charge transfer as R increases. Since the interference is removed, the GSD process is a sensitive probe of the transition amplitude in H^+ + D(1s) collisions at collision energies almost two orders of magnitude lower than are accessible by the best current experimental techniques. GSD provides an experimental window to behavior below 100 meV, and therefore can provide empirical guidelines for theoreticians who have, to date, had this energy regime all to themselves.

In chapter 2 the various theoretical problems associated with calculating the adiabatic potential energy curves of hydrogen molecules will be discussed, paying

particular attention to the special problems involved with heteronuclear isotopes. Once the potentials and the coupling between them are calculated, scattering calculations can be made. Previous calculations of the adiabatic potential energy curves and scattering cross sections will be reviewed. A new calculation preformed by our group (mostly by Professor Esry and Dr. Sadeghpour) to complement the experimental work that comprises the bulk of this thesis will be briefly presented. We will also explore previous measurements of the charge transfer process at low collision velocities, and the difficulty in making similar measurements at even lower collision energies.

In Chapter 3, Ground State Dissociation will be introduced, and the calculation of the Franck-Condon overlap integrals leading to the determination of the ratio of bound-free to bound-bound transitions will be described. The asymmetry in the electron distribution above the dissociation limit will be contrasted with the microwave spectroscopy work of Alan Carrington and co-workers, who studied HD^+ in vibrational states near the dissociation limit [1.4]. In addition, we will present an estimate of the charge transfer in these half collisions based on the Meyerhof formulation [1.5] of the Demkov model [1.6] for charge transfer. This simple model will be compared to quantum mechanical coupled channel calculations which are similar (in the method of calculation) to the calculations presented in chapter 2 for the full $H^+ + D(1s)$ collisions.

Since almost all astrophysical data is gathered from the photons that reach Earth, interpreting the observed data requires knowledge of the atomic and molecular physics processes involved in producing these photons. Chapter 4 deals with applications of this work to astrophysics as well as aeronomy, two fields where the charge transfer between a proton and a hydrogen atom is of some importance.

In chapter 5, two experimental methods are described. The first is a measurement of the probability of charge transfer in the very slow half collision process integrated over all dissociation energies. This measurement requires only the time-of-flight of the recoil ions to be measured, so that the fragments can be identified by their mass to charge ratio. The second is a measurement of the same process as a function of dissociation energy. To measure the energy of the dissociating fragments, we use a momentum-imaging method. Our experimental technique borrows many of the principles that have been developed for Cold Target Recoil Ion Momentum Spectroscopy (COLTRIMS) [1.7], although some features are modified to fit the special requirement of using a deuterium hydride gas target.

In Chapter 6, the results of the two measurements we have made for the GSD process are reported. The results of the measurements will be compared with both the simple model derived by Meyerhof [1.5] as well as the quantum mechanical coupled channels calculations.

Chapter 7 includes a summary and some conclusions we have been able to make from this series of experiments. In addition, some changes to the apparatus and technique are suggested that could improve the current measurement. Some related experiments and future directions for this work are briefly examined.

Finally, several technical appendices are included. The appendices contain details of the experimental technique and are intended as a reference.

Chapter 2

The charge transfer process between a proton and a hydrogen atom is such a basic one that it has been the subject of study for some time. Furthermore, the HD^+ system is an interesting one for structure calculations because of the difference in the mass of the nuclei. This chapter contains a review of previous experimental and theoretical work that is related to this dissertation.

2.1 The Homonuclear System: $H^+ + H(1s)$

A very basic system for the study of electron transfer is a proton and a hydrogen atom in its ground electronic state. Calculations of the adiabatic potential energy curves for this system may be performed within the Born-Oppenheimer approximation. Because of this, calculation of H_2^+ and D_2^+ potentials has been a popular topic for the last seventy years [2.1]. Experimental determination of charge transfer is a bit of a challenge, however, since the nuclear mass of the two bodies is identical. In this section previous work on this system will be examined, and the limitations of this work will be discussed.

2.1.1 Homonuclear Potentials

The adiabatic potential energy curves of the H_2^+ system can be calculated exactly using the Born-Oppenheimer approximation since the H_2^+ molecular ion has symmetry under the exchange of nuclei. In the Born-Oppenheimer approximation, the nuclei of the atoms in the molecule are held fixed, and the Schrödinger equation for the electrons is solved to obtain molecular energy curves that are functions of the relative location of the nuclei. In other words, application of the Born-Oppenheimer approximation allows the separation of the nuclear and electronic motions of the molecule, and thereby reduces the H_2^+ system from a three-body problem to a two-body problem. Once the system becomes a two-body problem, it is relatively easy to solve, which can be done analytically, or by a number of numerical methods. The Born-Oppenheimer approximation, however, does have limits even for the homonuclear case. For example, the adiabatic molecular curves formulated with the Born-Oppenheimer approximation yield a dissociation threshold of $-\frac{1}{2}$ a.u. for the lowest energy curves. The correct value is $-\frac{1}{2}\mu_{eH}$ where μ_{eH} is the reduced mass of the hydrogen atom. When this value is close to unity, the correction is negligible unless spectroscopic precision is required. If this kind of precision is warranted, fairly complicated corrections are required. Recent high precision microwave measurements of high angular momentum Rydberg electrons in H_2 molecules [2.2] have resulted in a new interest in high-precision calculations of H_2^+ and D_2^+ [2.3 – 2.5].

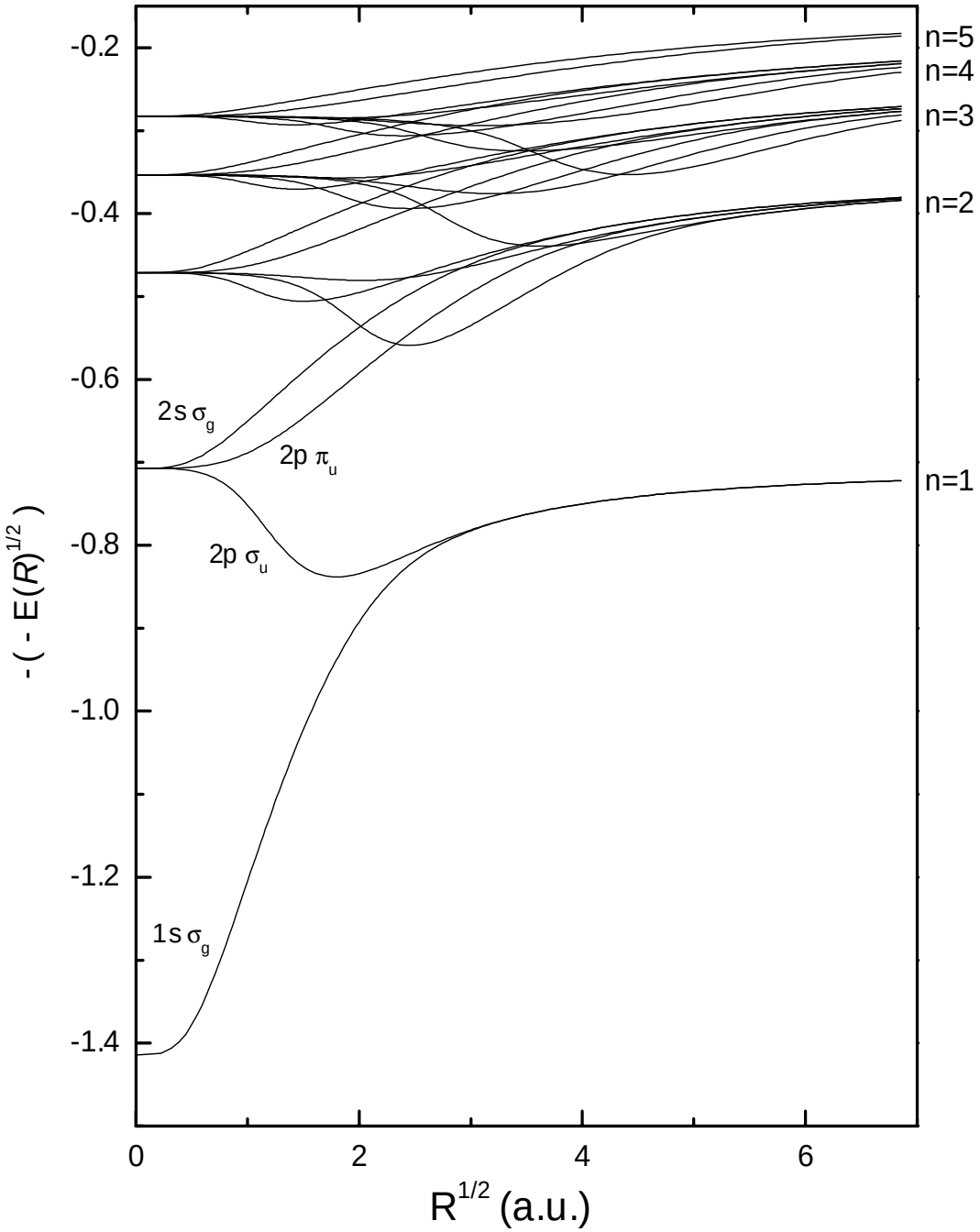

Figure 2.1: H_2^+ adiabatic potential energy curves. The values of n shown on the right indicate the principle quantum number in the separate atom limit. Note that the $1s\sigma_g$ and $2p\sigma_u$ curves are degenerate as $R \rightarrow \infty$. Allen Landers and the author calculated these curves as part of an assignment in Advanced Topics in Atomic Physics. The calculation used the OEDM.FOR (One Electron Diatomic Molecule) code written by James D. Power of the National Research Council of Canada.

2.1.2 Scattering Theory for H^+ + H(*1s*) Collisions

Theoretical calculations for this system date back at least to the 1953 semi-classical work of Dalgarno and Yadav [2.6]. In the next twenty years, several additional semi-classical approaches were proposed [2.7 – 2.18]. Smith was the first to see oscillations in the cross section for charge transfer at about 10 meV [2.19]. Most of the semi-classical results used the $1s\sigma_g$ and $2p\sigma_u$ potential energy curves calculated by Bates *et al.* that did not go beyond the Born-Oppenheimer approximation [2.20]. Adding first order corrections to the Born-Oppenheimer approximation *and* solving the H_2^+ scattering problem with a fully quantum mechanical treatment would not happen until the mid-1970's.

In 1975 G. Hunter and M. Kuriyan published a quantum mechanical treatment of electron scattering by hydrogen atoms [2.21]. Later that year, they generalized their treatment to proton collisions with hydrogen atoms and presented preliminary results at ICPEAC IX [2.22]. More complete results were published in 1977 [2.23]. For kinetic energies below 10.2 eV (the threshold for excitation of the n = 2 states of hydrogen) all of the two-center wavefunctions are neglected except the $1s\sigma_g$ and $2p\sigma_u$ states, which Hunter and Kuriyan calculated including first order corrections to the potentials obtained using the Born-Oppenheimer approach. Their quantum mechanical wave function phase shift scattering calculations showed significant differences from the most accurate semi-classical methods for collision energies less than 50 meV. Hunter and Kuriyan claimed their calculations have 6-digit numerical accuracy.

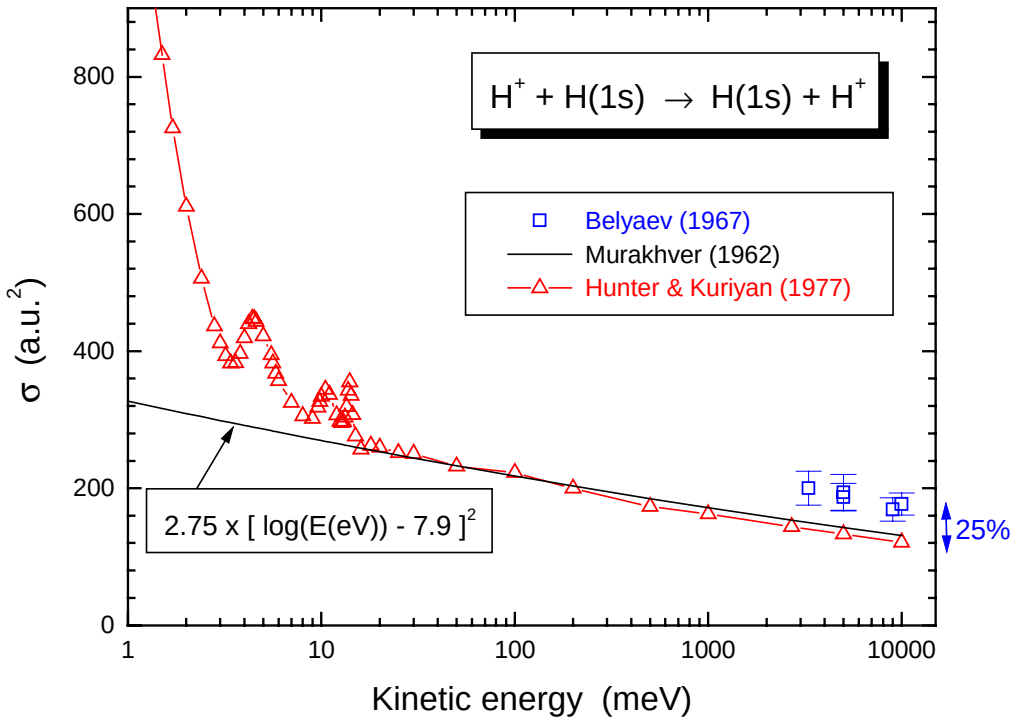

Figure 2.2: △: Theoretical calculations of Hunter and Kuriyan (ref. 2.23). □: Experimental points of Belyaev *et al.* (ref 2.60), which are about 25% above the semi-classical calculation of Murakhver (ref. 2.10) and about 40% above (2.7σ) the Hunter and Kuriyan calculation.

The basic difficulty in these calculations, even for the homonuclear case, is that it is necessary to introduce translational factors to allow for translational motion of the electron relative to the individual nuclei. These translational factors are often included in an *ad hoc* manner, making it difficult to generalize the H^+ + H(1*s*) system to other atomic systems [2.24, 2.25].

In 1978 Davis and Thorson used a different quantum mechanical treatment to calculate elastic scattering and resonant charge transfer in the H^+ + H(*1s*) system for the energy region of 0 to 0.1 eV [2.26]. Their total cross section calculations agree with Hunter and Kuriyan to 3%, although Davis and Thorson identified several shape

resonance structures not seen by Hunter and Kuriyan. Their analysis of the H^+ + H(*1s*) system was mainly meant to contrast their findings for the H^+ + D(*1s*) system, which will be described in section 2.2.2. Davis and Thorson devoted more attention to the translational factor issues in the scattering problem than did Hunter and Kuriyan, trying to eliminate the "spurious couplings" that arise when the Perturbed Stationary State (PSS) technique of Hunter and Kuriyan is applied.

In 1991, Hodges and Breig solved the coupled equations of the PSS technique using a different numerical approach in order to accommodate limited computer resources in exosphere model calculations [2.27]. Their results are indistinguishable from the 1977 results of Hunter and Kuriyan except that they show more structure due to their finer numerical grid. Since the calculations of Hodges and Breig in 1991, we are aware of no further calculations of charge exchange cross sections in the H^+ + H(*1s*) system.

2.2 The Heteronuclear System: H^+ + D(1*s*)

Like its homonuclear brethren, the H^+ + D(*1s*) or H(*1s*) + D^+ system is a very basic one for the study of charge transfer. Since the HD^+ system lacks symmetry under the exchange of nuclei, calculation of HD^+ potential energies has long been of interest to theorists. For our purposes, the basic difference between the heteronuclear and homonuclear cases is the 3.7 meV separation in energy between the higher $2p\sigma$ (H(*1s*) + D^+) state and lower $1s\sigma$ (H^+ + D(*1s*)) state that is found when the adiabatic potential energy curves are calculated beyond the Born-Oppenheimer approximation. At collision

energies below about 50 meV, this energy gap plays an important role in the charge transfer process.

2.2.1 Potential Energy Curves of HD^+

As stated in a previous section, detailed molecular structure calculations are relatively easy for H_2^+ or D_2^+ molecular ions because the Born-Oppenheimer Hamiltonian separates in an orthogonal coordinate system. In the HD^+ system, however, the nuclear center of mass and the geometric center (i.e. the center of charge) do not coincide, and one must go beyond the Born-Oppenheimer approximation to calculate the correct adiabatic potential energy curves.

Calculation of the HD^+ potential starts with the non-relativistic Hamiltonian in the center of mass for a one-electron diatomic molecular ion (using atomic units)

$$H = -\frac{1}{2\mu_{AB}}\nabla_R^2 - \frac{1}{2\mu_e}\nabla_r^2 + \frac{Z_A Z_B}{R} - \frac{Z_A}{r_A} - \frac{Z_B}{r_B}, \qquad (2.1)$$

with nuclei A and B, masses m_A and m_B, and charges Z_A and Z_B. To be more specific for the HD^+ problem, equation 2.1 may be re-written as

$$H = -\frac{1}{2\mu_{HD}}\nabla_R^2 - \frac{1}{2\mu_e}\nabla_r^2 + \frac{1}{R} - \frac{1}{r_H} - \frac{1}{r_D}, \qquad (2.2)$$

and the reduced masses given by

$$\frac{1}{\mu_{HD}} = \frac{1}{m_H} + \frac{1}{m_D}$$

$$\frac{1}{\mu_e} = \frac{1}{m_H + m_D} + 1. \qquad (2.3)$$

Most calculations of the HD^+ potential use a coordinate system with the origin at the geometric center of the nuclei. Electronic wavefunctions and energies are obtained as a function of the internuclear distance, usually starting with the Born-Oppenheimer Hamiltonian expressed in prolate spheroidal coordinates. Since this Hamiltonian cannot yield the correct dissociation limits for the H^+ + D(1*s*) and H(1*s*) + D^+ states, a symmetry-breaking term must be considered beyond the Born-Oppenheimer approximation. This correct mixing of the *gerade* and *ungerade* symmetries, in the context of a perturbation expansion of the H_2^+ wavefunction, is achieved by diagonalizing the symmetry-breaking operator, $-\frac{1}{2\mu_A}\nabla_r \bullet \nabla_R$, where

$$\frac{1}{\mu_A} = \frac{1}{m_H} - \frac{1}{m_D}. \qquad (2.4)$$

Various mathematical techniques have been employed to evaluate the symmetry-breaking term, including treating the symmetry-breaking term as a second-order perturbation [2.28 -2.31], a unitary transformation to move the symmetry-breaking term from the kinetic energy operator to the potential energy operator [2.32-2.38], and a variational approach [2.39].

Using a hyperspherical coordinate approach to this problem, as was first proposed by Macek and Jerjian [2.40], avoids many of the problems inherent in the Born-Oppenheimer approaches described above and gives the isotopically split HD^+ dissociation limits, even in the lowest order approximation. The hyperspherical adiabatic approximation gives the correct separated-atom limits because of the commutation of the generalized angular-momentum operator with the kinematic rotation operators [2.40-2.41]. Hara and co-workers [2.42] also applied hyperspherical coordinates to the HD^+

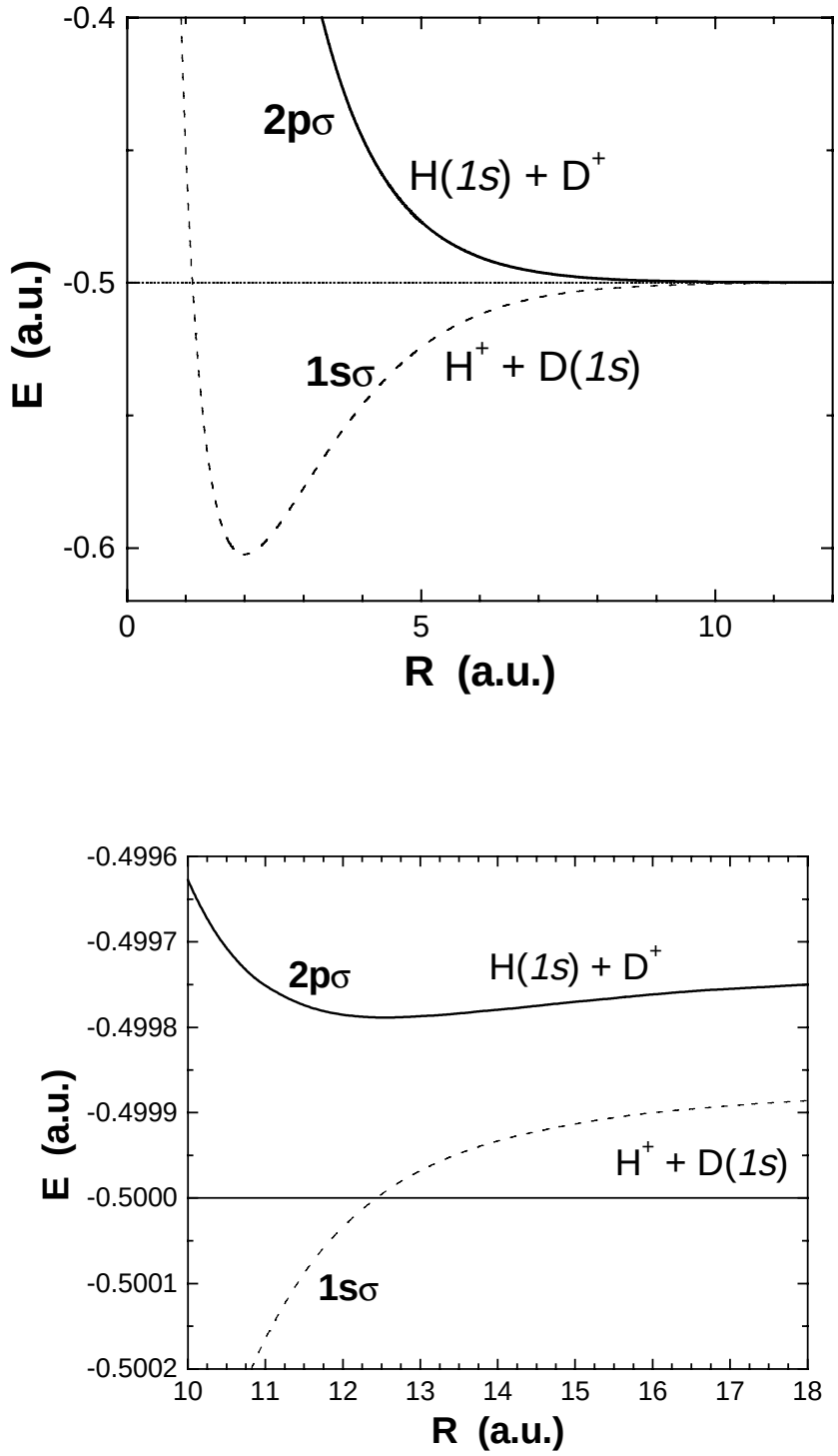

Figure 2.3: Adiabatic potential energy curves of HD^+. The top figure shows the entire energy range, the bottom figure has been expanded to show the isotopic splitting at the separate atom limit. These calculations are from reference [2.46].

problem, obtaining eigenfunctions and eigenvalues of the adiabatic Hamiltonian without neglecting any interactions, in contrast to Macek and Jerjian who neglected the parts of the Coulomb interaction on the order of $\frac{m_e}{m_p}$.

Another method of solving the HD^+ problem was used by Pack and co-workers, who diagonalized the HD^+ Hamiltonian in the center of mass of the nuclei in a basis of body-fixed wavefunctions, constructed from Slater Orbitals, which had a definite angular momentum along the internuclear axis [2.43-2.45].

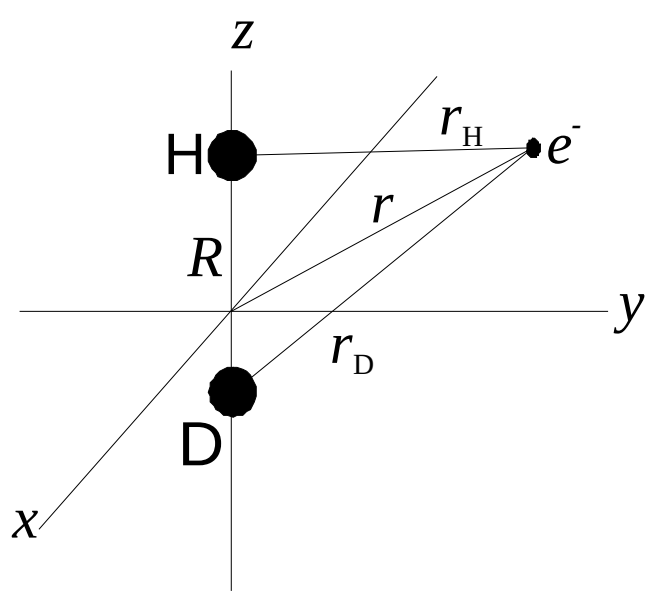

Figure 2.4: The Jacobi coordinate set used by Esry and Sadeghpour [2.45]. The origin is at the nuclear center of mass.

Finally, Esry and Sadeghpour have very recently formulated a new method for determining the adiabatic potential energy curves of HD^+ [2.46]. The Hamiltonian is written in prolate spheroidal coordinates with the origin at the nuclear center of mass (see figure 2.4). Since the center of the electronic coordinate is taken to be at the nuclear center of mass, for a one-electron system, this reduces to the Jacobi coordinates for a three-body system. In the initial steps, this approach is similar to that of Pack and

Hirschfelder [2.45], but it differs significantly in that whereas Pack and co-workers [2.43, 2.45] solve the adiabatic equation with an expansion over atomic orbitals, Esry and Sadeghpour express the electronic coordinates in terms of prolate spheroidal coordinates and solve the two dimensional equation that results using a B-spline technique [2.46].

2.2.2 Scattering Theory

The development of scattering theory for HD^+ systems dates to at least 1968, when Mapleton used a semi-classical approach to calculate cross sections for charge transfer in the H^+ + D(1s) system at energies greater than 200 eV [2.47]. In that same year, Crothers, Kennedy and Smith also used semi-classical methods to extend the calculations down to 5 eV [2.48].

In 1977 Hunter and Kuriyan used the computational methods developed for the homonuclear system [2.21-2.23] (discussed in section 2.1.2) to calculate the scattering states in the HD^+ system (H^+ + D(1*s*) and H(1*s*) + D^+ collisions) [2.49]. Their results, obtained by applying the Born-Oppenheimer approximation to separate the nuclear and electronic motion of the HD^+ system and solving the resulting coupled radial Schrödinger equations, are shown in figure 2.5. At collision energies below 50 meV, the energy difference between the 1*s*σ and 2*p*σ states begins to affect the cross section, with the H^+ + D(*1s*) final state having a higher cross section than the H(1*s*) + D^+ final state, which has a slightly higher energy at the separate atom limit.

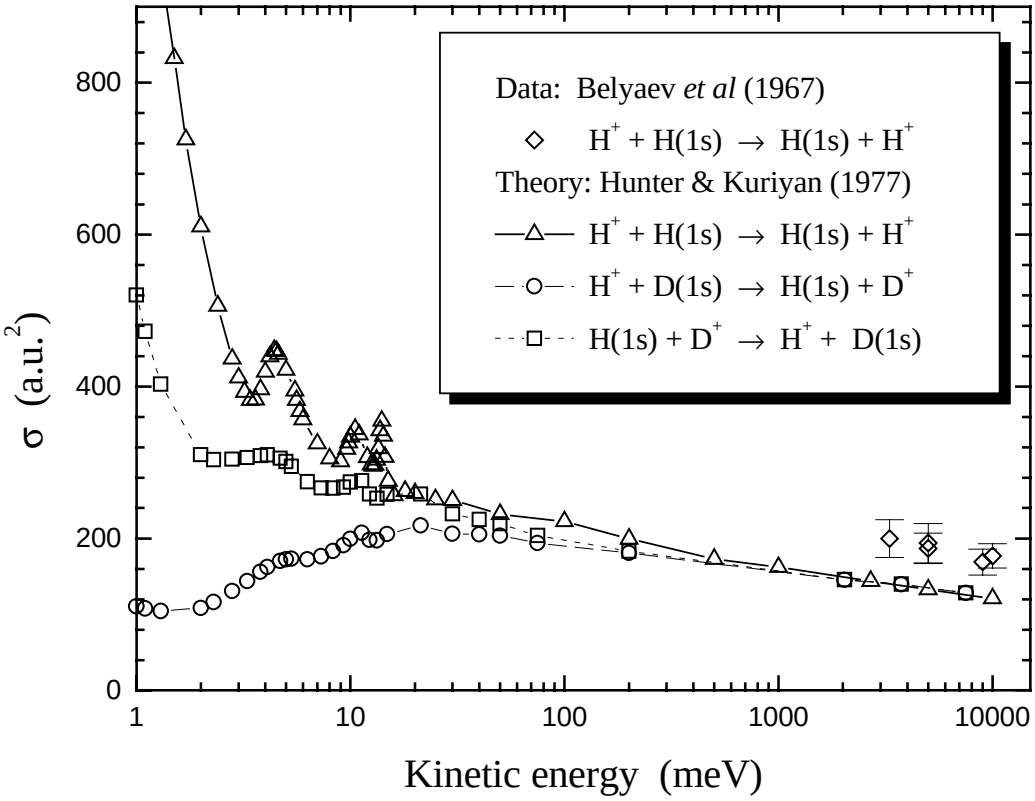

Figure 2.5: Theoretical cross sections for charge transfer in the H^+ + H(1*s*), H(1*s*) + D^+, and H^+ + D(1*s*) systems as computed by Hunter and Kuriyan [2.49]. Isotopic differences start to appear at collision energies of about 30 meV. The data (◇) is from reference [2.60].

Shortly after the calculation by Hunter and Kuriyan [2.49] appeared in the literature, a calculation by Davis and Thorson [2.26] also appeared. The focus of this study was to search for effects on the cross section arising from the difference in nuclear mass between the hydrogen and deuterium nuclei. Their main finding was that the perturbed stationary states (PSS) approach of Hunter and Kuriyan resulted in "spurious" couplings for the H^+ + D(1*s*) system, and therefore, those couplings had to be removed. The "spurious" couplings arise because the PSS theory does not account for the translation of a molecular electron, with respect to the center of mass, moving with the nuclei to which it is locally bound [2.50]. Davis and Thorson used the technique of

Thorson and Delos [2.51] that removed this defect by essentially identifying and ignoring these "spurious" couplings. In addition, Davis and Thorson [2.26] used a much finer numerical grid than Hunter and Kuriyan [2.49] allowing them to resolve features not seen in the previous calculation. The results for the electron transfer cross section are compared to the results of Hunter and Kuriyan in figure 2.6. Besides the lack of structure in the Hunter and Kuriyan calculation (due to the limited number of points calculated) the cross sections are about 5-10% lower than those of Davis and Thorson [2.26] from 30 to 100 meV. This is due to the coincidental overlap between the points calculated by Hunter and Kuriyan and the minima in the structure of the calculated values of Davis and Thorson.

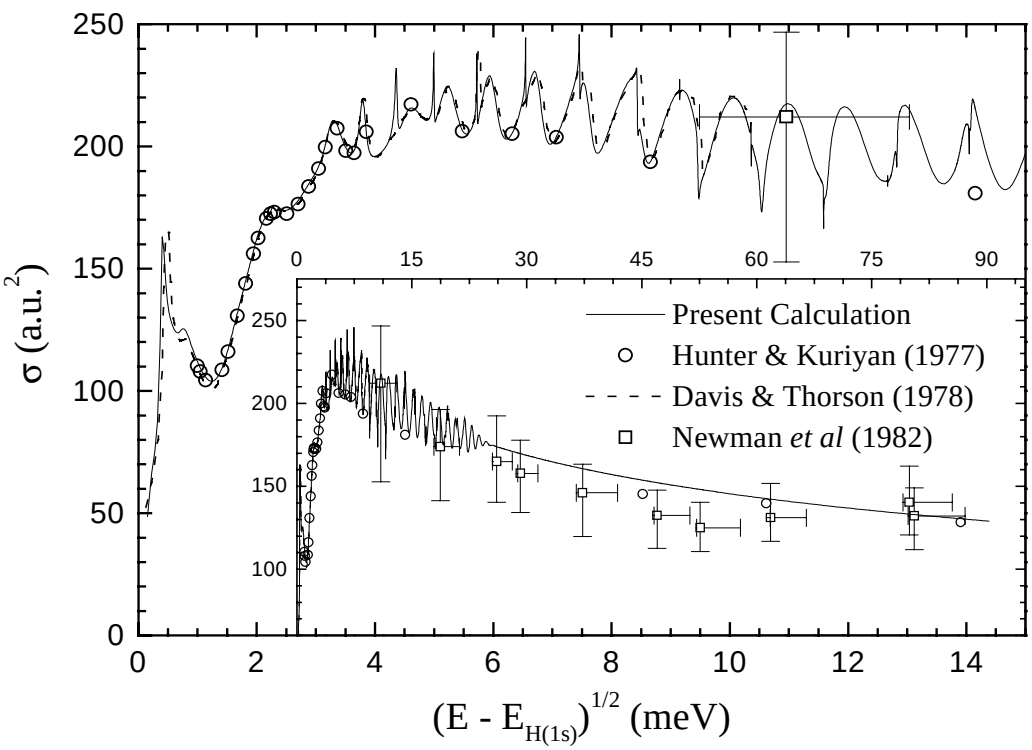

Figure 2.6: Comparison of calculations and experiment for the $H^+ + D(1s) \rightarrow H(1s) + D^+$ charge transfer reaction. The measured values of Newman et al. are from reference [2.62].

The truncated set of two-center coupled radial wave equations, derived by Hunter and Kuriyan, was solved in 1993 by Hodges and Breig [2.52] using a different numerical

technique. These results did show additional structure that was lacking in the original numerical approach of Hunter and Kuriyan [2.49], resolving, for example, the J = 10 shape resonance found by Davis and Thorson just slightly above threshold. The two methods are in reasonable agreement as for the overall magnitude of the electron transfer cross section, but the questions about the effect of including or excluding the "spurious" couplings remain unresolved.

We have recently completed scattering calculations [2.53] based on the adiabatic representation for diatomic molecular ions developed by Esry and Sadeghpour [2.46]. The major advantage of this representation is that it avoids many of the "translation factor" issues inherent in traditional Born-Oppenheimer representations by obtaining the exact finite atomic mass thresholds for the adiabatic potential curves. As discussed in section 2.2.1, the basic difference from the standard Born-Oppenheimer approach is the use of the center of mass of the nuclei as the origin of the electronic coordinates and in including selected pieces of the nuclear kinetic energy in the adiabatic Hamiltonian [2.53]. The resulting body frame Hamiltonian is

$$H = -\frac{1}{2\mu_{HD}}\nabla_R^2 - \frac{1}{2\mu_e}\nabla_r^2 + \frac{1}{R} - \frac{1}{r_H} - \frac{1}{r_D} + \frac{J(J+1) - 2\Lambda^2 + l^2}{2\mu_{HD}R^2} - \frac{\left(Y + \frac{3}{2}\right)^2}{2\mu_{HD}R^2} \qquad (2.5).$$

The quantum numbers J and Λ represent the usual total orbital angular momentum and its projection on the internuclear axis, respectively. The reduced masses are defined in equation 2.3. The operator $\boldsymbol{l}^2$ comes from the angular part of the nuclear kinetic energy and is the usual electronic orbital angular momentum. The operator $\boldsymbol{Y}$ originates from the radial part of the nuclear kinetic energy and is given in prolate spheroidal coordinates by

$$Y = \frac{1}{\xi^2 - \eta^2}\left[(\xi + \alpha\eta)(\xi^2 + 1)\frac{\partial}{\partial \xi} + (\eta + \alpha\xi)(1 + \eta^2)\frac{\partial}{\partial \eta}\right] \qquad (2.6).$$

Further numerical details of the calculation are beyond the scope of this thesis, but may be found in reference [2.53]. To obtain cross sections that converged to about 1%, only

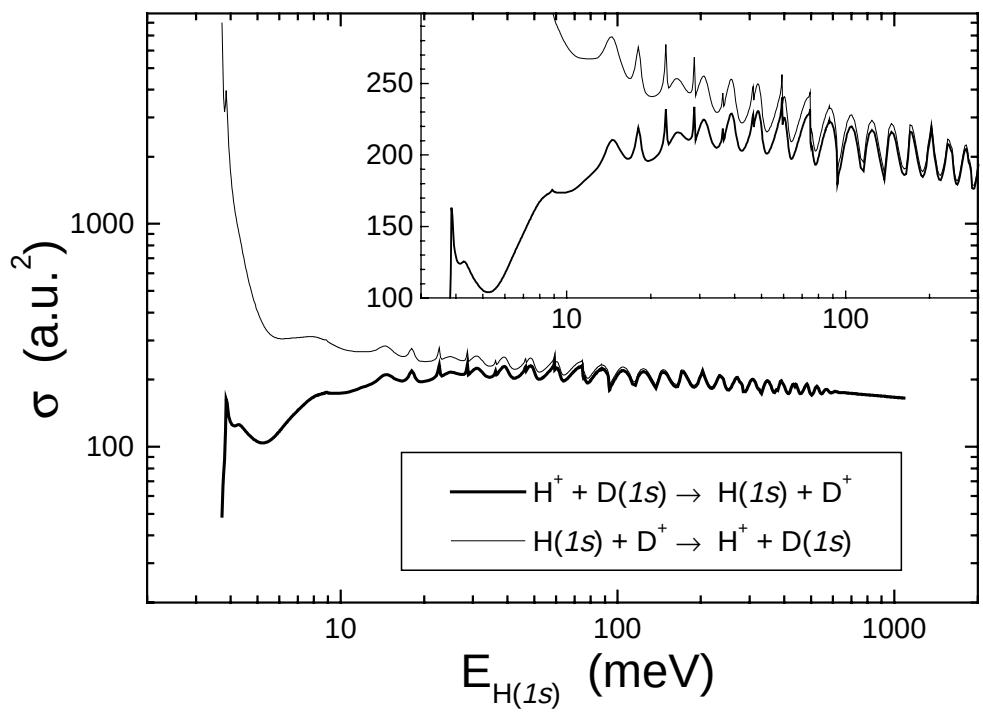

Figure 2.7: Charge transfer cross sections.

the n = 1 curves were needed. The n = 2 curves began to contribute about a 1% change in the elastic cross section only for collision energies near the 10 eV minimum of the n = 2 manifold of curves. For energies up to 1 eV above the H(1s) threshold, partial waves up to J = 100 were included to obtain convergence to 1%, while for energies ranging from 1 to 8 eV above the H(1s) threshold partial waves up to J = 300 were included. For energies in the gap between the H(1s) and D(1s) thresholds, convergence was obtained

with only 20 partial waves, since the centrifugal barrier goes above the H(1*s*) threshold for $J \approx 10$.

Our results for both possible charge transfer channels are shown in figure 2.7. The broad "oscillations" present in the cross section are caused by the numerous resonances that lie just above the top of the $1s\sigma$ potential barrier. These shape resonances are sometimes referred to as "orbiting resonances" [2.26] to differentiate them from the standard sharp shape resonances that lie in the $2p\sigma$ channel. It should be pointed out, however, that these broad shape resonances have often been misinterpreted as interference between charge transfer that occurs as the internuclear distance is decreasing (the way in) and charge transfer that happens as the internuclear distance is increasing (the way out). This interference is present, but the oscillations have a much larger wavelength than the shape resonances that appear in our calculations. The results of our calculations for the $H^+ + D(1s) \rightarrow H(1s) + D^+$ charge transfer channel are compared to previous results and experiment in figure 2.6. The agreement between the different theoretical methods shown is this figure is in some sense not very illuminating, since the features in the total cross section are almost totally controlled (above a few meV) by the $1s\sigma$ potential energy curve.

Our results for elastic scattering are shown in figure 2.8. The accuracy of the calculations are best verified by the locations of resonances. We have made a quantitative comparison for the Feshbach resonances below the H(1*s*) threshold (see Table 2.1) and found good agreement between our results and those of Wolniewicz and Orlikowski [2.31] and Kennedy *et al.* [2.54]. In addition, we were able to locate a second $J = 0$ resonance near the H(1*s*) threshold that previous methods failed to locate. The

agreement with Davis and Thorson is not nearly as good, which might indicate that their method is unable to adequately deal with the spurious coupling [2.26].

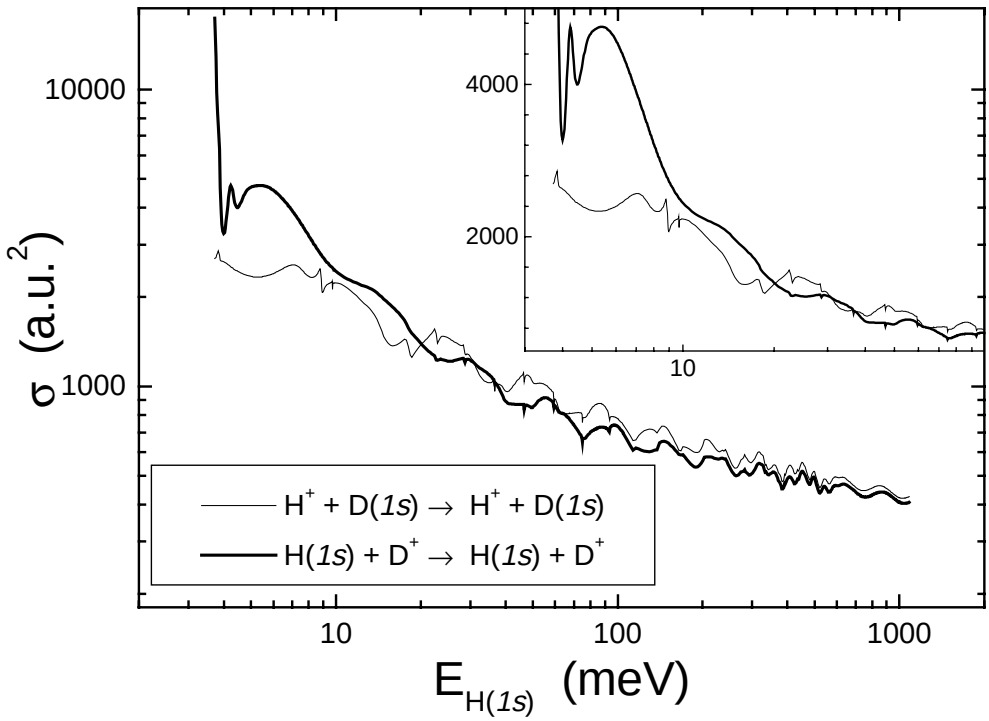

Figure 2.8: Elastic scattering cross sections.

	Present		Wolniewicz and Orlikowski		Davis and Thorson		Kennedy *et al.*
J	E(cm^{-1})	Γ(cm^{-1})	E(cm^{-1})	Γ(cm^{-1})	E(cm^{-1})	Γ(cm^{-1})	E(cm^{-1})
0	5.886	5.298	5.868	5.261	9.0	9.4	5.840
0	0.0808	0.214	-	-	-	-	-
1	5.219	4.668	5.196	4.632	8.44	8.89	4.974
2	3.795	3.369	3.769	3.336	6.58	7.13	3.304
3	1.509	1.725	1.478	1.707	3.51	4.57	0.987

Table 2.1: Feshbach resonances. Energies are energies below the H(1*s*) threshold.

In addition to our recent work, there is another very recent calculation by Akinori Igarashi and C. D. Lin [2.55] which uses a hyperspherical approach to calculate the D^+ + H(1*s*) $\rightarrow$ D(1s) + H^+ charge transfer reaction. HD^+ potentials have, of course, been

solved using hyperspherical methods for a number of years (see section 2.2.1). The scattering calculations are generally quite tedious, however, since a new hyperspherical potential must be calculated for each partial wave. Igarashi and Lin were able to find a numerical method in which the hyperspherical potential curves and coupling terms have to be calculated only once to obtain results for all partial waves. They also calculate Feshbach and shape resonances near the H(1*s*) threshold, and those results are generally in good agreement with ours, although they were unable to resolve the second $J = 0$ Feshbach resonance just below threshold.

2.3 Previous Experimental Work

Measurements of charge transfer in the $H^+ + H(1s)$ (or $H^+ + D(1s)$) system in the keV energy range can be accomplished using standard modulated crossed beam techniques, as well as using furnace target measurements. Fite *et al.* [2.56 – 2.58] made the pioneering measurements in the field, from 1958 to 1962. Gilbody has published a review of the subject that by now includes numerous measurements above 50 eV [2.59]. Measurements of charge transfer at lower collision energies (below a few eV) are comparatively rare.

Studies of charge transfer down to collision energies of 100 meV have been possible by means of the merged-beams technique. A beam of protons is merged with a beam of hydrogen atoms moving in the same direction. The beams typically have about a keV of energy, but by merging two beams of nearly equal energy, charge transfer may be studied at low center of mass energies. The largest difficulty with measurements of this

type is separation of the ion-atom collision signal from collisions with the background gas. In addition, since the atomic beam is typically produced by neutralization in a gas target, the atomic beam may contain an unknown fraction of atoms in excited states. Cross sections for charge transfer of highly excited hydrogen are up to several orders of magnitude larger than cross sections for collisions involving ground state hydrogen [2.60], and as a result even a small metastable population in the beam could influence the results of the experiment. The energy resolution of such a measurement is determined by the ability to measure the relative velocity of the two beams as well as the energy spread within each beam. To measure charge transfer at low collision energies, the beams must have a very small relative velocity, and as a practical matter, as the uncertainty in the relative velocity nears the value of the relative velocity, the energy resolution gets correspondingly worse.

Using such a beam overtaking technique, Belyaev *et al.* managed to measure a cross section for charge transfer in the $H^+ + H(1s)$ and $D^+ + D(1s)$ systems down to 5 eV [2.61]. In this experiment, the metastable H(2*s*) atoms were removed from the atomic beam by electric field quenching. The experimental value obtained is about 40% above the theoretical prediction of Hunter and Kuriyan (see figure 2.2). Two possible sources of error in this experiment follow: First, the electric field quenching might not be sufficient to remove all $n > 2$ states. Second, Hunter and Kuriyan argued (see reference [2.23]) that those ions produced by charge transfer at angles less than $\theta = \pi$ will have less momentum in the beam direction than the original atom. Ions produced by direct scattering at an angle greater than $\theta = 0$ would gain some momentum in the beam direction from the unretarded hydrogen atom. Since direct scattering is more intense than charge transfer, the net effect of ion scattering at angles away from the peaks at $\theta = \pi$ and

$\theta = 0$ is to produce more higher energy protons in the emergent beam than are predicted by the theoretical charge transfer cross section.

In 1982, Newman *et al.* studied $H^+ + H(1s) \rightarrow H(1s) + H^+$ and $H^+ + D(1s) \rightarrow H(1s) + D^+$ reactions in the range 0.1 to 150 eV using a merged beams technique [2.62]. The apparatus used for these experiments is discussed by Rundel and co-workers in reference [2.63]. An electric field was used to ionize hydrogen atoms in states above $n = 18$, as well as to quench H(2*s*) atoms. Long-lived atoms in $9 \leq n \leq 19$ reached the beam interaction region. Collision products arising from these excited states, however, could be separated using a retarding potential analyzer from the resonant charge transfer process. The measurement is compared with various theoretical results in figure 2.6. The largest contribution to the uncertainty in the absolute cross section was the determination of the overlap between the two beams and uncertainties in various detection efficiencies. The uncertainty in the collision energies was due almost entirely to difficulty in determining the exact reactant beam velocities. The uncertainty in the experimental result is large enough that it does not provide a stringent test of the calculations, although the experimental results seem to be in reasonable agreement with the theoretical predictions.

2.3.1 Limit of the Merged-Beams Technique

Since the 120 meV collision energy measured by the Stebbings group at Rice [2.62] did not reach the energy region were the calculations of Hunter and Kuriyan [2.49] begin to show isotopic effects, it is reasonable to speculate about the limit of the merged-beams approach, and therefore its ability to probe the calculations below 100 meV. A state-of-the-art ion-atom merged-beams apparatus at Oak Ridge National Laboratory developed by Havener *et al.* [2.64, 2.65] has been used for many measurements of electron capture cross sections in collisions between hydrogen atoms and multi-charged ions, but rarely do the collision energies extend below a few hundred meV.

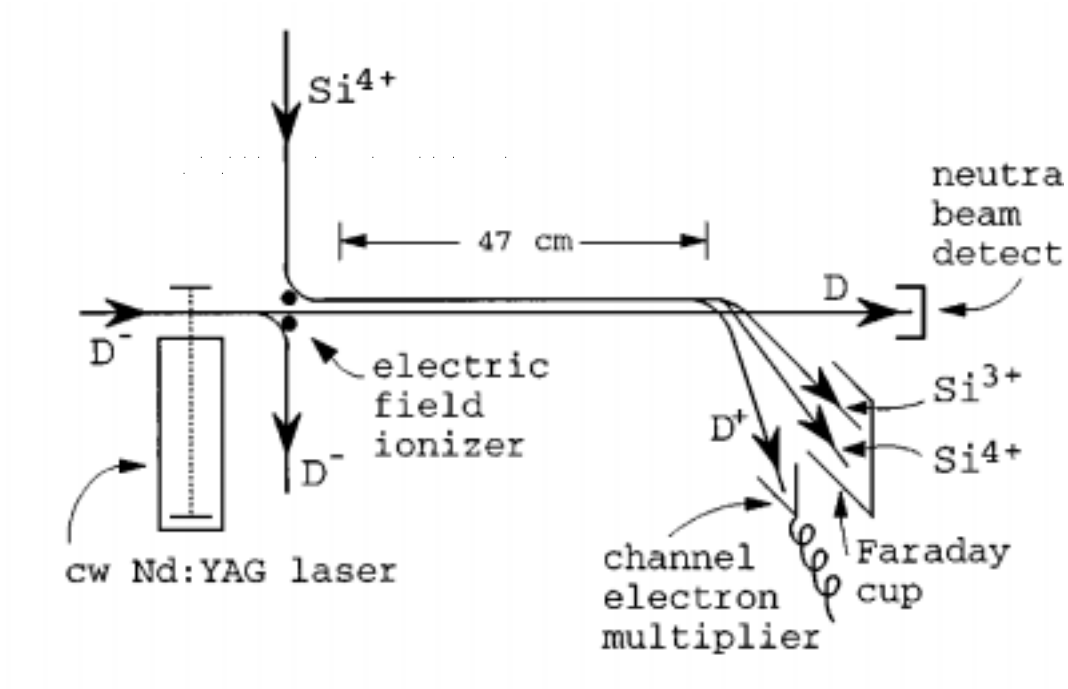

Figure 2.9: Simplified schematic picture of the ion-atom merged-beams apparatus at Oak Ridge National Laboratory. The ion beam is produced by an ECR ion source, and the laser is used to create a D (H) beam by photodetachment of the D^- (H^-) beam. The beam overlap occurs in the 47-cm long merge section. The merged-beams are then charge separated by a magnetic field. Figure is from [2.66].

The center-of-mass energy in a merged-beams system is given by:

$$E_{c.m.} = \left[\frac{E_1}{m_1} + \frac{E_2}{m_2}\right] - 2\sqrt{\frac{E_1}{m_1}\frac{E_2}{m_2}}\cos(\theta) \qquad (2.7)$$

where E_1 and m_1 refer to the energy (eV) and mass (a.u.) of the neutral beam and E_2 and m_2 are those of the ion beam. As Pieksma *et al*. [2.66] have pointed out; the merge angle (θ) sets a limit on the lowest center-of-mass energies that can be achieved. In practice, before that limit is reached, the uncertainty in the collision energy becomes large due to the finite divergence of the beams and the energy spread of the neutral and ion beams. The lowest energy measurement the Oak Ridge group was able to produce for the Si^{4+} + H(1s) system was 0.02 eV [2.66]. Using the experience of the Havener group as a guide, we can estimate the limits of this type of apparatus for the H^+ + H(1*s*) system.

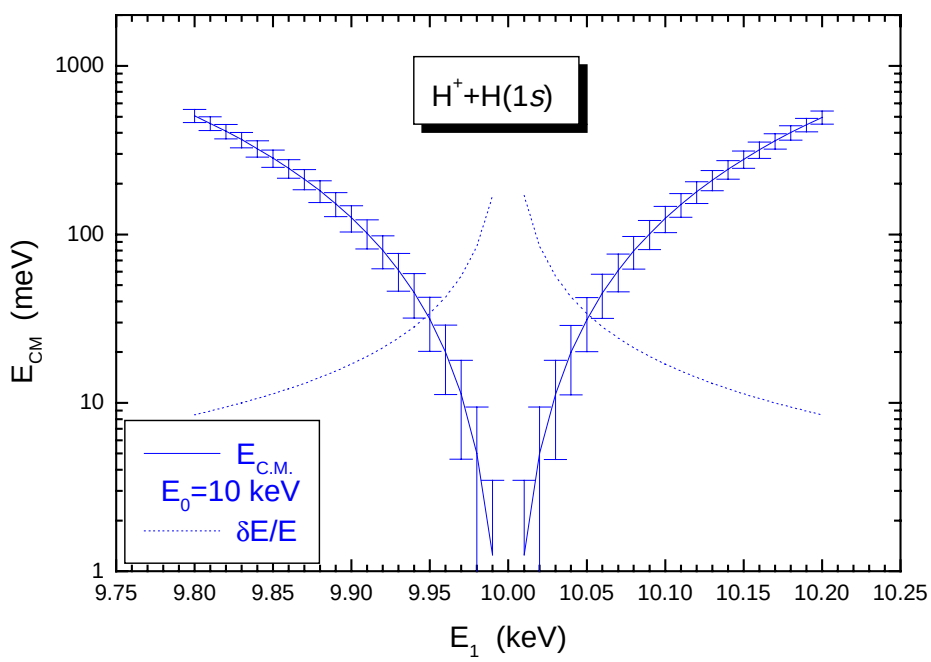

Figure 2.10: An estimate of the uncertainty in the center-of-mass energy of a H^+ + H(1*s*) merged-beams experiment. The dashed line is δE/E, which increases rapidly as the two beams reach the same energy (10 keV).

Assuming neutral and ion beams with 10 keV of energy could be produced, we can calculate the uncertainty due to the energy spread of the beams. We have assumed a 6.5 eV spread in E_1 [2.67, 2.68] and a 6 eV spread in the neutral beam due to the duoplasmatron [2.68, 2.69]. The results are shown in figure 2.10.

The estimate clearly shows that as the center-of-mass energy is reduced, the uncertainty increases rapidly. At $E_{c.m.}$ = 100 meV, the relative uncertainty is about 20%. At $E_{c.m.}$ = 10 meV, the relative uncertainty is about 60%. Furthermore, this estimate represents something of a best case scenario, since there are technical problems getting a H^+ and a H beam of nearly identical energy using the facility at Oak Ridge, most notably the limited dynamic range of the ECR ion source [2.65]. If an experiment is to seriously probe the calculations of charge transfer in H^+ + H(1*s*) or H^+ + D(1*s*) collisions, a different experimental technique needs to be explored.

Chapter 3

The difficulties in using a traditional merged-beams approach to study $H^+ + D(1s)$ collisions in the energy regime where the quantum mechanical interest is most acute have been discussed in the preceding chapter. Our approach to this problem is to utilize the properties of the HD molecule itself as an "accelerator" and measure the energy of the fragments after the collision has taken place. In this chapter the ground state dissociation (GSD) process will be described. Once the molecule dissociates, there is a possibility of charge transfer in the "half collision" following the removal of the electron. The charge transfer process can be roughly described using a simple model, or more completely using a coupled channel calculation, both of which are discussed in this chapter.

3.1 Ground State Dissociation

When one electron of a hydrogen molecule is rapidly ionized, the most likely result is the creation of a vibrationally bound HD^+ molecular ion in a $1s\sigma$ electronic state. A small percentage of the transitions, however, between the initial HD target and the HD^+ ground electronic state end in the vibrational continuum. When this process, illustrated

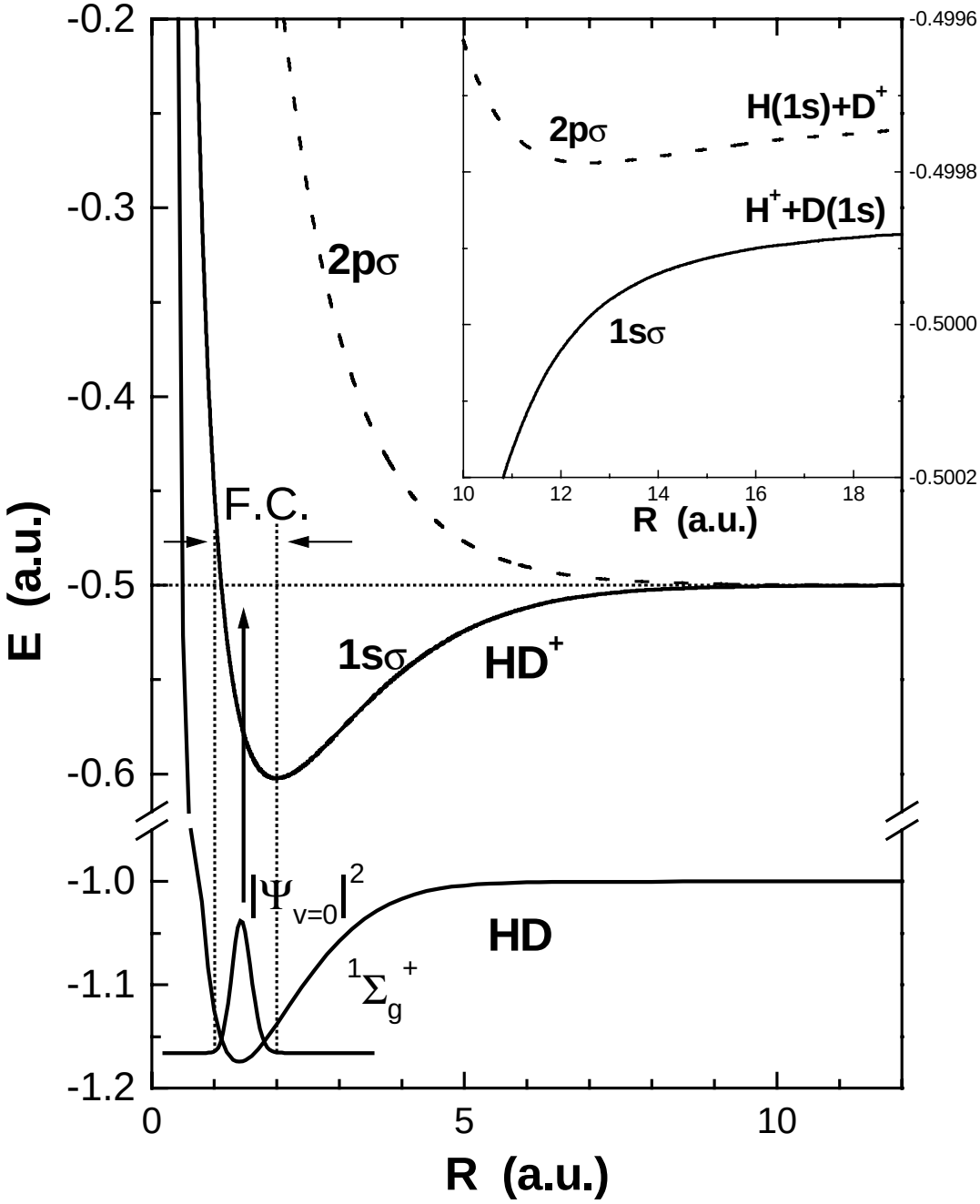

Figure 3.1: The potential energy curves for HD $^1\Sigma^+$ and the two lowest electronic states of HD^+, $1s\sigma$ and $2p\sigma$. In the GSD process, a fast projectile ionizes one electron of the neutral HD molecule, making a vertical (or Franck-Condon) transition to the HD^+ electronic ground state. If the result of the vertical ionization is a HD^+ molecular ion in the vibrational continuum, the molecule will dissociate into a H^+ ion and a D(1*s*) atom. A charge transfer reaction may take place near the avoided crossing at about R = 12 a.u. This region is shown in the inset. The energy gap between the $1s\sigma$ and $2p\sigma$ final states at the separate atom limit is 3.7 meV. The potential energy curves are from references [3.10] and [3.11].

in figure 3.1, occurs, the result is a dissociation of the HD^+ ($1s\sigma$) molecular ion. We have taken to calling this process ground state dissociation, or GSD.

The overall probability of this type of transition, and the probability as a function of dissociation energy can be calculated using the Franck-Condon approximation [3.1] or a reflection method [3.2,3.3], although the Franck-Condon approximation is the better one [3.4]. The Franck-Condon approximation rests on two assumptions: The first is that the electronic transition of interest takes place so quickly on a vibrational time scale that the internuclear distance remains essentially constant during the transition. The second assumption is that the electronic part of the matrix element of the transition operator depends, at most, very weakly on the internuclear distance [3.1]. These assumptions, first stated by Condon [3.5], have been profitably applied to vertical ionization and other processes for many years [3.6-3.8]. In the collisions under study in this work, the transition from the vibrational ground state of the molecule to any final vibrational state is much faster than the vibrational time of the molecule, and the Franck-Condon approximation should be valid.

Tadjeddine and Parlant [3.9], and, more recently, Ben-Itzhak *et al.* [3.4] have evaluated the GSD fraction (i.e. the relative probabilities of bound-bound and bound-free transitions from the neutral $HD(^1\Sigma^+)$ molecule to the electronic ground state of HD^+. Although differing in some numerical techniques, the two calculations are essentially similar. Since the electronic transition rate depends only very weakly on the internuclear distance, the transition rate is proportional to the square of the overlap integral between the initial and final vibrational states. In other words,

$$T_{v_f} = \left| \int_0^\infty \phi_{v_f}(R)\psi_0(R)dR \right|^2 \qquad (3.1)$$

where ϕ_{v_f} is the final bound vibrational state of $HD^+(1s\sigma)$ and ψ_0 is the vibrational ground state of $HD(^1\Sigma^+)$. Using the new method, described in section 2.2.1, to obtain the HD^+ potential energy curves [3.10] and using the H_2 curves calculated by Kołos *et al*. [3.11], for the neutral molecule, Esry and co-workers then use the Fourier grid method [3.12] to obtain the bound and continuum wavefunctions. Using the potential energy curves of H_2 instead of calculations done specifically for HD is justified by examining the work of Carrington *et al*., (discussed more extensively in section 3.3) which shows that for low lying vibrational states, the difference between HD and H_2 is negligible [3.13]. About 750 continuum states were calculated in the energy range of interest, defined by imposing the boundary condition $\phi(R) = 0$ at $R = 100$ a.u. [3.5]. The bound states are space normalized,

$$\delta_{v\,v'} = \int_0^\infty \phi_{v_f}(R)\phi_{v'_f}(R)dR, \qquad (3.2)$$

and the continuum states are energy normalized (using a Dirac delta)

$$\delta(E-E') = \int_0^\infty \phi_E(R)\phi_{E'}(R)dR. \qquad (3.3)$$

This normalization, for a discrete continuum, is analogous to multiplying the space-normalized wavefunction by a density of states factor. Therefore, if $\phi_n(R)$ is the *n*th state of the discrete continuum and is normalized as

$$\delta_{nn'} = \int_0^\infty \phi_n(R)\phi_{n'}(R)dR \qquad (3.4)$$

and $n(E)$ is the density of states in the continuum, the corresponding energy normalized state is

$$\phi_E(R) = \sqrt{\frac{dn(E)}{dE}}\,\phi_n(R). \qquad (3.5)$$

The results of this calculation for the HD isotope are shown in figure 3.2. The relative transition rates, T_{v_f}, to the final bound vibrational states peak at $v_f = 3$ and then falls with increasing v_f. This result [3.4] compares very well with the result of Tadjeddine and Parlant [3.9], although the more recent calculation included one additional bound vibrational state. From the point of view of this work, the more interesting result is the relative probability of the bound-free transitions as a function of dissociation energy. The probability of dissociation peaks at $E_k = 0$, where E_k is the kinetic energy release upon dissociation, and the width of this dissociation is about 300 meV, which is exactly the energy range in which merged-beams experiments become prohibitively difficult to perform. The accuracy of the calculation can be tested by using closure, that is, by subtracting the total transition probability to bound final vibrational states from unity. This yields a more precise GSD fraction, and comparison of the GSD fraction calculated in this manner with the one calculated by the less precise method of integrating over the continuum energy gives an estimate of the uncertainty in the calculation (about 0.036% for D_2) [3.4].

The GSD fraction should be independent of the collision velocity, as long as the collision that initiated the GSD process satisfies the Franck-Condon principle. Ben-Itzhak *et al*. measured the GSD fraction of D_2 over a range of collision velocities (see figure 3.3) and found excellent agreement with the calculated value [3.4]. This result has been subsequently verified several times in the course of this thesis work.

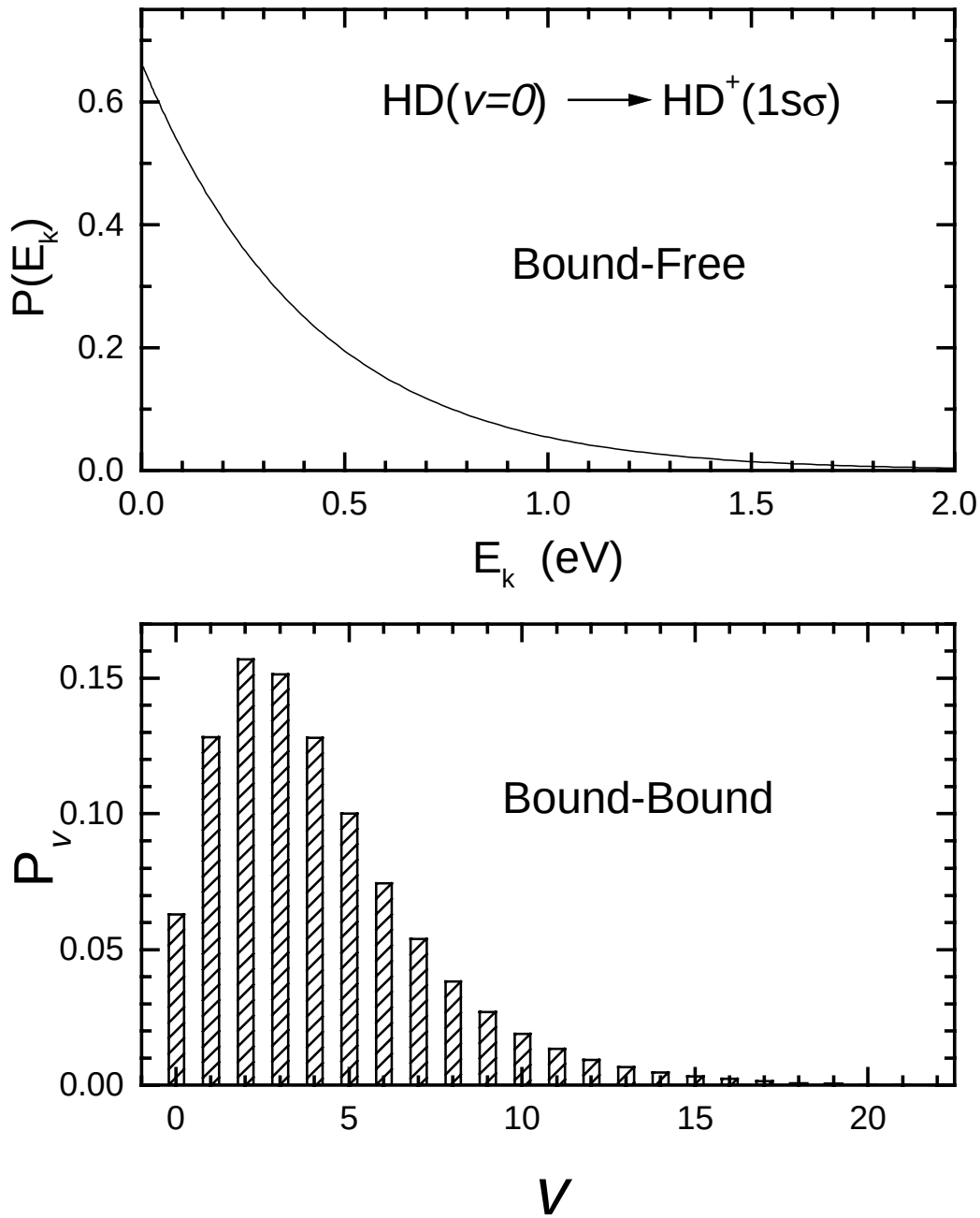

Figure 3.2: The transition probability from the HD vibrational ground state to the vibrational states (top) and vibrational continuum (bottom) of HD^+ (1sσ). Note that the width of the bound-free transitions is about 300 meV.

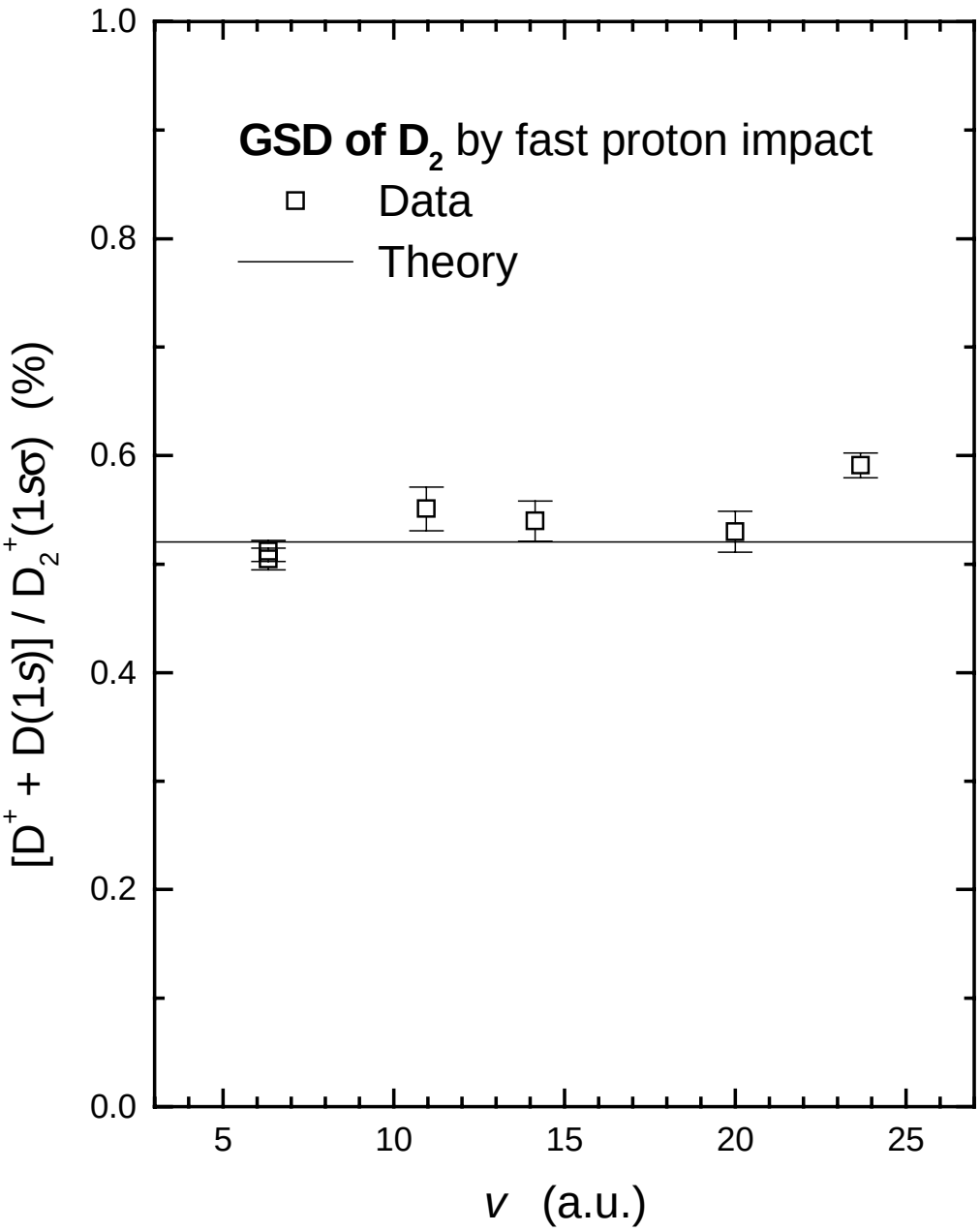

Figure 3.3: The ratio of D_2^+ ground-state dissociation to non-dissociation channels produced in proton-D_2 collisions as a function of collision velocity. From reference [3.4].

The GSD fraction is somewhat different for the different isotopes of the hydrogen molecule [3.4]. The difference in reduced mass results in the vibrational ground-state energy shifting up with decreasing nuclear mass, and the corresponding wavefuction

becoming wider. Therefore H_2, the lightest isotope, has the highest GSD fraction (see table 3.1).

Isotope	GSD Fraction
H_2	$1.4474 \pm 0.0082\%$
HD	$0.994 \pm 0.015\%$
D_2	$0.5206 \pm 0.036\%$

Table 3.1: The GSD fraction for three isotopes of the hydrogen molecule, calculated as described in section 3.1.

3.2 The Molecule as an Accelerator

In the form of the GSD process, nature has provided the experimentalist with a method of probing charge transfer at very low collision energies since the dissociation itself specifies the collision energy. The "accelerator" nature of the molecule is best illustrated by taking the derivative of the $HD^+(1s\sigma)$ potential energy curve, shown in figure 3.4. The result shows that for $R < R_0$, there is an initial strong acceleration (at $R = R_a$, 210 GeV/m!) that continues over a small range of R, followed by a weaker, but much longer lasting, deceleration.

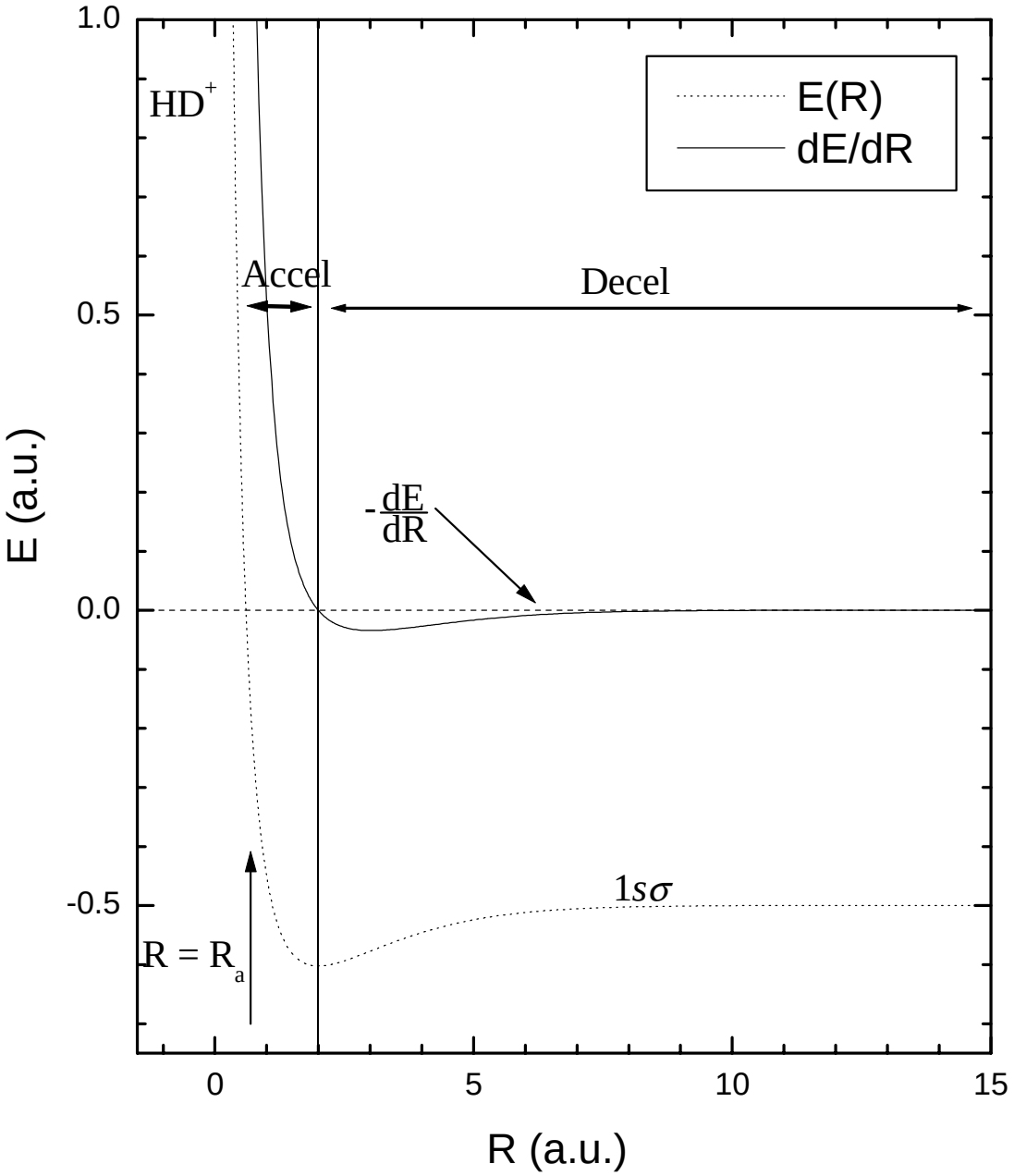

Figure 3.4: A plot of *E(R)* and *-dE(R)/dR* for the HD^+ ($1s\sigma$) adiabatic potential energy curve. The dissociating fragment initially accelerates rapidly, and then decelerates.

The exact amount of acceleration provided to the dissociating fragments by the "molecular accelerator" depends on where on the potential energy curve the dissociation

starts. This, of course, depends on the HD internuclear distance (R) at the time of the vertical transition to the HD^+ ($1s\sigma$) state. The closer R is to R_0, the smaller the acceleration, and the lower the dissociation energy. Since, as we have seen from the calculation of the Franck-Condon overlap integrals, the most likely value for R is nearest to R_0 because of the shape of the HD vibrational wavefunction (see figure 3.1), the most likely dissociation energy is just slightly above the threshold for dissociation. Thus, the GSD process provides the experimentalist with a method of reaching collision energies much lower then possible using a merged-beams technique. The molecule is an excellent low-velocity accelerator, but it is not easily tunable, at least not if an ion beam is used to pump the neutral molecule to the HD^+ electronic ground state. One experimental challenge, therefore, is to measure the dissociation energy accurately after the collision.

Another thing to realize about the GSD process is its two-step nature. The collision time for a 4 MeV proton to ionize the HD molecule is about 10^{-17} seconds. The dissociation time (defined here as the time needed to reach R = 15 a.u.) is approximately 10^{-13} seconds. Thus, the ionization is about 10,000 times faster than the dissociation, and a two-step picture (a pumping process followed by dissociation) is a justifiable one.

Finally, the GSD process always populates a known initial electronic state, the HD^+ ($1s\sigma$). If the $2p\sigma$ state is initially populated, the ionization-excitation process that results will produce fragments with higher kinetic energy, about 4 eV, and can be experimentally separated (as will be discussed in some detail in Chapter 5) from the events of interest. Since the dissociation of the electronic ground state of HD^+ is associated with the H+ + D(1s) final state, detecting a slow D^+ fragment, therefore, identifies a charge transfer in the half collision process following GSD, and detecting a slow H^+ represents the elastic channel.

3.3 Charge Transfer in Half Collisions

As the dissociation process proceeds, the electron, which is initially associated with the D nuclei, has some probability of transferring to the H nuclei. Some hints about the behavior of the electron can be found in the results of the microwave spectroscopy experiments done by Alan Carrington and co-workers at the University of Southampton [3.13-3.22]. These spectroscopic studies focus on the HD^+ molecular ion from v = 14 [3.15] to v = 22 [3.18], which is just below the dissociation limit. A conceptual picture of their apparatus is shown in figure 3.5. Their work clearly shows the breakdown of the Born-Oppenheimer approximation by measuring (for example) microwave transitions between the vibrational states of the $1s\sigma$ and $2p\sigma$ electronic states of HD^+. The spectroscopic measurements for high vibrational states agree with *Ab initio* calculations only if corrections to the Born-Oppenheimer approximation are included. This result is illustrated in figure 3.6.

The spectroscopic work also highlights the localization of the electron around the deuteron for higher vibrational states nearing the dissociation limit. Using the hyperfine multiplet splitting as a measuring tool, a large asymmetry (with the electron favored to be near the deuteron) was found for the v = 21 and v = 22 states [3.22], which are just 1.26 meV and 0.053 meV [3.23, 3.24] below the dissociation threshold, respectively. The lower v = 16 to 18 states, which lie 187.75 to 74.156 meV [3.23] below the dissociation threshold respectively, were found to be essentially symmetric in their electron distribution [3.15].

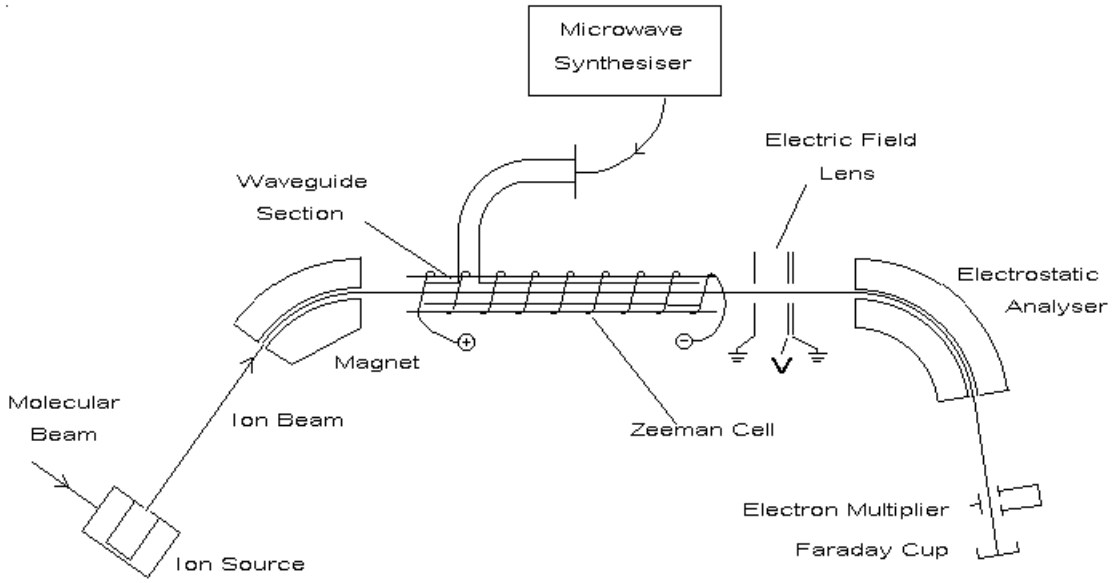

Figure 3.5: A simplified block diagram of the ion beam system used by Carrington *et al*. The ion beam is mass analyzed by the magnet and passes through a microwave region followed by an electric field lens. Fragments formed after the mass analyzer are separated from parent ions using an electrostatic kinetic energy analyzer and are detected by an electron multiplier. Figure adapted from reference [3.21].

When considering the possibility of charge transfer above the dissociation threshold, it is clear that the transfer is energetically forbidden for the first 3.7 meV above the threshold, below the energy of the $2p\sigma$ state at the separate atom limit. Above the H(1*s*) threshold, however, there should be some mixing of the $1s\sigma$ and $2p\sigma$ states. The mixing should asymptotically approach equal probabilities for the two dissociation limits as the energy above the H(1*s*) threshold increases. The population within the energy gap between the D(1*s*) and H(1*s*) final states will cause a preference for the H^+ + D(1*s*) channel, but the size of this preference in not immediately clear, since the gap is so small in comparison to the range of dissociation energies produced by the GSD process. The work of Carrington *et al*. [3.15] suggests, in fact, that the asymmetry will vanish completely within 70 meV of the H(1*s*) threshold, which is much smaller than the 300 meV width of the bound-free transitions shown in figure 3.2. Given the relative energy widths of the GSD process, and the gap between the H(1*s*) and D(1*s*) final states, one

could even reasonably guess that the asymmetry in the H(*1s*) and D(1*s*) final states would not be measurable. If this is in fact the case, the usefulness of the GSD process as an experimental probe of charge transfer at very slow collision energies is greatly reduced.

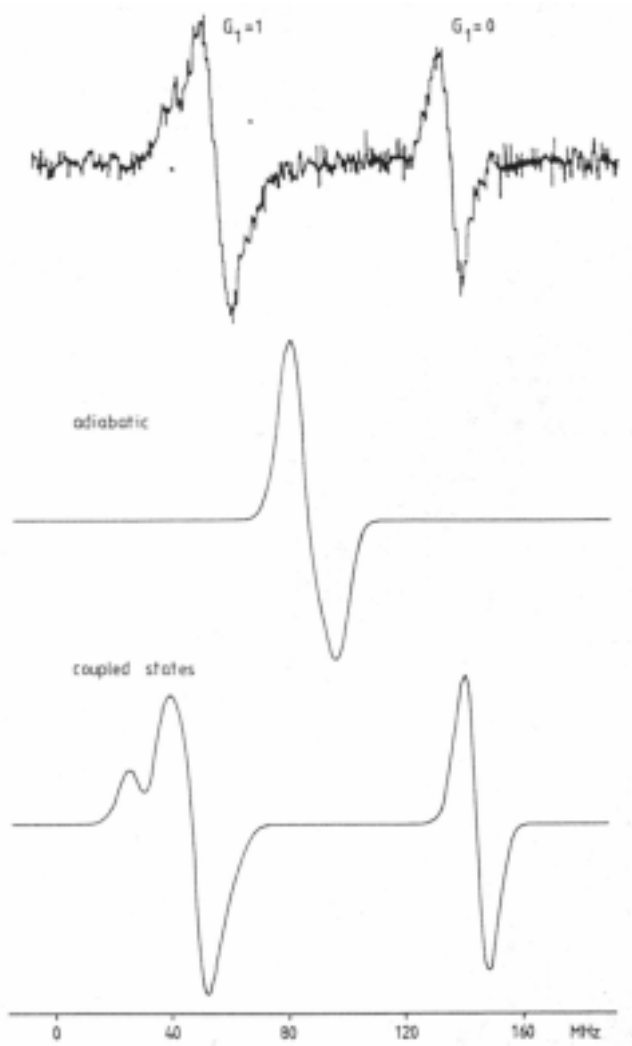

Figure 3.6: Experimental results of Carrington *et al*. The microwave spectroscopy spectrum clearly shows agreement with the calculations (bottom) that have been corrected for the breakdown of the Born-Oppenheimer approximation in HD^+. The middle figure, an adiabatic calculation without corrections for the finite nuclear mass, clearly does not fit the experimental data. Figure is from reference [3.16].

As a first attempt at determining quantitatively the amount of charge transfer that will result from the GSD process, we have applied a model first developed by Walter Meyerhof to explain K-shell vacancy sharing in near symmetric heavy ion collisions

[3.25]. Meyerhof constructed an analytic formula, based on the charge transfer model of Demkov [3.26], for the transition probability, *w*, of an electron (or vacancy) between two nearly degenerate energy levels. The question Meyerhof was considering was this: If a vacancy was created for the $2p\sigma$ molecular oribital through rotational coupling at small internuclear separation (via $2p\sigma$-$2p\pi$ rotational coupling), what is the probability that the vacancy will be promoted to the $1s\sigma$ molecular orbital which correlates to the K-shell of the heavy atom collision partner? Starting with Demkov's formulation, Meyerhof was able to show, "after considerable algebra" [3.25] that the transition probability, *w*, could be written as

$$w = \frac{1}{1 + e^{|2x|}}, \tag{3.6}$$

where

$$x = \frac{\pi\left(I_1 - I_2\right)}{v\ \sqrt{8m_e I}} \tag{3.7}$$

and

$$v = \sqrt{\frac{2E_k}{\mu}}\ . \tag{3.8}$$

I_1 and I_2 are the K-shell binding energies of the colliding atoms, v the collision velocity, μ the reduced mass of the system, and I is some average binding energy, defined by Meyerhof to be

$$\sqrt{I} = \frac{1}{2}\left(\sqrt{I_1} + \sqrt{I_2}\right). \tag{3.9}$$

Equation (3.6) leads to the "two-passage" transfer probability deduced by Demkov [3.26] with the exception of an interference term that is only appropriate for a full collision system. For comparison, Demkov's transition probability is

$$w_D = 2w(1-w) = \frac{1}{2}\sec h^2(x). \qquad (3.10)$$

At first glance, the Meyerhof formulation for K-shell vacancy sharing might seem to have little to do with our half collision problem. A more careful consideration, however, suggests it might be somewhat useful as a first approximation. First, it is a model for a half, or "single pass" collision. Interference between charge transfer "on the way in" and "on the way out", which is treated in both the Demkov and Landau-Zener models, is not applicable to our problem. Second, the energy levels in the K-shell vacancy problem can be roughly scaled down to the levels in the H^+ + D(1s) half collision. That is, the kinetic energy release in the GSD of HD^+ is usually much larger than the 3.7 meV gap between the H(*1s*) and D(*1s*) final states, just as the difference in K-shell levels was much smaller than the collision energy in the problem Meyerhof was considering. Finally, while the algebra needed to derive the Meyerhof model is complex, the final result is easy to apply.

There are some assumptions in the Meyerhof model that should be noted. First, the formulation assumes a straight-line trajectory for the collision, and there will be deviations from this at low velocities that are not accounted for by the model. Second, and more importantly, the model has an inherent ambiguity in its energy scale, since it is not clear if the collision velocity defined in equation 3.8 should be defined relative to the H(*1s*) or D(*1s*) energy limit. The validity of Meyerhof's model for K-shell vacancy sharing was tested by the *Ab initio* calculations of Taulbjerg *et al*., who concluded that

Meyerhof's excellent agreement with experimental results is due to the mutual cancellation of effects from the approximations and model assumptions used in his derivation [3.27].

We have applied Meyerhof's model by using the dissociation limits of H(*1s*) and D(*1s*) for I_1 and I_2, which results in

$$w = \frac{1}{1 + e^{\frac{0.010416}{\sqrt{E_k}}}}, \tag{3.11}$$

and then convoluted this result with the bound-free transition probabilities, $P(E_k)$, as a function of dissociation energy. The product $wP(E_k)$ integrated over the entire range of dissociation energies gives the overall probability for charge transfer resulting in a D^+ + H(*1s*) final state, while integrating the quantity $(1 - w)P(E_k)$ yields the probability of a H^+ + D(*1s*) final state. The results are shown in Table 3.1. While the results obtained from the Meyerhof model are encouraging, suggesting a measurable asymmetry in the GSD process, there are enough problems with the assumptions made in the Meyerhof model, particularly at very low dissociation energies, that a more complete calculation is desirable.

Final State	Probability (Relative to total HD^+ production)
H^+ + D(*1s*)	0.529%
H(*1s*) + D^+	0.465%

Table 3.2: The probability of H^+ and D^+ final states relative to the HD^+ final state that result from the GSD process as predicted by a Meyerhof model.

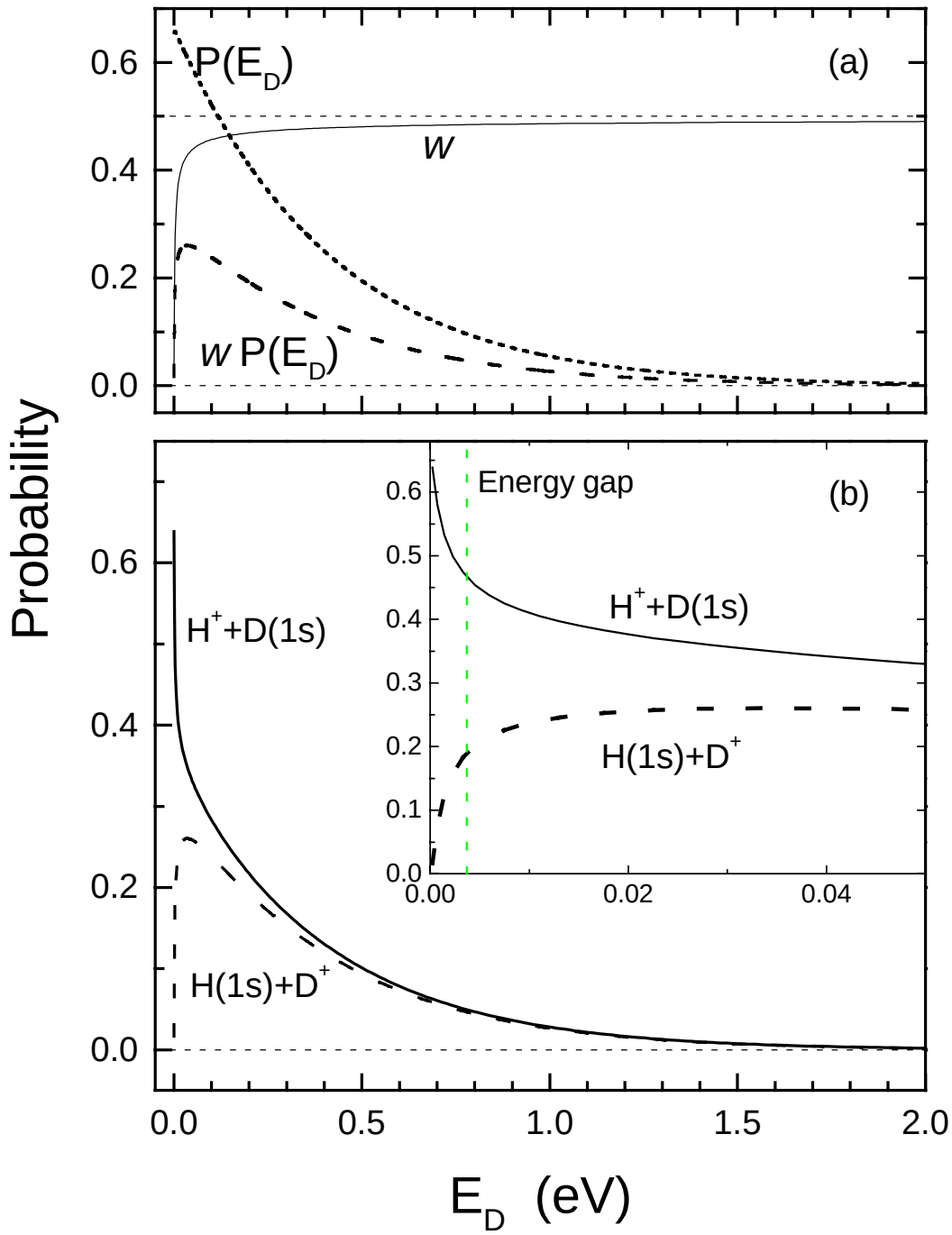

Figure 3.7: (a) The transition probability, w, calculated using the Meyerhof model. When convoluted with the P(Ek) curve, calculated from the Franck-Condon overlap integrals (section 3.1), the result is the probability of charge transfer as a function of kinetic energy, $wP(E_k)$. (b) The probabilities, as a function of dissociation energy, of the H^+ and D^+ final states in the GSD process. Note that the Meyerhof model does not deal correctly with the energy threshold.

Brett Esry has recently provided a full quantum mechanical treatment of this two-state coupled channel problem. Using the adiabatic potential energy curves calculated in reference [3.10], Esry solved the coupled channels problem using a variational R-matrix formulation with incoming-wave boundary conditions (see, for example, reference [3.28]). The boundary conditions for the two channels are provided by the dissociation limits of the H(1*s*) and D(1*s*) final states, in other words, the incoming flux is all in one channel or the other. A stationary state constructed using the energy-normalized physical incoming wave state [3.28] has outgoing waves asymptotically only in a single channel. Besides being relevant to our case, this type of calculation is used to describe photoionization where the electrons emerging from a single channel are detected. The Franck-Condon transition from the neutral molecule is taken into account by projecting these states onto the ground state of the neutral HD molecule. The transition probability, *w*, to the H(1*s*) + D^+ final state obtained with this calculation is shown in figure 3.8. To obtain $w(E_k)$, shown in figure 3.8, we have used the calculated cross sections for charge exchange and elastic scattering to arrive at

$$w(E_k) = \frac{\sigma_{exchange}(E_k)}{\sigma_{elastic}(E_k) + \sigma_{exchange}(E_k)}. \qquad (3.12)$$

While these new calculations can best be compared with our experimental results and the Meyerhof model (more on this in chapter 6) by looking at the charge exchange channel, in many respects the elastic channel is more interesting since resonances appear in this channel below the H(1*s*) threshold. Two types of resonances might appear. First, shape resonances, illustrated in figure 3.9, may appear when the energy is just slightly below the centrifugal barrier height. In this case, the incident particle is temporarily trapped in a metastable level. Second, the minimum in the $2p\sigma$ curve near R = 12 (see

figure 3.10) allows the temporary transition to the $2p\sigma$ level for energies just below the H(1s) threshold. This situation, called a Feshbach resonance, is analogous to the transient formation of doubly excited states during an electron-atom collision. A series of resonance structures appear in the elastic channel for different values of *l*. Resonances calculated near threshold for $l = 0$ and $l = 2$ are shown in figure 3.11.

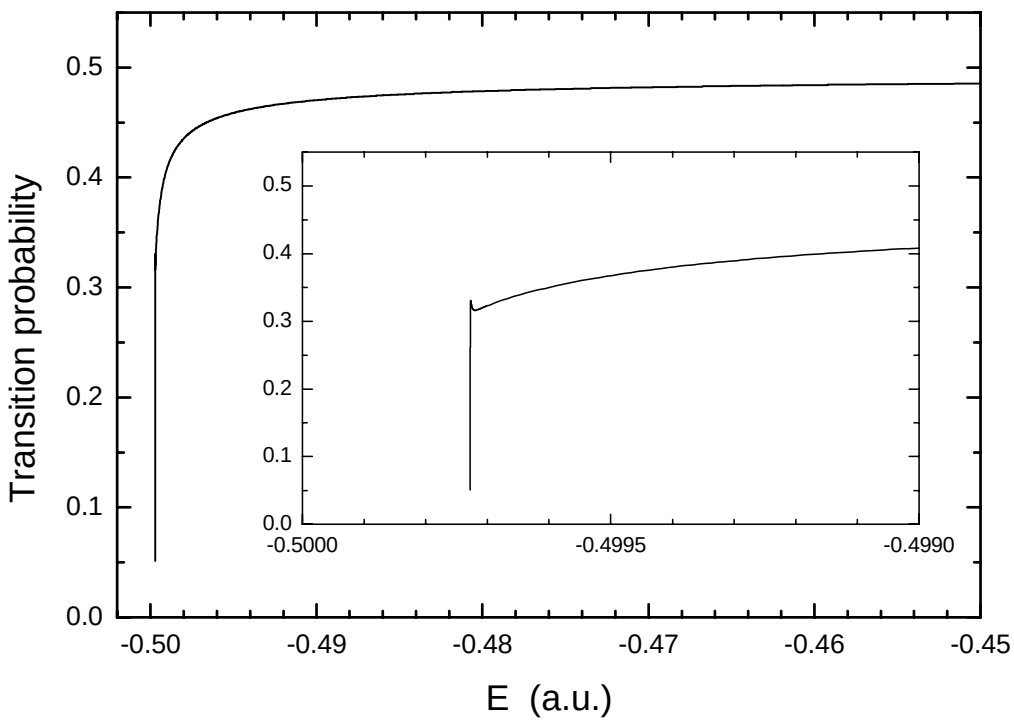

Figure 3.8: The transition probability, w, from the initial H^+ + D(1*s*) state to the final H(1*s*) + D^+ state calculated by Brett Esry. The inset shows an expanded view of the threshold region.

Our form of $w(E_k)$, given in equation (3.12) follows the derivation of Meyerhof [3.25] and can easily be compared to the experimental data (see chapter 6). It is different, however, than the standard definition of a transition probability which many theorists use:

$$\sigma_{1\to 2} = \frac{\left|S_{21}\right|^2}{k_1^2}. \tag{3.13}$$

Our definition has the effect of eliminating much of the structure that would be seen, for example, from shape resonances in high *l* channels, since the structure would appear in both the elastic and the charge exchange channel, and would be cancelled out in equation (3.12).

Since the coupled channels part of the half collision is calculated in essentially the same manner as Esry *et al*. [3.29] used for the full collision system (see Section 2.2.2), experimental results for the half collision system can be used to probe the validity of the calculation techniques for both the half and full collision systems.

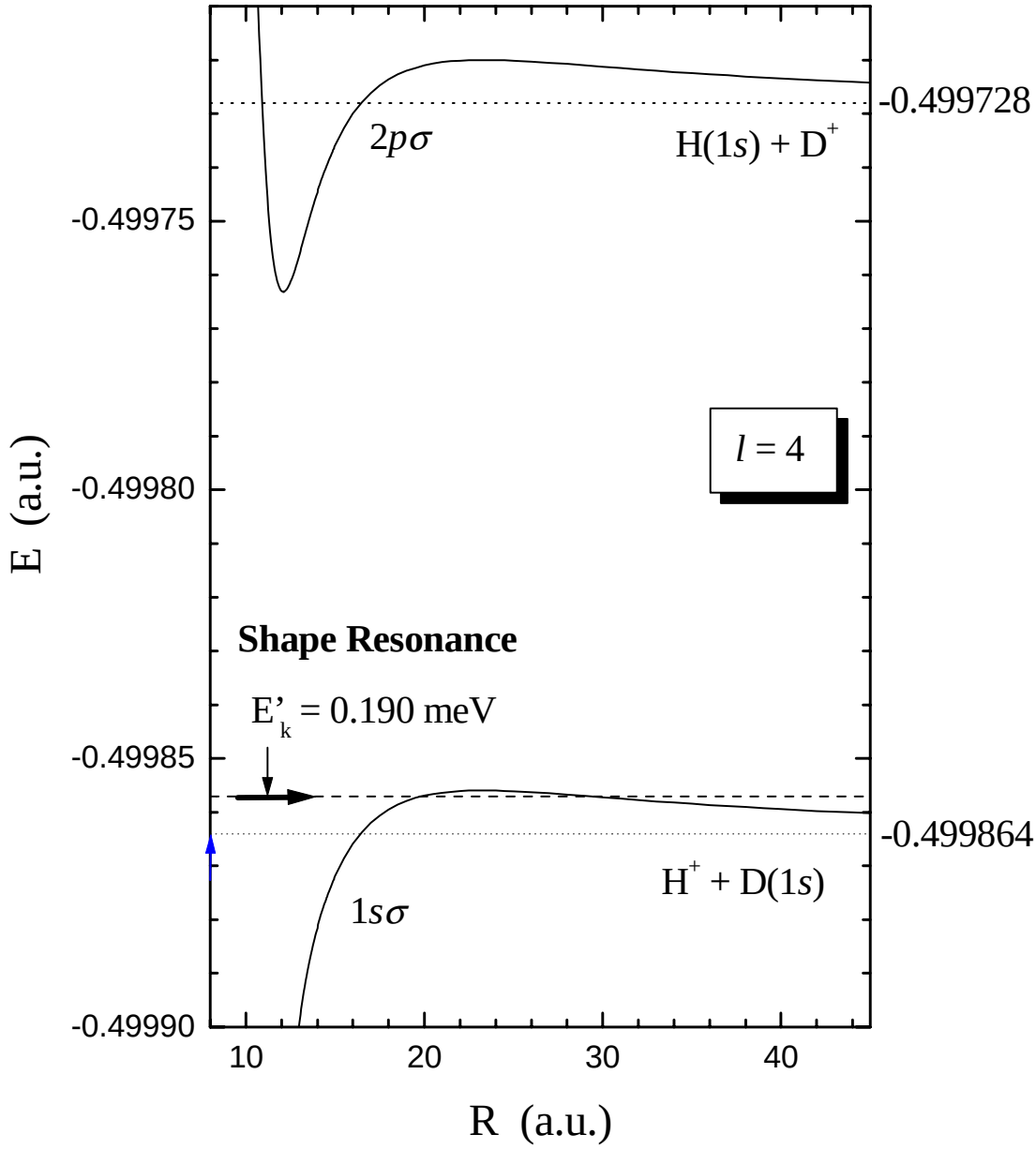

Figure 3.9: An expanded view of the energy gap between the 1sσ and 2pσ potential energy curves. A shape resonance, located 0.190 meV above the D(1s) limit for l = 4, is illustrated.

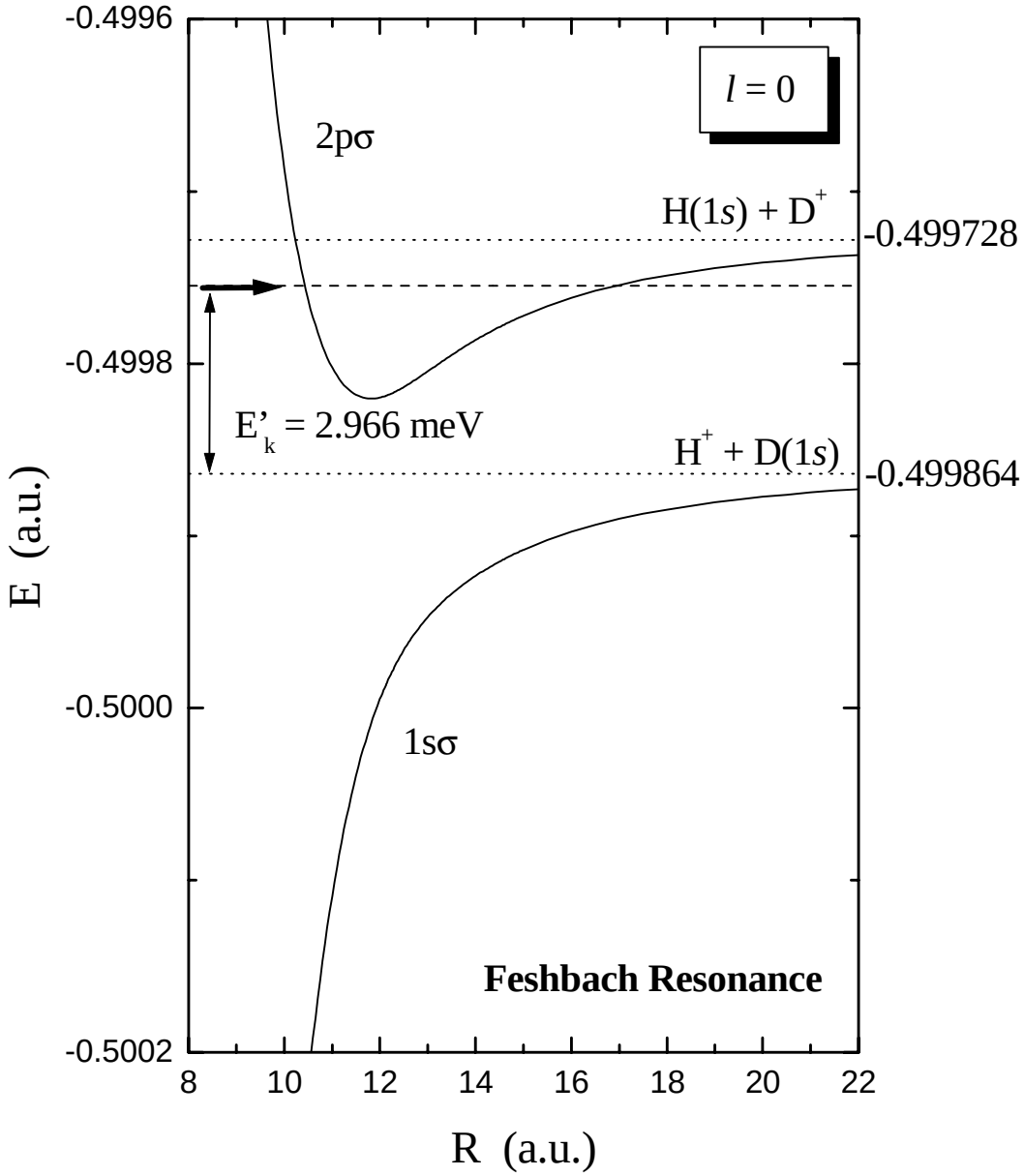

Figure 3.10: An expanded view of the energy gap between the 1sσ and 2pσ potential energy curves. A Feshbach resonance, located 2.966 meV above the D(1s) limit for l = 0, occurs when the outgoing particle temporarily crosses the upper $2p\sigma$ curve.

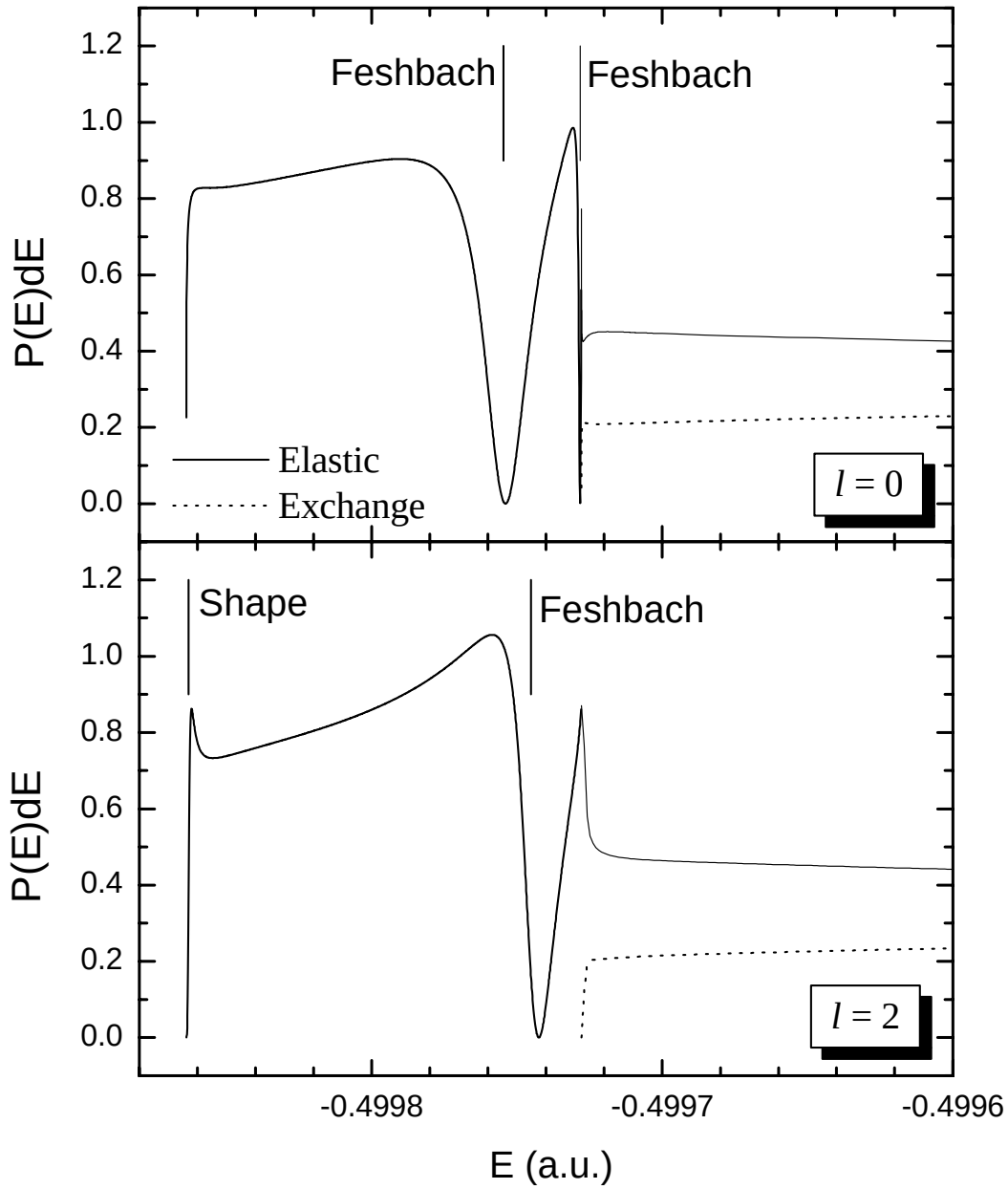

Figure 3.11: Calculated probability for charge exchange (dotted lines) and the elastic scattering (solid lines) for $l = 0$ (top) and $l = 2$ (bottom). The vertical lines mark the positions of resonance structures.

Chapter 4

So far in this dissertation, we have emphasized the fundamental reasons to study the charge transfer process using Ground State Dissociation of the HD^+ molecular ion. Understanding the physical process involved and providing an empirical test of the calculations is, of course, our primary interest. As with many atomic and molecular physics processes [4.1], however, the H^+ + D(1*s*) process we are studying has applications to other fields. In this chapter, a brief summary of a few, more applied problems connected to this work will be presented.

4.1 Aeronomy

The escape of gas species from atmospheres is an important problem in aeronomy [4.2]. In particular, momentum exchange in charge transfer interactions between abundant isotopic hydrogen neutrals and hot ionospheric protons regulate the neutral hydrogen distribution and escape from the terrestrial atmosphere [4.3,4.4], as well as Venus [4.5-4.8]. Measurements of the exospheric D/H ratio in Earth's atmosphere indicate that the total abundance of D relative to H is enhanced by about a factor of 3 compared to seawater [4.9]. This interesting result implies that, since the relative escape

rates of D and H are expected to be about ¾ the ratio found in seawater [4.9], the escape of D from the exosphere is suppressed by a factor of 4 relative to H. A possible explanation of this phenomenon was set forth by Hodges and Breig [4.10]. They examined the dominant non-thermal collision interactions affecting exospheric deuterium, namely electron transfer and elastic scattering in $H^+ + D(1s)$ and $D^+ + H(1s)$ collisions below 10 eV. They reproduced the calculations of Hunter and Kuriyan (see Section 2.2.2) [4.11] in order to obtain temperature dependent rate coefficients for the charge exchange reactions. Their results indicate that the $H + D^+ \rightarrow H^+ + D$ reaction is the most likely source for production of hot escaping D, and the traditional exosphere approximation treating charge transfer as a "fly-by" process, having negligible momentum transfer, was invalid. Due to this large momentum transfer, the charge transfer reaction is effective in destroying cold D, and at elevated ion temperatures, the reverse reaction is a significant source of hot deuterium atoms in planetary exospheres. An exact quantitative explanation of the low terrestrial exospheric enhancement of the D/H ratio has not been found due to the need for ionosphere-exosphere coupling models [4.10], but it is clear that the $H + D^+ \rightarrow H^+ + D$ reaction plays a significant role in the exosphere.

4.2Astrophysics and Cosmology

Atomic and molecular processes contribute to the study of astrophysics in a myriad of ways [4.12]. For example, understanding the chemistry of deuterium in the post-recombination era of the early universe is important when trying to evaluate the

observed D/H ratio. Using this ratio, it is possible to derive constraints on the primordial deuterium, or, equivalently, on the allowed range of the baryon-to-photon ratio according

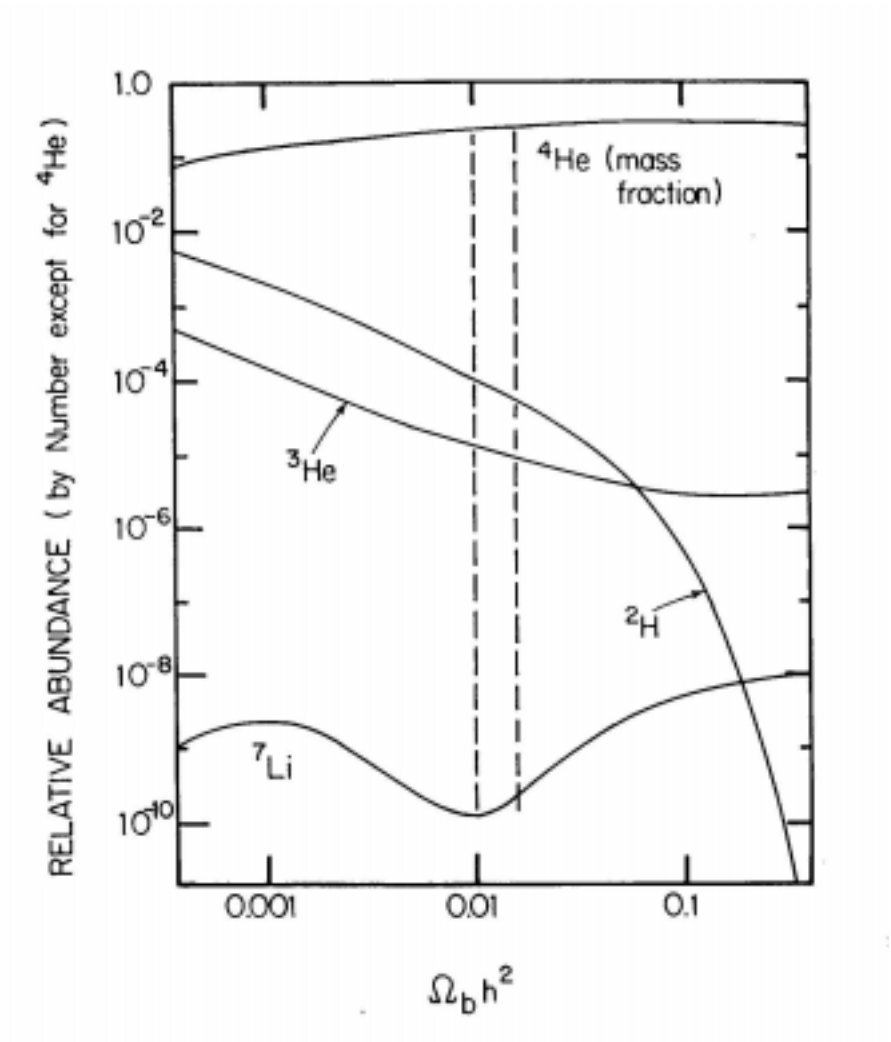

Figure 4.1: The production of light elements according to a big bang nucleosynthesis model. The relative abundance of D sets a limit on the primordial baryon density ($\Omega_b = 0.013 \pm 0.003h^{-2}$ [4.15], $\Omega_b = 0.019 \pm 0.001h^{-2}$ [4.16], where h is the Hubble constant). The figure is taken from reference [4.14].

to standard big-bang nucleosynthesis [4.13-4.18]. Besides the implications to studies of big bang nucleosynthesis, deuterated molecules in interstellar clouds provide a source of information on the fractional ionization in a cloud, and the galactic ionizing flux [4.19,4.20]. Additionally, the formation of deuterated molecules (HD in particular) in the

gas phase has an effect on the cooling mechanisms of the primordial gas and on the shocks that led to structure formation, such as galaxies and globular clusters [4.12, 4.21].

Measurements of D/H are made by selecting an interstellar cloud in the direction of a suitable quasar (for example, QSO 1009 + 2956 in the study done by Burles and Tytler [4.16].) and measuring the absorption spectrum using high-resolution spectroscopy. The result of this observation is then input into various models that predict the total D/H ratio, which may be different than the observed D/H ratio, since some D and H can exist in forms not suitable for observation by spectroscopic methods. As a result, understanding the chemistry of the interstellar medium is important, particularly in cases where the nuclear d/p ratio could be different than the atomic D/H ratio.

Charge transfer between D and H^+ (or D^+ and H) is one of the first steps in the formation of many deuterated molecules [4.12,4.21-4.23]. For example, the primary mechanism for HD formation in interstellar clouds is believed to be the sequence

$$H^+ + D \rightarrow H + D^+ \qquad (4.1)$$

followed by

$$H_2 + D^+ \rightarrow HD + H^+ \qquad (4.2)$$

[4.22-4.23]. HD plays a role in producing many other deuterated molecules. Understanding the deuterium chemistry in the early universe requires the formulation of a complicated model with many separate chemical reactions, for example 144 in reference [4.23]. Rates for all of the many contributing reactions need to be determined if the relative abundance of these deuterated molecules is to be evaluated. Because of the limited number of processes involved in HD formation, the abundance of HD in diffuse interstellar clouds serves as a key diagnostic for models of other molecules with more

complicated origins [4.24]. Having an accurate calculation of the charge transfer cross section in H^+ + D(1s) collisions is therefore important, because an error could propagate throughout a model.

In many astrophysical models it is assumed that the reactions

$$H^+ + D(1s) \rightarrow H(1s) + D^+, \qquad (4.3)$$

and

$$H(1s) + D^+ \rightarrow H^+ + D(1s) \qquad (4.4)$$

are equally likely. If, however, the energy of the collision is below about 0.1 eV (~ 1000 K), this is not valid. The ratio of the cross sections of the first reaction to the second, *R*, has been fitted by Galli and Palla [4.22] as

$$R = e^{-\frac{43}{T}}, \qquad (4.5)$$

where T is the temperature of the gas in Kelvin (the temperature is associated with the kinetic energy above the hydrogen ground state). This expression goes to 1 at high temperature, for which the charge transfer proceeds in both directions at the same rate. However, below about 200 K this approximate expression underestimates the calculated ratio *R*, as can be seen from figure 4.2. Note that this ratio is very smooth in contrast to the structure seen in the cross sections for each individual reaction shown in figures 2.7 and 2.8. We have shown [4.25] that to understand this smoothness and derive a simple analytic form for this ratio one should note that for two coupled non-degenerate states the cross section is given by

$$\sigma_{if} \propto \frac{1}{k_i^2}\left|S_{fi}\right|^2, \qquad (4.6)$$

with a similar expression for the second reaction. Thus,

$$R = \frac{\sigma_{12}}{\sigma_{21}} = \frac{\frac{1}{k_1^2}}{\frac{1}{k_2^2}} = \frac{E - E_{H(1s)}}{E - E_{D(1s)}} . \qquad (4.7)$$

This expression, in contrast with the fit of Galli and Palla [4.22], is exact over the entire energy (temperature) range, as long as there are only two channels dominating these reactions. In addition to being exact, the equation is as simple to apply as the fit used by Galli and Palla [4.22].

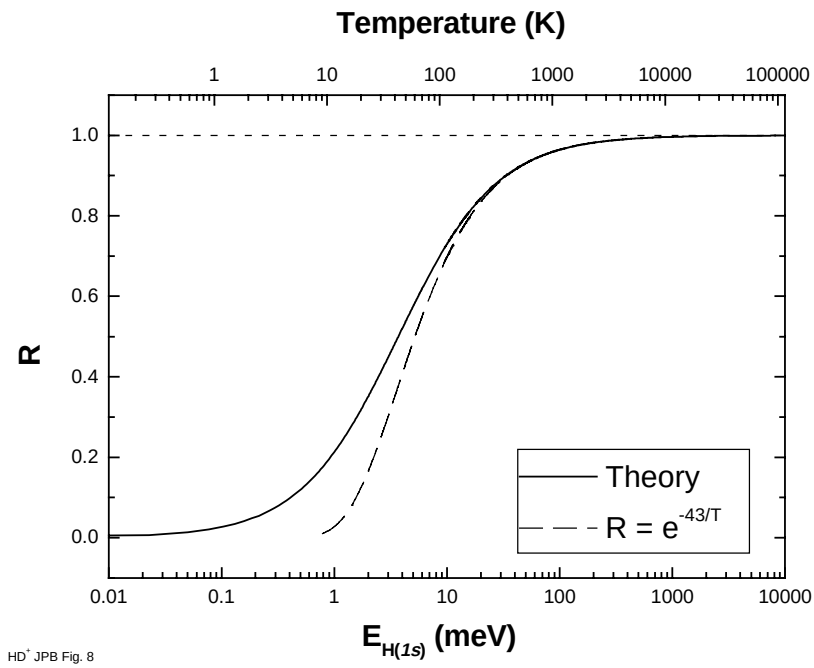

Figure 4.2: A comparison between equation 4.7 and the fit used by Galli and Palla [4.22].

Reactions that could contribute to a difference between the atomic D/H ratio and the nuclear D/H ratio are of particular interest, and are called deuterium fractionation mechanisms. One such reaction is the dissociative recombination (DR) of H_2D^+ below 10 meV of incident electron energy. The final states of this reaction are:

$$H_2D^+ + e \rightarrow H + H + D$$
$$\rightarrow HD + H$$
$$\rightarrow H_2 + D. \qquad (4.8)$$

Larsson and co-workers showed, in an experiment performed at CRYRING, an ion storage ring at the Manne Siegbahn Laboratory, that the branching ratio of the two-body final states of equation 4.8 differs from what would be expected statistically. The hydrogen atom is less likely to be found in a molecular final state than is the deuterium atom [4.26].

Branching ratio of dissociative recombination of H_2D^+		
Final Channel	Measured Branching Fraction	Relative Difference from Statistical two-body breakup
H + H + D	0.73	-
HD + H	0.20	+ 11%
H_2 + D	0.07	- 22%

Table 4.1: Results of the experiment by Larsson *et al.* [4.26]. If the dissociative recombination results in a two-body breakup, the deuterium atom is more likely to form a molecule than the hydrogen atom.

The Ground State Dissociation process we are studying is the breakup of a HD^+ molecular ion into a one-electron atom and a nuclei,

$$HD^+(E = 1s\sigma, v = \infty) \rightarrow H^+ + D(1s)$$
$$\rightarrow H(1s) + D^+. \qquad (4.9)$$

While the HD^+ molecular ion is most likely to remain in a bound vibrational state after the vertical ionization of one electron, the two breakup channels that result from reaching the vibrational continuum are not predicted to be equally likely, either by the coupled channel calculation or an application of the Meyerhof model (see section 3.3).

Predicted Branching Ratio of HD^+ Ground State Dissociation		
Final State	Meyerhof Branching Ratio	Coupled Channels Branching Ratio
$H^+ + D(1s)$	0.537	0.542
$H(1s) + D^+$	0.463	0.457

Table 4.2: Predicted branching ratio of the dissociation $HD^+(v = \infty)$. The lower energy final state is more likely, meaning that it is more likely to produce a D(1*s*) atom from this GSD process than a D^+ ion.

If this prediction is correct, and the H^+ + D(1*s*) final state is preferred, the question then turns to the astrophysical significance of this reaction. A high-energy proton is relatively rare in an interstellar medium compared to an electron with energy of a few eV; so one might reason that the chances of the GSD reaction being initiated are small compared to the dissociative recombination reaction of equation 4.8. The relative abundance of the targets, however, is also different, as can be seen in figure 4.3. The implications of the GSD process as a possible deuterium fractionation mechanism need to be investigated further, since it is possible that the larger abundance of HD makes the GSD process significant, even though the asymmetry in the branching ratio is smaller.

The GSD process can be initiated by any ionizing mechanism, as long as the resulting single ionization is fast enough that it satisfies the Franck-Condon conditions. Once the vertical ionization is accomplished, the resulting dissociation should be independent of the ionizing mechanism. The most likely way to start the GSD process in an interstellar medium is by electron impact. Cosmic rays have enough energy to ionize many atoms and molecules in an interstellar cloud, and the ionized electrons that result have enough energy to subsequently interact with other atoms and molecules. This is the usual source of the electron in equation 4.8, and that dissociative recombination reaction has been shown to be significant in analysis of observations of the D/H ratio in

interstellar clouds [4.25]. While a fast electron impact will probably result in a GSD process that is indistinguishable from the process generated by the fast proton impact in this study, the effect on the GSD process if an electron of about 25 or 30 eV is used to initiate the process is unknown, and would be an interesting candidate for further study. In fact, as the electron energy gets closer to the dissociation threshold, the asymmetry in the branching ratio might be expected to increase, since the width of the energy gap between the H(1*s*) and D(1*s*) states becomes relatively larger when compared to the kinetic energy release in the GSD processes. If that process generated a larger deuterium fractionation mechanism than is predicted for the GSD process initiated by heavy particle impact, it would be of considerable interest due to its applications to astrophysics [4.27].

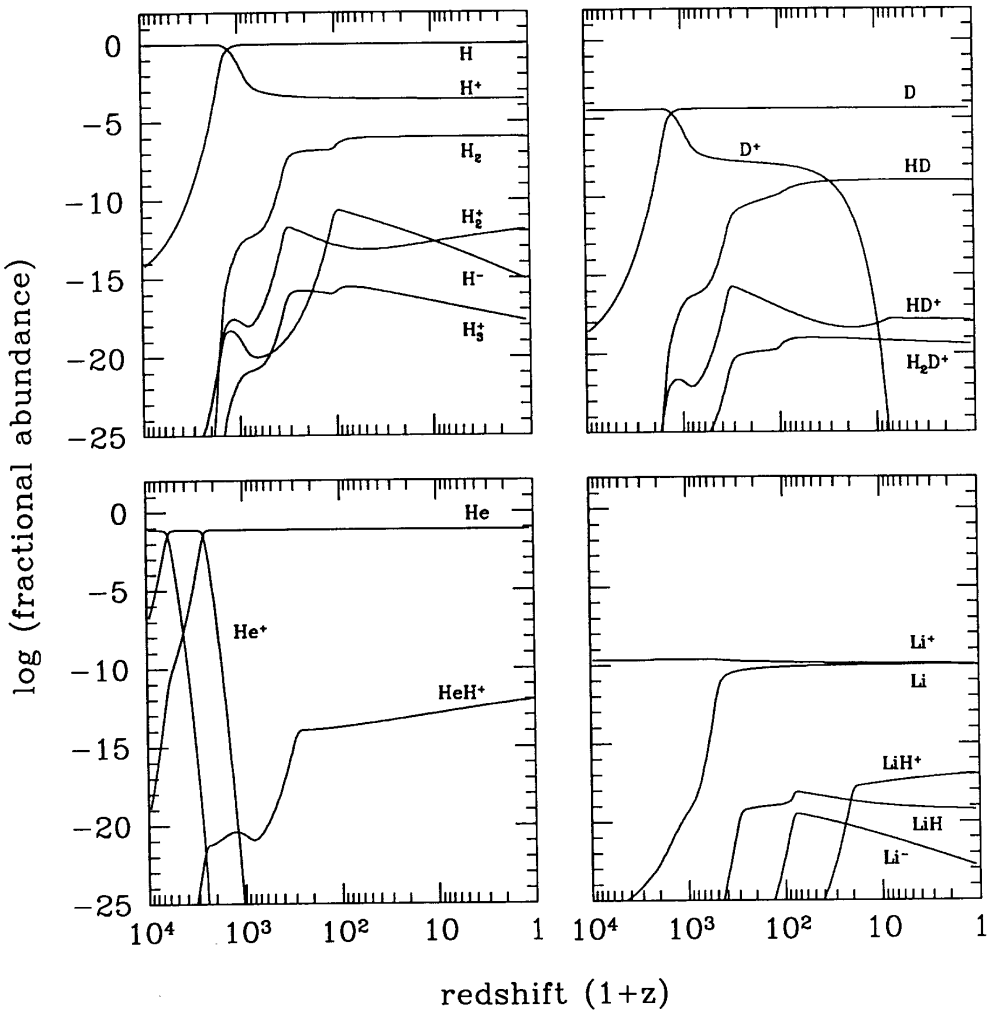

Figure 4.3: Relative fractional abundance of the chemical species considered in the standard model. Note that the HD molecule is several orders of magnitude more common than the H_2D^+ molecular ion studied in the experiment of Larsson *et al.* [4.25]. The figure is taken from reference [4.22].

Chapter 5

This chapter will detail the experimental technique we have used to study the Ground State Dissociation process. There are two main goals of this study. The first goal was to measure the asymmetry in the two possible dissociation channels of GSD, H^+ + D(1*s*) and H(1*s*) + D^+, regardless of the dissociation energy of the fragments. Once we verified that the asymmetry was measurable, as predicted by the theoretical models discussed in chapter 3, our second, and more important, goal was to develop a technique to measure the yield of dissociating fragments as a function of the kinetic energy release. This measurement would be a much more powerful test of the "half collision" calculations presented in chapter 3, and could measure the charge transfer probability in the H^+ + D(1s) system at collision energies almost two orders of magnitude lower than had previously been reported [5.1].

Some experimental techniques are common to both the integrated and differential measurements, and in fact, some of the techniques developed for the differential measurement were used to make a more precise measurement of the asymmetry integrated over all dissociation energies. The experimental techniques, however, can be broken into two different approaches. The first approach is to measure the time-of-flight of the dissociating ions. This technique was sufficient to make an integrated

measurement of the yield of dissociating fragments. To measure the energy of the dissociating fragments, we implemented a momentum imaging technique that incorporates many of the principles of Cold Target Recoil Ion Momentum Spectroscopy [5.2-5.4]. The main points of the two experimental techniques will be discussed in this chapter, while the more technical details will be relegated to appendices.

5.1 Single Ionization and Competing Processes

We used a fast ion to ionize the molecular hydrogen target. Any ion with enough velocity so the Franck-Condon approximation is valid can be used in this experiment, since the only function of the ion is to rapidly remove an electron. When a fast heavy ion is used to initiate the GSD process, however, there are several competing processes and these processes do depend on the velocity and charge of the projectile. If the projectile gives sufficient energy to the neutral HD molecule, the vertical ionization could reach one of the many excited electronic states of the HD^+ molecular ion. Since all of these curves are dissociative within the Franck-Condon region, they result in H^+ or D^+ fragments, just as GSD does. Other possibilities include double-ionization, producing $H^+ + D^+$ ion-pairs, and dissociative electron capture.

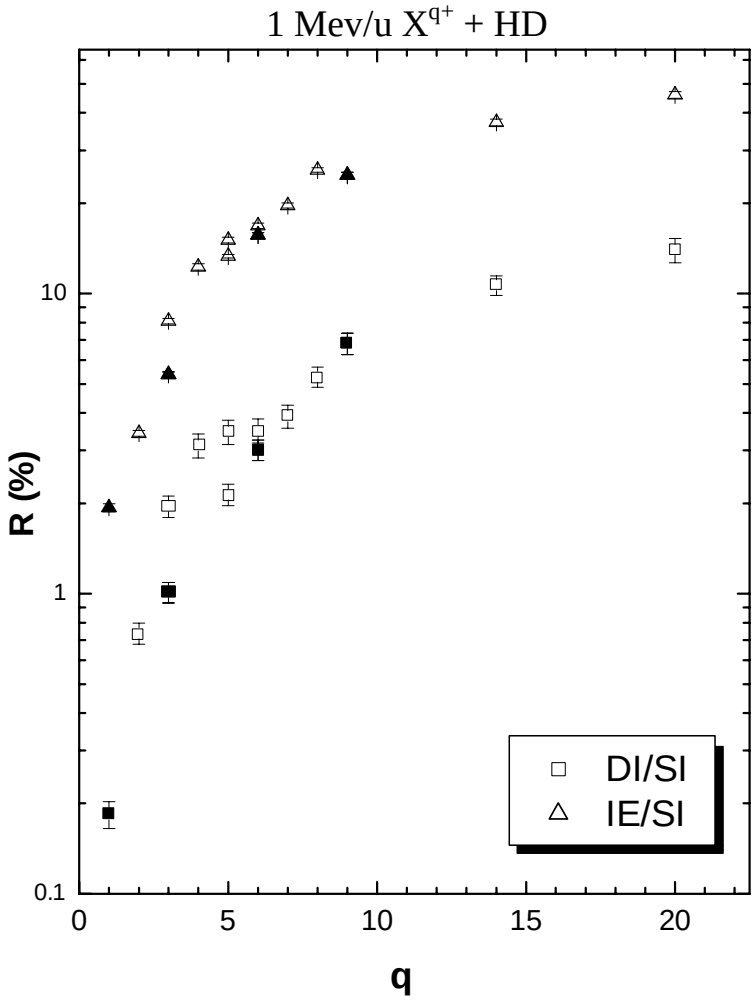

Figure 5.1: The ratios (R) of ionization-excitation to single ionization (IE/SI), and double ionization to single ionization (DI/SI) of hydrogen molecules by fast projectiles as a function of projectile charge. For all of the data shown in this figure, the projectile velocity corresponds to 1 MeV/amu. The solid symbols represent bare projectiles H^{+}, Li^{3+}, C^{6+} and F^{9+}. The open symbols are "dressed" Li^{2+}, C^{3+}, C^{5+}, $F^{4\text{-}8+}$, Cu^{14+}, and Cu^{20+} projectiles. This data is from reference [5.5].

The competing processes may be limited by choosing a projectile that produces the smallest amount of ionization-excitation (IE) and double ionization (DI) relative to single ionization (SI). For this reason, we typically use a fast proton beam, since it is the projectile with the lowest available charge. When seeking to limit the amount of ionization-excitation and double ionization, increasing the velocity is less critical than

picking a projectile with a low charge. The increase in both the IE/SI and DI/SI ratios is significant for change in the projectile charge of q = 1 to q = 2, as can be seen in figure 5.1, while increasing the velocity has a smaller effect (see figures 5.2 and 5.3). For protons, the ratio of double- to single-ionization is about 0.18% for a 1 MeV projectile [5.5], and falls to 0.13% for a slightly higher projectile energy [5.6]. The same trends are true for the ionization-excitation case for which the ratio of ionization-excitation to single ionization is 1.95% at the high velocity limit [5.5,5.7]. Finally, by choosing an ion with a few MeV/amu as the projectile, electron capture by the projectile is extremely unlikely, so dissociative capture processes are not a concern.

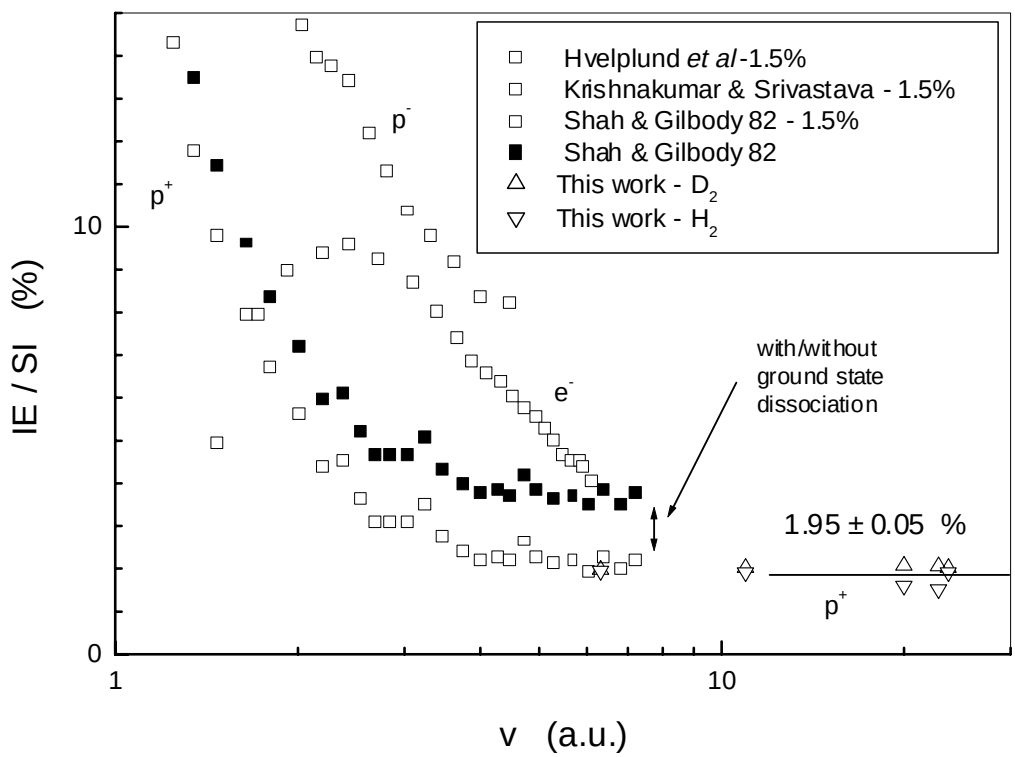

Figure 5.2: The ratio of ionization-excitation to single ionization of hydrogen molecules by proton impact as a function of projectile velocity. This figure is from reference [5.6].

While picking an appropriate projectile can limit the background of ionization-excitation and double-ionization, it does not eliminate them. Furthermore, GSD is itself a small process relative to the total amount of single ionization (about 1% for HD), and as a result other characteristics of the competing dissociative processes must be used to separate them experimentally. As was noted in chapter 3, the kinetic energy released in the GSD process is quite small, typically below 1 eV (see figures 3.2 and 5.4). The kinetic energy release of the competing processes, however, is much larger [5.8, 5.9] (see figure 5.4) and so the GSD process is identifiable by the low kinetic energy of the resulting fragments. The experimental method used to measure GSD, therefore, should allow discrimination against the higher energy fragments produced in ionization-excitation and double-ionization.

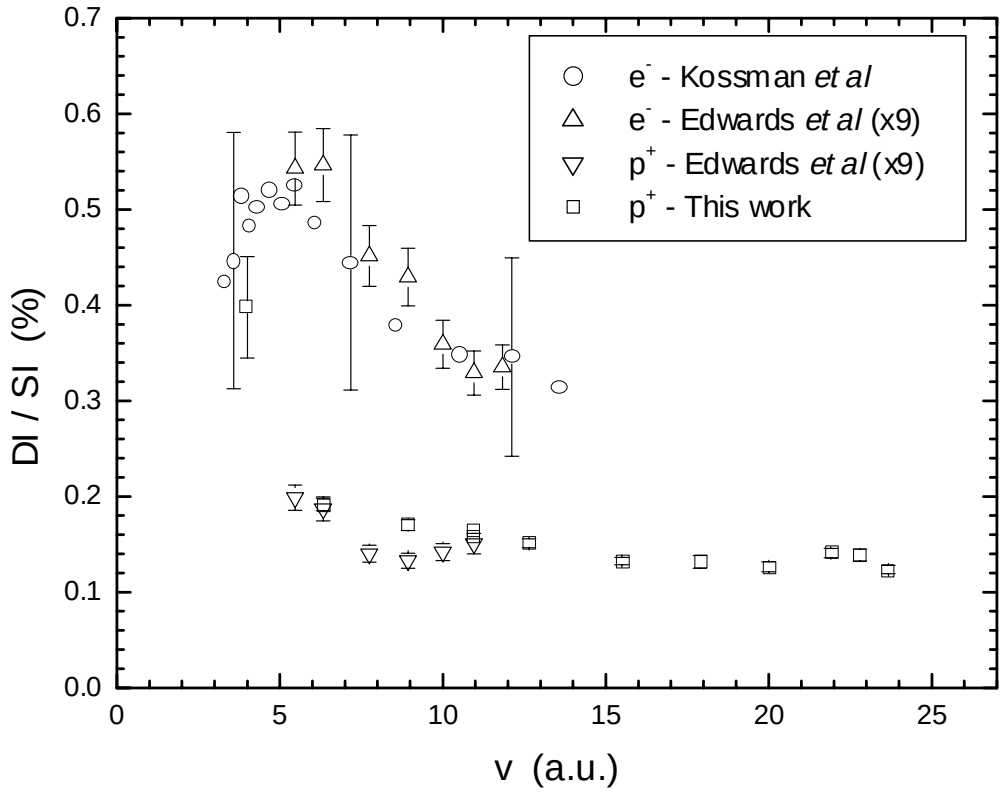

Figure 5.3: The ratio of double- to single-ionization of hydrogen molecules by proton impact as a function of projectile velocity. From reference [5.7].

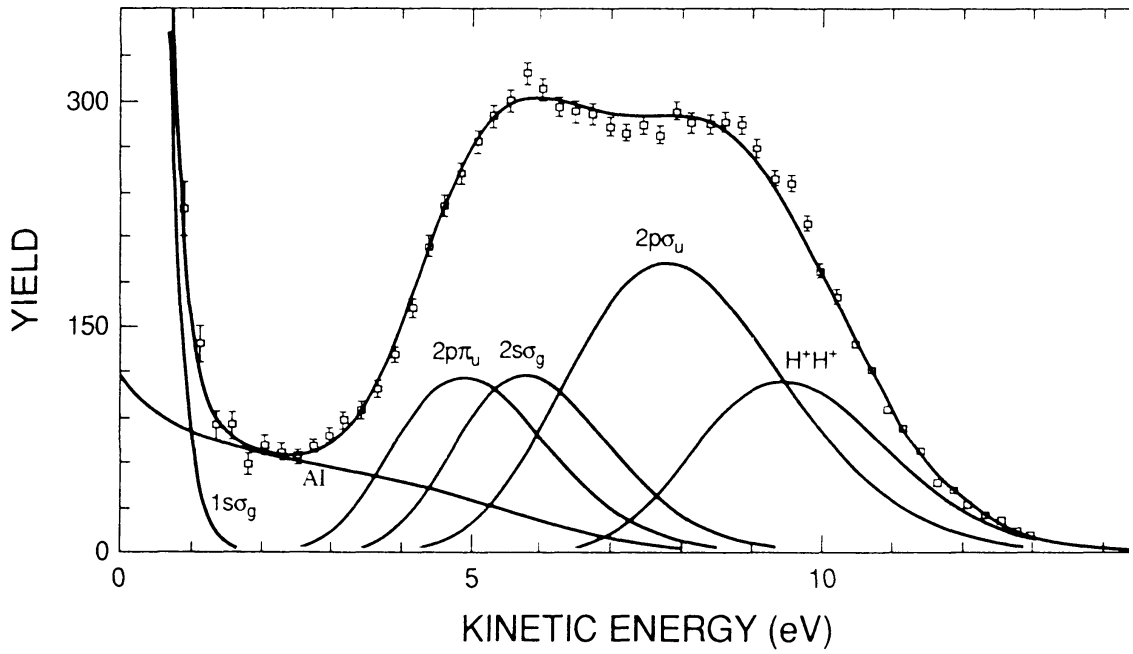

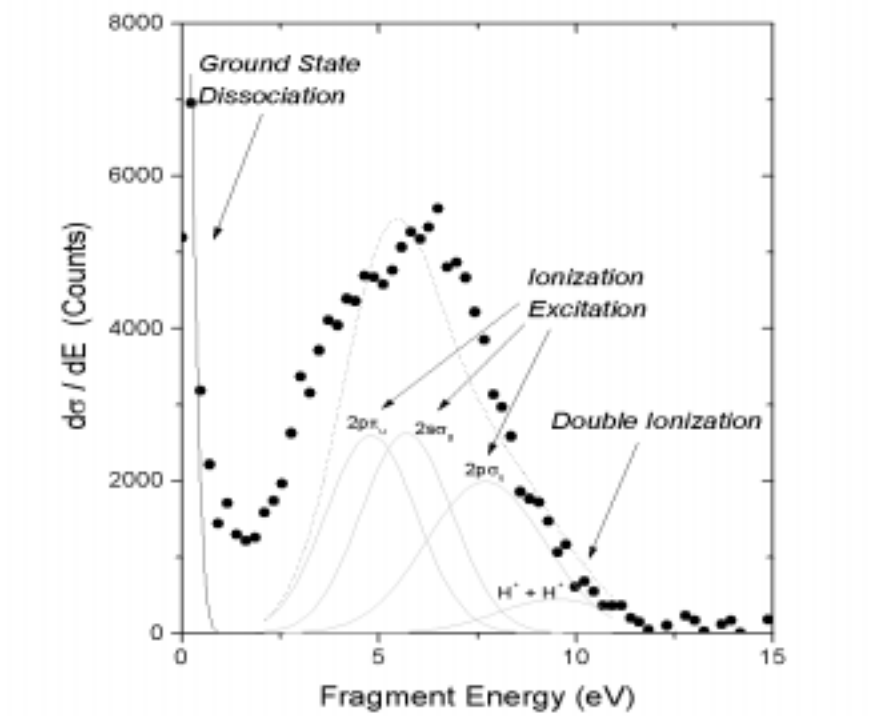

Figure 5.4: Fragment yield as a function of kinetic energy release for various dissociative processes. The top figure is the results from Edwards *et al.* [5.8] for the H_2 isotope, the bottom picture the results of Landers for D_2 [5.9]. Note that for either isotope, the GSD process (labeled $1s\sigma_g$ in the Edwards figure) is well separated in energy from the ionization-excitation channels.

5.2 General Experimental Considerations

As mentioned briefly above, we have developed two experimental methods to measure different aspects of the GSD process. First we describe elements common to both techniques, and then the details of the different methods.

The ion beam is accelerated by the EN Tandem Van de Graaff accelerator, collimated, and directed into a target region containing the HD gas target. When an ionizing collision happens in the target region, the ions are extracted by the electric fields of the spectrometer toward a recoil ion detector. Both experimental techniques use a bunched beam as a time reference. The main advantage of using bunched beam mode is that the experiment can be conducted at a higher rate, since the reference signal from the buncher clock provides the stop signal for measuring the time-of-flight of the recoil ions. If a projectile detector had to be used to provide a stop signal for the time-of-flight measurement, it would take weeks (or months!) of continuous accelerator time to collect data for a single extraction voltage that we took in 8 to 12 hours because of the limited counting rate of such detectors. See Appendix A for more information on bunched beam operations.

The detection efficiency for all recoil ions must be equal for an accurate measurement of the $H^+ + D(1s)$ to $H(1s) + D^+$ branching ratio. To ensure this was the case in our experiment, we accelerated the recoil ions to an energy above 3 keV just before hitting the front plate of the highly amplifying Z-stack micro-channel plate recoil ion detector. In addition, the lower level discrimination (LLD) of the constant fraction discriminator was set sufficiently low to accept all recoil ion signals (see figure 5.5). To

verify that the efficiency was the same for all ions, we checked that the ratio of He^{2+}/He^{+} for 4 MeV proton impact agreed fairly closely with the measurement of Knudsen *et al*. [5.10]. To ensure there were no discrimination effects due to recoil ion velocity, we measured the ratio of $\frac{H^+}{H_2O^+}$ as a function of the LLD setting and the detector voltage, and conducted the measurements well into the region where this ratio was constant. Appendix C.3 summarizes these efficiency checks.

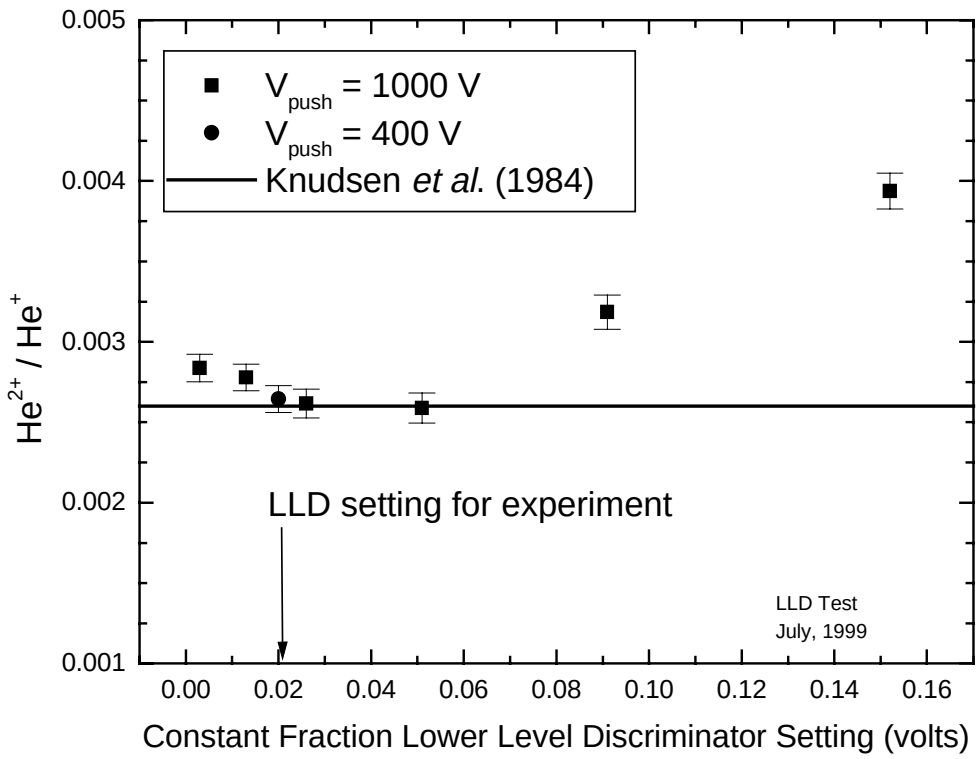

Figure 5.5: The ratio of He^{2+} to He^{+} as a function of the constant fraction lower level discriminator setting for 4 MeV proton impact. The solid line is the measured value of Knudsen and co-workers [5.10]. The error bars represent statistical errors only.

The recoil ions are identified by their mass to charge ratio using a time-of-flight technique (TOF $\propto \sqrt{\frac{m}{q}}$). For example, a typical time of flight spectrum measured with a weak extraction field is shown in figure 5.6. Under weak extraction field conditions,

most of the higher energy fragments miss the detector, while all of the molecular ions, which typically have thermal energies, are collected. In order for a higher energy fragment to reach the detector, the molecule must be oriented at the time of the collision in such a way that the resulting fragment has an initial velocity toward (or away from) the recoil detector. These "fast" fragments will either have a shorter (or longer) time-of-flight than the low energy molecular ions or GSD fragments. The fast fragments appear in the spectrum as shoulders around the $m/q = 1$ and $m/q = 2$ time-of-flight peaks. The low energy fragments of interest in this study are in the narrow center peak of the time-of-flight spectrum (see fig. 5.6). The extraction field strength must be chosen so that all of the molecular ions and fragments from GSD are collected, but most of the higher energy events from competing processes miss the detector or are separated in time from the low energy ions.

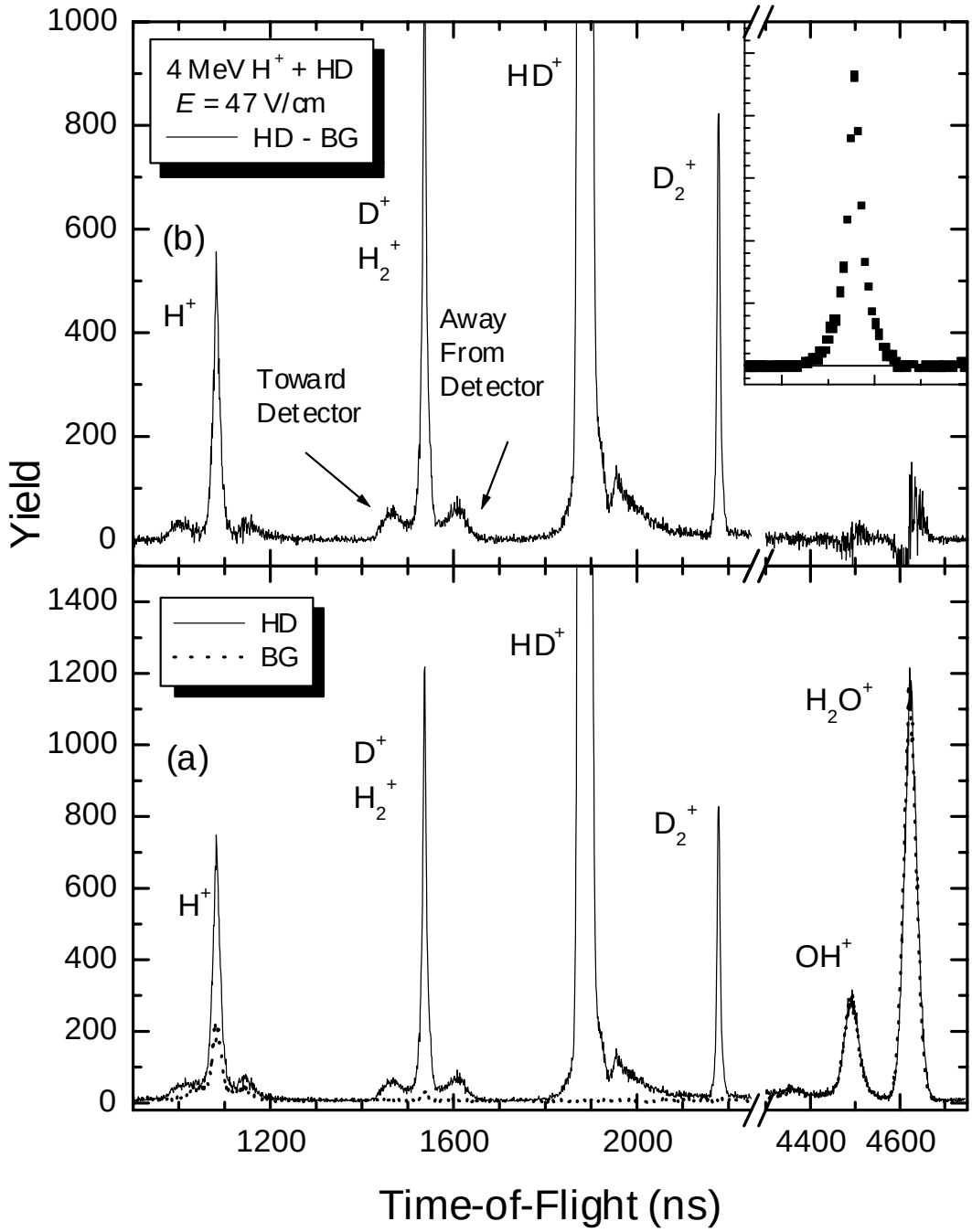

Figure 5.6: (a) Time-of-flight spectra for a HD target and background. (b) The remaining spectrum after the background components is subtracted. The inset shows the *m/q* = 2 peak after the "shoulders" of fragments from ionization-excitation and double-ionization are subtracted.

All measurements are carried out under single collision conditions as determined by a standard pressure dependence measurement. When a low extraction field is used, additional care must be taken to keep the target pressure very low, to ensure that no chemical reactions forming H_2D^+ or HD_2^+ occur before the recoil fragments exit the target cell. If such a reaction occurs, the H_2D^+ recoil ions are indistinguishable from the D_2^+ recoils ions in our time-of-flight spectrum. We verify that no reactions of this type occur by the absence of the $m/q = 5$ peak associated with HD_2^+ formation in the time-of-flight spectrum.

In addition to the H^+, D^+ and HD^+ recoils ions of interest in our studies, one can see in figure 5.6(a) contributions from water molecules and H_2 and D_2 contaminants in the HD bottle. The residual water vapor in the vacuum system contributes H^+ and H_2^+ fragments to the H^+ and D^+ peaks of interest, and thus it needs to be subtracted. To subtract this contribution, two measurements, with and without the HD target, are conducted, and then the background contribution, which is mostly residual water vapor, is subtracted after proper normalization of the area of the H_2O^+ peaks in both spectra. Since the two measurements are made under identical conditions, all contributions from the residual water are removed from the $m/q = 1$ and $m/q = 2$ peaks, where the H^+ and H_2^+ fragments from water overlap the H^+ and D^+ fragments from HD. The H^+ fragments of water are the major source of uncertainty in the evaluation of the $m/q = 1$ peak, while the H_2^+ fragments of water are only a minor source of error in the $m/q = 2$ peak (especially relative to the H_2 contamination in the HD bottle). The resulting time-of-flight spectrum, after the subtraction of the water background, is shown in figure 5.6(b).

One of the major experimental challenges in this experiment is to determine the amount of H_2 contamination in the bottle of HD target gas, since the H_2^+ fragments that

result from single ionization of the H_2 impurity contaminate the D^+ fragmentation channel. It is difficult to obtain a pure bottle of HD since over time the HD gas will recombine via $HD + HD \rightarrow H_2 + D_2$ until the three isotopes are present in equal amounts (see figure 5.7). It could be assumed from detailed balance that the amount of H_2 and D_2 contamination would be the same, but this is only true if the initial contamination of H_2 and D_2 are the same at the time the bottle is sealed. For this reason, negotiating with the specialty gas supplier to obtain a "fresh" bottle becomes an important part of the experiment. Appendix B examines the H_2 contamination problem in some detail, and discusses various methods to evaluate the contamination level.

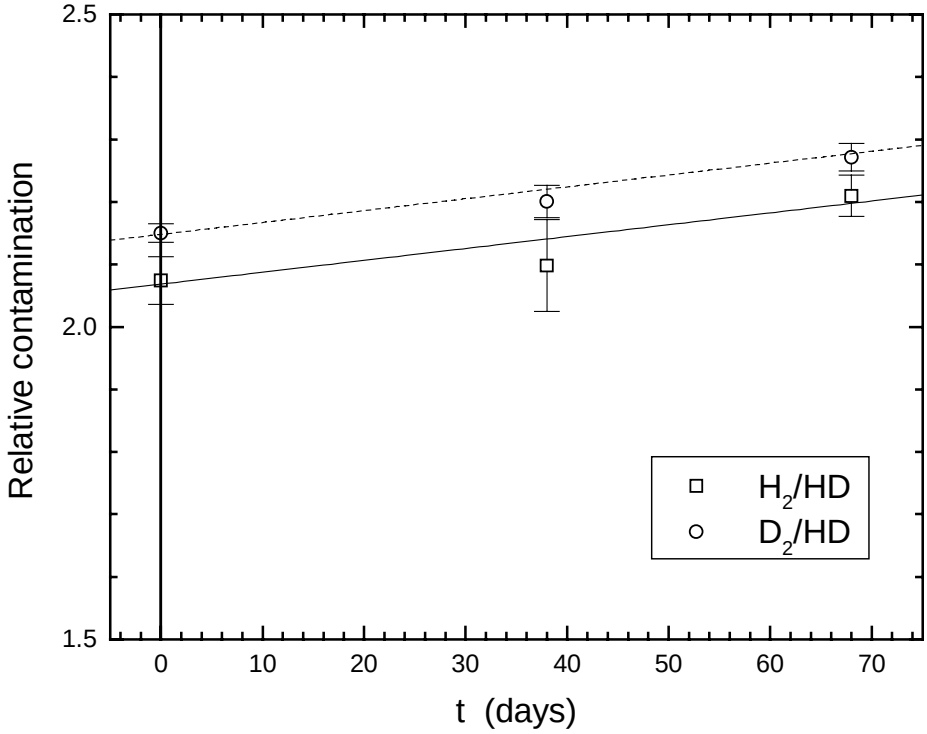

Figure 5.7: The increase in the relative H_2 and D_2 contaminations (in %) in a HD bottle over time.

Data acquisition and analysis tasks are performed on Digital VaxStation 4000s, in concert with dedicated Motorola MVME single-card computer front ends (running the pSOSystem real-time OS) attached to CAMAC electronics. The XSYS data acquisition

system is used to record the time-of-flight and (if applicable) the position of each recoil ion on an event-by-event basis. In the case of the momentum imaging measurement technique, the recoil ion momentum and energy are calculated from the time-of-flight and position information. The XSYS data analysis code for both the time-of-flight and momentum imaging techniques are included in Appendix I.

Both the time-of-flight and the momentum imaging experiments were done on Tandem Beamline L2 in the square room of the Macdonald Laboratory. Dimensions of L2 are given in Appendix H.

5.3 Time-of-Flight Method

The first measurements of the GSD process were made using the coincidence-time-of-flight method used in previous studies of ion-molecule collisions by our group. These methods have been discussed in detail in other publications [5.5-5.7, 5.11-5.13] and the development of this technique was not a part of this thesis work, aside from small adjustments made specifically for the measurement of the GSD process. Therefore, only a brief summary of this method will be presented here. A bunched proton beam was accelerated to 3 or 4 MeV/amu by the EN Tandem Van de Graaff accelerator, collimated, and directed into a target cell containing a thin deuterium hydride gas target. Recoil ions produced in the target cell were extracted and accelerated toward a Z-stack micro-channel plate detector by a uniform electric field in a time-of-flight spectrometer [5.11]. The time-of-flight spectrometer used was a two-stage Wiley-McLaren [5.14] design, and by choosing the correct ratio of voltages in the extraction and acceleration region, time

focusing conditions (see Appendix E) can be achieved for any length drift region [5.13,5.14].

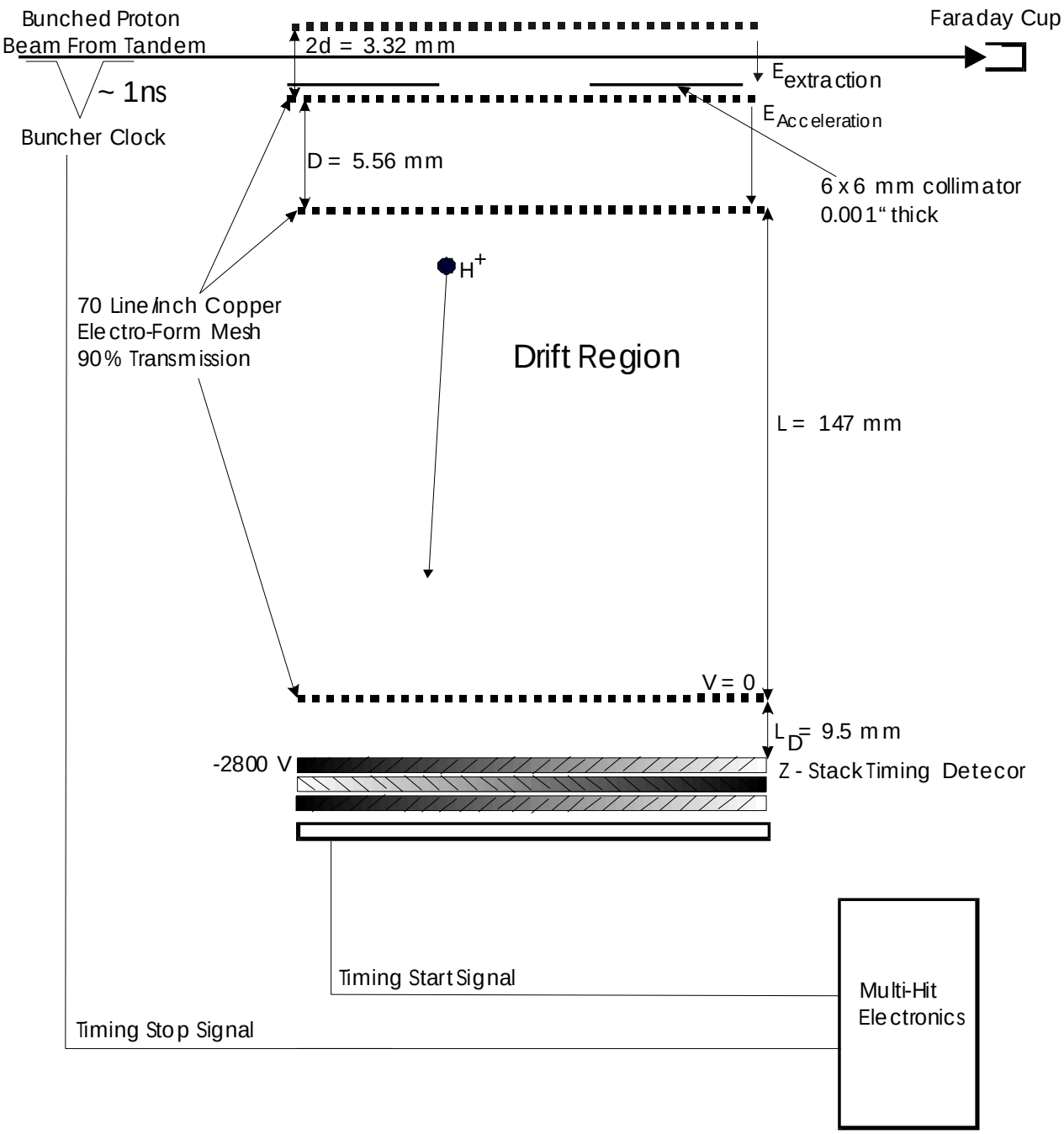

Figure 5.8: A schematic picture of the time-of-flight spectrometer used in these measurements.

The time-of-flight of the different ions was recorded by a multi-stop system relative to a common start signal synchronized with the beam bunch. The multi-stop

signal allowed double-ionization events to be identified, since they produce two recoil ions. The multi-hit electronics used either a Fast Timing Signal Sorter (FTSS) [5.15] or a multi-hit time-to-digital converter [5.11]. The electronics scheme for both this method and the momentum imaging method presented in section 5.4 are discussed in Appendix D.

Using a weak extraction field to discriminate against the IE and DI resulting from recoil ions (see figure 5.9), the GSD fragments and molecular ions are gathered on the micro-channel plate detector, and the resulting time-of-flight spectrum is shown in figure 5.6. The contributions from residual water vapor in the target region are subtracted as described in the previous section. The shoulders on the left and right hand side of the low energy center of the m/q = 1 and m/q = 2 peaks must also be subtracted to make an accurate measurement of the low energy ions in the center peak. These shoulders originate from fragments with a higher energy that have an initial velocity toward (or away from) the detector and are thus shifted in time from the GSD fragments or molecular ions. The shoulders are subtracted by fitting a second order polynomial to the baseline. This procedure is shown in figure 5.10. Figure 5.10(a) shows a typical m/q = 2 peak after the water contributions have been subtracted. The points in the center are removed in (b), and the shoulders are fit with a second order polynomial. The curved baseline fit in (b) is then subtracted from (a) leaving the peak without the shoulders (c). The area of the peak can then be evaluated with a simple numerical integration. It should be noted that the resulting peak does not have a simple shape (for example, Gaussian or Lorenzian) and peak fitting results in a systematic error, usually an underestimate of the GSD fragment yield.

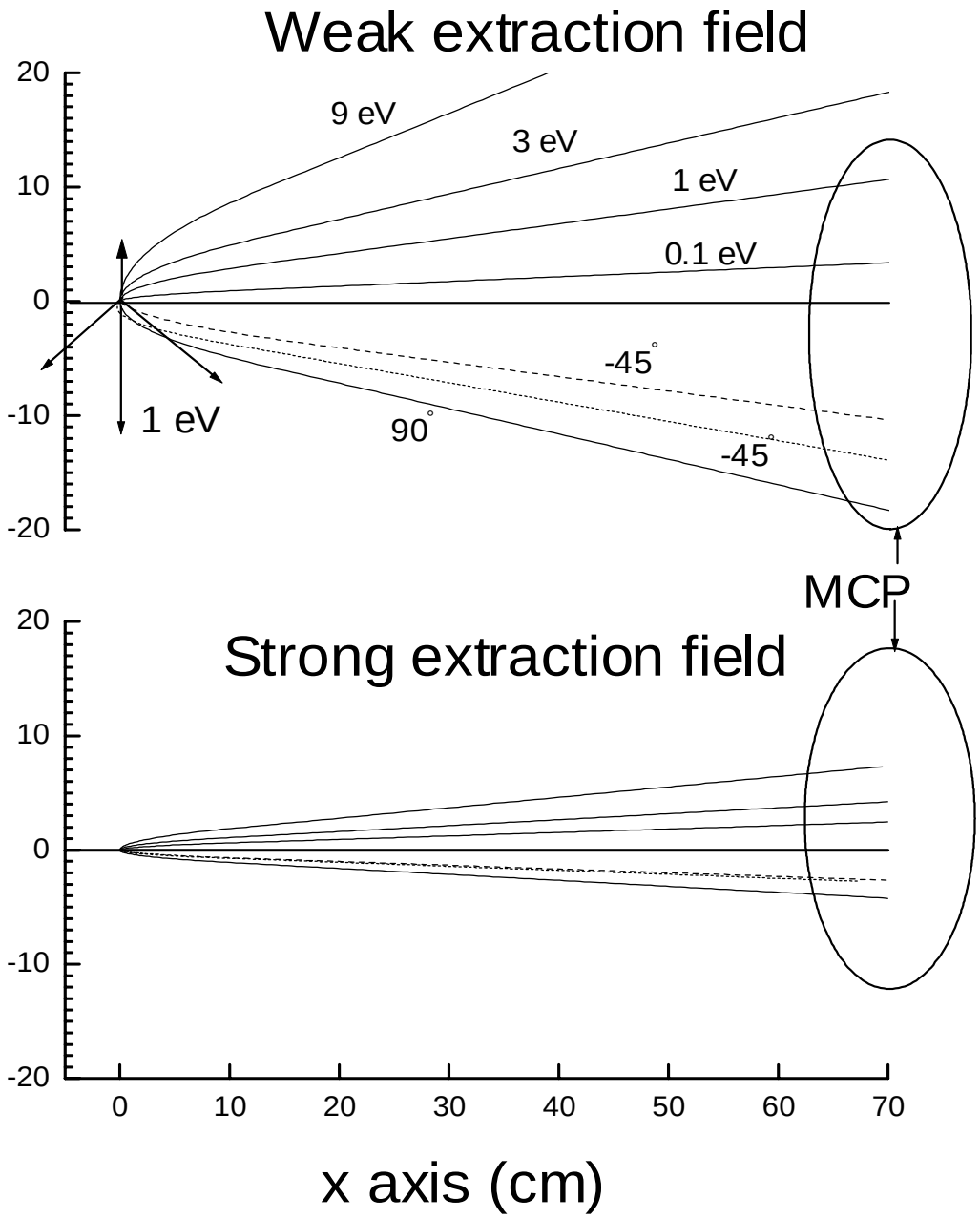

Figure 5.9: A plot of the recoil ion trajectories from the time-of-flight spectrometer under weak (top) and strong (bottom) extraction fields. In the weak field picture, the trajectories to the top of the centerline represent various energies with an initial angle parallel to the detector face. The trajectories to the bottom of the centerline represent 1 eV recoil ions with various initial angles. If the drift region is sufficiently long, a voltage can be chosen that will discriminate against most of the higher energy recoil ions from ionization-excitation and double-ionization.

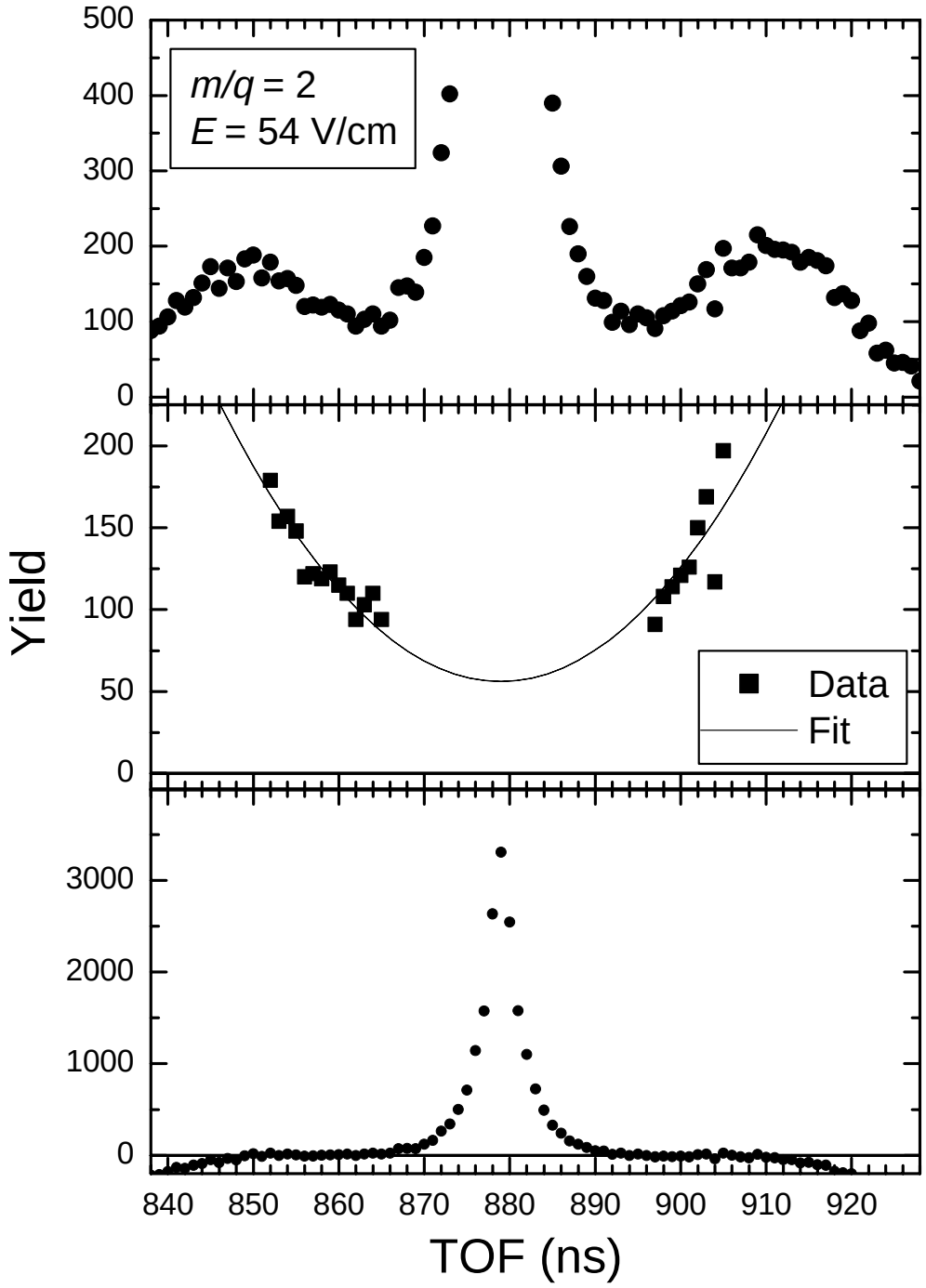

Figure 5.10: Baseline fitting procedure for the *m/q* = 1 and *m/q* = 2 (shown) peaks to separate the low energy GSD fragments and molecular ions from the higher energy recoil ions from ionization-excitation. See text for details of procedure.

Once the contributions from background and the high energy fragment shoulders have been removed, the remaining contributions to the *m/q* = 1 and *m/q* = 2 peaks are

$$A(1) = [HD^+(1s\sigma) \rightarrow H^+] + [H_2^+(1s\sigma) \rightarrow H^+], \qquad (5.1)$$

and

$$A(2) = [HD^+(1s\sigma) \rightarrow D^+] + [D_2^+(1s\sigma) \rightarrow D^+] + [H_2^+]. \qquad (5.2)$$

The contribution of D^+ from D_2^+ to A(2) can be evaluated using the theoretical GSD fraction for D_2, since the amount of D_2 relative to HD is measured directly from the time-of-flight spectrum (figure 5.6), unlike the H_2 contamination, which is more difficult to evaluate. Since we measure the yield of the four peaks shown in figure 5.6(b), (*m/q* = 1-4) and the presence of the H_2 and D_2 contamination means there are five species (H^+, D^+, HD^+, H_2^+, and D_2^+) contributing to those four peaks, we therefore impose a constraint on the analysis in order to determine the H_2 contamination. Using the calculated (see chapter 3.1) value for the total HD GSD yield (the sum of the H^+ and D^+ GSD fragments) as our constraint, the four measured yields can then be used to evaluate the H_2 as described in Appendix B. Using that analysis, the ratio of $[HD^+(1s\sigma) \rightarrow H^+]/HD^+$ can be determined. Since the algebra leading to the evaluation of the H_2 contamination links A(1) and A(2), an independent measurement of the $[HD^+(1s\sigma) \rightarrow D^+]/HD^+$ ratio cannot be made with this method. We choose to measure the $[HD^+(1s\sigma) \rightarrow H^+]/HD^+$ channel because the H^+ fragments from H_2 are a small contribution to this channel, while the H_2^+ contamination itself is often similar in size to the $[D_2^+(1s\sigma) \rightarrow D^+]$ channel. Therefore, the error in determining the H^+ channel is much smaller than the error in determining the D^+ channel.

5.4 Momentum Imaging Method

Over the last decade or so, an experimental technique called Cold Target Recoil Ion Momentum Spectroscopy (COLTRIMS) has proven to be a powerful experimental tool, and the basic apparatus design has been modified in many ways to fit the requirements of different experiments. A discussion of these developments can be found in the topical review by Ullrich *et al*. [5.3]. The proliferation of experiments has caused some of the original practitioners to complain about the abuse of the COLTRIMS name [5.4]. The design of our apparatus evolved from two main considerations: First, we wanted to measure the momentum of the low energy recoil ions that result from the GSD process with high precision. In order to do this, the target must be localized and cooled, and the velocity of the recoil ions must be measured. Using COLTRIMS techniques one can measure the momentum of low energy recoil ions (or electrons) with high precision, since lowering the extraction voltage spreads the distribution out over the detector. Second, we could not afford to expend large amounts of the rather costly HD gas. This eliminated the possibility of using a two- or three-stage supersonic jet typically used in modern COLTRIMS apparatus. A Frankfurt version of a COLTRIMS apparatus, circa 1996, is shown in figure 5.11.

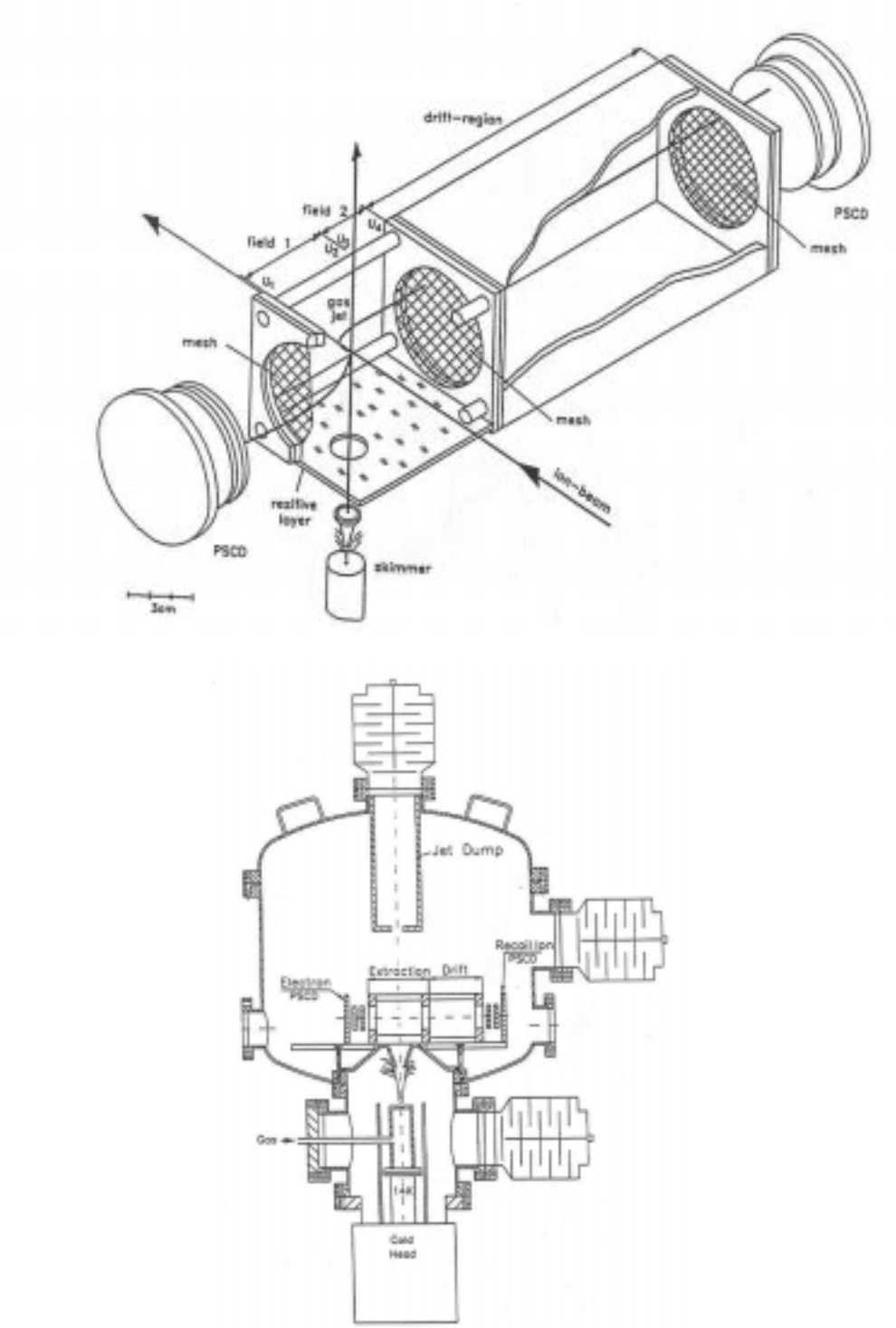

Figure 5.11: A typical COLTRIMS experimental setup. Note in the right figure the skimmer that is several cm away from the collision region. The Frankfurt group used this apparatus and the figures are taken from reference [5.16].

Our solution was to build a pre-cooled effusive jet to localize the target, extract the ions with a spectrometer that included a weak electrostatic lens for spatial focusing of the ions, and use a two-dimensional resistive anode position sensitive detector to measure the position of the recoil ions. This approach, while not a COLTRIMS apparatus by the strict definition of the term [5.4] because it lacks the electron detector to measure the momentum of all the ejecta (excluding the fast projectile) from an ionizing collision, retained many of the advantages of COLTRIMS while the gas consumption of the effusive jet was small enough to be economically feasible. A conceptual view of our apparatus is shown in Figure 5.12.

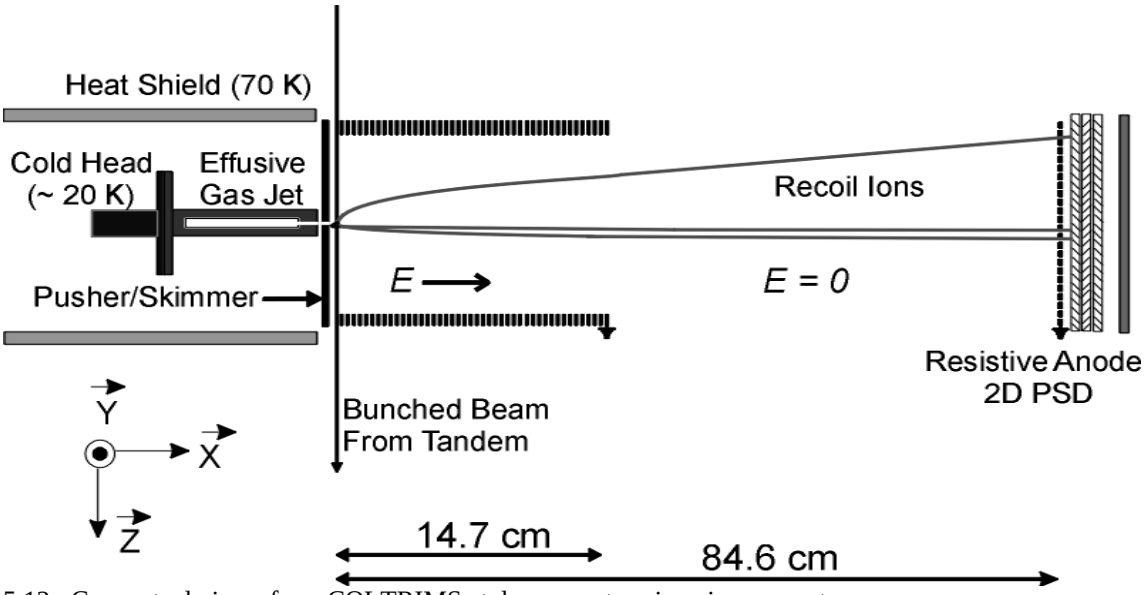

5.12: Conceptual view of our COLTRIMS-style momentum-imaging apparatus.

A small gas cell is mounted on the cold head of a cryo-pump (see figure 5.13). The HD gas flows into this cell and is cooled to approximately 25 K by collisions with the cell walls. A heat shield at liquid nitrogen temperatures surrounds most of the cold head and gas cell, limiting radiative heating of the gas cell by the rest of the apparatus, which is at room temperature. An effusive jet of the pre-cooled gas traveling toward the

recoil ion detector is formed when the gas escapes out of a 0.36 mm diameter hole at one end of the cylindrical gas cell. The gas pressure in the cell is kept low enough that molecular flow conditions are valid. The length to width ratio of the tube is about 9:1; therefore, the resulting effusive jet gives a directional flow [5.16] that further cools the target gas in the transverse direction. The effusive jet is further collimated by a 1 mm diameter hole in the pusher plate of the spectrometer. The resulting target is about 1.5 mm square in the collision region (about 2 to 3 mm from the pusher plate) where it intersects the fast proton beam that has been collimated to about 0.5 x 0.5 mm. More details about the effusive jet are found in Appendix F.

Figure 5.13: The cryo-pump and cold head with the gas cell mounted on top of it. The heat shield has been removed for this picture.

Figure 5.14: SIMION simulation of our spectrometer showing three sets of ions being focused. These ions start from a 2 mm wide target. One group of H^+ recoil ions has an initial velocity toward the detector, one has an initial velocity "down" in this figure, and one has an initial velocity "up" in this figure. In this simulation all of the ions have 150 meV initial energy. The recoil ions are focused to spots on the detector that reflect only the initial momentum of the ions, rather than the size of the target. For a more detailed description, see Appendix E.

The recoil ions are extracted and accelerated by the electric fields of the spectrometer. The spectrometer consists of 31 (63.5 x 63.5 x 1 mm) brass plates separated by ceramic spacers. The first plate (the pusher/skimmer) has a 1 mm hole in the center to allow gas flow from the effusive jet. The other 30 plates have a 57 mm diameter hole in the middle. The distance from the front of one plate to the front of the adjacent plate is 5.6 mm. 980 kΩ resistors connect each adjacent pair of plates. Spatial focusing of the target is accomplished by applying voltage to the pusher and one other spectrometer electrode (the focus electrode, plate number 11, where the pusher/skimmer is plate number 1). This creates two uniform potential gradients on either side of the focus, and since there is no grid at the focus electrode, the change in the electric field from one gradient to the next forms an electrostatic lens, a common COLTRIMS technique to improve momentum resolution [5.9, 5.16, and 5.18]. Once the ions leave the spectrometer, they travel through a 699 mm drift region. A 200 lines/inch electroform mesh is placed 5.5 mm in front of the first micro-channel plate of the recoil ion detector, which operates at approximately - 2.4 kV. In Figure 5.14 we show the result of a SIMION [5.19] simulation for this spectrometer. Recoil ions with a uniform initial momentum, starting from a distribution 2 mm wide in the vertical (y) and beam (z)

directions are focused to a spot on the detector that is about 0.15 mm. This size is comparable to the detector resolution, essentially making the target a point source.

The time of flight of the recoil ions was measured in much the same way as described in Section 5.2. The start signal for the timing is taken from the rear of the last channel plate of the Z-stack micro-channel plate detector, because this signal has a much faster rise time than the signal from the resistive anode. Once again, a signal synchronized with the bunched proton beam was used as a stop. Since the back plate signal is not quite as clean [5.13] as the signal from the metal anode of the timing detector discussed in Section 5.2, a longer blocking time is needed on the constant fraction discriminator (CFD) to prevent electronic "ringing" from providing numerous false "second hits". Some ion-pair events are not recorded because of this, but this is not of major concern for two reasons. First, the efficiency for detecting ion-pairs is quite low in any case, since the 200-lines/inch mesh on the front of the recoil ion detector has a relatively low transmission. Second, ion-pairs, because of the high kinetic energy release in double ionization, will only hit the detector if the molecule is oriented such that the separation between the ion pairs is quite large, longer than the maximum 150 ns blocking on the CFD for most of the extraction fields used in this experiment.

A spectrometer with a homogeneous extraction field has first order focusing in the time-of-flight direction if the drift region is twice as long as the acceleration region. The lens described in the previous paragraph requires a longer drift region for time focusing. Our detector position was chosen for the best combination of focusing in all three spatial dimensions. The details of choosing the correct spectrometer voltages to obtain focusing conditions are discussed in Appendix E.

The long drift region, in combination with the relatively weak extraction fields used, results in recoil ion flight times of at least several microseconds. The period of the proton bunch was typically 21.2 μs, although measurements have been made with periods as long as 84 μs. In practice, the timing resolution is limited by the width of the proton bunch, approximately 1-2 ns for the data reported here. The electronic resolution of the system is slightly above 1 ns, mainly because we use a 1 ns time-to-digital-converter (TDC) to record the time of flight.

The two-dimensional resistive anode recoil ion detector used has a position resolution of 0.18 mm/channel. A detailed description of the detector is found in Appendix C. The position is computed using the full 12-bit information recorded by the Phillips 7164 analog to digital converter (ADC), and while it is compressed for display purposes to 256 x 256 channels, the 12-bit information is retained in the analysis for the momentum calculation.

The time-of-flight of the recoil ions is used to identify the mass of the recoil ion, since all the recoil ions we are interested in are singly charged, and from that information, gated position spectra are created. If the mass of the ion is known, the momentum of the fragments in the *y* (vertical) and *z* (beam) directions can be calculated, on an event-by-event basis, using the time of flight and the distance the ion has traveled from the peak center. For example, for a H^+ recoil ion,

$$P_y = \frac{m_H (y - y_0)}{t_H},$$

$$P_z = \frac{m_H (z - z_0)}{t_H}. \qquad (5.3)$$

The momentum in the x (jet and time-of-flight) direction is calculated by measuring the difference between the centroid of the time-of-flight distribution and the time-of-flight of the actual event, and then using the time-to-momentum conversion function constructed (for the particular fields used) from a SIMION simulation (see Appendix E). The time-to-momentum conversion has the form,

$$P_x = a_1 t + a_2 t^2 \tag{5.4}$$

where $t = t' - t_0$ is the difference between the measured time-of-flight for a specific event (t') and the centroid of the time-of-flight peak (t_0). A simulation is needed to determine a_1 and a_2, since the non-uniform focusing fields make an analytic solution difficult to obtain.

The HD^+ molecular ion peak is a valuable diagnostic tool. Because it is the largest molecular ion peak available, it is used to determine the temperature of the jet by fitting a Maxwell-Boltzmann distribution to the peak shape. The similarity of the shapes of the HD^+ and H_2^+ peaks is employed in the determination of the H_2 contamination (see Appendix B). Furthermore, the center of the molecular distribution is used to determine y_0 and z_0 for the position spectrum of each mass species. Residual magnetic fields in the drift tube (about 1 guass) cause some very slight shifts (0.2 to 1.0 mm, depending on the velocity of the ion) in y_0 and z_0 for the different ions, so the values of y_0 and z_0 for the H_2^+, HD^+, and D_2^+ peaks are used to extrapolate the value of y_0 and z_0 for the H^+ fragments. Near $E_k = 0$, the energy distribution becomes quite sensitive to the values of x_0, y_0, and z_0 used. The centroid location must be carefully placed to prevent a systematic broadening of the energy distributions.

Since the momentum of the fragment is calculated with respect to the center of the molecular ion distribution, the measurement is with respect to the center of mass of the HD^+ molecular ion. The measured momentum can be easily converted to an energy measurement, specifically to the kinetic energy release of the molecule (E_k) when it dissociates. Since the mass of the H^+ fragments is less than the D^+ fragments, their energy must be scaled slightly differently when converting to E_k. Using conservation of momentum and energy, it is easy to arrive at the conversion factors,

$$E_k = \frac{3}{2} E_H ,$$

and

$$E_k = 3E_D . \qquad (5.5)$$

Since the H^+ fragment energy is only multiplied by half as much as the D^+ fragment energy, the measurement of E_k is inherently more accurate for the H^+ fragments, assuming the measurement has the same energy resolution in all other regards.

There is an additional point to be considered when subtracting the H_2 contamination from the $P(E_k)$ distribution for m/q = 2 ions. This peak contains two species, H_2^+ molecular ions, which need to be subtracted, and D^+ GSD fragments. To convert E_D to E_k, the energy of the D^+ fragments needs to be multiplied by 3 (see equation 5.5), which is done in practice by scaling the $P(E_D)$ distribution on an event-by-event basis in offline data analysis to create the $P(E_k)$ spectrum. To correctly subtract the H_2^+ ions, a spectrum must be created, using the HD^+ ions for the shape, where the energy distribution is scaled by a factor of 3 and the amplitude is scaled by the value of $\frac{H_2^+}{HD^+}$

determined from the analysis described in Appendix B. This spectrum is then subtracted from the $m/q = 2$ $P(E_k)$ spectrum to create the final D^+ $P(E_k)$ spectrum.

Extraction Field at Collision Region (V/cm)	**Pusher Voltage (V)**	**Maximum Kinetic Energy Release (E_k) Collected with 4π Efficiency (meV)**
1.8	60	24
3.1	100	38
7.8	250	98
12.7	400	150
18.5	600	200
30	1000	275
93	3000	1125

Table 5.1: Typical extraction voltages used and the corresponding maximum energy fragments collected with 4π detection efficiency.

One of the key advantages of this experimental technique is the ability to examine the lowest energy fragments at the highest resolution possible by lowering the extraction field so those fragments are spread over the entire detector surface (diameter ≈ 40 mm). To measure the entire GSD distribution, we repeat the measurement several times with various extraction fields. With a high enough extraction field, all of the GSD fragments were collected, while by lowering the extraction field, pieces of the distribution, progressively nearer threshold, were measured. The lowest extraction field used, ≈ 2 V/cm at the collision region, collects only fragments with a kinetic energy release of up to ≈ 25 meV. This effect of achieving higher resolution at lower extraction fields is exactly what has made COLTRIMS such a powerful experimental tool for measuring low energy recoil ions and electrons. Table 5.1 shows some typical voltages used, and the energies that can be measured with those extraction voltages.

When a large extraction field is used, the compression of the distribution onto the detector is the dominating factor in the resolution. As the extraction field is reduced,

however, other factors become more important. For example, 25 K is equivalent to about 2 meV, so at very low extraction voltages, the thermal distribution limits the resolution more than the detector resolution. The various factors influencing our resolution are summarized in Appendix G, along with a discussion of our error analysis.

Chapter 6

In this chapter the results of our measurements of the ground state dissociation (GSD) process will be reported. In Section 6.1, the earlier measurements, integrated over all dissociation energies, will be discussed and compared to the predictions of the Meyerhof model and the coupled channels calculation. The results of the more recent measurements of the relative GSD fractions as a function of kinetic energy release are given in Section 6.2.

In this chapter, as throughout the dissertation, we use the following notation to denote the laboratory reference frame: The *x*-axis is defined to be in the time-of-flight direction, the *z*-axis is along the beam, and the *y*-axis is defined to be vertical, orthogonal to the other two. This is the standard notation for the COLTRIMS experiments done at the Macdonald Lab; so choosing this notation generally facilitates in-house discussions of the experiment. It should be noted, however, that the standard COLTRIMS design has the jet in the *y* direction, while the flow of our effusive jet is in the *x* direction. An illustration of this axis convention is shown in figure 6.1.

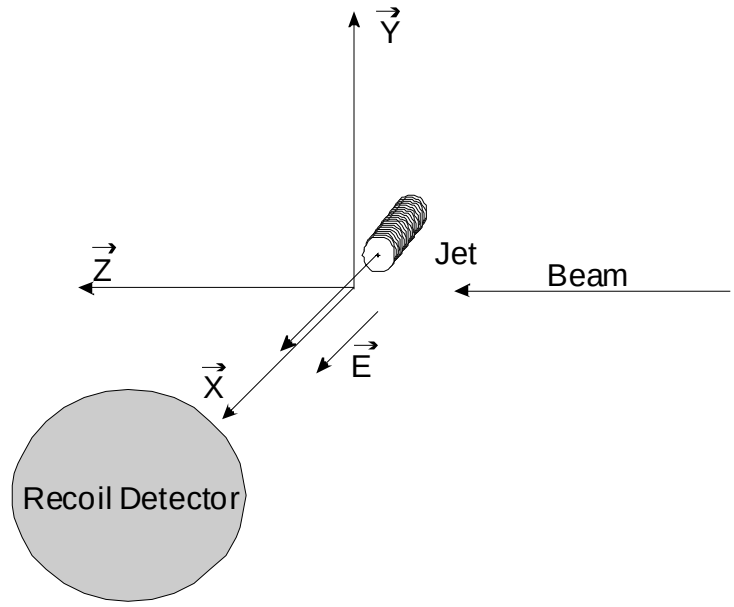

Figure 6.1: Coordinate system used in this dissertation.

6.1 Integrated Measurements of the GSD Fractions

Using the time-of-flight (TOF) method described in Chapter 5, the total yields of H^+ and D^+ GSD fragments were measured, and when divided by the measured HD^+ yield, relative probabilities of each GSD channel were determined. The ratios of $\frac{HD^+(1s\sigma_g) \rightarrow H^+}{HD^+}$ and $\frac{HD^+(1s\sigma_g) \rightarrow D^+}{HD^+}$ are determined using equations (5.1) and (5.2) along with the techniques for evaluating the H_2^+ contamination described in Appendix B. Our results are shown in figure 6.2 as a function of the extraction field on the TOF spectrometer. The extraction field is varied to diminish the possibility of systematic errors related to ion impact energy and spot size on the detector. For very low extraction fields, below 23 V/cm, some of the light H^+ fragments from the GSD process had enough velocity (in the *y* and *z* directions) to miss the detector. On this basis, the data point taken with the lowest extraction field shown in figure 6.2 (15.6 V/cm) is excluded. When using only the TOF measurement, the yields of the H^+ and D^+ channels

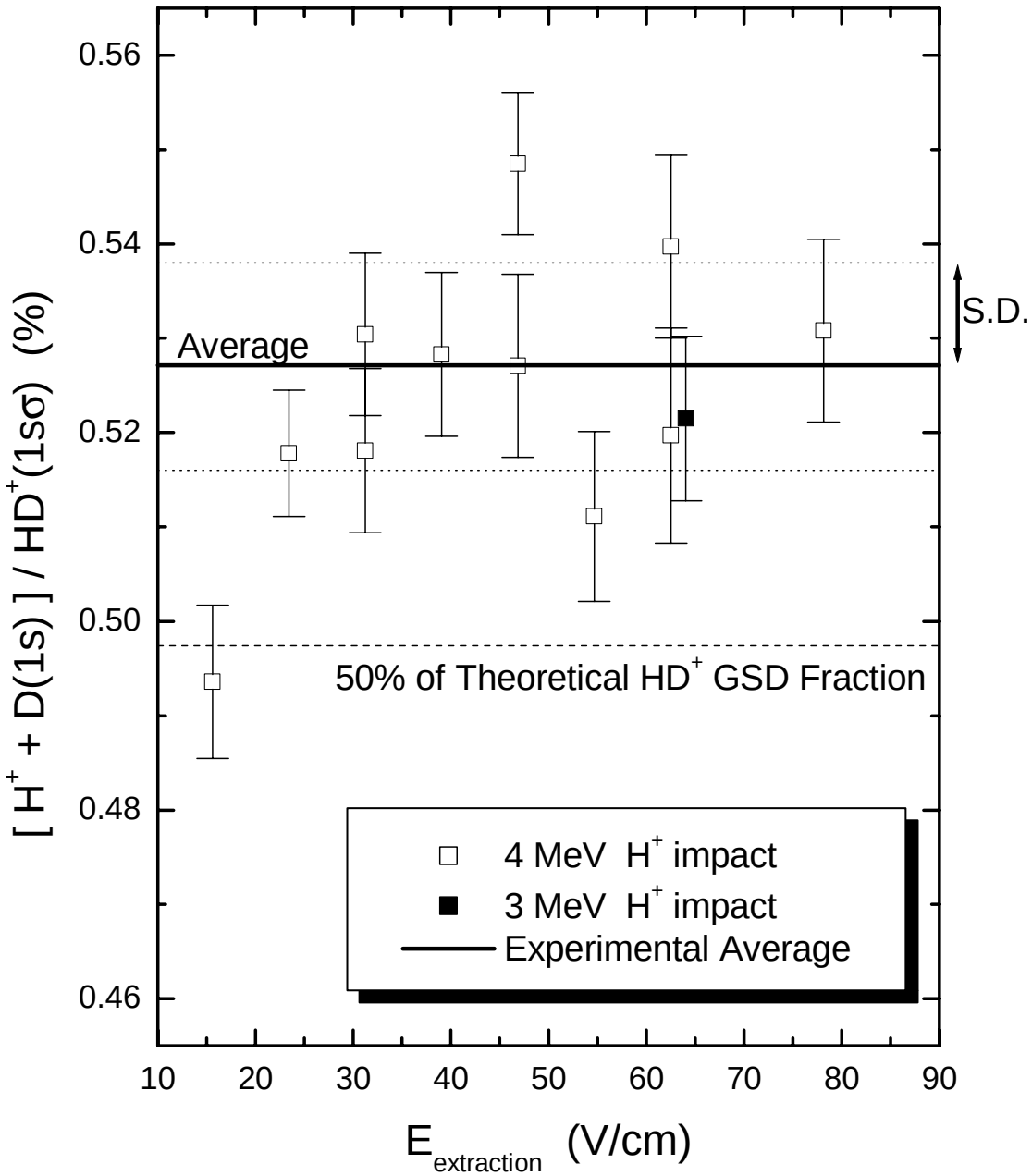

Figure 6.2: The ratio of $\frac{[H^+ + D(1s)]}{HD^+}$ measured using the time-of-flight technique described in chapter 5.3. The measured values are clearly above the values for a symmetric dissociation. The measurements are displayed as a function of the extraction field used in the measurement. The dotted line above and below the solid line represents one standard deviation from the average value.

are linked by the constraint that their sum equals the total theoretical GSD fraction for HD (see appendix B.1), and thus, are not measured independently [6.1]. We can,

however, select one channel to compare with theory to determine if there is a measurable asymmetry in the two GSD final states. Having our choice, we compare the H^+ yield with theory, since the H_2 contamination level plays a smaller role in this channel than it does in the D^+ channel, and as a result, the measurement of the H^+ yield is more precise. Using this method, we find the ratio of $\frac{H^+}{HD^+}$ = 0.527%, the average value for the data points shown in figure 6.2. The standard deviation (σ) of these points is 0.011%, while the value for a symmetric dissociation (equal probability for H^+ and D^+ fragments) is 0.497%. Thus, our measured value is 2.5σ above the symmetric value.

While using only the time-of-flight of the recoil ions is sufficient to demonstrate there is a measurable preference for the lower H^+ + D(1*s*) channel, by using the momentum imaging information gathered with our second-generation apparatus, we determine the H_2 contamination without resorting to the calculated GSD values and the algebra discussed in Appendix B.1 (the time-of-flight technique). Using the shape of the HD^+ distribution to fit the amount of H_2^+ present in the *m/q* = 2 momentum distribution, as described in Appendix B.2 (the momentum imaging technique), allows an independent measurement of both the H^+ and D^+ channels. These results are shown in Table 6.1.

The measurements of the relative yields of the two GSD channels (both relative to the HD^+ channel) show that the H^+ + D(1s) channel is the favored one, independent of the technique used to determine the H_2^+ contamination. The difference between the two dissociation channels, while smaller than in the time-of-flight measurement, is significant (2.1σ) indicating a measurable symmetry breakdown in the ground state dissociation of HD^+. This empirically demonstrates, for the first time, that the isotopic effect leading to the breakdown of the Born-Oppenheimer approximation for HD^+ causes not only small

changes of the potential energy curves and localization of the electron density on the deuteron for highly excited vibrational states, but also is responsible for the measurable preference of D(1*s*) over H(1*s*) in the dissociation of the molecular ion. Stated another way, the localization of the electron density on the deuteron occurs not only for vibrationally bound states, but also in the vibrational continuum. Demonstrating this fact accomplishes the first goal of this project.

Method	**H^+ + D(1*s*) (%)**	**H(1*s*) + D^+ (%)**	**GSD (HD^+) (%)**
Time-of-flight	0.527 ± 0.011	-	-
Momentum Imaging[a]	0.525 ± 0.009	0.464 ± 0.021	0.989 ± 0.022
Momentum Imaging[b]	0.522 ± 0.012	0.478 ± 0.022	1.000 ± 0.025
Coupled Channels	0.539	0.455	0.994
Meyerhof KER = $E - E_{D(1s)}$	0.534	0.460	-
Truncated Meyerhof KER = $E - E_{D(1s)}$	0.536	0.458	-
Meyerhof KER = $E - E_{H(1s)}$	0.529	0.465	-

Table 6.1: The results of our integrated measurements. The experimental results include the results obtained using only the time-of-flight measurement (shown in figure 6.2), and measurements using momentum imaging to determine the H_2 contamination with 4 MeV Protons Projectiles[a], and with 20 MeV C^{3+} Projectiles[b]. These results are compared to calculated values obtained with coupled channels calculations and the Meyerhof model. The various values obtained with the Meyerhof model differ in the evaluation of the "collision" velocity as discussed later in the text.

The $1s\sigma$ to $2p\sigma$ transition probability, *w*, calculated with the coupled channels technique (see chapter 3.3) is shown in figure 6.3 as a function of energy relative to the D(1*s*) threshold. Also shown is the same quantity calculated using the Meyerhof model, relative to both the H(1s) and the D(1s) threshold. The transition probability increases rapidly from zero at threshold and later approaches 0.5 asymptotically (below the n=2 manifold) for both the coupled channels calculations (see chapter 3.3) and Meyerhof's analytic formula [6.2, 6.3], as shown in figure 6.3(a). While there is a nice overall

agreement between the two, a closer look at these calculated probabilities, shown in figure 6.3(b) reveals some differences. First, Meyerhof's formula overestimates the transition probability at large energies, but only by about 0.7%, not a large price to be paid in inaccuracy for the associated gain in simplicity. In contrast, near threshold the disagreement between Meyerhof's formula and the coupled channels calculations is significant, as shown in the inset of figure 6.3(b). Notice that not only does Meyerhof's formula fail to describe the threshold behavior properly, it is not clear what threshold one should use to evaluate the relative nuclear speed, *v*, from equation (3.8). If one uses the lower D(1*s*) threshold the agreement with the coupled channels probability extends to lower energies, but transitions are allowed to occur in the energetically forbidden region. This is avoided if one uses the higher H(1*s*) threshold, but then Meyerhof's formula underestimates the coupled channels probability significantly and over a wider energy range. It seems that the best way to apply the Meyerhof formula is to use the lower threshold to evaluate the nuclear speed but set the probability to zero below the D(1*s*) threshold.

The total fraction of GSD transferred to the $2p\sigma$ final state, which was the measured value in this experiment, is given within the Meyerhof model by

$$P_{2p\sigma} = \int_0^\infty P(E_k) w(E_k) dE_k \,, \tag{6.1}$$

where P(E_k) is the probability for a kinetic energy release E_k. The value of P(E_k) is given by the Franck-Condon factors for the vibrational continuum [6.1, 6.4] (see also chapter 3). The probability for GSD remaining on the initial $1s\sigma$ state is given by

$$P_{1s\sigma} = \int_0^\infty P(E_k) dE_k - \int_0^\infty P(E_k) w(E_k) dE_k = \int_0^\infty P(E_k) dE_k - P_{2p\sigma} \,. \tag{6.2}$$

The computed values using the different versions of the Meyerhof formula discussed above are given in Table 6.1. It can be seen that the integrated value using the kinetic energy release relative to the H(1*s*) threshold fits the coupled channels calculation best, because of the cancellation of the underestimate at low energies with the overestimate at high energies. Furthermore, using this threshold prevents transitions in the energetically forbidden region below the H(1*s*) threshold. As can be seen from figure 6.3(b), however, this probability fails more noticeably in describing the transfer probability just above threshold. If one uses the truncated probability which best approximates the behavior near threshold, the deviation of the integrated value is minimal, much smaller than our experimental errors in the measurement of the total transition probability. Since the sum of the two final channels must, within the Meyerhof model, sum to the total GSD transition probability for HD, when w changes, it has the artificial effect of also changing the probability for elastic scattering, i.e. the $(1 - w)$ term. While applying the Meyerhof model to this problem may seem crude compared to the more fundamental quantum mechanical calculations, the Meyerhof formula does give a remarkably accurate estimate of the asymmetry we measure. For making quick estimates of this type, the Meyerhof model is a valuable tool. The Meyerhof model cannot, however, predict any kind of resonance behavior, since these quantum mechanical effects are not included in the model.

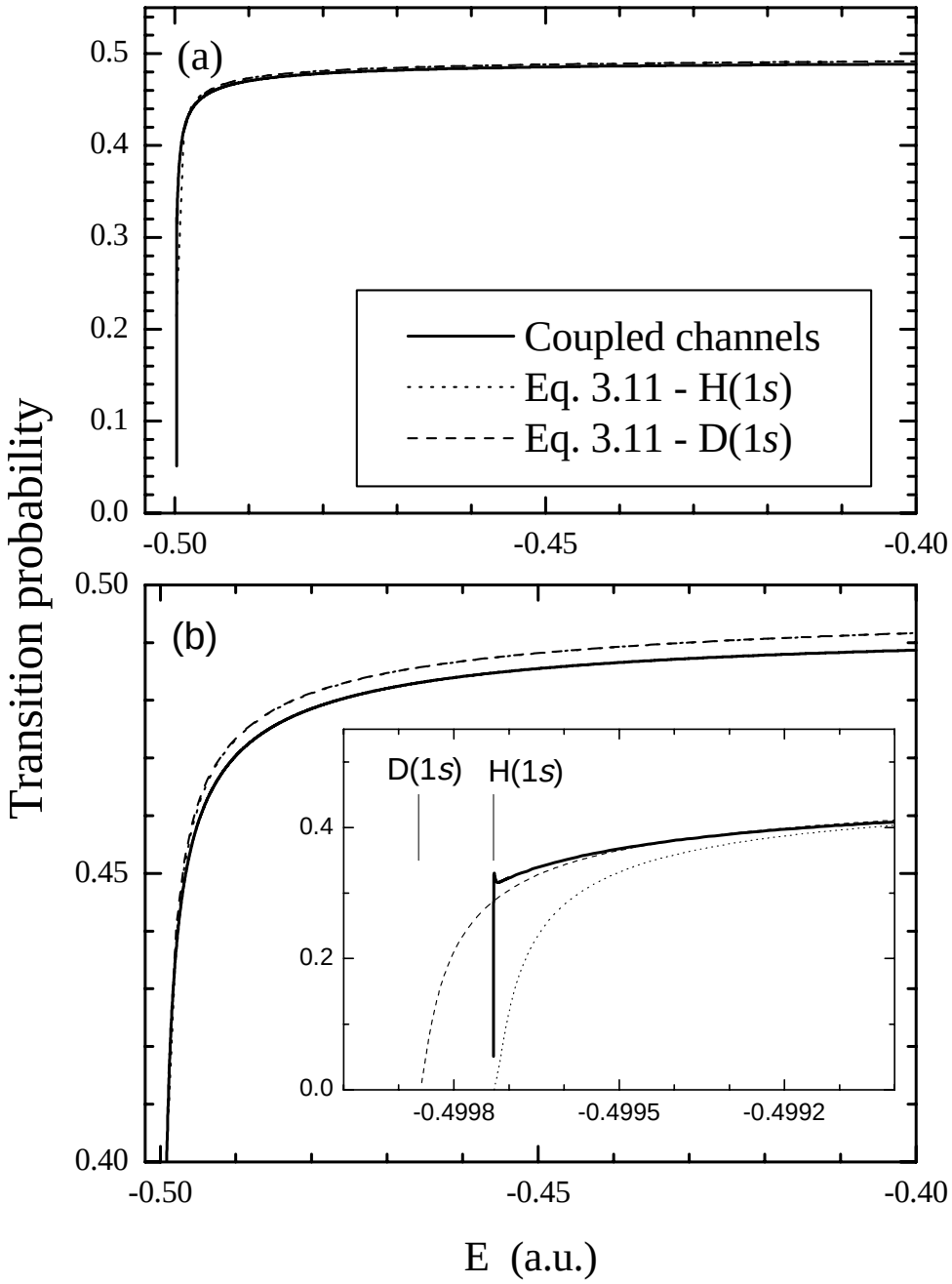

Figure 6.3: A comparison of the calculated transition probabilities using the Meyerhof model given in equation (3.11) and the coupled channels calculation. The entire range is shown in (a), the threshold region is expanded in (b). The inset shows the variation in the Meyerhof model caused by the ambiguity in defining the nuclear velocity (see text).

We have made this measurement with two projectiles, 3 and 4 MeV protons and 20 MeV C^{3+} (the reasons for using C^{3+} will be discussed more in section 6.2). Changing the projectile used to initiate the vertical transition to the HD^+ vibrational continuum had no appreciable effect on the results, except that the higher charge state created more competing processes that had to be separated from the GSD fragments (see chapter 5.1). This problem was more significant for the H^+ channel, since the change to a C^{3+} projectile led to an increase in the H^+ yield from residual H_2O in the target. This is the primary reason for the increase in the error of the measured H^+ channel.

The error in this measurement is dominated by the error in determining the H_2 contamination, particularly in the D^+ channel (see Appendix G). In the H^+ channel, the statistical error and the error in the background subtraction are larger than the error associated with the H_2 contamination.

6.2 Differential Measurements of the GSD Fractions

While the integrated measurements presented in chapter 6.1 show that there is a measurable preference for the electron to be associated with the deuteron, a much more interesting measurement would be to probe this preference as a function of energy. In other words, the quantity to be measured is the transition probability, w, between the lower $1s\sigma$ and the upper $2p\sigma$ states. This is equivalent to measuring w as a function of kinetic energy release, E_k, where w is defined as

$$w(E_k) = \frac{\left[\dfrac{HD^+(1s\sigma_g) \to D^+}{HD^+}\right]}{\left[\dfrac{HD^+(1s\sigma_g) \to D^+}{HD^+} + \dfrac{HD^+(1s\sigma_g) \to H^+}{HD^+}\right]} . \qquad (6.1)$$

$$= \frac{HD^+(1s\sigma_g) \to D}{\left[\left(HD^+(1s\sigma_g) \to D^+\right) + \left(HD^+(1s\sigma_g) \to H^+\right)\right]}$$

This can be compared to the Meyerhof transition probability given in equation (3.11) or the results of the coupled channels calculation, from which we have defined the transition probability in a similar way as

$$w(E_k) = \frac{\sigma_{exchange}(E_k)}{\sigma_{elastic}(E_k) + \sigma_{exchange}(E_k)} . \qquad (6.2)$$

The ability to probe the transition probabilities experimentally rests on the precise measurement of the momentum of the dissociating fragments. Using the techniques described in chapter 5.4, we have, for the most part, succeeded in this goal and the results will be presented in this section.

One factor that influences the resolution of our differential measurement is ability to cool the target HD gas. A room temperature (300 K) distribution of gas would have an average thermal energy of 25 meV, completely obscuring the information we are interested in measuring. A key result for understanding our energy resolution, therefore, is a measurement of how well our pre-cooled effusive jet functions. While building our apparatus, we have used thermocouple wire attached to the cold head to get an idea of the cold head temperature, measuring 30 ± 15 K. According to the manufacturer's specifications, the cold-head should reach 15 K, but the cryo-head is configured much differently now than it was for its original use as a vacuum pump. Rather than trying to estimate the heat load from the heat shield and gas cell, as well as the radiation that

reaches the cold-head, we have made a temperature measurement using the energy distribution of the HD^+ molecular ions in our experiment. By fitting the measured energy shown in figure 6.4 with a Maxwell-Boltzmann distribution, we arrive at a temperature of the gas. There are two components to this distribution, the cold gas from the jet, which makes the narrow peak near zero energy, and the much wider tail, which is due to the gas in the target that is not in the jet flow (often called the "warm" gas). We fit our measured shape to the sum of two Maxwell-Boltzmann distributions, and find the temperature for each of them. For the fit shown in figure 6.4, the jet temperature is 14.4 K with an uncertainty of about 1 K. The warm gas is measured to be 98 K, which is reasonable, since many of the surfaces in our chamber are colder than room temperature (the heat shield and liquid nitrogen trap are both 70 K). The 14.4 K temperature of the jet translates to an average thermal energy of 1.2 meV for our target.

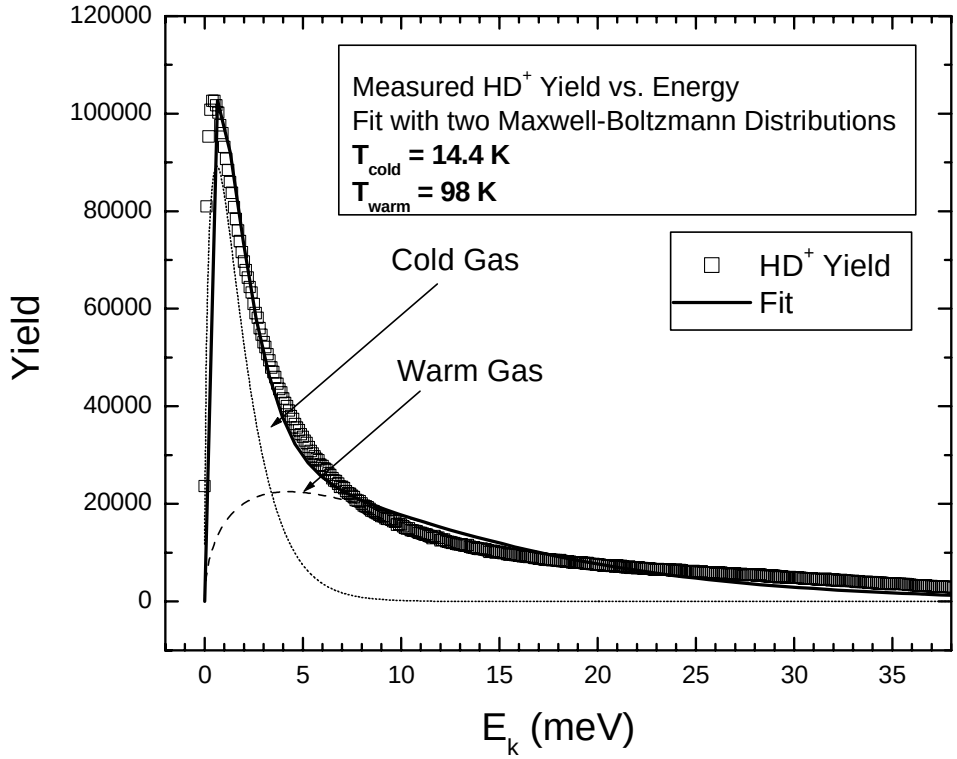

Figure 6.4: The measured energy distribution of the HD^+ molecular ion fitted with the sum of two Maxwell-Boltzmann distributions. The temperature of the gas in the jet is measured to be 14.4 K.

Besides its usefulness to determine the temperature of the gas, the HD^+ peak is valuable to the experiment in other ways. The GSD process occurs after the single ionization of the neutral HD molecule, so the resulting fragments have not only some velocity from the dissociation, they also have velocity from the center of mass motion of the molecular ion. Using the HD^+ peak as a guide, since it also has the same center of mass motion, we measure the velocity of the dissociating fragments with respect to the average velocity of the center-of-mass. It should be understood, however, that since we do not measure the momentum of the ionized electron, we do not determine the center-of-mass motion of the molecular ion on an event-by-event basis. The error induced by this deviation from a traditional COLTRIMS technique is quite small (~1 meV) relative to some of the other sources of error in this experiment, as discussed in Appendix G.

Since the only significant process that can contribute to the HD^+ peak in our experiment is non-dissociative single ionization, the recoils ions that have $m/q = 3$ form a thermal distribution of molecular ions without any other contribution. A two-dimensional plot of the P_y vs. P_z momentum distribution for HD^+ molecular ions is shown in figure 6.5. Note the sharp central region in the middle of the distribution. In contrast, the same P_y vs. P_z momentum distribution for $m/q = 2$ is shown in figure 6.6. This distribution contains contributions from two sources, H_2^+ molecular ions resulting from single ionization of the H_2 contamination in the HD bottle, and D^+ fragments from the GSD of HD^+. The H_2^+ molecular ions are localized in the central region just as in the HD^+ distribution shown in figure 6.5. We use this similarity in the shapes of the momentum distributions to determine the amount of H_2^+ contamination. This momentum imaging procedure for determining the H_2 contamination is described in Appendix B.2.

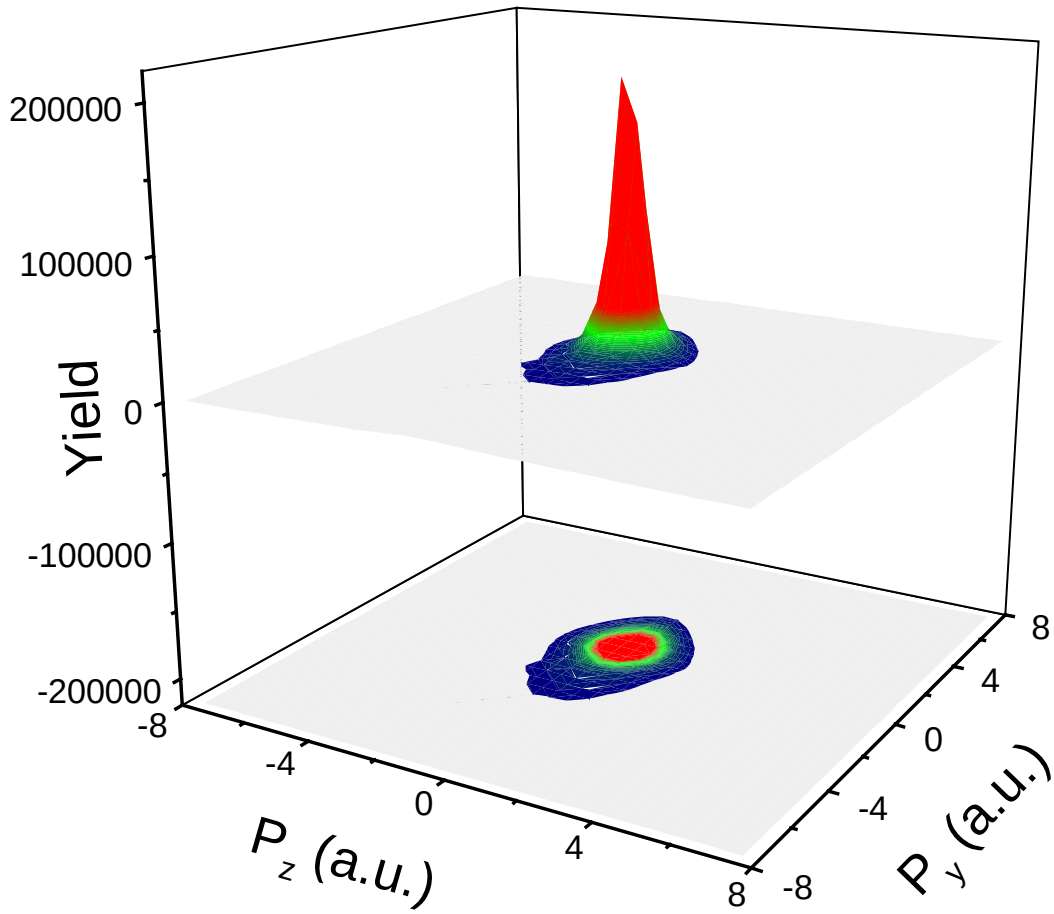

Figure 6.5: P_z vs. P_y for HD^+ molecular ions.

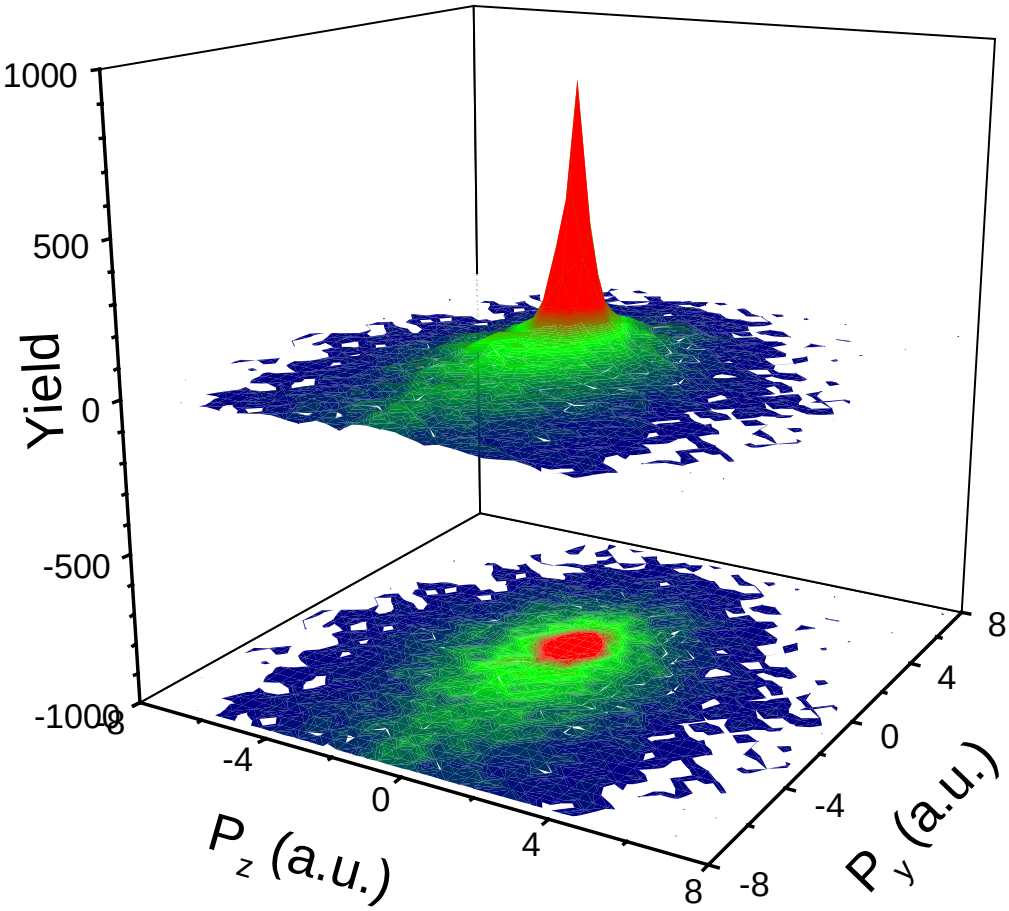

Figure 6.6: P_z vs. P_y for the H_2^+ molecular ions and D^+ fragments from GSD. Both have m/q = 2, and therefore cannot be separated by time-of-flight.

The momentum imaging technique works well for finding the amount of H_2 contamination. It yields results consistent with our previous method, which utilized the time-of-flight measurement and the calculated GSD fractions [6.1]. Since we are ultimately interested in making a measurement as a function of the kinetic energy release of the dissociating molecule, we need to be able to determine the H_2^+ contamination in a differential way as well as determining the integrated amount of H_2^+. The process we use to do this again involves using the shape of the HD^+ molecular ion. Since we have determined the integrated amount of H_2^+ relative to HD^+ from the momentum

distributions (Appendix B.2) scaling the HD^+ peak by that amount should produce a high precision simulation of the H_2^+ molecular ion distribution, including instrumental and thermal broadenings, since it is measured at the same time as the *m/q* = 2 peak and therefore under the same conditions. While we have no reason to believe that there is anything conceptually wrong with this idea, there unfortunately does seem to be some systematic problem with this method. Figure 6.7 shows the measured energy distributions for *m/q* = 2, HD^+ and D_2^+. The HD^+ and D_2^+ peaks are normalized to the height of the *m/q* = 2 distribution in this figure. The width of the peaks clearly increases as the mass of the ions decreases. Since the shape of the distributions is different, normalizing the HD^+ energy distribution by the ratio of $\frac{H_2^+}{HD^+}$ determined from the momentum imaging technique yields a simulated H_2^+ energy distribution that is too strongly peaked near zero. When this distribution is subtracted from the *m/q* = 2 distribution, the result is a negative yield of D^+ fragments near threshold. One might reason that it would be better to just normalize the HD^+ distribution to the amplitude of the *m/q* = 2 distribution, as was done for illustration purposes in figure 6.7. This is incorrect, however, giving a substantially overestimated value for the transition probability far away from threshold, since the entire H_2^+ population was not subtracted.

To date, we have not determined the reason for this systematic error. There is no simple reason to believe that the energy distributions for the different isotopes should be different. We have investigated several potential sources of error. First, as stated in Chapter 5.4, there are some small magnetic fields present in our drift region, and these fields cause small shifts in the z_0 and y_0 positions for the different isotopes. Locating z_0 and y_0 for the HD^+ distribution is easier than the other isotopes because of the higher

statistics in the distribution. An incorrect location for y_0 or z_0 will increase the magnitude of P_y^2 and P_z^2 (see equation 5.3), and a simulation we constructed to examine potential sources of error indicated that the momentum distributions can be quite sensitive to even small changes in y_0 and z_0. We have two reasons to suspect this is not the source of the error. First, the momentum imaging method for determining the H_2^+ contamination uses the z and y information as well, and seems to work satisfactorily. Second, the values of y_0 and z_0 are equally hard to locate for the D_2^+ distribution as they are for the m/q = 2 distribution, and the measured D_2^+ energy distribution is even narrower than the HD^+ distribution. One possible source of the systematic error that we suspect, but have not fully investigated, is the speed of the effusive jet. The characteristics of the effusive jet are described in Appendix F. We have not been able to directly measure the speed of the jet, either through a separation of the "cold" and "warm" gas in the time-of-flight spectra, or in deviations of the values of x_0 from those predicted by SIMION [6.5]. If the jet speed behaves as predicted by theory (see Appendix F),

$$\bar{v} = \sqrt{\frac{8kT}{m\pi}}\,, \tag{6.3}$$

the average velocity will be different for the three molecular ions, scaling as the square root of the mass. Furthermore, the situation is more complicated for the m/q = 2 distribution, since the H_2^+ ions will have a average jet speed for m = 2, and the D^+ fragments resulting from GSD of the parent HD^+ molecular ion will have an average jet speed for m = 3. Further investigation of this issue is needed. For example, it could be helpful to run the experiment with $D_2/H_2/HD$ mixed target. With higher statistics and no competing GSD processes, the differences in the energy distributions of the molecular ions could be examined. While this systematic error is the largest single problem with

our measurements, it should be noted that the problem is only significant for a few meV above threshold, and the majority of the energy range of GSD has been mapped.

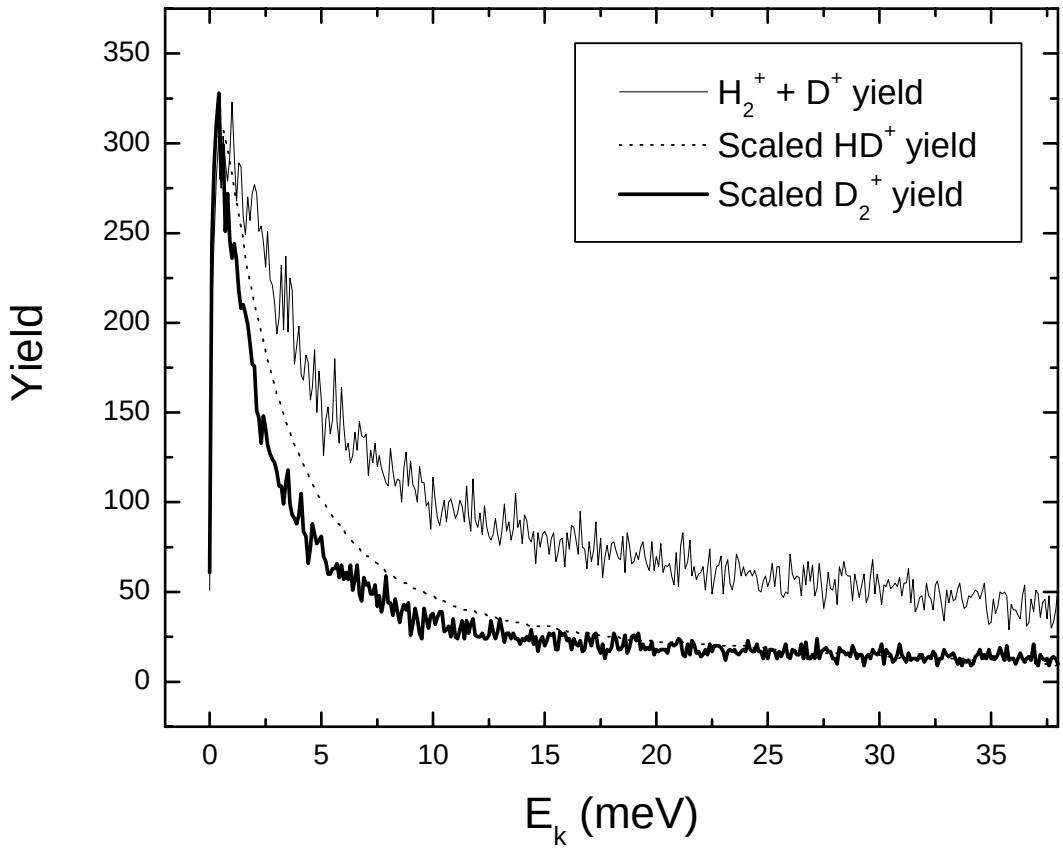

Figure 6.7: Measured energy distributions for three different masses present in our spectra.

If figures 6.5 and 6.6 are examined carefully, it is apparent that the distributions shown are not completely symmetric. The increased population for $P_y < 0$ was due to a design flaw in an early version of our momentum imaging spectrometer. The ceramic spacers used to separate the spectrometer electrodes were too close to the beam, and scattered electrons from surfaces charged up the electrodes. This charge then influenced the trajectory of the recoil ions. Enlarging the spectrometer and moving the ceramic

spacers further from the beam axis eliminated this problem. During the time it took to rectify this situation, however, a few unfortunate things happened in the laboratory, affecting the progress of this experiment. A catastrophic accident rendered the diode ion source inoperative, and that problem is not yet resolved. The accelerating column has been refurbished and should be installed soon. Since the diode ion source is by far the preferred source for generating a bunched beam of protons (see Appendix A) we were forced to choose another projectile. The remaining data presented in this dissertation was obtained using fast (20 MeV) C^{3+} projectiles to initiate the GSD process. The GSD process itself is expected to be unaffected by the change in projectile, but the cross section for the background ionization-excitation and double-ionization processes is much larger (see Chapter 5.1). Additionally, the accelerator itself is temporarily unavailable for use, so we have been unable to investigate the systematic error in the subtracting the H_2^+ contamination further.

One main result of this part of the experiment, namely the charge transfer probability as a function of kinetic energy release, is presented in figures 6.8 and 6.9. A key feature of our experimental method is the ability to "zoom in" on the lowest energies by lowering the extraction field of the spectrometer. Figure 6.8 shows data from $0 \leq E_k \leq$ 1100 meV, taken with four different extraction fields. Figure 6.9 shows the data taken with the two lowest extraction voltages near threshold. The error in the measured energy, excluding the uncertainties from thermal broadening, the H_2 and H_2O subtractions, and the momentum transfer, scales as

$$\delta E_{measured} = \alpha\varepsilon\sqrt{E_{measured}} \tag{6.4}$$

where α is a constant depending on experimental factors (see Appendix G) and $\varepsilon = 3$ for D^+ fragments and $\frac{3}{2}$ for H^+ fragments, due to the conversion from measured energy to center of mass energy, E_k, given in equation (5.4). Additionally, since the probability for a bound-free transition to occur peaks at $E_k = 0$ and falls off rapidly (see chapter 3.1), the statistics of the measurement are best near threshold. For both of these reasons, it is reasonable to bin the measured energy in smaller steps nearer to $E_k = 0$. Following equation (6.4) we increased the bin size approximately with $\sqrt{E_k}$. The horizontal error bars in figures 6.8 and 6.9 are the measurement errors, while the bin size can be inferred from the spacing of the data points. The vertical error bars come from the errors associated with background subtraction and the statistical error.

The general trends of the data shown in figures 6.8 and 6.9 agree well with the theoretical predictions, although, so far, we do not have enough resolution near threshold to be able to distinguish between the Meyerhof model and the complete quantum mechanical coupled channels calculations. The results shown in figures 6.8 and 6.9 decrease the energy range that the probability for charge exchange has been measured in the H^+ + D(1s) system by an order of magnitude, from 120 meV [6.6] to about 12 meV. The energy resolution of the current measurement is superior, due to the difficulty in determining the relative velocity of the two beams in a merged-beams technique. Furthermore, the results demonstrate that the technique of using the GSD process to measure charge exchange in very slow “half” collisions is sound, and if some systematic errors are eliminated, and the experiment can be repeated soon with the ideal projectile, further improvements should be forthcoming.

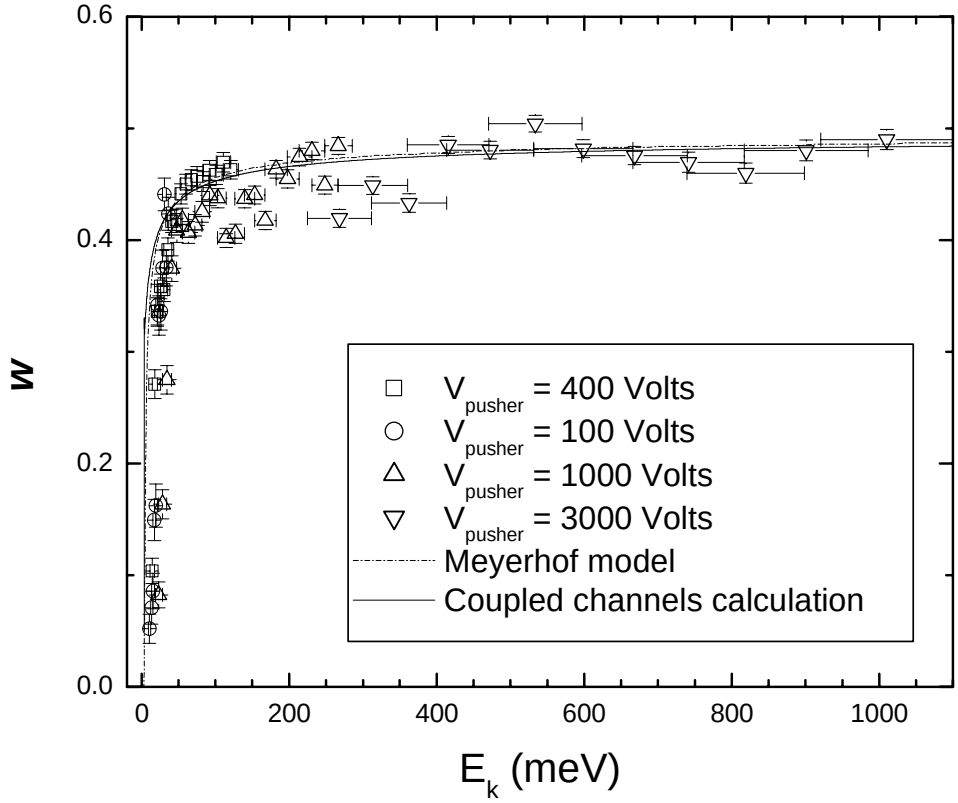

Figure 6.8: The measured transition probability, *w*, as a function of E_k. The results are compared to the coupled channels calculations and the Meyerhof model. Results from runs using 4 different extraction voltages are combined.

Figure 6.9 shows the data from figure 6.8 on an expanded scale. The problems associated with the subtraction of the H_2^+ molecular ions are more apparent on this energy scale. The over-subtraction of the molecular ions results in an unphysical negative probability for charge transfer near threshold, and means that we cannot make meaningful measurements of the charge transfer probability until we are about 10 – 15 meV away from threshold. For E_k greater than about 50 meV, the agreement between theory and experiment is excellent.

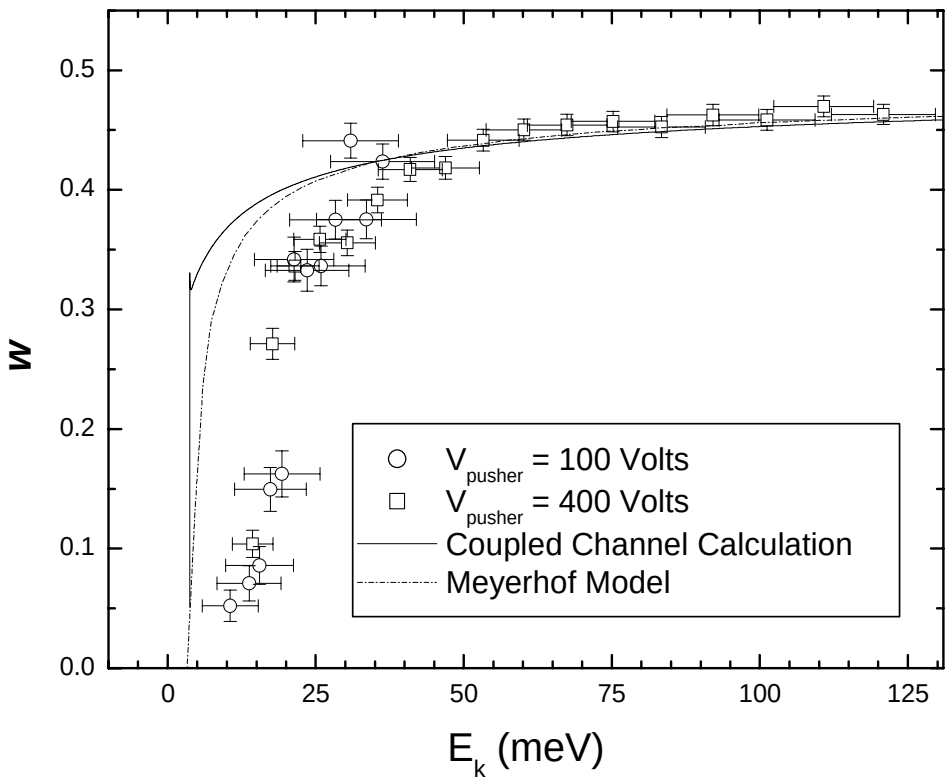

Figure 6.9: The measured transition probability, w, as a function of E_k. The results are compared to the coupled channels calculations and the Meyerhof model. The systematic error in the H_2 subtraction is clear in this figure, with the threshold for a transition appearing to be at about 13 meV, rather than the 3.7 meV predicted by theory. In the region above $E_k \approx 50$ meV, where the H_2 contamination plays only a small role, the agreement between theory and experiment is quite good.

Besides the charge exchange probability that has been our primary focus, there are two other quantities that we can study with this technique. First, we measure the elastic scattering probability,

$$P_{elastic}(E_k) = \frac{HD^+(1s\sigma) \rightarrow H^+}{HD^+}(E_k). \qquad (6.5)$$

This channel is particularly interesting just below the H(1s) threshold, where two Feshbach resonances are located for l = 0. Figure 6.10 shows the calculated elastic scattering probability and the measured data. We obtain reasonable agreement with

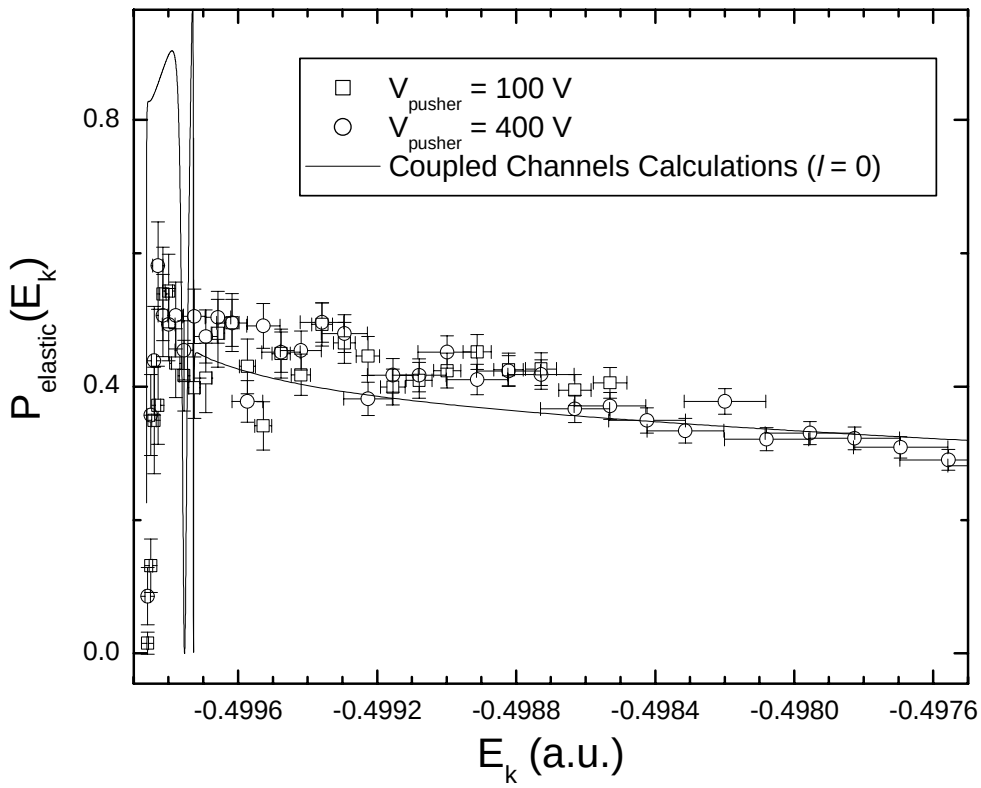

Figure 6.10: The measured and calculated probabilities for elastic scattering measured in this experiment. The calculated value is for l = 0 only, which to a very good approximation, is the only state populated in our measurement, since the temperature of the target is approximately 15 K.

theory for the entire range of E_k above threshold. Since this measurement depends only on the H^+ channel, the energy resolution is inherently twice as good as the D^+ channel, (see equation 5.4) and the H_2^+ contamination is not a major concern. It is important to note the presence of the HD^+ term in the definition of our elastic scattering probability (equation 6.5). In equation 6.5, we define HD^+ as the total yield of single ionization, which is equal to the measured number of HD^+ events divided by 0.99006, a factor needed to account for the single ionization that results in GSD. Since we measure the yield of HD^+ molecular ions as a part of this experiment, the probability of elastic

scattering is automatically normalized in the measurement, and results shown in figures 6.10 and 6.11 are not normalized at an arbitrary point. Stated another way, there are no free parameters in the elastic scattering data.

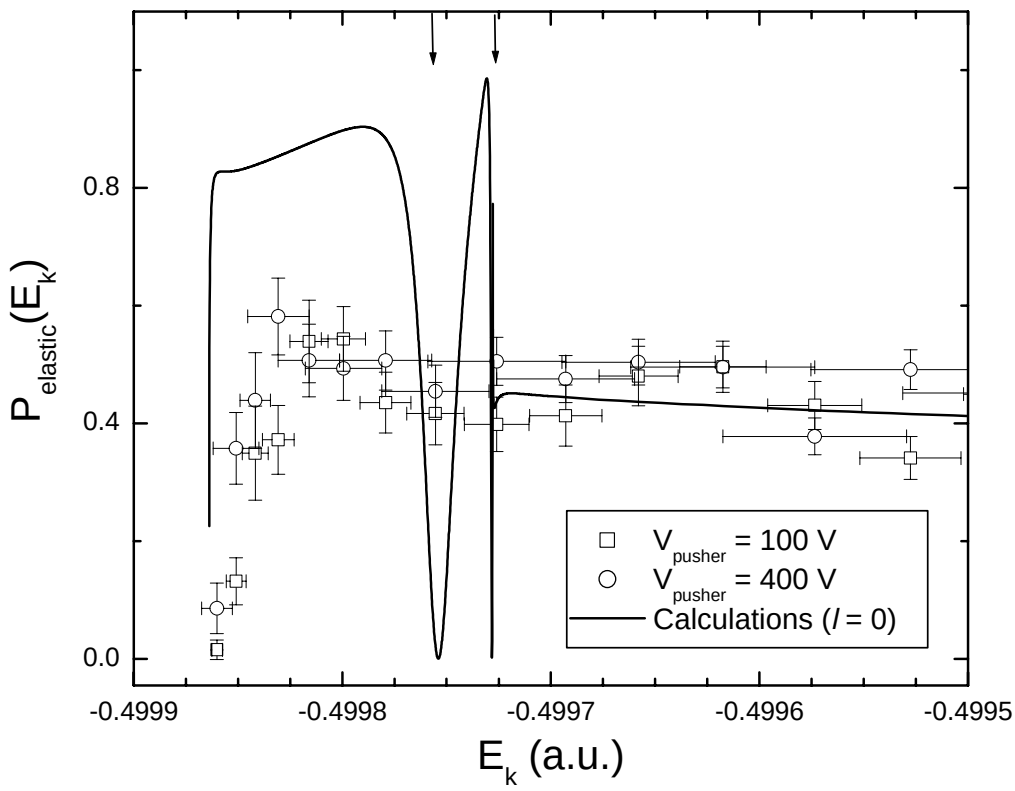

Figure 6.11: The measured and calculated probabilities for elastic scattering in the region of the H(1s) threshold. The calculated value is for l = 0 only, which to a very good approximation, is the only state populated in our measurement, since the temperature of the target is approximately 15 K. The arrows point out the locations of the two l = 0 Freshbach resonances just below the H(1s) threshold (see Table 2.1).

Our results for the probability of elastic scattering in the region around the H(1*s*) dissociation limit are shown in an expanded view in figure 6.11. Near threshold, we do not currently have the resolution to map the resonance structure, but it will hopefully be possible in the near future. The V_{pusher} = 100 V data already shows tantalizing hints of an increase in the probability around 2.5 meV ($\approx 1 \times 10^{-4}$ a.u.) below the H(1*s*) threshold.

There are several ways to improve the resolution. First, the apparatus could be made ultra-high vacuum (UHV) compatible. The major background for this channel is residual water vapor in the target, and with a UHV apparatus, the system could be baked prior to the experiment, removing the water vapor from the interior surfaces. Second, using a fast proton beam instead of the C^{3+} beam used in this measurement will significantly reduce the background, as discussed in section 5.1. Measuring the momentum of the ionized electron could further improve the momentum resolution. If these two things are accomplished, mapping the Feshbach resonances in the elastic channel should be feasible.

The final quantity obtained in this measurement is the sum of the H^+ and D^+ GSD fragments, which can be compared to the Franck-Condon bound-free transition probabilities. The ratio of bound-free to total single ionization is defined as

$$P(E_k) = \frac{H^+(E_k) + D^+(E_k)}{HD^+} \quad . \qquad (6.6)$$

As in equation 6.5, the HD^+ term represents the measured HD^+ yield divided by 0.99006. Again, the self-normalizing nature of our experiment means that we have no free parameters for our comparison with theory. The measurement of $P(E_k)$, for the two lowest extraction voltages, is shown in figure 6.12. Since the D^+ channel is needed in this measurement, the problems associated with the subtraction of the H_2^+ molecular ions are again apparent. Once the data is far enough above threshold that the difficulties arising from the subtraction of the H_2^+ contamination are not a large source of error, the agreement between the predicted value and the data is excellent.

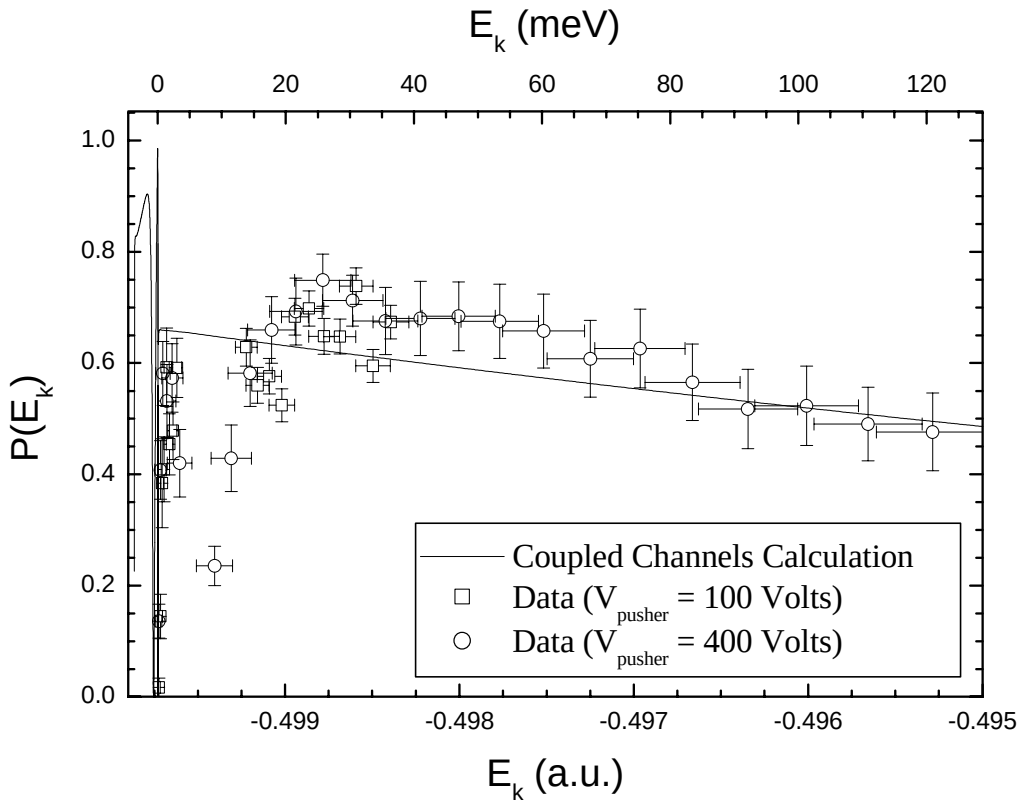

Figure 6.12: A comparison between the calculated ratio of bound-free to total transitions and the results of our measurement. The deviations near zero are caused by the systematic error in the subtraction of the H_2^+ contaminant. The theory shown is the coupled channels calculations.

Chapter 7

When our group decided to undertake this project, two main objectives were specified. The first objective was to show that there was a measurable difference between the two ground state dissociation channels, that is, that the lower H^+ + D(1*s*) channel was more likely than the slightly higher H(1*s*) + D^+ channel. The work of Carrington *et al* [7.1] hinted that if the behavior of the electron above the gap was similar of the electron below the gap, there should be some asymmetry in the two channels, but it was still unclear if this would be measurable, given the relative widths of the energy gap and the range of the kinetic energy release from GSD. We were able to empirically demonstrate, for the first time, that the localization of the electron density on the deuteron occurs not only for vibrationally bound states near the dissociation limit, but also in the vibrational continuum. The isotopic effect leading to the breakdown of the Born-Oppenheimer approximation, therefore, is responsible for the measurable preference (≈ 7%) of D(1*s*) over H(1*s*) in the dissociation of the molecular ion. The major experimental challenge in this part of the experiment was determining the amount of H_2 contamination present in the HD target, which has been done in two different ways [7.2,7.3] with consistent results (see Appendix B). Demonstrating a measurable

asymmetry was the first objective of this project, and this objective has been met to our satisfaction.

The 7% asymmetry in the GSD of HD is similar in magnitude to the deuterium fractionation mechanism reported by Larsson *et al.* in dissociative recombination of H_2D^+, which has been shown to be important interstellar deuterium chemistry models [7.4]. Since the population of ionizing photons or particles in an interstellar medium is smaller than the population of low energy electrons that initiate the dissociative recombination process in H_2D^+, it is difficult to determine the astrophysical relevance of the measured GSD asymmetry. Given that the abundance of HD is many orders of magnitude larger than H_2D^+, however, we feel that *a priori* exclusion of GSD as a significant reaction in interstellar chemistry is also unwarranted. Further study to determine if, and to what extent, the GSD process is significant in astrophysics, is needed.

The second objective of this project was to measure the previously mentioned asymmetry as a function of the kinetic energy release upon dissociation of the molecular ion. This objective was technically more challenging, since it retained the major obstacle, in the form of the H_2 contamination problem, of the first part of the experiment and added the need to measure the energy of the dissociating fragments with high precision. Borrowing many principles of the COLTRIMS technique that have been painstakingly developed in this laboratory (as well as others, notably the University of Frankfurt) over the last decade, we have constructed an apparatus that is capable of this measurement.

The first results of the differential measurements are encouraging. We have been able to measure the probability for charge transfer in the H^+ + D(1*s*) "half" collision

process from near the D(1s) threshold to the edge of the distribution of the kinetic energy release from the GSD process (about 1.1 eV). This represents a significant improvement in the energy range for which this process has been measured. The previous limit of the merged-beams technique (see section 2.3.1) was set by the Stebbings group at Rice [7.5] almost 20 years ago. Their lowest measurement was at a collision energy of 120 meV and had a resolution of approximately 60 meV. In contrast, our experimental resolution becomes better as the kinetic energy release decreases, enabling us to make precise measurements all the way down to threshold. We have demonstrated that the idea of using the GSD process as a mechanism for studying very slow half collisions in the H^+ + D(1*s*) systems is valid.

While we are pleased with what we have accomplished so far, there are still improvements that can be made to this measurement. Foremost among them is the need to understand the systematic error in determining the correct shape of the energy distribution of the contaminant H_2^+ molecular ion. This issue has been discussed at length in chapter 6.2, and is the major source of experimental error in the present differential measurements. We are somewhat optimistic that with some further analysis and testing we will be able to overcome this problem. In addition, this experiment has yet to be run under ideal conditions. The detector resolution for the results reported here was 20% worse than we are usually able to achieve. Ill-timed problems with the accelerator, the diode ion source, the spectrometer design, and the prebuncher amplifier have so far prevented us from running the experiment with a proper spectrometer (which we now have) and the optimum beam of bunched protons (which should be available soon).

We have compared our results to two calculations, one based on Meyerhof's analytic model for vacancy sharing; the other a quantum mechanical coupled channels calculation conducted by Brett Esry. The resolution of the experiment is (so far) not good enough near threshold to differentiate between these two calculations, but the general trends of the data agree well with the calculations. The sum of the elastic and charge exchange channels can be compared to the probability of bound-free vertical transitions calculated by means of the Franck-Condon overlap integral. Our data agrees well with the calculated values once it is far enough away (~20 meV) from threshold that the error associated with the H_2^+ contamination does not affect the results.

Since we have established this method as a probe of the half collision processes in the H^+ + D(1*s*) system, the question arises if there are any other systems to which this method could be applied. Two obvious ones are the tritium isotopes of the hydrogen molecule, HT or DT. Of these two, HT would be the more interesting to study since it would have a larger energy gap. There are significant experimental problems associated with using tritium, however, since it is radioactive. Other diatomic molecules with an isotopic difference might be considered, such as $^{14}N^{15}N$ or $^{16}O^{18}O$, but the relative mass difference is smaller, and the additional electrons complicate the system, making them less attractive candidates for study.

There are, however, several other future directions for this project. One source of uncertainty in our current experiment arises from the fact that we do not measure the momentum of the ionized electron, and therefore cannot determine the center-of-mass motion of the molecular ion on an event-by-event basis. By rotating the jet 90° from its current configuration, two things would be accomplished. First, an electron detector

could be added. Second, a “catcher” could be built opposite the effusive jet to collect the gas flow, reducing the amount of warm gas in our target region.

If the electron were detected, this would open another possible improvement to the experiment. We could, in principal, use the time-focusing properties of the LINAC accelerator to further reduce the width of our beam bunch. Using this technique, proton bunch widths of 400 ps have been obtained on a regular basis [7.6]. There is a problem with this for our experiment. Using the prebuncher and the LINAC to time-focus the projectiles produces bunches with a period of 82.4 ns. The deflector is not used in this procedure since it is expected to reduce the beam current to a level where obtaining a phase lock for the LINAC resonators would be difficult. We would have no trouble measuring a time difference between the fast electron and the master clock signal, but associating this start signal with the correct recoil ion signal is problematic, since the flight times of the recoil ions are very long. In fact, the width of a single time-of-flight peak is often greater than 80 ns, not to mention the difference in arrival times between the different recoil ions. To make this configuration work, we would need to either find a way to phase lock a resonator on much less beam current than is currently used, or determine a way to correctly associate the recoil ion and electron signals.

Controlling the magnitude of the energy used to ionize the electron would also be attractive, since by doing this and measuring the electron and recoil momentum, a kinematically complete experiment could be done. This could be done with a photon, via the photoionization process, and should yield sufficient resolution to map the Feshbach resonances in the elastic channel, shown in figure 3.11. The photo-ionization process would require approximately 19 eV to reach threshold. Beamline 10.0.1 at the Advanced Light Source (ALS) operates in this energy range ($E = 17 – 340$ eV, with $E/\Delta E \sim 10{,}000$).

While doing this experiment is conceptually possible, the period of the light pulses produced by the ALS (a few hundred ns), even when running in two-bunch mode, is much shorter than the time-of-flights of the recoil ions, so we would face the same problem of associating the correct electron and recoil ions signals with each other that was mentioned in the preceding paragraph.

The electron-hydrogen molecule collision is far more common in astrophysical environments than heavy ion-hydrogen molecule collisions (see chapter 4). An asymmetry of the type we have reported [7.7] (and in chapter 6) would be interesting if it also occurs in the electron impact case, since a single cosmic ray can generate a large number of secondary electrons as it ionizes the H_2 and He in an interstellar cloud. Ionizing collisions between these secondary electrons and HD molecules are more common than direct interactions between the cosmic rays and the HD molecules. Furthermore, as the energy of the secondary electron nears the H(1s) threshold, the asymmetry in the branching ratio might increase. Since many of the electrons in an astrophysical environment have energies in this region, the result could be a substantial deuterium fractionation mechanism. Therefore, from an astrophysical standpoint, the most interesting future incarnation of this experiment would be a slow electron impact ionization experiment. From a technical point of view, such an experiment would require the development of a bunching system that would work for an electron beam. The effort involved in building such a system might be considerable, but this system, if built, could have applications beyond the experiment suggested here.

Finally, measurements of the type shown in figure 6.11 can be a sensitive test of the validity of the Franck-Condon approximation. Measuring the $P(E_k)$ of the GSD process can be done with a homonuclear isotope of the hydrogen molecule, making it a

less costly experiment. Probing the validity of the Franck-Condon approximation for collisions between slow highly charged ions and molecular targets has been of recent interest [7.8] and this method might offer one of the best approaches, since the effect of a post-collision interaction should be visible in the measured $P(E_k)$ distribution.

In short, using the ground state dissociation process to study the half collision processes in the H^+ + D(1*s*) system has proved to be a successful method for probing collisions at energies below those feasible with a merged-beams technique. Our results are the first empirical tests of the calculations for this system at these very low collision energies. Beyond improving the energy resolution of the current apparatus, particularly near the H(1*s*) threshold, there are several interesting future directions for similar work.

Bibliography

Chapter 1

1.1 Gilbody, H.B., *Advances in Atomic, Molecular, and Optical Physics* **33**, 149 (1994).

1.2 Stancil, P.C., Lepp, S., and Dalgarno, A., *The Astrophysical Journal* **509**, 1 (1998).

1.3 Mies, F.H., and Giusti-Suzor, A., *Phys. Rev. A* **44**, 7547 (1991).

1.4 Carrington, Alan, *Science*, **274**, 1327 (1996).

1.5 Meyerhof, W.E., *Phys. Rev. Lett.* **31**, 1341 (1973).

1.6 Demkov, Yu. N., *JEPT* **18**, 138 (1964).

1.7 Ullrich, J., Moshammer, R., Dörner, R., Jagutzki, O., Mergel, V., Schmidt-Böcking, H., and Spielberger, L., *J. Phys. B.* **30**, 2917 (1997).

Chapter 2

2.1 Born, M., and Oppenheimer, R., *Ann. d. Physik*, **84**, 457, (1927). For a more recent review, see: Carrington, A., McNab, I.R., and Montgomerie, C.A., *J. Phys. B* **22**, 3551 (1989).

2.2 Fu, Z.W., Hessels, E.A., and Lundeen, S.R., *Phys. Rev A* **46** R5313 (1992).

2.3 Bhatia, A.K., and Drachman, R.J., *Phys. Rev. A.* **59**, 205 (1999).

2.4 Shertzer, J., and Greene, C.H., *Phys. Rev. A* **58**, 1082 (1998)

2.5 Jacobson, P.L. *et al*., *Phys. Rev. A* **56** R4361 (1997).

2.6 Dalgarno, A., and Yadav, H.N., *Proc. Phys. Soc*. **66**, 173 (1953).

2.7 McDowell, M.R.C., *Proc. Phys. Soc*. **72**, 1087 (1958).

2.8 Dalgarno, A. *Proc. Phys. Soc.* **75**, 374 (1960).

2.9 Bates, D.R., and Boyd, A.H., *Proc. Phys. Soc*. **80**, 1301 (1962).

2.10 Murakhver, Yu. E., *JETP* **15**, 849 (1962).

2.11 Smirnov, B.M., *JETP* **19**, 692 (1964).

2.12 Smith, F.J., *Proc. Phys. Soc*. **92**, 866 (1967).

2.13 Parcell, L.A., and May, R.M., *Proc. Phys. Soc*. **91**, 54 (1967).

2.14 Chen, J.C.Y., and Watson, K.M., *Phys. Rev.* **188**, 236 (1969).

2.15 Bates, D.R. and Sprevak, D., *J. Phys. B ser. 2.* **3**, 1483 (1970).

2.16 Knudson, S.K., and Thorson, W.R., *Can. J. Phys*. **48**, 313 (1970).

2.17 Matveenko, A.V., and Ponomarev, L.I., *JEPT* **30**, 1131 (1970).

2.18 Bates, D.R., and Tweed, R.J., *J. Phys. B ser. 2.* **7**, 117 (1974).

2.19 Smith, F.J., *Planet. Space Sci*. **14**, 929 (1966).

2.20 Bates, D.R., Ledsham, K., and Stweart, A.L., *Phil. Trans. R. Soc. Lond. A* **246**, 215 (1953).

2.21 Hunter, G. and Kuriyan, M., *Proc. R. Soc. Lond. A.* **341**, 491 (1975).

2.22 Hunter, G. and Kuriyan, M., in *Electronic and Atomic Collisions, vol. 2*, 1025 (1975).

2.23 Hunter, G. and Kuriyan, M., *Proc R. Soc. Lond. A.* **353**, 575 (1977).

2.24 Bates, D.R. and McCarrol, R., *Proc. R. Soc. London. Ser. A* **245**, 175 (1958).

2.25 Delos, J.B., *Rev. Mod. Phys*. **53**, 287 (1981).

2.26 Davis, Jon, and Thorson, W.R., *Can. J. Phys*. **56**, 996, (1978)

2.27 Hodges, R.R. Jr., and Breig, E.L., *Journal of Geophysical Research*, **96** No. A5, 7697 (1991).

2.28 Wolniewicz, L., and Poll, J.D., *J. Chem Ph*ys. **73**, 8225 (1980).

2.29 Carrington, A., and Kennedy, R.A., *Mol Phys*. **56**, 935 (1985).

2.30 Wolniewicz, L., and Poll, J.D., *Mol. Phys*. **59**, 953 (1986).

2.31 Wolniewicz, L., and Orlikowski, T., *Mol. Phys*. **74**, 103 (1991).

2.32 Moss, R.E., *J. Phys. B* **32** L89 (1999).

2.33 Balint-Kurti, G.G., Moss, R.E., Sadler, I.A., and Shapiro, M., *Phys. Rev.* A **41**, 4913 (1990).

2.34 Moss, R.E. and Sadler, I.A. *Mol Phys*. **66**, 591 (1989).

2.35 Moss, R.E., and Sadler, I.A., *Mol Phys.* **61**, 905 (1987).

2.36 Guryanov, A.V., and Rebane, T., *Sov. J. Struct. Chem*. **23**, 55 (1982) and references therin.

2.37 Thorson, W.R., Choi, J.H., and Knudson, S.K., *Phys. Rev. A* **31** 22 (1985).

2.38 Thorson, W.R., Choi, J.H., and Knudson, S.K., *Phys. Rev. A* **31** 34 (1985).

2.39 Bishop, D.M., and Cheung, L.M., *Phys. Rev. A* **16**, 640 (1977).

2.40 Macek, Joeseph and Jerjian, Khachig A., *Phys. Rev. A* **33**, 233 (1986)

2.41 Smith, T.F., *Phys. Rev*. **120**, 1058 (1960).

2.42 Hara, S., Fukuda, H., and Ishihara, T., *Phys. Rev. A* **39**, 35 (1989).

2.43 Pack, Russell T., *Phys Rev. A* **32**, 2022 (1985).

2.44 Struensee, Michael C., Cohen, James S., and Pack, Russell T., *Phys. Rev. A* **34**, 3605 (1986).

2.45 Pack, R.T., and Hirschfelder, J.O., *J. Chem. Phys*. **49**, 4009, (1968).

2.46 Esry, B.D., and Sadeghpour, H.R., *Phys. Rev A* 60, 3604 (1999).

2.47 Mapleton, R.A., *J. Phys. B.* **1**, 529 (1968).

2.48 Crothers, D.S.F., Kennedy, M., and Smith, F.J., *Proc. Phys. Soc. Ser. 2*, **1**, 1141 (1968).

2.49 Hunter, G., and Kuriyan, Mary, *Proc. R. Soc. Lond. A* **358**, 321 (1977).

2.50 Riera, A., and Salin, A., *J Phys. B*. **9**, 2877, (1976).

2.51 Thorson, W.R., and Delos, J.B., *Phys. Rev. A.* **18**, 117 (1978).

2.52 Hodges, R.R. Jr., *Journal of Geophysical Research*, **98**, 10833 (1993).

2.53 Esry, B.D., Sadeghpour, H.R., Wells, E., and Ben-Itzhak, I., to be submitted *to J. Phys. B* (2000).

2.54 Kennedy, R.A., Moss, R.E., and Sadler, I.A., *Mol. Phys*., 64, 177 (1988).

2.55 Igarashi, Akinori and Lin, C.D. *Phys. Rev. Lett*. 83, 4041 (1999).

2.56 Fite, W.L., Brackmann, R.T., and Snow, W.R., *Phys. Rev*. **112**, 1161 (1958).

2.57 Fite, W.L., Smith, A.C.H., and Stebbings, R.F., *Proc. Roy. Soc. A* **268**, 527 (1962).

2.58 Fite, W.L., Stebbings, R.F., Hummer, D.G., and Brackmann, R.T., *Phys. Rev*. **119**, 663 (1960).

2.59 Gilbody, H.B., *Advances in Atomic, Molecular, and Optical Physics* **33**, 149 (1994).

2.60 Koch, P.M., and Bayfield, J.E., *Phys. Rev. Lett*. **34**, 448 (1975).

2.61 Belyaev, Y.A., Brezhnev, B.G., and Erastov, E.M., *JEPT* **25**, 777 (1967).

2.62 Newman, J.H., Cogan, J.D., Zeigler, D.L., Nitz, D.E., Rundel, R.D., Smith, K.A., and Stebbings, R.F., *Phys. Rev. A*. **25** 2976 (1982).

2.63 Rundel, R.D., Nitz, D.E., Smith, K.A., Geis, M.W., and Stebbings, R.F., *Phys. Rev. A* **19**, 33 (1979).

2.64 Havener, C.C., Huq, M.S., Krause, H.F., Schulz, P.A. and Phaneuf, R.A., *Phys. Rev. A.* **39**, 1725, (1989).

2.65 Pieksma, Marc, Bannister, M.E., Wu, W. and Havener, C.C., *Phys. Rev. A.* **55**, 3526 (1997).

2.66 Pieksma, Marc, Gargaud, M., McCarrol, R. and Havener, C.C., *Phys. Rev. A.* **54**, R13 (1996).

2.67 Antaya, T.A., *J. Phys. (Paris) Coloq*. **50**, C1-707 (1989).

2.68 Havener, C.C., private communication (1998).

2.69 Collins, L.E., and Gobbett, R.H., *Nucl. Instrum. Methods* **35**, 277 (1965).

Chapter 3

3.1 Bransden, B.H. and Joachain, C.J., *Physics of Atoms and Molecules*, (Addison Wesley Longman, Ltd. Essex, UK, 1983) pp. 442-444.

3.2 Wood, R.M., Edwards, A.K., and Steuer, M.F., *Phys. Rev. A* **15**, 1433 (1977).

3.3 Krishnakumar, E., Bapat B., Rajgara, F.A., and Krishnamurthy, M., *J. Phys. B.* **27**, L777 (1994).

3.4 Ben-Itzhak, I., Krishnamurthi, Vidhya, Carnes, K.D., Aliabadi, H., Knudsen, H., Mikkelsen, U., and Esry, B.D., *J. Phys. B.* **29**, L21 (1996).

3.5 Condon, E.U., *Phys. Rev*. **32**, 858, (1928).

3.6 Coolidge, Albert Sprague, James, Herbert M. and Present, Richard D., *J. Chem. Phys.* **4**, 193 (1936).

3.7 Hagstrum, Homer D., and Tate, John, T., *Phys. Rev.* **59**, 354 (1941).

3.8 McCulloh, K.E., and Rosenstock, H.M., *J. Chem. Phys*. **48**, 2084 (1968).

3.9 Tadjeddine, M., and Parlant, G., *Mol. Phys.* 33, 1797 (1977).

3.10 Esry, B.D. and Sadeghpour, H.R., *Phys. Rev A* 60, 3604 (1999).

3.11 Kołos, W., Szalewicz, K., and Monkhorst, H.J., *J. Chem. Phys.* **84**, 3278 (1986).

3.12 Marston, C.C., and Balint-Kurti, G.G., *J. Chem. Phys*. **91**, 3571 (1989).

3.13 Carrington, Alan, *Science*, **274**, 1327 (1996).

3.14 Carrington, Alan, and Buttenshaw, Juliet, *Mol. Phys*. **44**, 267 (1981).

3.15 Carrington, Alan, Buttenshaw, Juliet, and Kennedy, Richard A., *Mol. Phys*. **48**, 775 (1983).

3.16 Carrington, Alan, and Kennedy, Richard A., *Mol. Phys*. **56**, 775 (1985).

3.17 Carrington, Alan, McNab, Iain R., and Montgomerie, Christine, A., *Mol. Phys*. **64**, 679 (1988).

3.18 Carrington, Alan, McNab, Iain R., and Montgomerie, Christine, A., *Mol. Phys*. **64**, 983 (1988).

3.19 Carrington, Alan, McNab, Iain R., and Montgomerie, Christine, A., *Mol. Phys*. **65**, 751 (1988).

3.20 Carrington, Alan, McNab, Iain R., Montgomerie, Christine, A., and Brown, John M. *Mol. Phys*. **66**, 1279 (1989).

3.21 Carrington, Alan, Leach, Christine A., Marr, Andrew J., Moss Richard E., Pyne, Christoper H., and Steimle, Timothy C., *J. Chem Phys*. **98**, 5290 (1993).

3.22 Carrington, Alan, McNab, Iain R., Montgomerie-Leach, Christine A. and Kennedy, Richard A., *Mol. Phys*. **72**, 735 (1991).

3.23 Balint-Kurti, G.G., Moss, R.E., Sadler, I.A., and Shapiro, M., *Phys. Rev.* A **41**, 4913 (1990).

3.24 Wolniewicz, L. and Orlikowski, T., *Mol. Phys*. **74**, 103 (1991).

3.25 Meyerhof, W.E., *Phys. Rev. Lett*. **31**, 1341 (1973).

3.26 Demkov, Yu. N., *JEPT* **18**, 138 (1964).

3.27 Taulbjerg, Knud, Vaaben, Jørgen and Fastrup, B., *Phys. Rev. A*. **12**, 2325 (1975).

3.28 Aymar, Mireille, Greene, Chris H. and Luc-Koenig, Eliane, *Rev. Mod. Phys*. **68**, 1015, (1996).

3.29 Esry, B.D., Sadeghpour, H.R., Wells, E., and Ben-Itzhak, I., to be submitted *to J. Phys. B* (2000).

Chapter 4

4.1 Dunn, G.H. *et al*., in *Atomic, Molecular, and Optical Science, An Investment in the Future.* (National Academy Press, Washington D.C., 1994).

4.2 Fox, J.L., in *Atomic, Molecular, and Optical Physics Handbook*, G.F.W. Drake, ed. (AIP Press, New York, 1996) pp. 940-968.

4.3 Hodges, R.R., Tinsley, B.A., and Rohrbaugh, R.P., *J. Geophys. Res.* **86**, 6917 (1981).

4.4 Shizgal, B., and Lindenfeld, M.J., *J. Geophys. Res.* **87**, 853 (1982).

4.5 McElroy, M.B., Prather, M.J., and Rodriquez, J.M., *Science*, **215**, 1614 (1982).

4.6 Rodriques, J.M., Prather, M.J., and McElroy, *Planet. Space. Sci*., **32**, 1235 (1984).

4.7 Hodges, R.R., and Tinsley, B.A., *J. Geophys. Res*. **91**, 13649 (1986).

4.8 Shizgal, B., *Adv. Space. Res*. **7**, 73 (1987).

4.9 Yung, Y.L., Wen, J.-S, Moses, J.I., Landry, B.M. Allen, M. and Hsu, K.J., *J. Geophys. Res.* **94**, 14971 (1989).

4.10 Hodges, R.R., and Breig, E. L., *J. Geophys. Res.* **98**, 1581 (1993).

4.11 Hunter, G., and Kuriyan, Mary, *Proc. R. Soc. Lond. A* **358**, 321 (1977).

4.12 Dalgarno, A., and Lepp, S., in *Atomic, Molecular, and Optical Physics Handbook*, G.F.W. Drake, ed. (AIP Press, New York, 1996) pp. 919-929.

4.13 Penzias A.A., Wannier P.G., Wilson R.W., and Linke, R.A., *The Astrophysical Journal*, **211**, 107 (1977).

4.14 Schramm, D.N., *Physica Scripta*, **T36**, 22 (1991).

4.15 Peebles, P.J.E., *Principles of Physical Cosmology* (Princeton University Press, Princeton, New Jersey, 1993) pp. 149-51, 475-77.

4.16 Burles, S., and Tytler, D., *The Astrophysical Journal* **507**, 732 (1998).

4.17 Fuller, G.M., and Cardall, C.Y., *Nucl. Phys. Proc. Suppl. B* **51** 71 (1996).

4.18 Schramm, D.N. and Turner, M.S., *Rev. Mod. Phys.* **70**, 303 (1998).

4.19 Dalgarno, A., and Lepp, S., *The Astrophysical Journal* **287**, L47 (1984).

4.20 Millar, T.J., in *Molecular Astrophysics*, T.J. Hartquist, ed. (Cambridge University Press, Cambridge, 1990) pp. 115.

4.21 Palla, F., Galli, D., and Silk J., *The Astrophysical Journal* **451**, 44 (1995).

4.22 Galli D., and Palla, F., *Astron. Astrophys*. **335,** 403 (1998).

4.23 Stancil, P.C., Lepp, S., and Dalgarno, A., *The Astrophysical Journal* **509**, 1 (1998).

4.24 Watson W.D., Christensen R.B., and Deissler R.J, *Astron. Astrophys*., **69**, 159 (1978).

4.25 Esry, B.D., Sadeghpour, H.R., Wells, E., and Ben-Itzhak, I., to be submitted *to J. Phys. B* (2000).

4.26 Larsson, M., Lepp, S., Dalgarno, A., Strömholm, C., Sundström, G. Zengin, V., Danared, H., Källberg, A., af Ugglas, M. and Datz, S., *Astron. Astrophys*., **309**, L1, (1996).

4.27 Dalgarno, A., private communication (1998).

Chapter 5

5.1 Newman, J.H., Cogan, J.D., Zeigler, D.L., Nitz, D.E., Rundel, R.D., Smith, K.A., and Stebbings, R.F., *Phys. Rev. A.* **25** 2976 (1982).

5.2 Cocke, C.L., *Phys. Rev. A.* **20**, 749 (1979).

5.3 Ullrich, J., Moshammer, R., Dörner, R., Jagutzki, O., Mergel, V., Schmidt-Bocking, H., and Spielberger, L., *J. Phys. B.* **30**, 2917 (1997).

5.4 Abdallah, M.A., Achler, Matthias, Bräuning, H., Bräuning-Deminiam, Angela, Cocke, C.L., Czasch, Achim, Dörner, R., Landers, A., Mergel, V., Osipov, T., Schmidt-Böcking, Singh, M., Weber, T., Wolff, W., and Wolf, H.E., in Proceedings *of the 18th International Conference on X-Ray and Inner Shell Processes, Chicago, 1999*, R. W. Dunford, D. S. Gemmell, E. P. Kanter, B. Krössig, S. H. Southworth, and L. Young ed., (AIP Press, College Park, Maryland, 2000) pp 101.

5.5 Wells, E., Ben-Itzhak, I., Carnes, K.D., and Krishnamurthi, V., *Phys. Rev. A.* **60**, 3734 (1999).

5.6 Ben-Itzhak, I., Krishnamurthi, Vidhya, Carnes, K.D., Aliabadi, H., Knudsen, H., Mikkelsen, U., and Esry, B.D., *J. Phys. B.* **29**, L21 (1996).

5.7 Ben-Itzhak, I., Krishnamurthi, Vidhya, Carnes, K.D., Aliabadi, H., Knudsen, H., and Mikkelsen, U., *Nucl. Instrum. Methods Phys. Res.* **99**, 104 (1995).

5.8 Edwards, A.K., Wood, R.M., Beard, A.S., and Ezell, R.L., *Phys. Rev. A* **42**, 1367 (1990).

5.9 Landers, A.L., Ph.d thesis, Kansas State University (unpublished) p. 43, (1999).

5.10 Knudsen, H., Anderson, L.H., Hvelplund, P., Astner, G., Cederquist, H. Danared, H., Liljeby, L., and Rensfelt, K.G., *J. Phys. B.*, **17**, 3545 (1984).

5.11 Ben-Itzhak, I., Ginther, S.G., Carnes, K.D., *Nucl. Instrum. Methods Phys. Res. B* **66**, 401 (1992).

5.12 Ben-Itzhak, I., Ginther, S.G., Carnes, K.D., *Phys. Rev. A*, **47**, 2827 (1994).

5.13 Ginther, Stuart, M.S. thesis, Kansas State University (unpublished) (1992).

5.14 Wiley, W.C. and McLaren, I.H., *Rev. Sci. Instrum*. **26**, 1150 (1955).

5.15 Ben-Itzhak, I., Carnes, K.D., and DePaola, B.D., *Rev. Sci. Instrum*. **63**, 5780 (1992).

5.16 Mergal, V., *Dynamische Elektron Korrelation in Helium* (Shaker Verlag, Aachen, 1996).

5.17 Pualey, H., in *Atomic and Molecular Beam Methods Vol. 1*, edited by Giacinto Scoles (Oxford University Press, New York, 1988), pp. 87-92.

5.18 Dörner, R., Braning, H., Feagin, J.M., Mergel, V., Jagutzki, O., Spielberger, L., Vogt, T., Khemliche, H., Prior, M.H., Ullrich, J., Cocke, C.L., and Schmidt-Bocking, H., *Phys. Rev. A.* **57**, 1074 (1995).

5.19 Dahl, David A., SIMION 3D Version 6.0, Lockheed Martin Idaho Technologies, Idaho National Engineering Laboratory, (1995).

Chapter 6

6.1 Ben-Itzhak, I., Wells, E., Krishnamurthi, Vidhya, Carnes. K.D., Aliabadi, H., Mikkelsen, U., Weaver, O.L., and Esry, B.D., *Nucl. Instrum. Meth. Phys. Res. B* **129**, 117 (1997).

6.2 Meyerhof, W.E., *Phys. Rev. Lett*. **31**, 1341 (1973).

6.3 Ben-Itzhak, I., Wells, E., Carnes, K.D., Krishnamurthi, V., Weaver, O.L., and Esry, B.D., *submitted to Phys. Rev. Lett*. (1999).

6.4 Ben-Itzhak, I., Krishnamurthi, Vidhya, Carnes, K.D., Aliabadi, H., Knudsen, H., Mikkelsen, U., and Esry, B.D., *J. Phys. B.* **29**, L21 (1996).

6.5 Dahl, David A., SIMION 3D Version 6.0, Lockheed Martin Idaho Technologies, Idaho National Engineering Laboratory, (1995).

6.6 Newman, J.H., Cogan, J.D., Zeigler, D.L., Nitz, D.E., Rundel, R.D., Smith, K.A., and Stebbings, R.F., *Phys. Rev. A.* **25** 2976 (1982).

Chapter 7

7.1 Carrington, Alan, McNab, Iain R., Montgomerie-Leach, Christine A. and Kennedy, Richard A., *Mol. Phys*. **72**, 735 (1991).

7.2 Ben-Itzhak, I., Wells, E., Krishnamurthi, Vidhya, Carnes, K.D., Aliabadi, H., Mikkelsen, U., Weaver, O.L., and Esry, B.D., *Nucl. Instrum. Meth. Phys. Res. B* **129**, 117 (1997).

7.3 Wells, E., Esry, B.D., Carnes, K.D., and Ben-Itzhak, I., to be submitted to *Phys. Rev. A*. (2000).

7.4 Larsson, M., Lepp, S., Dalgarno, A., Strömholm, C., Sundström, G. Zengin, V., Danared, H., Källberg, A., af Ugglas, M. and Datz, S., *Astron. Astrophys*. **309**, L1, (1996).

7.5 Newman, J.H., Cogan, J.D., Zeigler, D.L., Nitz, D.E., Rundel, R.D., Smith, K.A., and Stebbings, R.F., *Phys. Rev. A*. **25** 2976 (1982).

7.6 Landers, A.L., PhD thesis, Kansas State University (unpublished) (1999).

7.7 Ben-Itzhak, I., Wells, E., Carnes, K.D., Krishnamurthi, V., Weaver, O.L., and Esry, B.D., *submitted to Phys. Rev. Lett*. (1999).

7.8 DuBois, R.D., Ali, I., and Cocke, C.L., in the Proceedings of the *XXI International Conference of the Physics of Electronic and Atomic Collisions*, (1999).

Appendix A

A.1 Wells, E., Ben-Itzhak, I., Carnes, K.D., and Krishnamurthi, V., *Phys. Rev. A*. **60**, 3734 (1999).

A.2 Landers, A.L., PhD thesis, Kansas State University (unpublished) p. 140, (1999).

A.3 *Ionex 1610 Nanosecond Pulsing System*, General Ionex Corporation, 19 Graf Rd, Newburyport, Massachusetts, 01950.

A.4 Carnes, K.D., *Prebuncher Analysis*, J.R. Macdonald Laboratory Report (unpublished) (1999).

A.5 Whiteway, F.E., *Ion Bunching Systems for Particle Accelerators*, U.K. AWRE Report No. O-12/61 (1961).

Appendix B

B.1 Ben-Itzhak, I., Krishnamurthi, Vidhya, Carnes, K.D., Aliabadi, H., Knudsen, H., and Mikkelsen, U., *Nucl. Instrum. Methods Phys. Res. B* **99**, 104 (1995).

B.2 Wells, E., Ben-Itzhak, I., Carnes, K.D., and Krishnamurthi, V., *Phys. Rev. A.* **60**, 3734 (1999).

B.3 Ben-Itzhak, I., Wells, E., Krishnamurthi, Vidhya, Carnes. K.D., Aliabadi, H., Mikkelsen, U., Weaver, O.L., and Esry, B.D., *Nucl. Instrum. Meth. Phys. Res. B* **129**, 117 (1997).

B.4 Ben-Itzhak, I., Krishnamurthi, Vidhya, Carnes, K.D., Aliabadi, H., Knudsen, H., Mikkelsen, U., and Esry, B.D., *J. Phys. B.* **29**, L21 (1996).

B.5 Wells, E., Esry, B.D., Carnes, K.D., and Ben-Itzhak, I., to be submitted to *Phys. Rev. A.* (2000).

B.6 Wiley, W.C. and McLaren, I.H., *Rev. Sci. Instrum*. **26**, 1150 (1955).

Appendix C

C.1 Wiza, Joseph Ladislas, *Nucl. Instrum. Meth. Phys*. **162**, 587 (1979).

C.2 Colson, W.B., McPherson, J., and King, F.T., *Rev. Sci. Instrum.* **44**, 1694 (1974).

C.3 Ben-Itzhak, I., Ginther, S.G., Carnes, K.D., *Nucl. Instrum. Methods Phys. Res. B* **66**, 401 (1992).

C.4 Ginther, Stuart, M.S. thesis, Kansas State University (unpublished) (1992).

C.5 Lampton, M., and Carlson, C.W., *Rev. Sci. Instrum*. **50**, 1093 (1979).

C.6 Cheng, S., PhD thesis, Kansas State University, (unpublished) (1991).

C.7 Knudsen, H., Anderson, L.H., Hvelplund, P., Astner, G., Cederquist, H. Danared, H., Liljeby, L., and Rensfelt, K.G., *J. Phys. B.*, **17**, 3545 (1984).

C.8 Gray, T.J., Cocke, C.L., and Justiniano, E., *Phys. Rev. A.*, **22**, 849 (1980).

Appendix D

D.1 Ben-Itzhak, I., Carnes, K.D., and DePaola, B.D., *Rev. Sci. Instrum*. **63**, 5780 (1992).

D.2 Ginther, Stuart, M.S. thesis, Kansas State University (unpublished) (1992).

Appendix E

E.1 Wiley, W.C. and McLaren, I.H., *Rev. Sci. Instrum*. **26**, 1150 (1955).

E.2 Ben-Itzhak, I., Ginther, S.G., Carnes, K.D., *Nucl. Instrum. Methods Phys. Res. B* **66**, 401 (1992).

E.3 Ginther, Stuart, M.S. thesis, Kansas State University (unpublished) (1992).

E.4 Landers, A.L., PhD thesis, Kansas State University (unpublished) (1999).

E.5 Abdallah, Mohammad A., PhD thesis, Kansas State University (unpublished) (1997).

E.6 Abdallah, M.A., Achler, Matthias, Bräuning, H., Bräuning-Deminiam, Angela, Cocke, C.L., Czasch, Achim, Dörner, R., Landers, A., Mergel, V., Osipov, T., Schmidt-Böcking, Singh, M., Weber, T., Wolff, W., and Wolf, H.E., in Proceedings *of the 18th International Conference on X-Ray and Inner Shell Processes, Chicago, 1999*, R. W. Dunford, D. S. Gemmell, E. P. Kanter, B. Krössig, S. H. Southworth, and L. Young ed., (AIP Press, College Park, Maryland, 2000) pp 101.

E.7 Dahl, David A., SIMION 3D Version 6.0, Lockheed Martin Idaho Technologies, Idaho National Engineering Laboratory, (1995).

E.8 Mergal, V., *Dynamische Elektron Korrelation in Helium* (Shaker Verlag, Aachen, 1996).

E.9 Frohne, M.V., PhD thesis, Kansas State University (unpublished) (1994).

E.10 Dörner, R., Braning, H., Feagin, J.M., Mergel, V., Jagutzki, O., Spielberger, L., Vogt, T., Khemliche, H., Prior, M.H., Ullrich, J., Cocke, C.L., and Schmidt-Böcking, H., *Phys. Rev. A.* **57**, 1074 (1995).

Appendix F

F.1 Pualey, H., in *Atomic and Molecular Beam Methods Vol. 1*, edited by Giacinto Scoles (Oxford University Press, New York, 1988), pp. 87-92.

F.2 Vályi, L., *Atom and Ion Sources*, (John Wiley & Sons, London 1977).

F.3 Hasted, J.B., Physics of Atomic Collisions, (American Elsevier Publishing Company, Inc., New York 1972) pp. 153-161.

F.4 Kantrowitz, A., and Grey, J., *Rev. Sci. Instrum*. **22**, 328 (1951).

Appendix I

I.1 XSYS/IUCF Data Acquisition Software, Indiana University Cyclotron Facility, Bloomington, IN 47405.

Appendix A: Bunched Beam Operation

The main advantage of working with a pulsed, or "bunched" beam in this experiment is the increase in the rate of single ionization events. Using a bunched beam of protons, and with a typical target thickness for this experiment, 50 pA of protons produce a counting rate of about 1000 Hz, the vast majority of which are single ionization events. From chapter 3, we know that for an HD target, about 1% of these events are the GSD process of interest, so the rate of GSD events is 10 Hz (assuming a 1000 Hz single ionization rate). The highest rate projectile detector we have in the lab is the scintillator/photo-multiplier tube that our group has used for a projectile detector on some occasions [A.1]. That detector can handle about a 1 MHz counting rate, or a beam current of about 0.2 pA. This would scale to a single ionization rate of 4 Hz, and a GSD rate of 0.04 Hz. Making an accurate measurement of charge transfer in $H^+ + D(1s)$ collisions as a function of energy requires the collection of on the order of 100,000 GSD events, a process that would take roughly 4 weeks of continuous accelerator time. Furthermore, this estimate is quite optimistic, since at 1 MHz, the number of stops by a random projectile would be comparable to the number of stops by a true projectile, which would be a significant problem in the time-of-flight spectrum [A.1]. By eliminating the

need to measure the projectile, the counting rate of the experiment can therefore be improved considerably.

Using a bunched beam allows the time-of-flight of the recoil ion to be determined without a measurement of the projectile, since the projectiles are known to arrive at specified intervals. The resolution of the time-of-flight measurement, then, depends on the width of the beam pulses, since we have no way of knowing which particle in the bunch interacts with the hydrogen target. One way to compress the bunches is to use the time-focusing properties of the KSU LINAC, which has been used to produce bunches with a width of 150 – 500 ps, depending on the projectile [A.2]. The major drawback with this approach, for our purposes, is that the bunched beam has a period of 80 ns, much shorter than the flight time of our recoil ions, which can be longer than 40 μs for some of the very low extraction fields used in this experiment. In order to bunch the beam to around 1 ns and work with a period of at least several microseconds, we use a deflector system in combination with the prebuncher for the LINAC.

The General Ionex Corporation 1672 Traveling Wave Beam Deflector [A.3] consists of 12 pairs of opposing plates, each 1” long with a 0.25” gap between consecutive plates (see figure A.1). The voltage between two opposing plates is pulsed between 0 and 500 volts, with a rise time of each pulse on the order of 20 ns. The deflector control module generates twelve output pulses that are simultaneously variable in width. The time delay between leading edges is also variable. The circuitry of the control module consists of 12 dual D flip-flops that are wired so each flip-flop functions as a one shot multivibrator. The 12 one shots are cascaded so that the trailing edge of the first circuit triggers the following circuit, and the resulting chain sets up the delay

between the start of each output pulse. The delay pulse widths are controlled by the front panel pulse delay control and the output pulse widths are controlled by the pulse width control, both of which are located on the console in the Tandem/LINAC control room.

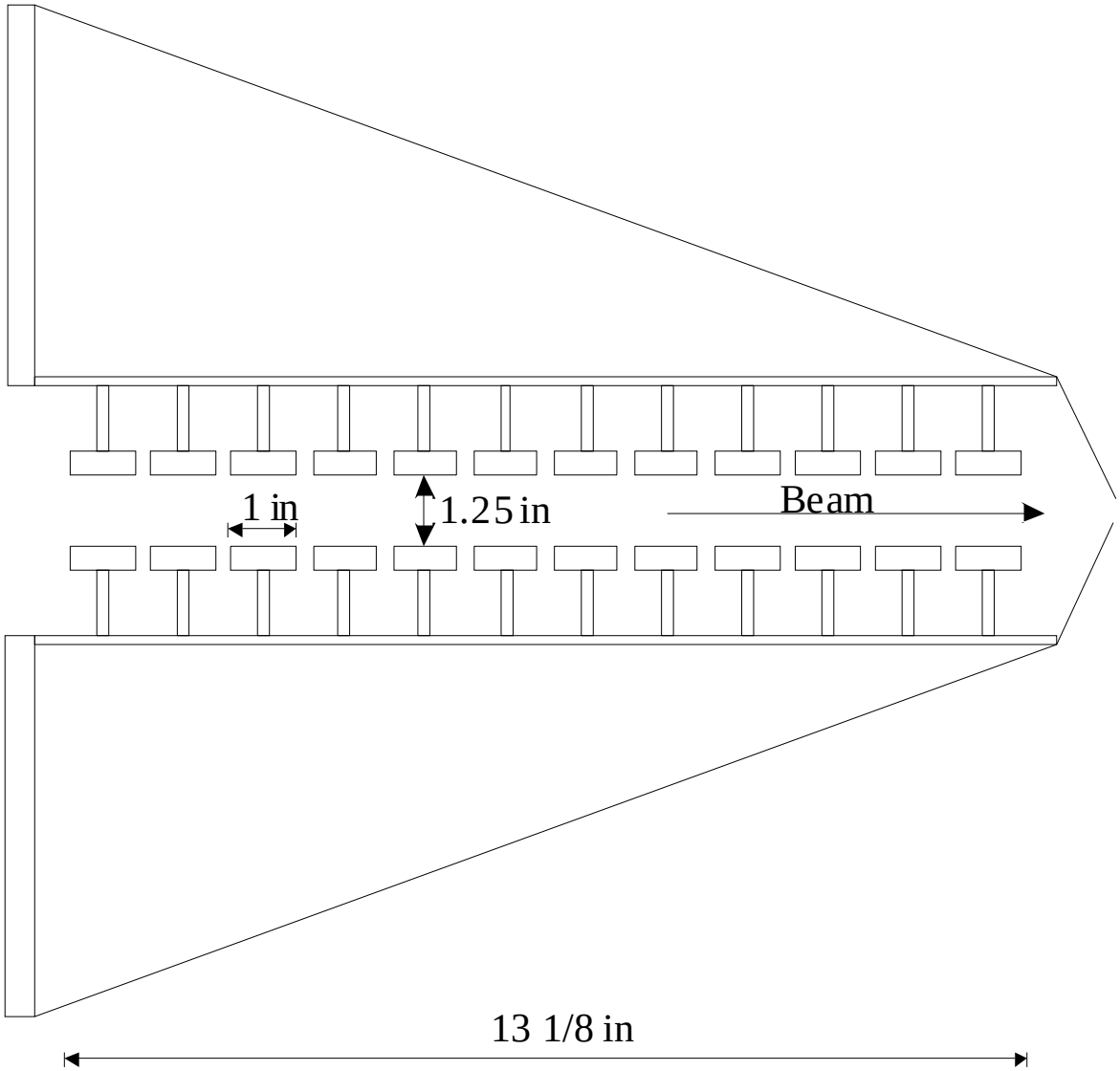

Figure A.1: A schematic picture of the deflector assembly. The 12 pairs of opposing plates are used to deflect the entire beam from the source, except for a traveling wave of undeflected beam. The plates oscillate between ground and ±250 volts.

The deflector amplifier contains six identical channels and is packaged in two sections, a pre-amplifier and a final amplifier. The input from the control module is fed into a three-stage transistorized amplifier, boosting the signal in voltage to drive the grid

of a 4CX350F (8322) vacuum tube tetrode in the final amplifier. In the plate circuit of this vacuum tube is the primary of a dual secondary pulse transformer. These two secondaries are connected to two opposing deflector plates in a manner so that one secondary winding delivers a positive pulse, the other a negative pulse. The positive bias voltage is connected to the coil that delivers the negative pulse so that the pulse oscillates from +250 volts to ground and back to +250 volts. The opposite occurs on the opposite plate. Therefore, the voltage on the opposing deflector plates pulses from 500 volts DC to 0 and back to 500 volts.

There are actually two deflector amplifier assemblies mounted on the 1672 deflector, each driving six pairs of deflector plates. One amplifier drives the odd numbered plates, the other the even numbered. When bunching protons, this is useful, since the transit time of the protons (because of their small mass) is fast enough that consecutive plates cannot respond quickly enough. By using only every other plate, the deflector can respond quickly enough to set up a traveling wave, and since the protons are light, there is still enough deflection to separate the deflected and undeflected beams.

The deflector produces a traveling wave of undeflected beam, roughly 40-70 ns wide (depending on the width setting) with a period of 0.67 to 169.6 μs. The prebuncher further reduces this width. The JRM prebuncher was built from a design for a similar device used on the Argonne National Laboratory (ANL) ATLAS accelerator (see figures A.2 and A.3). The best reference on the JRM prebuncher is the analysis done in August 1999 by Kevin Carnes [A.4], and some of that report is reproduced here. Whiteway explained the operating principle of the prebuncher system in 1961 [A.5]. Defining E_0 as the initial energy of the ion, e_m as the energy given to an ion at the bunching gap, t as the

time of arrival at the gap, and τ as the transit time of the ions to the bunching detector, Whiteway derived the ideal waveform for bunching, provided the ion trajectories are across a drift space, as

$$e_m = \frac{E_0}{(1-\frac{t}{\tau})^2} - E_0 . \tag{A.1}$$

If the period of the periodic bunching waveform is small compared to the total ion transit time ($t << \tau$) the waveform may be approximated by a sawtooth wave:

$$e_m = \frac{2E_0 t}{\tau} . \tag{A.2}$$

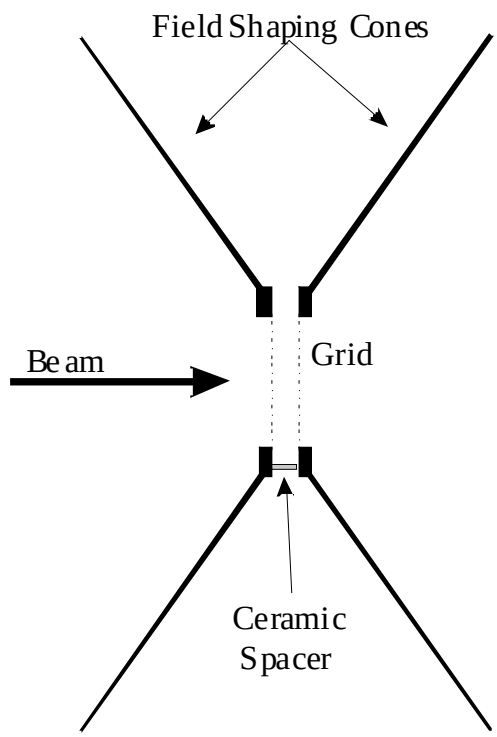

Figure A.2: A schematic figure of the prebuncher. Two grids provide the bunching gap the beam passes through. The voltage on the grids is varied to compress the width of the beam pulses that passes through the deflector.

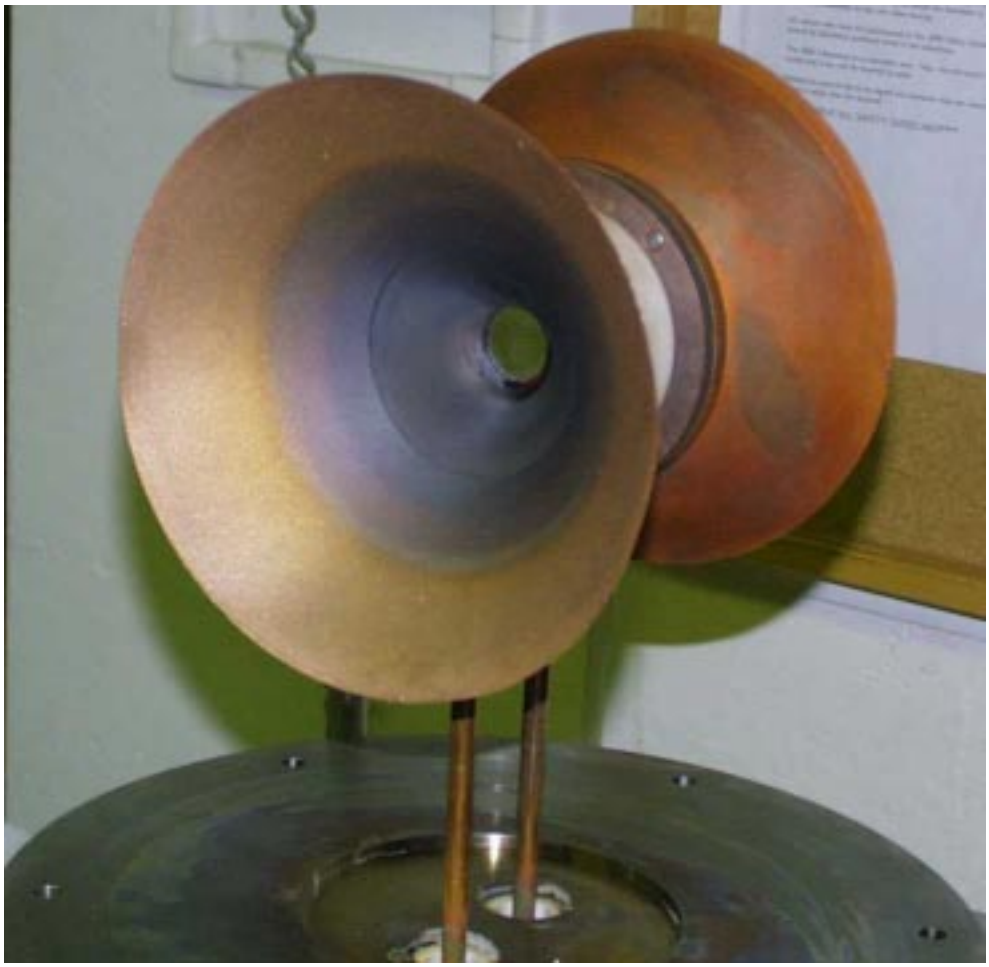

Figure A.3: The field shaping cones of the prebuncher.

In the specific case of JRM, the ions pass through a series of acceleration regions (the Tandem acceleration regions, and drift regions in the beamlines and the stripper canal) and drift regions before reaching the target, which is the region where the particles need to be focused. Figure A.4 shows the accelerating and drift regions between the source and the bunching detector immediately before the LCM1, and table A.l lists the lengths of the different regions. For a region of the particle's flight path of length L with uniform acceleration beginning at energy E_i and ending with E_f, the time-of-flight (TOF) can be calculated explicitly [A.4], with the result being:

$$TOF = \frac{\sqrt{2m}\frac{L}{c}}{\sqrt{E_i} + \sqrt{E_f}}. \qquad \text{(A.3)}$$

In equation A.3, E is in MeV, c is the velocity of light, and m is the particle mass in MeV/c^2. If $E_i = E_f$, this equation is valid for a drift region.

Region	**Length (m)**
Prebuncher to Low Energy Column (Drift)	1.435
Low Energy Column (Acceleration)	4.059
Stripping Canal (Drift)	1.118
High Energy Column (Acceleration)	3.967
High Energy Column to Bunching Diagnostics (Drift)	15.088

Table A.1: Lengths of the regions between the prebuncher and the bunching diagnostics located just before LCM1.

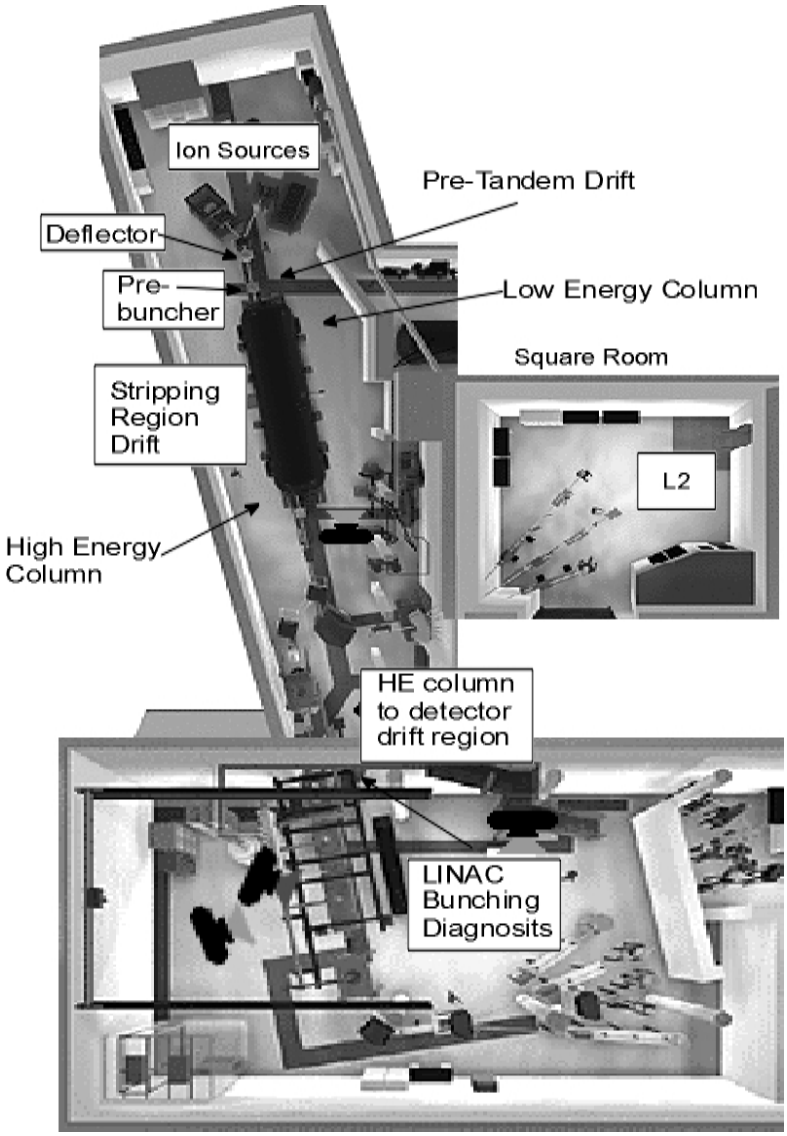

Figure A.4: The flight regions between the prebuncher and the bunching diagnostics.

Alternatively, using the approximation $e_m << E_0$, Whiteway separates the final TOF equation into terms that depend on e_m and those that do not, which is the same form as the TOF for a single drift space. Therefore, the constant term in the equation gives the mean transit time of the ions, and the coefficient of the e_m term gives the value of τ used in equation A.1 [A.5]. As a result, the forms of the ideal and approximate waveform remain the same, even when acceleration regions are involved in the calculation.

When protons are accelerated out of the diode source (the preferred source, as will be discussed later), E_0 = 55 kV, and for 4 MeV (our standard beam), the Tandem terminal voltage is 2 MV. Using Whiteway's approximation [A.5], τ can be calculated and compared to a value of τ determined by choosing a distribution of e_m values and calculating a TOF for each one, and then fitting to the ideal waveform. The values of τ determined by these two different methods were found to be almost identical (509.8 ns and 509.5 ns) [A.4].

It is relatively easy to create a sine wave bunch, since high Q tuned circuits can be used to reduce the power required to create the required bunching voltage. The trade off is that the linear portion of the waveform is small relative to the overall waveform, reducing the bunching efficiency. Using multiple harmonic sine waves combined to approximate a sawtooth, however, increases the efficiency. The fundamental frequency of the pre-tandem buncher must be a sub-harmonic of the fundamental frequency of the post-tandem buncher (12.125 MHz for the prebuncher, 97 MHz for the LINAC) which also dictates the repetition rate of the deflector, since both the prebuncher and the deflector are run from the same master clock signal. The harmonics used at KSU are 12.125, 24.250, and 36.375 MHz. The coefficients of these waveforms are calculated initially as the first three terms in a Fourier expansion of the sawtooth waveform. The coefficients are

$$b_1 = b_0 ,$$

$$b_2 = -\frac{1}{2} b_0 ,$$

$$b_3 = \frac{1}{3} b_0 \tag{A.4}$$

with

$$b_0 = \frac{4E_0}{\omega\tau} \tag{A.5}$$

where the Fourier expansion has the form

$$\begin{aligned} f(x) = \tfrac{1}{2} a_0 + a_1 \cos x + a_2 \cos 2x + a_3 \cos 3x + \ldots \\ + b_1 \sin x + b_2 \sin 2x + b_3 \sin 3x + \ldots \end{aligned} , \tag{A.6}$$

$$b_n = \frac{1}{\pi} \int_{-\pi}^{\pi} f(x) \sin nx dx , \tag{A.7}$$

and the a_n terms are zero since the function is odd in x ($x = \omega t$). For the standard example of protons taken from the diode source and accelerated to 4 MeV, b_0 = 5.66. ANL uses the coefficients 1, -0.4, and 0.18 as a better approximation of a sawtooth, and the best approximation is 1, -0.284, and 0.056. These coefficients require a smaller b_0 term, and thus narrower bunch widths, and have a correspondingly worse efficiency, since the linear (bunching) part of the waveform shrinks with respect to the total waveform. A comparison of the different values for the coefficients is shown in figure A.5.

Several Digital Visual FORTRAN programs written by Basil Curnutte and modified by Kevin Carnes are used for prebuncher analysis. These programs take user specified values of the harmonic coefficients, calculate the total TOF of an ion, and obtain the best value for b_0. These programs were used to determine the coefficients of the waveforms shown figure A.5.

Figure A.6 shows that the actual TOF distribution for particles with no initial energy spread contains structure that becomes more pronounced as the "wiggles" in the 3-harmonic sawtooth (see figure A.5) approximation become more pronounced. Since the actual ions do have an initial energy spread due to ripple on the ion source power supplies and small source instabilities, we typically are unable to resolve this microstructure.

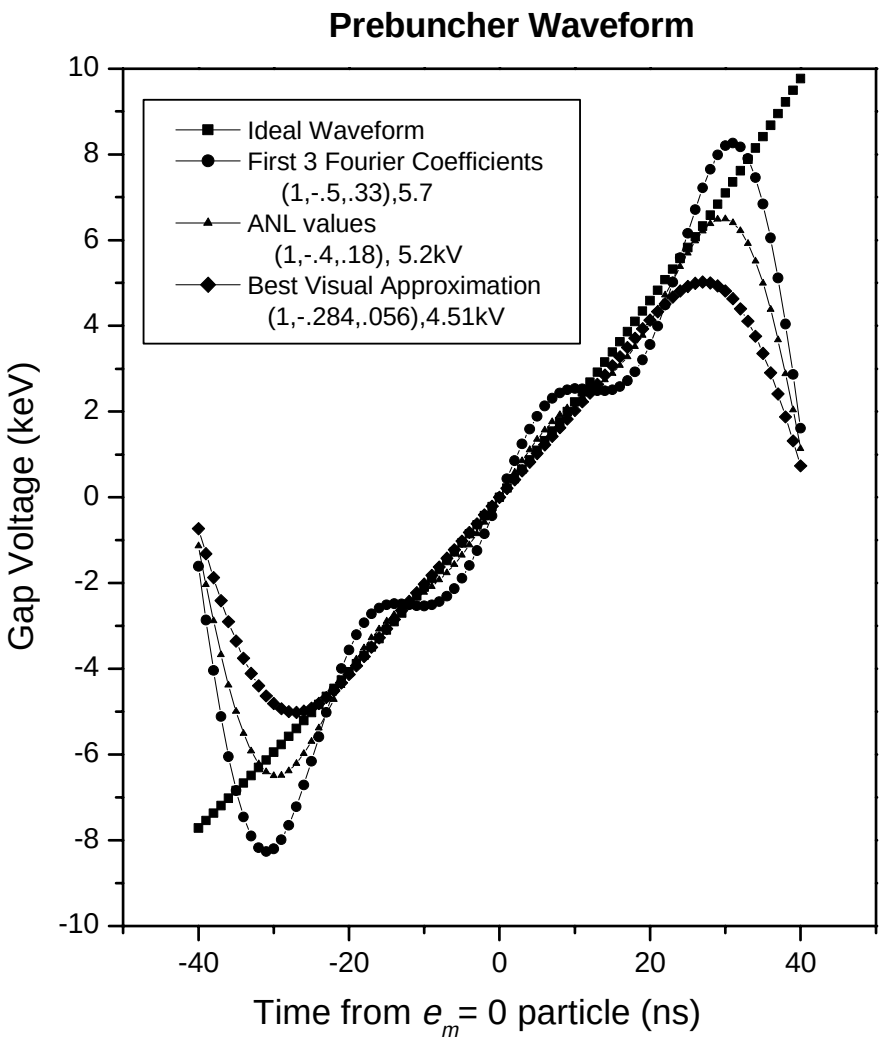

Figure A.5: A comparison between several prebuncher waveforms (see text) and the ideal sawtooth waveform.

In addition to this theoretical analysis, we have conducted measurements of the bunching resolution. A thin gold foil is mounted on a motion feed-thru that can be inserted into the beam. As the projectiles strike the foil some of the projectiles are Rutherford scattered to a surface barrier detector located at a forward angle (54.74° for the diagnostic cube before LCM1, 22° for the L2 diagnostic cube). The time signal is taken from this detector, amplified, and compared to the time reference signal from the master buncher clock. The figure of merit in the measurements is the FWHM of this TAC peak, where the detector signal is used for the start of the TAC, and the master clock provides the stop. Some observations from the measurements follow. A more complete explanation can be found in reference [A.4].

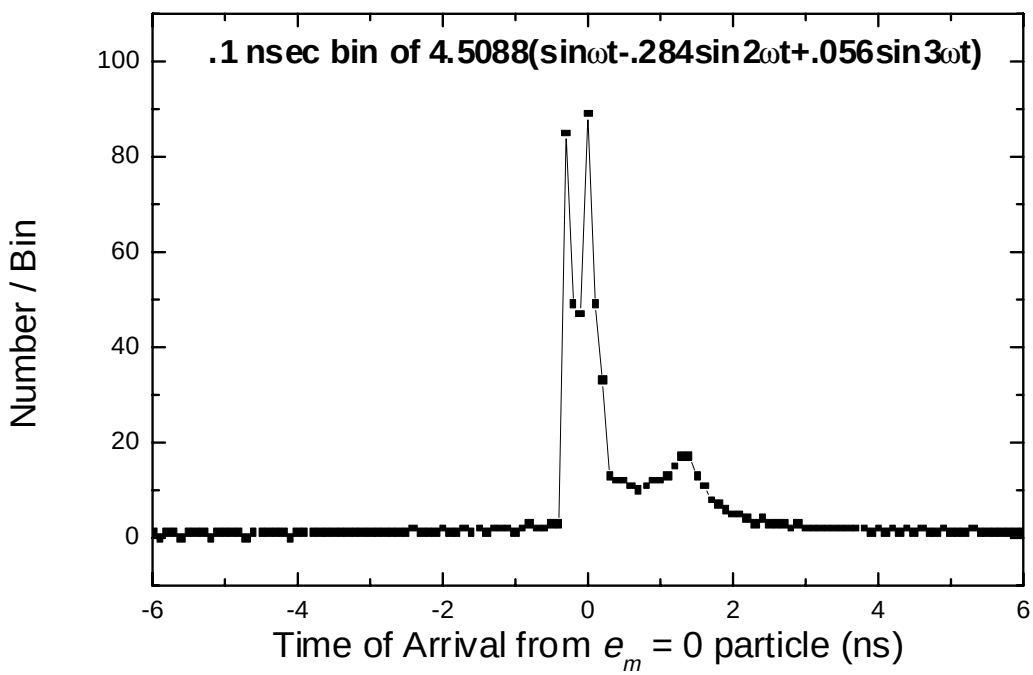

Figure A.6: The structure in the arrival times of ideal ions due to "wiggles" on the three harmonic sawtooth prebuncher wave. We are typically unable to resolve the sharp structure on the left.

The measured values for the optimal buncher amplitude are 5.12 kV_{pp} for 4 MeV protons out of the diode source and 3.12 kV_{pp} for 19 MeV F^{4+} from the sputter source. The diode source provided 55 keV injection energy and the sputter source 65 keV injection energy for these measurements. The optimum calculated values, using a waveform with minimal "wiggles", are 9.0 kV_{pp} and 2.9 V_{pp}, respectively. Obviously, the calculated value is much more accurate for the heavier ions. One possible explanation of this is the field-shaping cones (see figures A.2 and A.3) used on the prebuncher grids, which were designed to minimize the effect of the fields extending beyond the gap. They were optimized for heavier ions, since that is the primary interest both at ANL and JRM, so it is possible that 55 keV protons (β = 0.011) will be significantly influenced by these fields while 65 keV F^{4+} (β = 0.003) is not.

We were able to bunch 4 MeV protons out of the diode source to a resolution of 600 ps FWHM and very small "wiggles". The optimum buncher setting for these 4 MeV protons was A_{12} = 7.17, while for 19 MeV F^{4+} it was A_{12} = 3.84.

Asymmetry in the TAC peak (such as in the simulated peak shown in figure A.6) can be corrected by adjusting the harmonic phases to "tilt" the buncher waveform derivative displayed on the scope. Such a waveform is shown in figure A.7. A tilted derivative corresponds to additional curvature in the ramp portion of the simulated sawtooth. When the left shoulder of the derivative is higher than the right, there is more asymmetry on the left side of the TAC peak, and vice versa. When the top of the derivative is flat, any asymmetry in the TOF peak may be corrected by tilting the derivative one way or the other. This asymmetry is inherent in the TOF distribution and not due primarily to stray phase shifts in the control electronics. As the waveform

derivative is tilted, the overall amplitude must also be adjusted to obtain minimum FWHM in the TAC peak.

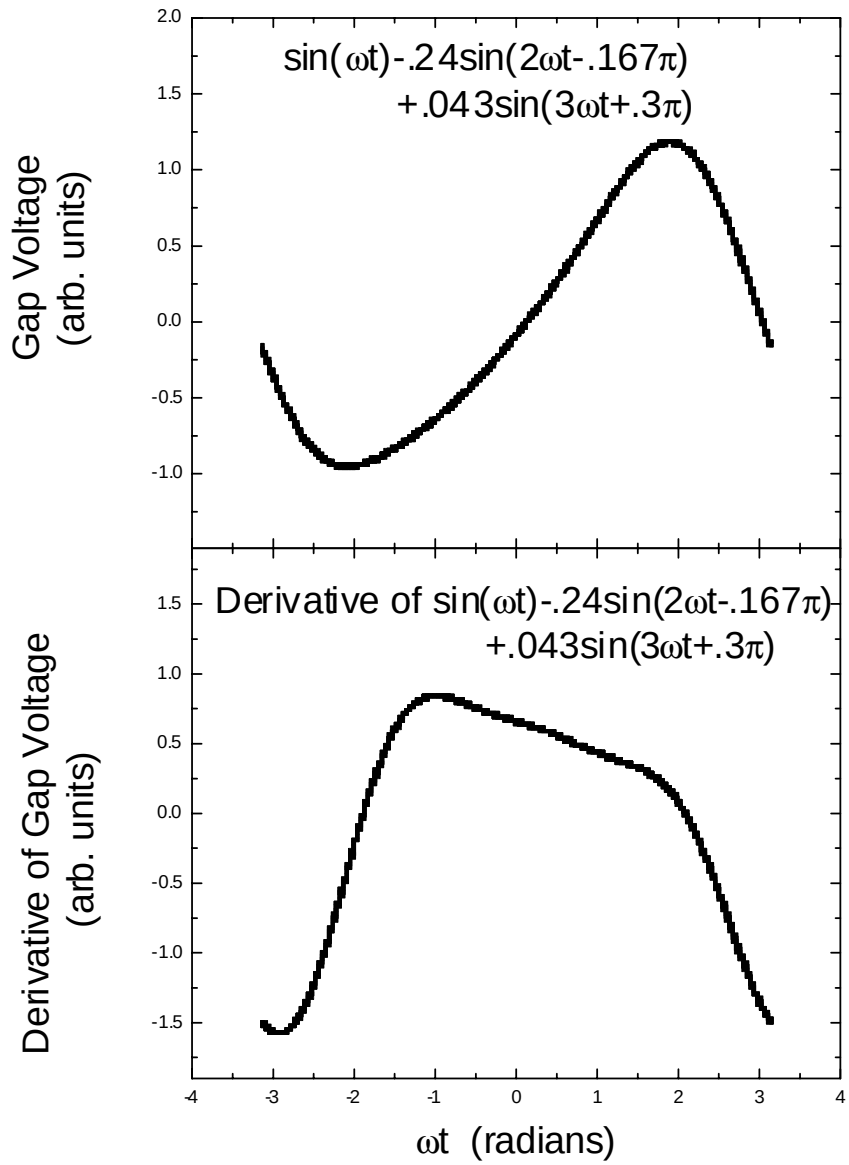

Figure A.7: Asymmetry in the measured shape of the bunched beam distribution can be corrected by varying the harmonic phases to produce an asymmetric derivative (bottom) on the scope display in the control room.

While the prebuncher is fairly well characterized as a stand-alone system, the situation becomes less clear when the deflector and prebuncher are considered together. One reason for this is that it is simply harder to make measurements of the combined

deflector/prebuncher using the Rutherford scattering setup because the event rate decreases substantially when the deflector is added (the period with the prebuncher alone is 80 ns, the period with the combined setup is much longer, from 0.67 to 169.6 μs). The diagnostic cube on L2, with its detector located at a more forward angle (22° compared to 54°) improves this situation somewhat. Even so, waiting for enough statistics to see small features on the tails of the timing peaks is a slow process.

One key step in setting up the prebuncher/deflector combination is matching the phase of the prebuncher to the phase of the deflector. When matching the phases, it is advantageous to be able to see the small "skirts" on the TOF peak. The "skirts" are the tails on the peak left over from the very wide tails of the deflector traveling wave. Since the counting rate for the L2 bunching diagnostic cube is sometimes quite small, waiting for the small "skirts" to become visible with that measurement technique is a long process. Alternatively, the TOF spectrum of the HD^+ recoil ions (or any other gas target) measured with either type of spectrometer used in this experiment can produce a quicker measurement of the relative phase. To minimize the width of the TOF peak caused by thermal motion, the spectrometer should be set to the highest extraction field possible. While the thermal motion of the recoil ions makes tuning the buncher and deflector parameters by this method difficult, we have found it to be the best way to measure the relative phase, and in fact, the recoil ion TOF spectrum should always be checked to make sure the buncher has not been set to compress the edge of the traveling wave created by the deflector plates. Using the TOF spectrum as a diagnostic tool is tricky, since the thermal motion of the recoil ions typically produces much more width than the bunching, but it does allow us to see many small features, such as the one shown in figure

A.8. There are many features of this type that appear in the TOF measurements that can be tuned away by selecting the appropriate prebuncher and deflector operating parameters, despite the fact that the reasons for these features appearing is not well understood.

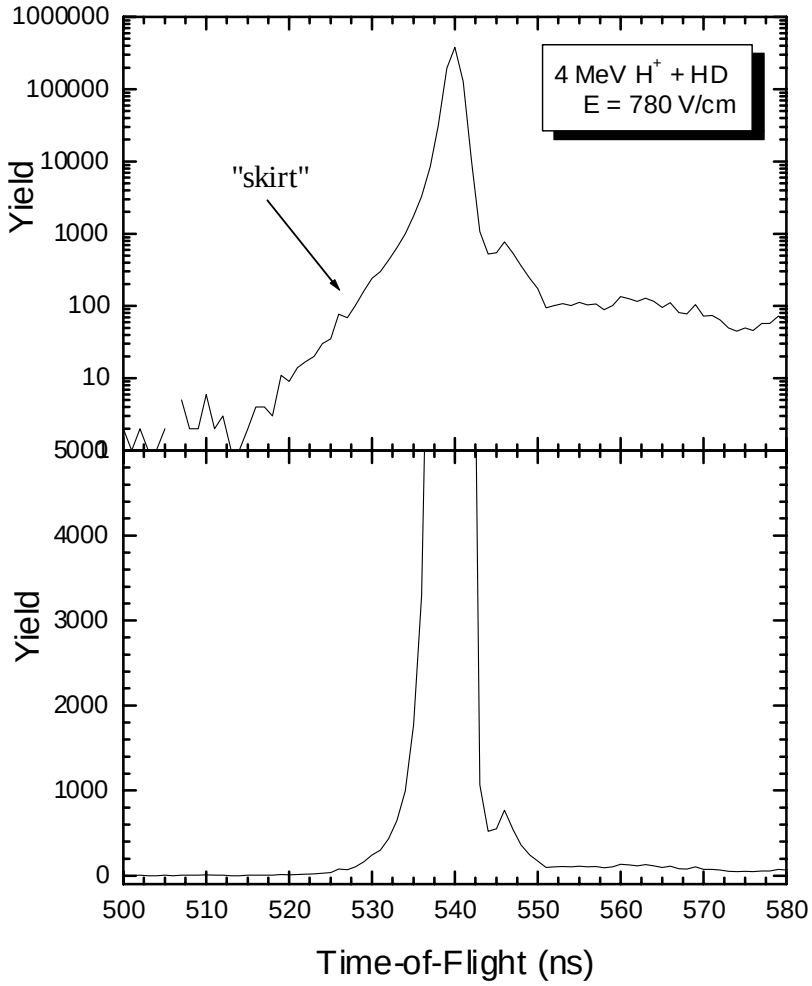

Figure A.8: A HD^+ TOF peak shown on a log scale (top) and a greatly expanded linear scale (bottom). This spectrum was measured with our TOF spectrometer. The top figure shows the "skirt" on the edge of the peak. The peak center can be changed relative to the "skirt" by adjusting the relative phase of the prebuncher and deflector (see text). The bottom figure shows a buncher phenomenon that occasionally plagues our experiments, the small peak on the right edge of the main peak. Problems of this sort can usually be eliminated by patient tuning of the prebuncher and deflector parameters, but the origins of these phenomena are not well understood.

Finally, we have found that achieving a reasonably bunched beam of protons from the diode ion source is much easier than with the sputter source. The reasons for this are unclear, and this phenomenon seems limited to protons. Heavy ions originating from the sputter ion source can be easily bunched. The primary problem in obtaining a bunched proton beam from the sputter source is an inability to separate the deflected and undeflected beams. The bunched portion of the beam often seems to be located on the "shoulder" of the DC beam, and no matter how the low energy steering parameters are adjusted, separation of the bunched and DC portions of the beam cannot be achieved. This would be less puzzling if it was impossible to separate the DC and bunched beams, but we have, on a number of occasions, separated the bunched beam from its DC neighbor. This achievement, however, is not sufficiently reproducible (so far) to be of much practical value. In the rare event that a separation can be achieved, the minimum bunch width of sputter source protons cannot usually be reduced below 2 ns, while we have been able to get 600 ps widths for diode source protons. The difference in typical platform voltages of the two sources (55 kV for the diode, 65 for the sputter) is one possible explanation for the difficulty in obtaining a good proton bunch from the sputter source. We have investigated this by varying the platform voltage on the sputter source as low as 45 kV, with no apparent difference in the minimum bunch width or ease of separation. As of this time, we have no good explanation for the difficulty in getting an adequate bunched beam from the sputter ion source, and can only guess that there is some difference between the ion optics of the two sources that is not fully understood.

In addition, the diode source (under normal operating conditions) produces a much higher proton current than the sputter source, and this is quite important in our experiment, since we not only work with bunched beam, but also with slow repetition

rates (periods of up to 84 μs), and as a result, slit control of the Tandem is often an issue. This particular problem, however, has recently been diminishing in importance as the JRM technical staff members responsible for the sputter source (Bob Krause and Tracy Tipping) have gained more experience with the titanium hydride cathodes used to produce protons in the sputter source, obtaining beams of approximately 15 μA at the low energy Faraday cup.

In conclusion, the operation of the deflector and the prebuncher are fairly well understood individually, but somewhat less so in combination. We are, however, regularly able to achieve bunch widths of about 1 ns for both protons and heavier ions, which is sufficient for this experiment. The diode source is by far the preferred source for bunching protons.

Appendix B: H_2 Contamination Analysis

Perhaps the single biggest experimental challenge in this measurement is the determination of the amount of H_2 present in the HD bottle. The H_2^+ molecular ions produced from single ionization of the H_2 contamination have the same m/q as the D^+ recoil ions of interest in this work. Since non-dissociative single ionization of the H_2 molecule has a much higher cross section than the ground state dissociation process we are interested in, contaminant H_2^+ molecular ions can have roughly the same yield as the D^+ GSD fragments. This contamination is difficult to determine because it has the same mass to charge ratio as the D^+ fragments that are produced by collisions with the HD target. Furthermore, the contaminant changes over time (see figure 5.7) so the H_2 contamination must be measured every time the experiment is done.

One may hope to determine the H_2 and D_2 contamination levels directly by measuring the double ionization of the different hydrogen isotopes which yields distinguishable ion-pairs, i.e. coincidence events of $H^+ + H^+$ or $D^+ + D^+$, respectively. We tried to measure the yield of these ion pairs in coincidence by using an extraction field weak enough to allow sufficient time difference between the forward- and backward-moving fragments such that a coincidence can be detected, and strong enough so that the fraction of ion pairs directed toward the detector is still a sufficiently large fraction of the total. Even though it is hard to determine that fraction, one can also use pure H_2 and D_2

gas targets under the same conditions, and then use the ratio of ion-pairs to molecular ions from the measurements using the different isotopes to determine the H_2 and D_2 contamination levels. This would appear to be a reasonable method to determine the contamination level, as it is free of assumptions and independent of theoretical calculations. Unfortunately, the method failed due to practical problems. Double ionization (DI) caused by fast proton impact is about 0.13% relative to single ionization [B.1]. In addition only a small fraction (5-10%) of the ion pairs produced is detected. Thus, given that we are looking at a contamination level of about 1% or less, one has a $H^+ + H^+$ or $D^+ + D^+$ event rate of roughly 1 count per 1000 seconds for about 1 kHz total recoil ion counting rate. This situation can be improved by using highly charged ions, like 1 MeV/amu F^{9+} for which DI/SI is larger than for protons (about 7%) [B.2]. This improves the $H^+ + H^+$ and $D^+ + D^+$ coincidence rate to about 1 every 20 seconds. However, the random coincidence rate of $H^+ + H^+$ and $D^+ + D^+$ ion pairs from two singly ionized HD molecules in the same beam bunch is comparable to the true coincidence rate, because the HD constitutes at least 97% of the target density and the ionization-excitation (IE) process is more likely then DI. Due to all these difficulties, we were unable to determine the contamination levels to better than ± 20-50% accuracy. This accuracy was determined by comparing the D_2 contamination level determined by the $D^+ + D^+$ coincidence method to the one evaluated directly from the singles spectrum (the ratio of D_2^+/HD^+ in the time-of-flight spectrum, figure B.1).

If one were to use an imaging detector on which ion pairs originating from the different isotopes of the hydrogen molecule could be distinguished from each other even when using a strong extraction field, then this approach might give the H_2 and D_2 contamination levels directly with sufficient precision. Any detector used in this type of

experiment would have to be capable of measuring at a very high rate. The use of such detectors might also improve the ratio of true to random coincidences because one could eliminate all random coincidences for which linear momentum of the center of mass of the ion-pair is too large.

Lacking such a detector, we have been forced to develop other methods to determine the H_2 contamination level. The two methods we have employed in this work are discussed below. The first uses only the time-of-flight measurement and our theoretical knowledge of the GSD fractions (see chapter 3) to determine the H_2 contamination. An extensive discussion of this method is available in reference [B.3]. The second method uses momentum imaging in two dimensions to separate the H_2^+ ions, which have a thermal distribution, from the typically higher energy D^+ fragments produced by GSD.

B.1 Time-of-Flight Technique

Figure B.1 shows a typical time-of-flight spectrum after background contributions have been subtracted. The shoulders on the m/q = 1 and m/q = 2 peaks from the higher energy fragments may be subtracted by using a second order polynomial to fit the baseline [B.3]. The baseline is quite small near the peak center since the fast fragments that are not shifted in time from the peak center must have a relatively large velocity component parallel to the detector and, for the weak extraction filed used, miss the detector altogether.

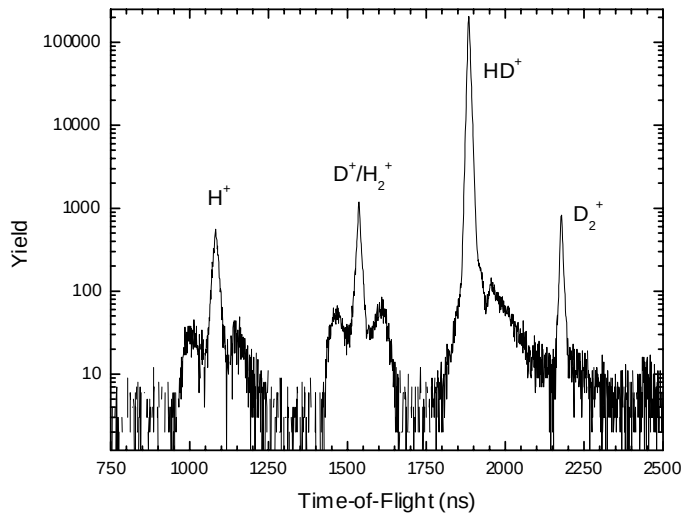

Figure B.1: A typical time-of-flight spectrum measured with a low extraction field (47 V/cm) in our Wiley-McLaren type spectrometer [B.6]. This spectrum is shown on a log scale after the contributions from the background water vapor have been subtracted. For more details about the spectrometer and experimental technique, see chapter 5.

After subtraction of the water background and the baseline of fast fragments, the remaining contributions in the spectrum are either molecular ions (with thermal energies) or low energy fragments resulting from GSD of H_2, HD, or D_2.

The peak at m/q = 4 is D_2^+, a result of the single ionization of the D_2 contamination in the HD bottle. Evaluation of the area of the D_2^+ peak relative to the HD^+ peak easily gives the D_2 contamination level

$$\frac{D_2^{\ +}}{HD^+} = \frac{A(4)}{A(3)}, \qquad \text{(B.1)}$$

where we have adopted the notation that A(*m/q*) is the measured number of events in a peak with a given *m/q*. Since the amount of GSD from D_2 and HD isotopes are different, a small correction to the measured value must be done (see references [B.3-B.5]). Using the same notation, A(1) and A(2) have the following contributions,

$$A(1) = [HD^+(1s\sigma) \rightarrow H^+] + [H_2^+(1s\sigma) \rightarrow H^+], \qquad \text{(B.2)}$$

and

$$A(2) = [HD^+(1s\sigma) \rightarrow D^+] + [D_2^+(1s\sigma) \rightarrow D^+] + [H_2^+]. \qquad \text{(B.3)}$$

Calculation of the GSD fractions for H_2, HD, and D_2 gives theoretical results for the ratio of bound-free to bound-bound transitions (see references [B.3-B.5]). These calculated values are identified using the notation

$$GSD(H_2^+) = \frac{[H_2^+(1s\sigma) \rightarrow H^+]}{[H_2^+]},$$

$$GSD(HD^+) = \frac{[HD^+(1s\sigma) \rightarrow H^+] + [HD^+(1s\sigma) \rightarrow D^+]}{[A(3)]},$$

$$GSD(D_2^+) = \frac{[D_2^+(1s\sigma) \rightarrow D^+]}{[A(4)]}. \qquad \text{(B.4)}$$

The $GSD(HD^+)$ term is the probability for dissociation only; it contains no information about the branching ratio of the H^+ or D^+ final states. Adding equations B.2 and B.3 and dividing by A(3) yields,

$$\frac{A(1)+A(2)}{A(3)} = GSD(HD^+) + GSD(D_2^+)\frac{A(4)}{A(3)} + [1 + GSD(H_2^+)]\frac{H_2^+}{A(3)}. \qquad \text{(B.5)}$$

Solving for H_2^+ results in

$$\frac{H_2^+}{A(3)} = \frac{1}{[1 + GSD(H_2^+)]}\left[\frac{A(1)+A(2)}{A(3)} - GSD(HD^+) - GSD(D_2^+)\frac{A(4)}{A(3)}\right]. \qquad \text{(B.6)}$$

In equation B.6 the A(*m/q*) are the areas evaluated experimentally from the time-of-flight spectrum while the remaining GSD terms come from the calculated Franck-Condon factors. Note that to evaluate the ratio of neutral H_2 to HD a small correction is needed since the amounts of GSD from H_2 and HD isotopes are different [B.3-B.5].

The D_2 contamination level is always determined with better precision, typically to about ±2% compared to about ±7% for H_2. Having determined the H_2^+ and D_2^+ contamination levels, equations B.2 and B.3 can be used to determine the branching ratio

for the HD^+ GSD channels as described in chapters 5.3 and 6.1. It is important to note that while the determination of the H_2 contamination level using this method depends on the calculation of the GSD fractions, the measurement of the relative magnitude of the two HD^+ dissociation channels added together does not. Furthermore, the evaluation of the H(1*s*) + D^+ dissociation channel is always the less accurate of the two dissociation channels because of the H_2^+ contamination present in that channel (see appendix G for a further discussion of the error analysis). In addition, the H_2^+ contamination was determined using A(1), so the two dissociation channels are not evaluated independently. Thus, only the measured H^+ + D(1*s*) channel can be compared with theoretical results as an independent measurement when the H_2 contamination is evaluated using this technique.

B.2: Momentum Imaging Technique

This technique uses a COLTRIMS-style apparatus (described in section 5.4) to directly measure the H_2 contamination level by means of momentum imaging. The advantage of this technique is that the H_2 contamination can be evaluated independently of any calculations, and the measurements of the H^+ + D(1*s*) and H(1*s*) + D^+ dissociation channels are not linked by the algebra leading to equation B.6. In addition, since the measurements of the two dissociation channels are not linked, the sum of the two channels can be used to test the validity of the calculations of the GSD fraction,

$$GSD(HD^+) = \frac{\left[HD^+(1s\sigma) \rightarrow H^+\right] + \left[HD^+(1s\sigma) \rightarrow D^+\right]}{\left[HD^+\right]},$$

for HD^+ in references [B.3-B.5].

As in the time-of-flight technique described in Section B.2, the identity of the ions was determined by their time of flight, and much of the same analysis of the yields of the low energy H^+ and D^+ fragments was made to remove contributions from the background water vapor. In contrast, however, information from the momentum distributions was used to determine the H_2 contamination. A prediction of the energy distribution of the *m/q* = 2 peak is shown in figure B.2. If a Maxwell-Boltzmann distribution is assumed for the cold molecular ions (30 K in this figure) then the GSD contribution and the H_2 contamination should be separable by their energy, or equivalently, their momentum. Consider the measured distributions shown in figure B.3. This data was taken using a very low extraction field (12.5 V/cm at the collision region). The sharp peak in the middle of the *m/q* = 2 distribution (b) is the molecular ions resulting from single ionization of the H_2 contamination. Those H_2 molecular ions, since they were measured at the same time as the HD^+ molecular ions, should have a similar shape as that "pure" molecular peak, since they each have the same thermal distribution. The difference in mass of the molecular ions, however, does mean that the H_2^+ distribution is slightly narrower, since

$$\frac{P_{H_2^+}}{P_{HD^+}} = \sqrt{\frac{m_{H_2^+}}{m_{HD^+}}} \,. \qquad \text{(B.7)}$$

The D^+ fragments in the *m/q* = 2 peak, on the other hand, have a wide distribution due to the kinetic energy released upon dissociation, as well as a minimum at $\boldsymbol{P} = 0$ due to the threshold behavior. The two components of this distribution, a narrow peak of molecular ions and a wide distribution of events from GSD, can be seen in figure B.3(b).

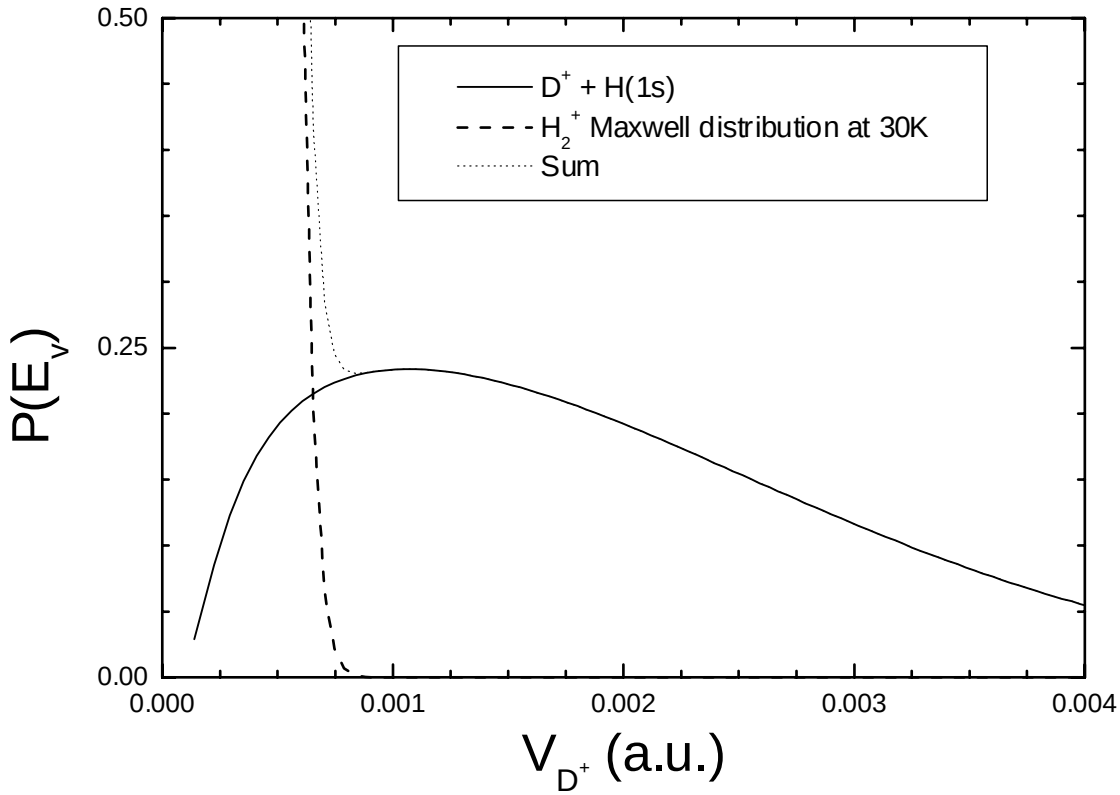

Figure B.2: A comparison between the expected distribution of H_2^+ molecular ions at 30K and D^+ fragments from GSD.

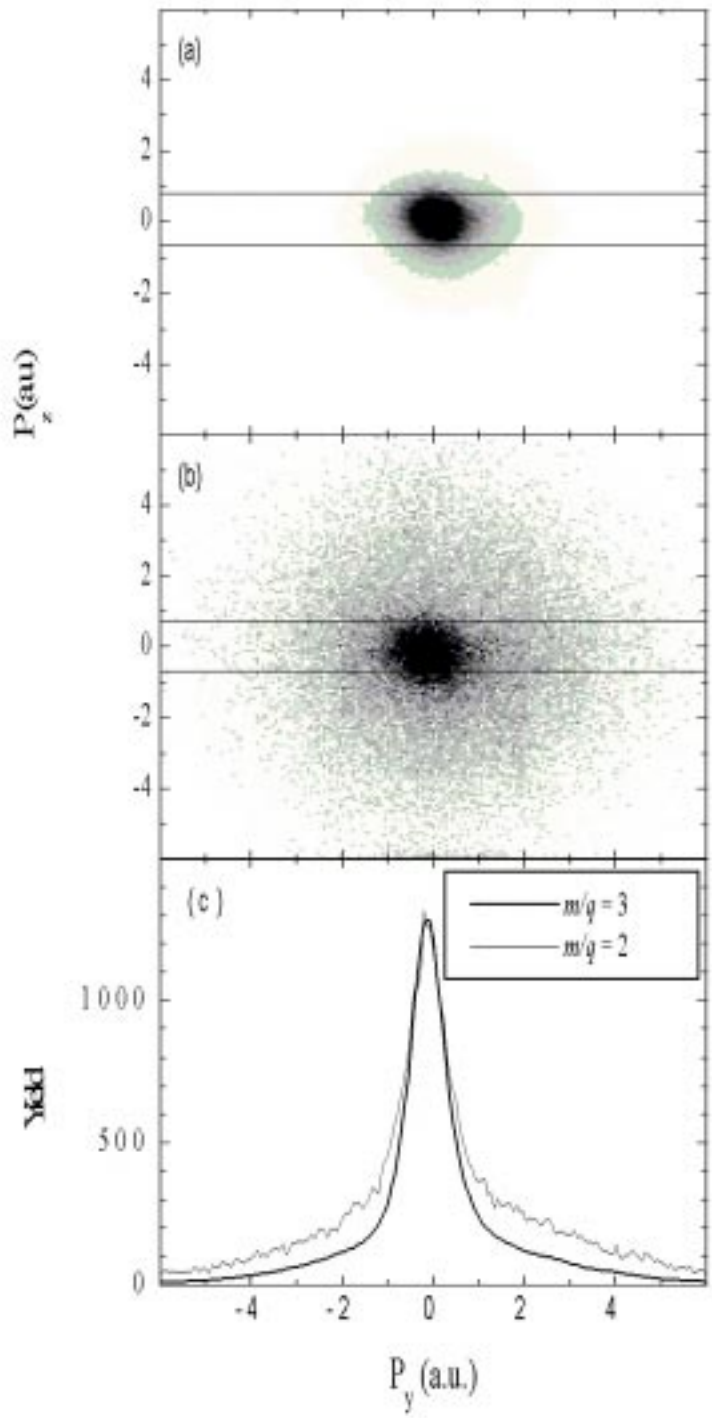

Figure B.3: (a) Momentum distribution for HD^+ ion. The distribution is scaled using equation B.7. (b) Momentum distribution for the combination of H_2^+ molecular ions and D^+ GSD fragments. In both (a) and (b) the same shades of gray represent the same percentage of the maximum. (c) Slices of (a) and (b) where the m/q = 3 slice has been scaled to have the same amplitude as the m/q = 2 slice.

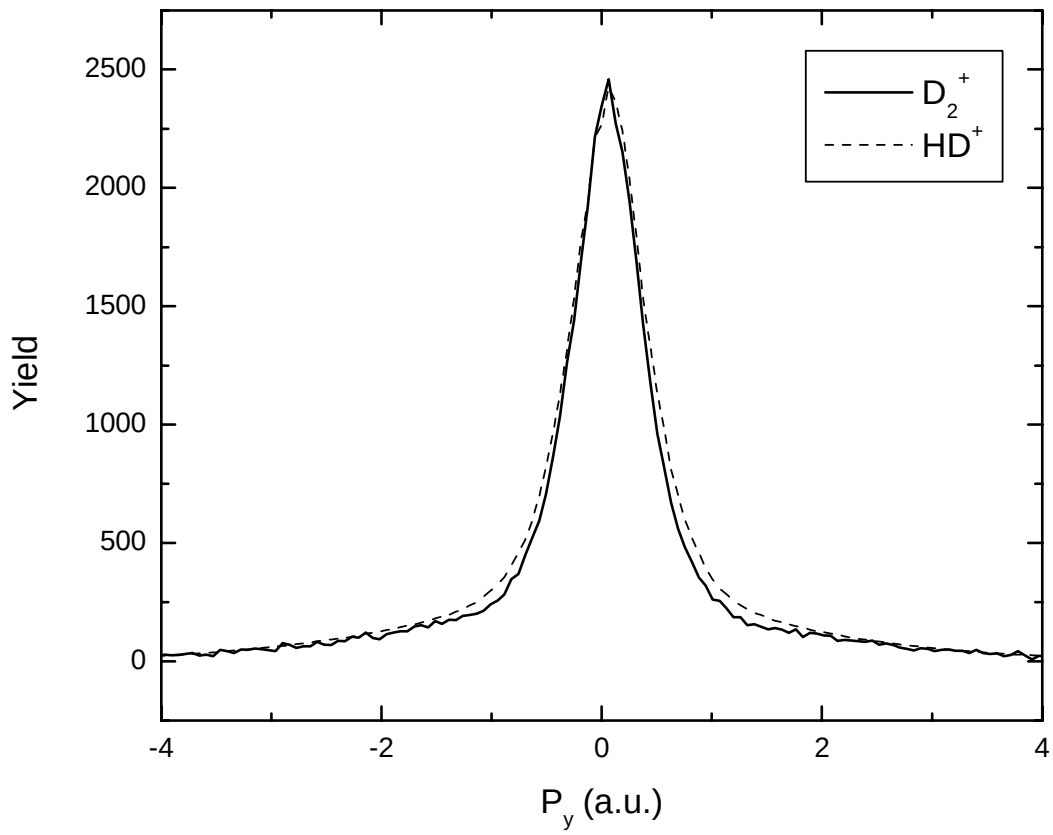

Figure B.4: A comparison of a momentum slice (see figure B.4) of D_2^+ ions scaled in momentum by $\sqrt{3/4}$ according to equation B.7 and the same momentum slice of HD^+ ions. The amplitude of the HD^+ distribution has been scaled for comparison of the peak shapes.

To evaluate the H_2^+ fraction relative to the dominant HD^+ channel, we first scale the HD^+ distribution by the factor given in equation B.7 in offline sorting on an event-by-event basis. To show that the scaling of the momentum of HD^+ peak is correct, the D_2^+ peak, which includes only molecular ions but differs from HD^+ in mass, is used for comparison (see figure B.4). Projecting a vertical slice out the momentum distributions shown in figure B.3 onto the $\boldsymbol{P_y}$ axis accomplishes two things: First, it reduces somewhat the contribution from collisions that occurred outside the jet (sometimes referred to as a

"hot gas" contribution) along the beam direction. Second, the slice is chosen so the entire H_2^+ contribution is included in the slice, but only a small percentage of the GSD events appear in the slice. An identical slice is taken out of the scaled HD^+ distribution. Since the middle of the two projections have the same shape, determining the H_2 contamination just a matter of scaling the HD^+ peak so it matches the H_2^+ peak in amplitude. The m/q = 2 distribution has D^+ fragments in the background, so only the center portion of the projection is considered. Subtracting the scaled HD^+ peak from the H_2^+ peak leaves only the contribution from the D^+ peak, which must have a minimum near $\boldsymbol{P_y} = 0$. This minimum is the indicator that determines the scaling factor for the amplitude of the HD^+ peak. Too large of amplitude gives a minimum value significantly less than zero. Too small of an amplitude does not produce a satisfactory minimum. We define the average of these two values as the best fit, and the difference between the "too large" and "too small" gives the uncertainty in the fit. This procedure is illustrated in figure B.5.

Since the width and the shape of the peak is determined experimentally, (and by the scaling for the mass of the fragment) this leaves only one free parameter for our fit, the number of H_2^+ molecular ions relative to the number of HD^+ molecular ions. Determining the H_2 contamination level by this method eliminates the need to use theoretical values for the GSD fractions that appear in equations B.2, B.3, and B.6. In order to get enough resolution to make the best fit of the H_2 contamination, the extraction field must be lowered to a value for which many of the fragments from GSD miss the detector. To evaluate the total yield of the GSD fragments, the extraction field must be raised to a value where all of the GSD fragments are collected, but, as in the first method, most of the fragments from the ionization-excitation or double ionization either miss the detector or are shifted in time from the molecular ions and GSD fragments. From the

time-of-flight spectrum taken with this higher extraction field (usually around 94 V/cm at the collision region) A(1), A(2), A(3) and A(4) are evaluated as before, and the yield of both the H^+ + D(1*s*) and H(1*s*) + D^+ channels were evaluated directly from equations B.2 and B.3. Only the H_2 contamination is determined with the lower extraction field.

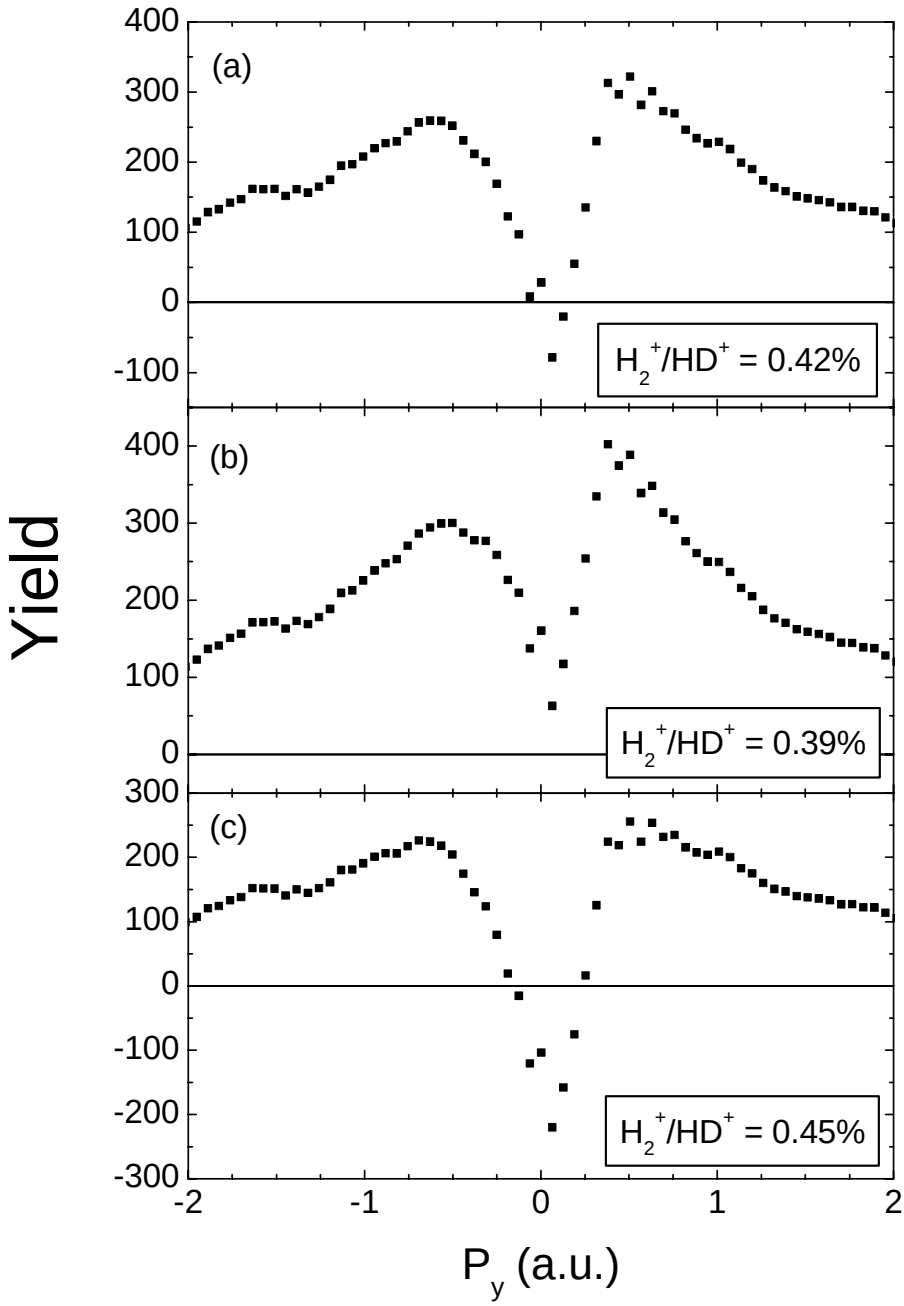

Figure B.5: The remaining part of the m/q = 2 momentum slice after the scaled HD^+ momentum slice has been subtracted. In (b), the estimate of H_2^+/HD^+ was too small, and D^+ events with $\boldsymbol{P_y} = 0$ still remain. In figure (c), on the other hand, too much has been subtracted, and the resulting minimum in the momentum slice is too wide. Figure (a) shows the average of these two values, which is our best fit for this particular data.

Appendix C: Recoil Ion Detectors

Two different detectors were employed in this project. The first detector, used for the time-of-flight measurements, had a simple metal anode that recorded the arrival time of the recoil ions. The momentum imaging part of the experiment used a two-dimensional position sensitive resistive anode to measure the position of the recoil ions upon impact. Both detectors use micro-channel plates (MCP) to generate the electrical signal recorded by the anode. A MCP is an array of 10^4 to 10^7 miniature electron multipliers oriented parallel to one another (see figure C.1). When a charged particle impacts onto the first MCP in the stack, numerous secondary electrons are generated if the charged particle lands on a channel (see figure C.1). The channels, typically 10 μm in diameter on 12 μm centers for the plates used on our detectors, are slightly angled so many collisions with the walls take place, generating the secondary electrons. The channel matrix is fabricated from lead glass in such a way as to optimize the secondary emission characteristics of each channel. In addition, the channel walls need to be semiconducting to allow charge replenishment from an external voltage source. The average gain of two consecutive plates is of the order of 10^6 or 10^7 for the normal

voltages (between 750 and 900 volts/plate) applied to the plates. The secondary electron shower from the last MCP in the stack is accelerated toward the anode if the anode is held at a more positive potential than the back of the last channel plate. Reference [C.1] contains an excellent introduction to MCPs and MCP detectors.

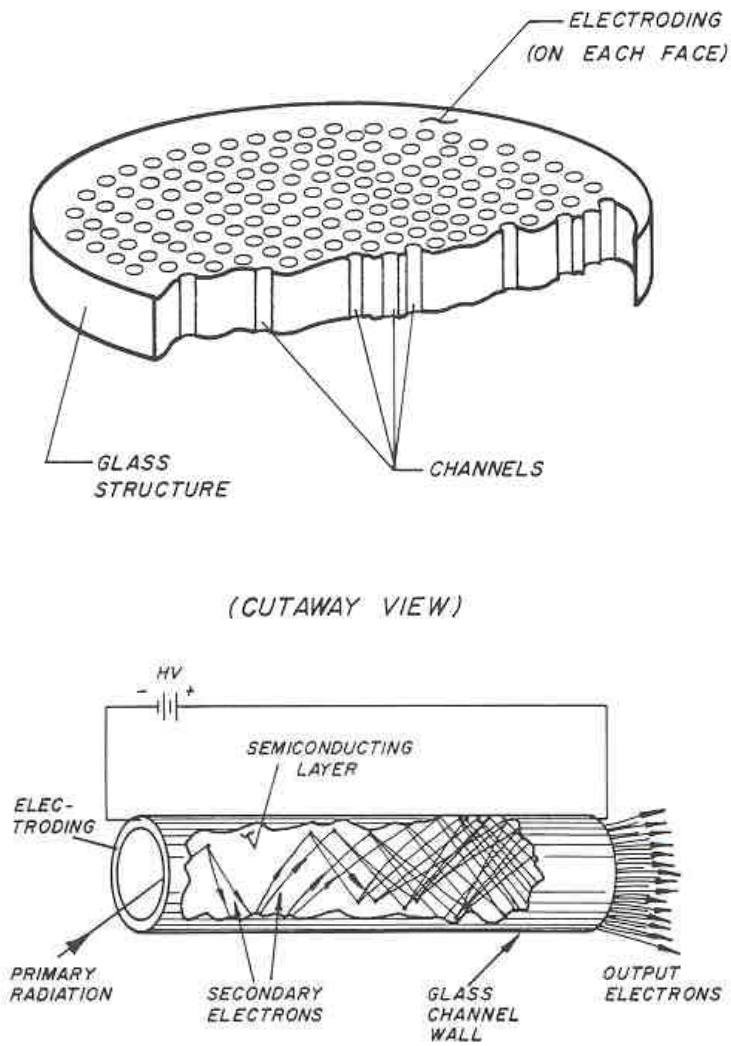

Figure C.1: Top: A cutaway view of a MCP. The channels are typically angled by about 8 degrees relative to the top of the plate. Bottom: An illustration of how a single channel acts as an electron multiplier. Both figures are from reference [C.1].

When multiple channel plates are stacked together, the channels are angled in opposite directions to suppress ion feedback. When two plates are stacked in this manner (a Chevron configuration, see reference [C.2]) the consecutive channels provide a

sufficiently large directional change (usually from +8 to –8 degrees) to inhibit positive ions produced at the output of the rear plate from reaching the input of the front plate. A Chevron configuration is shown in figure C.2. Adding a third MCP for additional amplification (which we do to ensure uniform detection efficiency of all recoil ions, see Section C.3) of the signal is called a Z-Stack configuration.

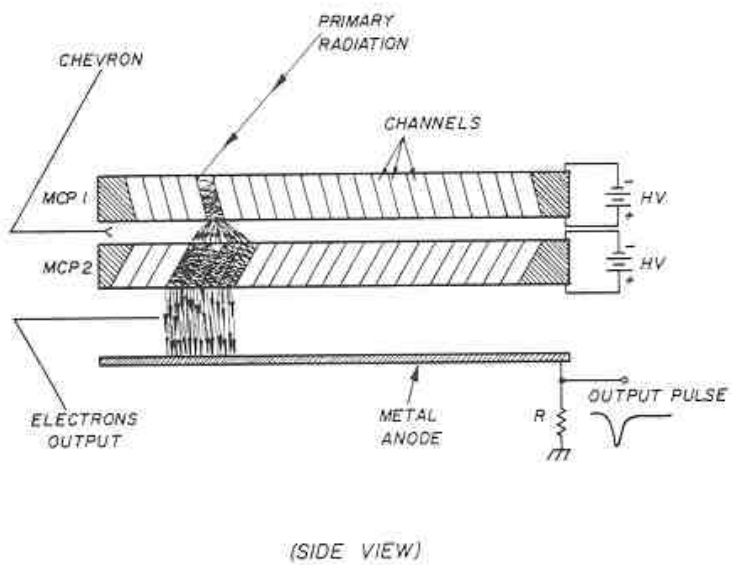

Figure C.2: A side view of a typical Chevron configuration. The purpose of alternating the channel direction is to achieve suppression of ion feedback. The figure is from [C.1].

After a channel fires, some time elapses before the charge on the channel walls can be replenished. Because of the exponential nature of the charge multiplication along the length of a channel, most of the charge is removed from the last 20% of the channel length [C.1]. If the MCP is considered as a parallel plate capacitor, 1 mm thick, made of Corning 8161 glass (ε = 8.3) the effective plate capacitance (C_c) is on the order of 8 x 10^{-17} F, which must be recharged through a channel resistance (R_c) of 3 x 10^{14} Ω [C.1]. The channel recovery time, T_c, is then

$$T_c = R_c C_c \approx 25 \text{ ms.} \tag{C.1}$$

This recovery time is for one channel only. If the particles are spread uniformly over the entire surface of the MCP, the effective dead time of the entire MCP is on the order of a few ns. Since, in practice, the particles are more localized in the center of the MCP, the effective dead time is between these two extremes. We observe these dead time effects only for a particle counting rate of 2 to 3 kHz localized to a 1 to 2 mm diameter spot on the MCP.

Using three channel plates in a stack instead of two (a Z-stack instead of a chevron configuration) amplifies the signal more, due to the additional gain of the third channel plate. The high amplification gives a better signal to noise ratio, and gives a larger gap between the signal and noise where the value of the constant fraction lower level discriminator can be set (see section C.3).

C.1 Timing Detector

The timing detector used in this experiment consists of a Z-stack MCP followed by a simple metal anode used to collect the charge of the electron shower initiated by the ion striking the first channel plate. Three MCPs are used in a Z-stack configuration to ensure uniform detection efficiency of all the very slow recoil ions of interest in our studies. The channel plates provide a very fast signal for timing (< 100 ps) [C.1]. This charge signal is then collected on the metal anode, and an RC pickoff circuit captures the charge signal, which is then processed by the coincidence-time-of-flight electronics (see Appendix D). The rise time of the signal taken off of the metal anode was on the order of 1 ns. The signal from the metal anode is larger than a signal taken from the rear of the last channel plate, and has fewer oscillations on its tail (see Appendix D), which is a key

consideration when measuring multiple hits. The timing detector used in this experiment is discussed in references [C.3] and [C.4], and since development of this detector was not a major part of this experiment, the details will not be presented here.

C.2 Resistive Anode Detector

Resistive anode technology has been used for a number of years [C.5] to image charged particles. In fact, the anode used in this experiment is believed to be the same one used by Cheng [C.6] in his thesis work almost a decade ago. The key operating principle of the resistive anode is its coating of uniform resistivity combined with its special shape, shown in figure C.3.

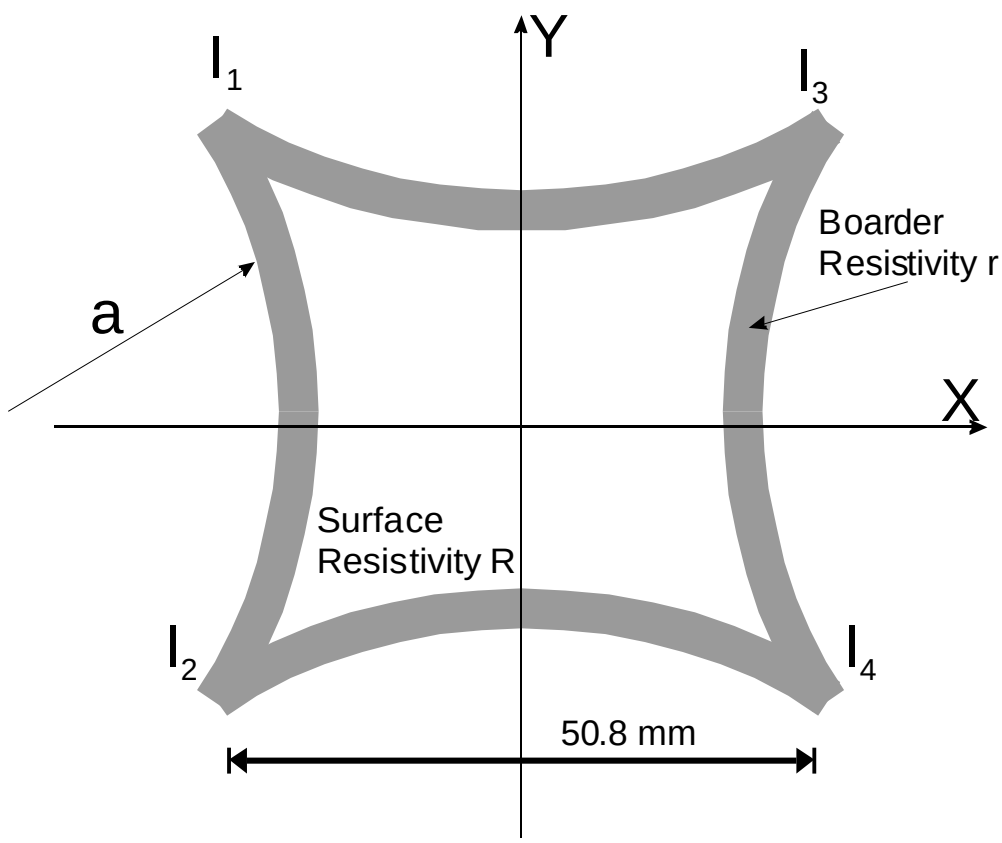

Figure C.3: The shape of a resistive anode. The radius of curvature (a) of the four sides is the same, and equal to the ratio of the surface resistivity (R) to the line resistivity of the border (r).

The border resistor is formed by four intersecting rings of radius a. When combined with the specifically chosen resistivity on the edge of the anode, a distortion-free two-dimensional image can be produced. This is achieved by a careful selection of the ratio of the plane resistivity, *R*, of the anode surface and the line resistivity, *r* ($r = \frac{\Omega}{m}$), of the anode edge. Consider figure C.4:

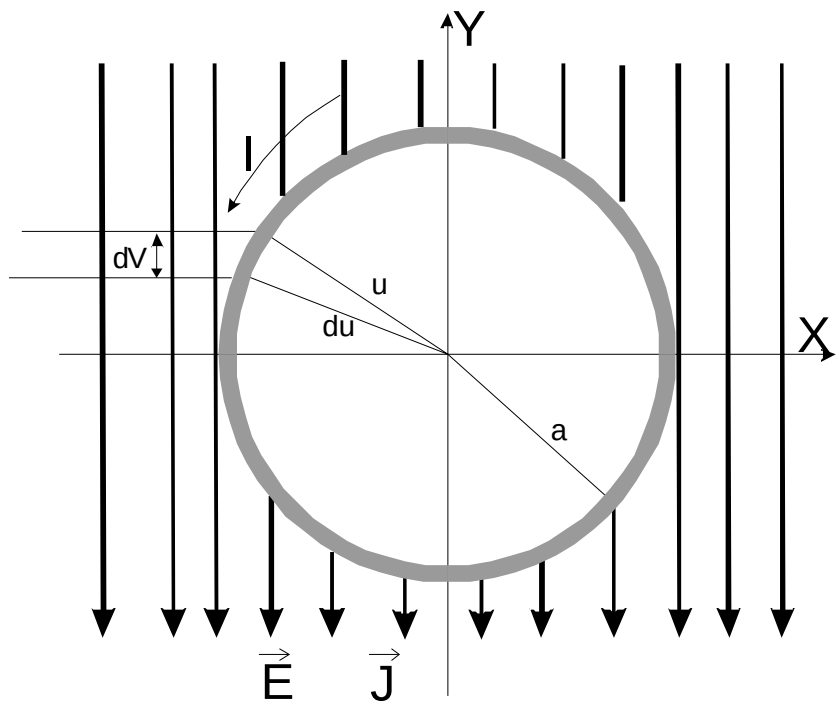

Figure C.4: An illustration of a ring (radius a, with a different resistivity than the surroundings) embedded in the field lines of an infinite medium. *I* is the current, $\vec{E}$ the electric field, and $\vec{J}$ the current density.

By calculating the potential difference *dV* in the above figure, it can be demonstrated that the correct ratio of $\frac{R}{r}$ is equal to *a*, the radius of the plane. In the region outside the ring (shown in figure C.4),

$$dV = Edy = Ea\sin(u)du \ . \qquad \text{(C.2)}$$

On the ring itself,

$$dV = IdR = Iradu\,, \tag{C.3}$$

where I is related to the electric field (E) by:

$$I = \vec{J} \bullet \vec{x}t = Jat\sin(u)\,, \tag{C.4}$$

where t is the thickness of the ring, and

$$\vec{J} = \frac{\vec{E}}{\rho v}\,, \tag{C.5}$$

where ρv is the volume resistivity outside of the ring (Ω·m). On the ring then,

$$dV = \frac{\vec{E}}{\rho v} at\sin(u) radu\,. \tag{C.6}$$

Combining equations C.2 and C.6 yields

$$r = \frac{\rho v/t}{a} \tag{C.7}$$

and by defining R = $\rho v/t$ as the surface resistivity,

$$a = \frac{R}{r}\,. \tag{C.8}$$

When equation C.8 is true, then the potential difference in the region outside the ring is equivalent to what the potential difference would be if it were an infinite medium. Since we have shown that placing one ring in the electric field is not going to disturb the field lines, imbedding more than one will not have any effect either, provided the geometry prescribed by equation C.8 is maintained. Four rings, placed in a manner so that the center-to-center distances of adjacent rings are equal and less than the diameter of the

ring form the shape of the anode. Inside the boundary of the anode, the field lines behave as if they were in an infinite medium.

The electron shower generated when the recoil ion impacts the channel plates is collected on the anode, and acts as a current source. The bias applied to the four corners of the anode acts as a voltage source. This generates a current on each corner of the anode, and the two-dimensional position of the electron shower can be determined from these four currents (I_1, I_2, I_3, and I_4) in the following manner:

$$x = \frac{I_1 + I_2}{\sum_{n=1}^{4} I_n}, \tag{C.9}$$

and

$$y = \frac{I_1 + I_3}{\sum_{n=1}^{4} I_n}. \tag{C.10}$$

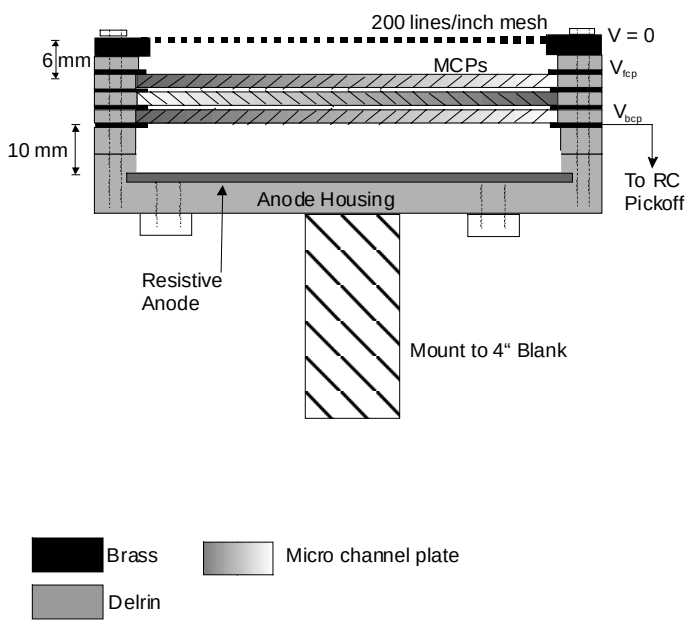

Figure C.5: An assembly drawing of the resistive anode position sensitive detector used in these experiments.

The assembly of the resistive anode two-dimensional position sensitive detector used in our experiments is shown in figure C.5. A 200 lines/inch electroform mesh is stretched across the face of the detector, as shown in figure C.5. This mesh is held at V = 0 to define one end of the field free drift region between the end of the spectrometer and the detector. Some assemblies add a second grid between the first grid and the front MCP, which is kept at a slightly more negative voltage than the front MCP. The field defined by this mesh repels electrons created if the particle impacts on the surface of the MCP rather than a channel. The repelled electrons have a good chance of landing in a channel and producing a signal. This technique increases the efficiency of the detector. It works best, however, for higher energy particles then we collect, so we decided against this approach.

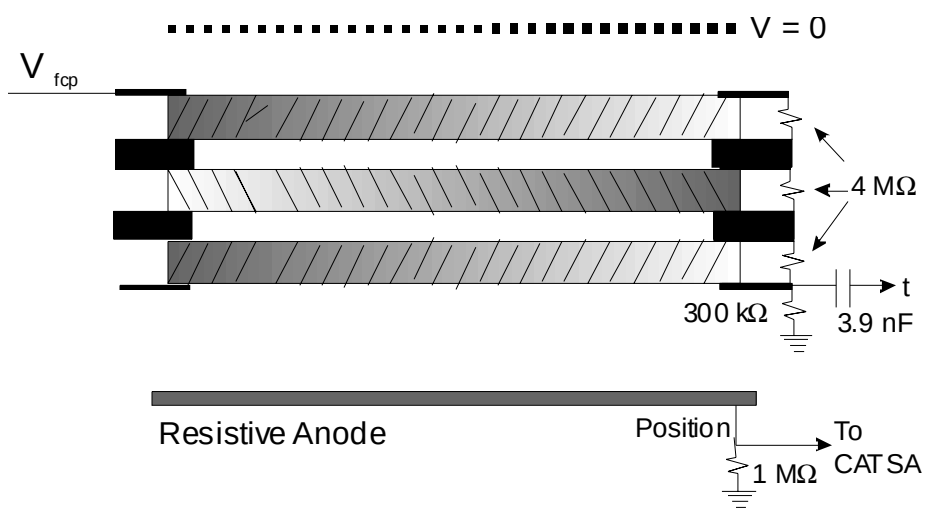

Figure C.6: A drawing of the electrical connections of the resistive anode position sensitive detector. Each of the four corners of the anode produce a position signal, only one connection is shown here. Building the voltage divider circuit allows the detector to be operated with only one power supply.

The electrical connections for the detector are shown in figure C.6. A simple voltage divider circuit is constructed to distribute the voltages to the three channel plates. The resistors are chosen so that the voltage is split evenly over the three plates, and there

is enough voltage between the back MCP and the anode to accelerate the electron shower into the anode before it can spread too much, and thereby reduce the resolution of the position information. By making the last resistor to ground variable, the voltage between the back MCP and the anode can be varied. Using this approach, we determined that a field of 50 V/cm between the back MCP and the anode was sufficient. The typical front MCP voltage is -2400 volts, which for our circuit gives 780 volts/plate, and 60 volts between the back MCP and the anode. The detector could easily be run with higher volts/plate, if not for the fact that the resulting signals become too large and saturate the CATSA pre-amplifiers (see Appendix D).

The detector assembly consists of a series of metal rings and insulating spacers (see figure C.5). The voltage divider circuit is attached to the metal rings, which cover the edge of the MCP. The entire stack of rings slides over 6-32" Teflon all-thread rods, and the stack is held together with pressure applied by nuts threaded on the rods. This method of assembling the detector, while simple and quite robust, does have two main drawbacks. First, the rings completely surround the MCP, meaning the detector interior cannot be pumped except through the channels themselves, and this process is slow. Applying voltage to the plates in poor vacuum conditions can cause a discharge, which would ruin the plates. Second, Teflon and Delrin materials are used in the assembly, and therefore the detector is not UHV compatible.

The linearity and resolution of the anode is determined by placing a mask with regular holes over the detector. Using ions produced from an ion gauge or a helium gun, the entire detector plane is illuminated with ions, and an image of the mask is obtained. One mask image is shown in figure C.7. Since the spacing of the mask pattern is known,

a conversion from channels to real distance is obtained. Besides the round holes, our mask has four slots in a pattern that gives an unambiguous method of comparing detector coordinates with the lab coordinates, and hence avoiding any discussions of whether "up" is really "up". The slots in the mask are also used to determine the detector resolution. By taking a slice across a slot in the mask (see figure C.8), and examining the number of channels it takes the detector to respond to the sharp edge of the slot, a value for the resolution can be found. The procedure for doing this is to take the derivative of the yield as a function of position. The derivative will have a peak on each side of a slot (see figure C.8). We fit a guassian to the derivative peaks, and take the width of that guassian as the detector resolution. This procedure is repeated several times for different slots on the mask and an average value is determined. The resolution of the detector used in this experiment was measured several times to be approximately 0.18 mm. Unfortunately, for the C^{3+} + HD data reported in this thesis, the measured resolution was 0.21 ± 0.03 mm. The degradation of the resolution is believed to be the result of a slight problem with the signal processing of the I_3 channel. The linearity of the detector is excellent, as long as the point in question is slightly (≈ 2 mm) away from the edge of the anode.

While the resistive anode has excellent spatial resolution (about a factor of two better than most of the backgammon type anodes used in JRM), the high resistivity of the anode makes for a very slow signal (RC ≈ 100 ns [C.6]) and is therefore a poor choice for obtaining a timing signal. To avoid this problem, the timing signal is taken from the rear of the last MCP. The rise time of this signal is very fast (< 1 ns), making it a good choice for a timing signal, although it typically has more oscillations on its tail ("ringing") than a corresponding signal from a metal anode. Signal processing is discussed further in Appendix D.

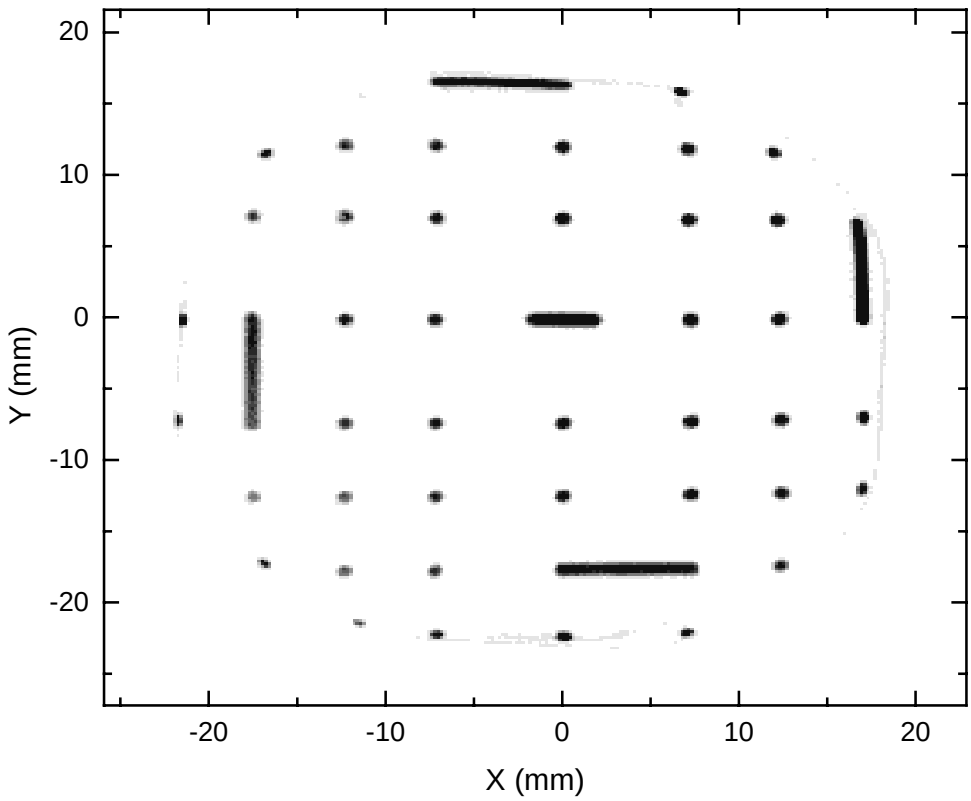

Figure C.7: An image of the mask used to determine the detector resolution and linearity. On the plot, x = 0 and y = 0 are defined by the center of the mask, rather than the center of the anode. The mask has been placed slightly off center, which causes the top and right slots to be closer to the edge than the bottom and left slots. The spacing between the center three rows of the mask is greater than the spacing between the other rows.

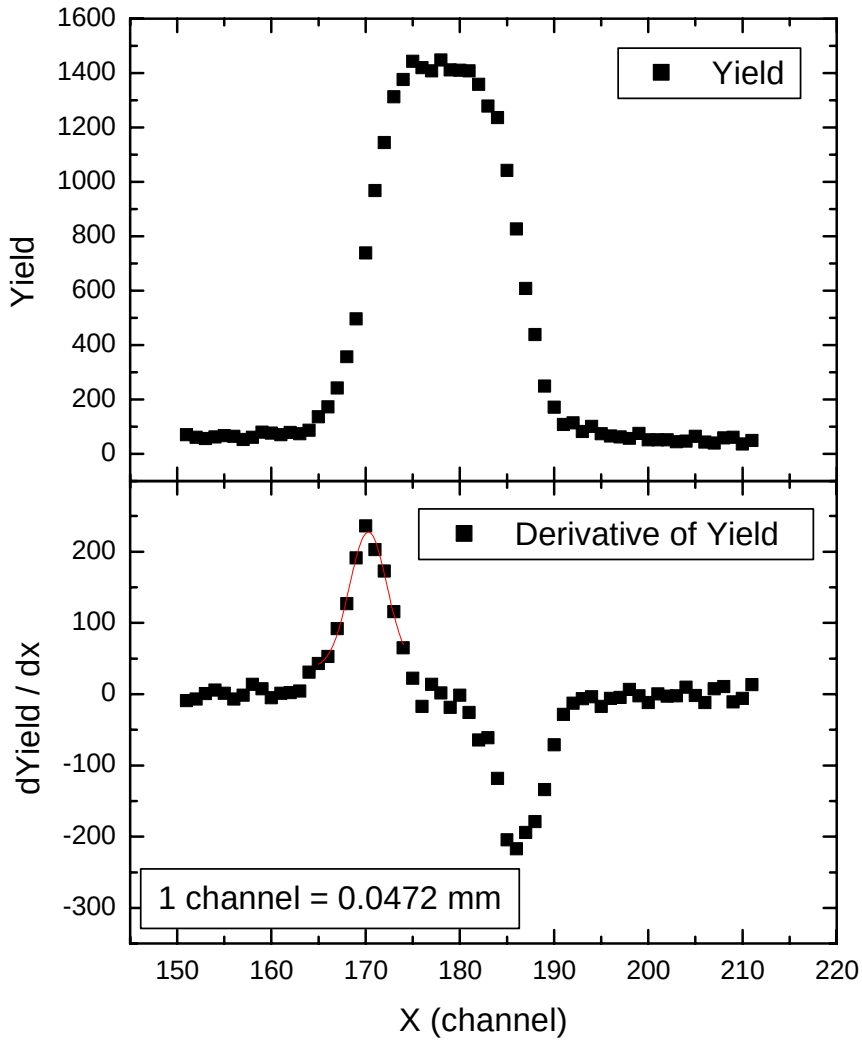

Figure C.8: The top figure shows a 25 channel wide slice of the left hand vertical slot in figure C.7 projected down onto the x-axis. The bottom figure is the derivative of that slice. By fitting the resulting two peaks with a guassian, the detector resolution is determined.

C.3 Ensuring Uniform Detection Efficiency

Since this experiment measures a branching ratio, we must be sure that the detection efficiency of each branch is the same. To ensure uniform detection of all recoil ions, even when using the very low extraction fields in this experiment, we used three micro-channel plates to generate the electrical signal measured by the resistive anode. The highly amplifying Z-stack design allows for clean separation of the recoil ion signals from the electronic noise, allowing a window between the signal and noise where the lower level discriminator (LLD) of the constant fraction discriminator can be set. To confirm this was the case, we carry out several tests while setting up the experiment.

The most sensitive test for detection efficiency is to ensure that ions with different charges are detected with the same efficiency. Since the hydrogen molecule does not produce any multiply charged recoil ions in these collisions, we are forced to use another target gas for these measurements. We use both helium and neon for this purpose, measuring the ratio of double to single ionization (and, in the neon case, the ratio of triple to single ionization) as a function of LLD setting and the voltage applied to the front MCP. The higher the charge on the ion, the easier it is to detect, since the initial hit on the MCP produces more secondary electrons [C.1]. If the LLD is set too high, it could discriminate against singly charged ions. When the LLD setting starts to cut into the signals from the singly charged ions, the ratio of double to single ionization (or triple to single ionization) will increase. If the LLD is not cutting into the signals from singly charged ions, the ratio of multiple to single ionization will remain constant. The same principle holds for the setting of the detector voltage. The amplification must be high enough that the singly charged ions are not detected less efficiently than the multiply charged ions. For proton impact, our ratios for helium are compared with the results of

Knudsen *et al.* [C.7], and the ratios for neon are compared to the results of Gray *et al.* [C.8] for highly charged fluorine. Since our experiment is only concerned with measuring singly charged recoil ions, these checks set far more stringent conditions on the efficiency than does the actual experiment, so our data should be free of any error in this regard.

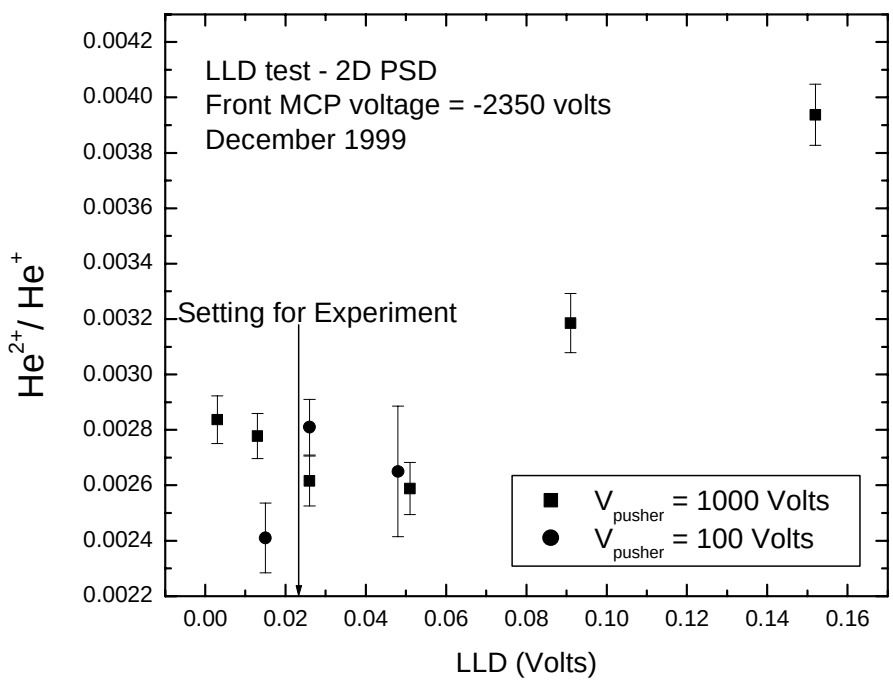

Figure C.9: A measurement of the ratio of double to single ionization of helium by 20 MeV C^{3+} ions as a function of the LLD setting.

Besides the checks we do with multiply charged recoil ions, we can check for effects on the efficiency due to the velocity of the recoil ions. This is easily done by comparing the ratio of ionization of a heavy (slower) ion to a light (faster) ion. The heaviest ion we are concerned with measuring is H_2O^+ (for background subtraction) and the lightest is H^+. Since they are both present due to residual water vapor in the target

region, we can measure the ratio $\frac{H^+}{H_2O^+}$ as a function of LLD and detector voltage using the residual gas in the collision area as a target.

Figures 5.5, C.9 – C.11 give some examples of these efficiency checks. We decrease the voltage (or increase the LLD) until we see some change in the measured ratio, and then select experimental parameters that are well within the limits set by the efficiency checks.

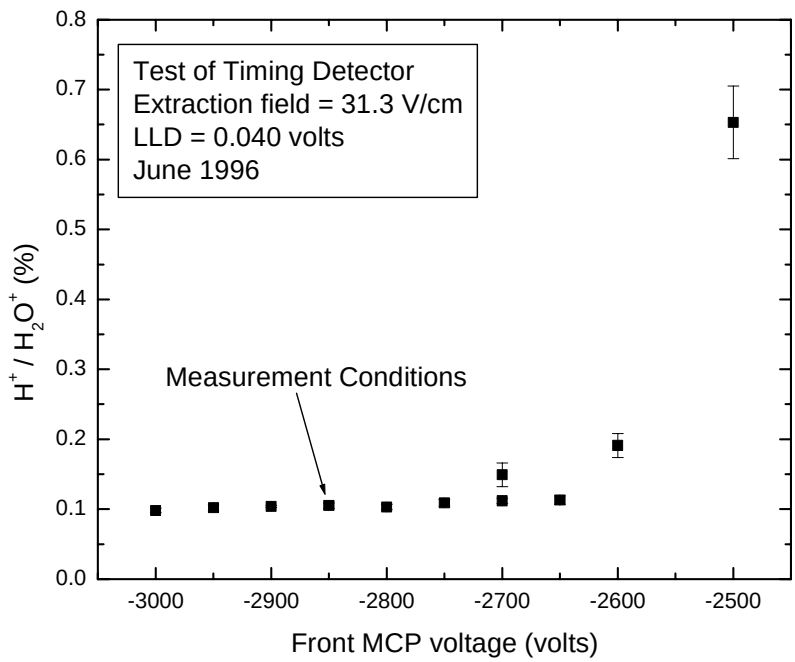

Figure C.10: A measurement of the $\frac{H^+}{H_2O^+}$ ratio as a function of the voltage on the detector. This measurement is for the TOF spectrometer and timing detector and was done in June 1996.

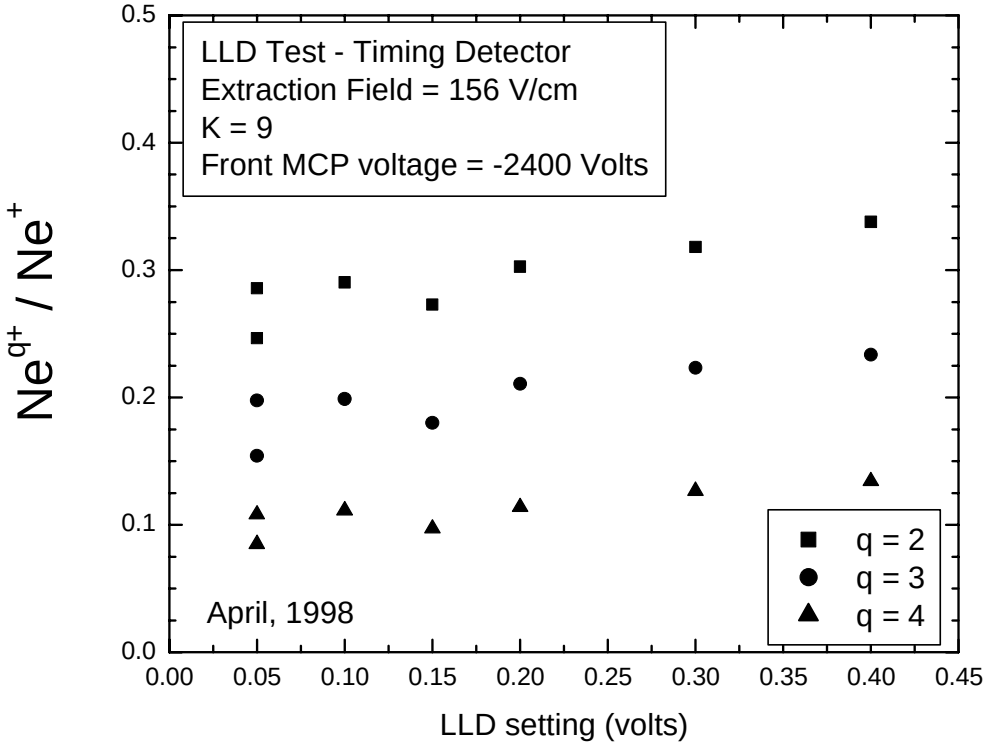

Figure C.11: A measurement of the double to single, triple to single, and quadruple to single ionization ratios of neon by 19 MeV F^{4+} impact as a function of the LLD setting. This measurement is done with a TOF spectrometer and the resistive anode detector.

Appendix D:
Electronics and Signal Processing

This section gives an explanation of the processing required to convert the signals collected by the detector into signals that are usable by the CAMAC electronics attached to the data acquisition computers. In the first stages of this measurement, only the time-of-flight of the recoil ions was measured. In the second part of the experiment, information about the position of the recoil ions was recorded in addition to the time-of-flight, which was measured in much the same way as when only the time-of-flight was measured.

D.1 Time-of-Flight

The time-of-flight of each recoil ion was measured with multi-hit electronics with respect to a time signal synchronized to the beam bunch (see Appendix A). While the multi-hit information was not strictly needed for this experiment, it did give information about the number of double ionization events recorded. Furthermore, the coincidence time-of-flight (CTOF) setup was the basic operating mode of our experimental group,

since aside from this experiment, almost all of our work deals with the measurements of all the charged fragments resulting from a molecular breakup. As a result, all of these measurements were made with a multi-hit timing configuration.

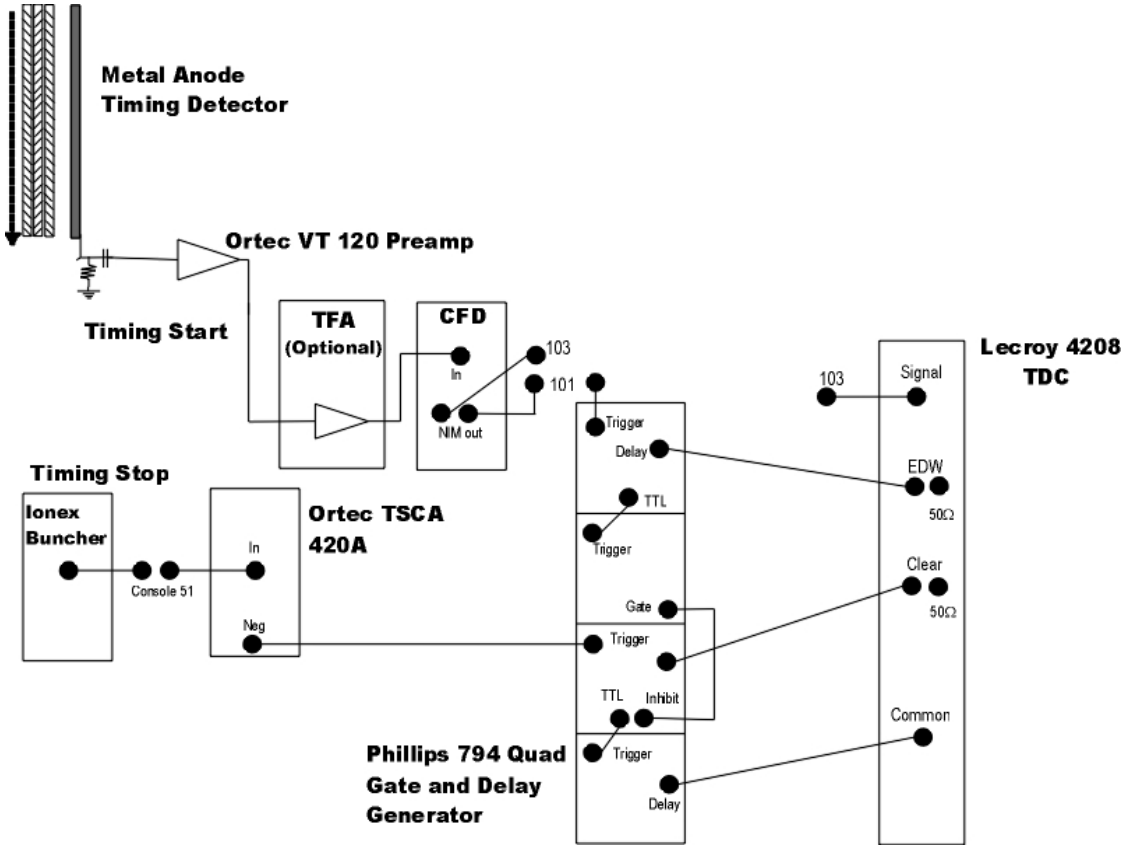

Figure D.1: A block diagram of the primary time-of-flight electronics used in this experiment.

A block diagram of the electronics used for the processing of the time-of-flight signals is shown in figure D.1. The metal anode of the timing detector provides a fast negative signal when a recoil ion impacts the micro-channel plates (MCP) of the detector. These signals are picked off the anode using a RC circuit and are then amplified by an EG&G/Ortec VT 120 pre-amplifier. The values used in the RC pickoff box (3.6 kΩ and 3.9 nF) are chosen empirically to produce the smallest oscillations on the tail of the timing signal, (or "ringing") which is important for CTOF measurements. These

oscillations can be damped by a number of other factors, including changing cable lengths between the power supply and the detector, using shielded wire to transmit the signal from the anode to the BNC vacuum feed-thru, isolating the detector from the electrical noise generated by the turbo-molecular pumps, and eliminating ground loops between the "clean" power used for the electronics and the "dirty" power used to run beamline equipment. In addition, a timing-filter amplifier (Ortec 474 or similar) is sometimes employed after the pre-amplifier to differentiate the signal (a time constant of 10 or 20 ns is usually the best setting) and reduce the ringing. Integration of the time signal should be avoided, since it usually increases the rise time dramatically. Minimization of the ringing is of great concern in a CTOF measurement, but since it is not a primary concern in this experiment, the details of this black art will not be presented here.

After the pre-amplifier, the signal is usually large enough (due to the high amplification of the three channel plates used in the Z-stack configuration) to proceed directly to a constant fraction discriminator (CFD). A typical signal size from the Z-stack timing detector, measured after the VT-120, is between 0.5 and 1 V. If further amplification is needed before the CFD, a single (10x) stage of a fast amplifier (Phillips Scientific 774 or equivalent) is usually used. The CFD converts the signal to a fast timing NIM signal.

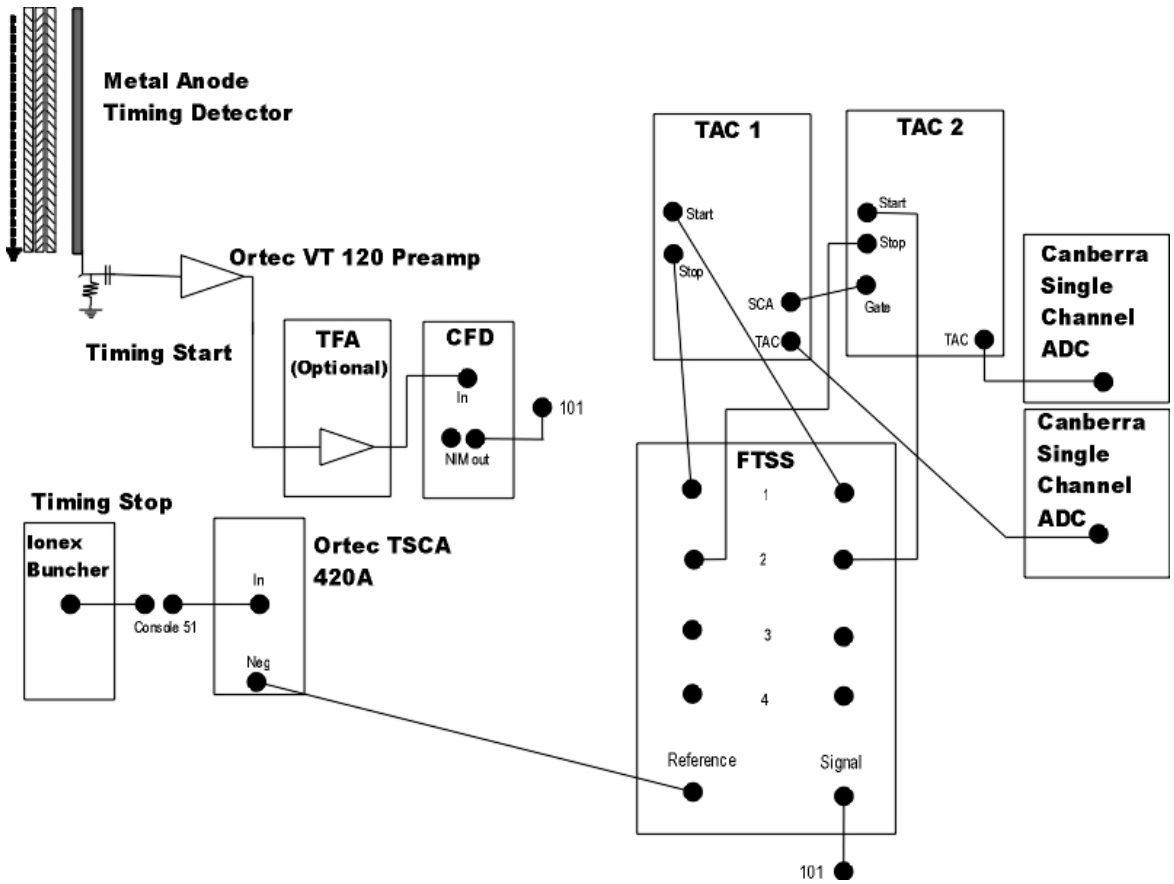

Figure D.2: A block diagram of the electronics used for a coincidence time-of-flight measurement if the FTSS and two TACs are used instead of the TDC shown in figure D.1. More than two recoil ions may be measured by adding additional TACs.

The positive square pulse from the Ionex deflector system master clock is converted to a NIM signal using an Ortec 420A Timing Single Channel Analyzer (TSCA). At this point there are multiple options for converting the time difference between the detector signal and the signal from the Ionex clock to time-of-flight information in the computer. One method is to use a multi-hit time-to-digital converter (TDC). The LeCroy 4208 TDC we used has a fixed resolution of 1 channel = 1 ns over a wide range of times (up to 8 ms). If the spectrometer field is high enough, and therefore the time-of-flights short enough, a time-to-amplitude converter (TAC) may have higher resolution than the TDC. In this case a fast timing signal sorter (FTSS) [D.1] was used to

provide start and stop signals for two (or more) TACs, which record the time-of-flight of each ion with respect to a common stop. In most cases in this experiment, however, the ion time-of-flight was long enough that the 11-bit resolution (2048 channels) of the Canberra 8075 single channel ADC was inferior to the 1 ns resolution of the TDC. A block diagram of the electronics setup using the FTSS and two TACs is shown in figure D.2.

To use the TDC, one of the NIM signals from the CFD is sent to the signal input of the TDC. The other NIM signal from the CFD triggers the first unit of a Phillips Scientific 794 quad gate and delay generator. The delayed signal from this unit is used as the end-of-window signal for the TDC, which stops all time counters of the TDC and produces a CAMAC look-at-me (LAM) signal from the TDC. There are two inputs for end-of-window signals on the TDC, and the unused one needs to have 50Ω termination. Meanwhile, the TTL signal from the first unit of the quad gate and delay generator is used to trigger the second gate and delay unit. This unit is used to produce a gate signal which is fed into the inhibit input of the third unit of the gate and delay generator. This unit receives its trigger from the NIM signal originating from the deflector. The delayed signal from this unit (which is inhibited by the gate signal triggered by a recoil signal) is used to clear the TDC after all the events are recorded. This clear signal resets the counters to zero. Since the TDC takes 8 μs to read the signal, a premature clear (if there was no inhibit) could erase the signal information. The clear signal needs to have a width of greater than 50 ns to be properly recognized by the TDC. The unused second clear input on the TDC, like the second end-of-window input, needs 50Ω termination. Finally, the TTL signal on the third gate and delay unit is used to trigger the fourth gate and delay unit. This delayed signal from this unit provides the common start signal to the TDC.

The common start signal must be preceded by the clear signal by 200 ns. The time difference between each recoil ion and the start signal was recorded event-by-event to maintain the correlation between all times-of-flight associated with the same beam bunch. The relative time ordering of the four signals to the TDC (clear, common, signal, end-of-window) is shown in figure D.3. There are other combinations of electronic units that could be used to provide the four required signals to the TDC, (see. for example, reference [D.2]) but we found this one to be the most compact.

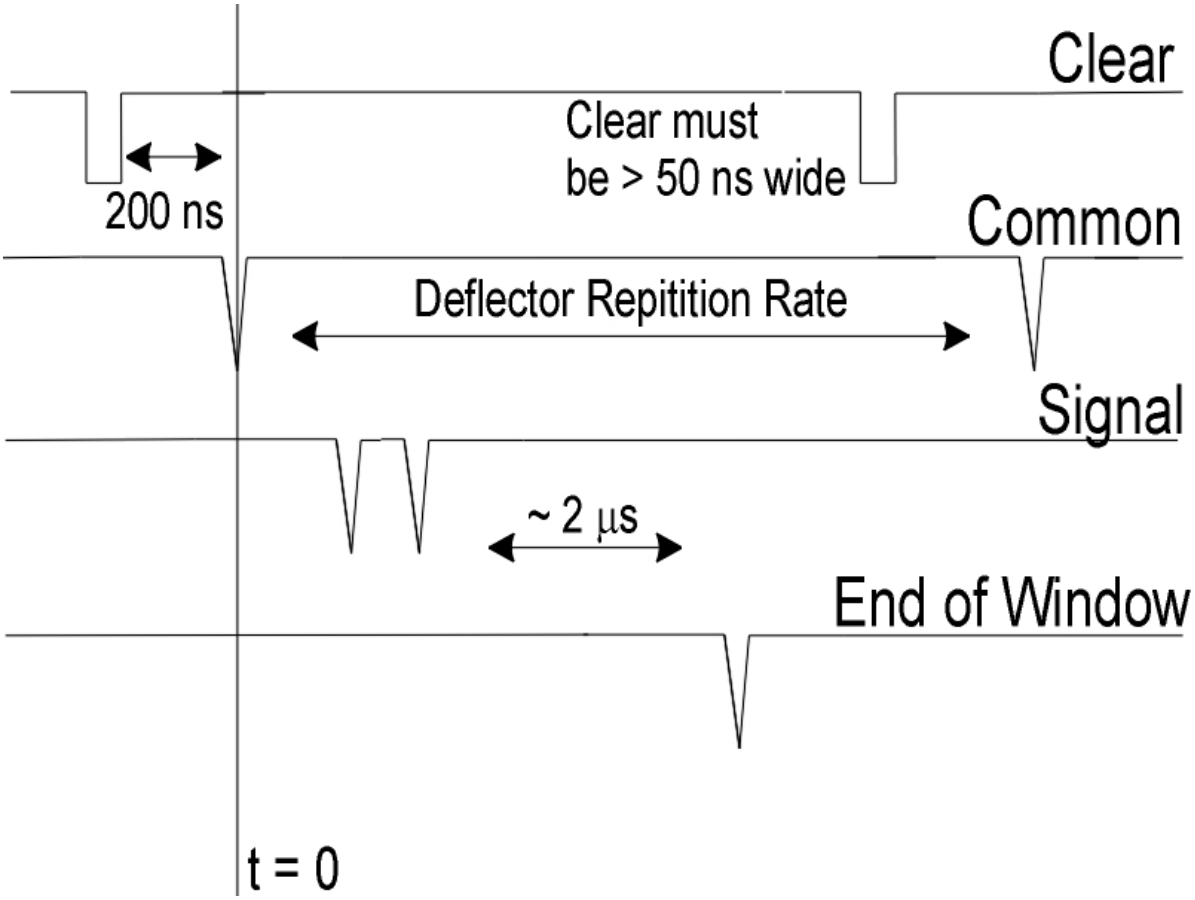

Figure D.3: The time ordering of the four signals sent to the TDC. The common start signal is generated using the prebuncher master clock as a reference, and has the repetition rate of the deflector. This is typically 10.6 to 84.8 μs. The clear signal must precede the common by 200 ns, and be 50 ns wide. The end-of-window signal is usually set to arrive about 2 μs after the first recoil ion signal.

In some cases, the flight times of the recoil ions can be so long that they arrive at the detector after the next deflector signal has arrived. These true "wrap arounds' cannot

be discriminated against with the electronics, and if these “wrap around” signals overlap events of interest in the time-of-flight spectrum, it can be a significant problem. The solution to this problem is either to lengthen the time between bunches, or to pick a spectrometer voltage where the “wrap around” signals arrive at a time that is not of interest in the experiment. The latter solution is preferable since the former option leads to a corresponding reduction in beam current and, at times, problems with the Tandem slit control.

The timing resolution can be determined using a passive delay box, such as the Phillips Scientific 774, and a tail pulse generator to add a few ns of delay to either the timing start or stop, and measure the number of channels shifted on the computer. By repeating this a few times, a linear fit can be made of the different delays, and a conversion factor can be determined. In practice, the timing resolution when using the TDC is just slightly over 1 ns/ channel. When using the FTSS, it is the TAC range used divided by 2048 or 4096, i.e. the number of channels available on the ADC.

D.2 Position Signals

As this experiment evolved and the recoil ion detector was changed to a two-dimensional position sensitive resistive anode detector, the time-of-flight signal processing stayed the same, except that the timing signal is now picked off of the back of the last channel plate rather than the anode. The resistive anode is far too slow to have an accurate timing signal. The values of the RC pickoff circuit are changed slightly since the signal is picked from a different place. Since the incoming ion results in an electron shower from the MCPs to the anode, the signal picked off of the back of the last channel plate is positive, and must be inverted for use as a timing signal. To accomplish this, we

use an EG&G barrel type inverting transformer before the VT-120 pre-amplifier. The signal distortion by the transformer is minimal, although it might be significant for a true CTOF measurement. The signal from the back channel plate is similar to the metal anode signal we discussed in the previous section, but seems to have some additional oscillations in the tail not present with the metal anode signal [D.2]. This signal is also smaller than the signal from the metal anode, and as a result the timing signal sometimes needs to be amplified (by, for example a Phillips Scientific 774 fast amplifier).

The charge signals from the four corners of the resistive anode detector (see Appendix C) are amplified by four charge sensitive pre-amplifiers. These pre-amplifiers are built in-house at GSI, and are called CATSA pre-amplifiers. When working properly, the CATSA pre-amplifiers do a nice job of taking the charge signal from the anode and converting it into a signal that can be amplified by the Tennelec TC-247 dual amplifiers. The TC-247 requires an input signal with a rise time of less than 700 ns and a fall time of greater than 30 μs. It is somewhat difficult to find a reasonably priced pre-amplifier that accomplishes this task and so, at first glance, the CATSAs seem to be a good solution. There are several problems, however, with the CATSAs. First, there are several different varieties of CATSA pre-amplifiers at JRM as well as several different varieties of the corresponding motherboard. The documentation on the different varieties is sparse. As a result, it is possible to put perfectly working CATSAs in a perfectly working but entirely incompatible motherboard. The different varieties of CATSAs also have different power requirements. For many years, the standard location to plug in the CATSA motherboard power supply was the power output supplied on the back of the TC-247. With the new varieties of CATSAs, this did not work, a fact that had to be determined empirically. In response, the JRM electronics staff built a NIM module that would simultaneously power

4 pre-amplifiers or motherboards and was compatible with all known CATSA/motherboard designs. Second, the gain of the different varieties of CATSAs can be quite different, and is not easily adjustable without proper documentation. Therefore, obtaining four CATSAs with a similar gain can be problematic. In addition, for the highly amplifying Z-stack detector we use, the gain of the CATSAs is uniformly too large, and most position signals saturate the TC-247, and the position information is then lost. To combat this problem, the TC-247 dual amplifiers used in this experiment have been modified to attenuate the input signals by 10. Finally, the CATSA design is not very robust, and when floating the detector at a high voltage, CATSA failure is likely. Fortunately, we do not need to float our detector, so this is not a problem in our experiment. Even without floating the detector at high voltage, the failure rate for the CATSAs seems to be higher than for any other single piece of electronics used in this experiment.

Given those problems, it might seem worthwhile to investigate other options for a charge sensitive pre-amplifier. We have done this. The venerable Ortec 142PC and 109A are available in our laboratory, and they do produce an output signal that is acceptable for the TC-247 dual amplifier. We discarded this idea, however, after tests with a tail pulse generator showed that the Ortec 142PC pre-amplifiers were unacceptably noisy and our position resolution would be compromised. This was most likely the case simply because the particular pre-amplifiers we had access to were approximately 20 years old. Since that time, however, one group in the laboratory has purchased new Ortec 142PC pre-amplifiers for use with a position sensitive detector, and those seem to be working well.

Another option would be to use a fast amplifier (such as the VT-120 used for timing) in combination with a charge sensitive ADC. While we have used this system to process the signals from a metal backgammon anode, the signals from the resistive anode are not ideal for such a system. In addition, setting up the separate gates needed for each ADC channel is tricky, and would make setting up the experiment more difficult.

Our solution was to use the CATSA pre-amplifiers despite their considerable drawbacks. It is possible to make the CATSAs work for our purposes by carefully avoiding all of the problems listed above and by being very careful not to damage the CATSAs once four working pre-amplifiers are found. In the meantime, a long-term solution is on the way, in the form of a more robust, lower gain, charge sensitive pre-amplifier built by the Kansas State University Electronics Design Laboratory. The prototype has been tested and appears promising.

The Z-stack configuration results in one other problem when using the CATSA pre-amplifiers. The input impedance of the CATSA is large enough (200 MΩ) that at high recoil ion rates, there is not a sufficient path to ground for the charge on the anode. As a result, charge can build up on the anode, eventually making the anode voltage more negative than the back plate voltage. This causes the charge signals collected from the anode to flip polarity. This situation was avoided by adding a 1 MΩ resistor to ground in parallel with the input resistor of the CATSA, effectively lowering the input impedance and allowing a path to ground for the charge on the resistive anode.

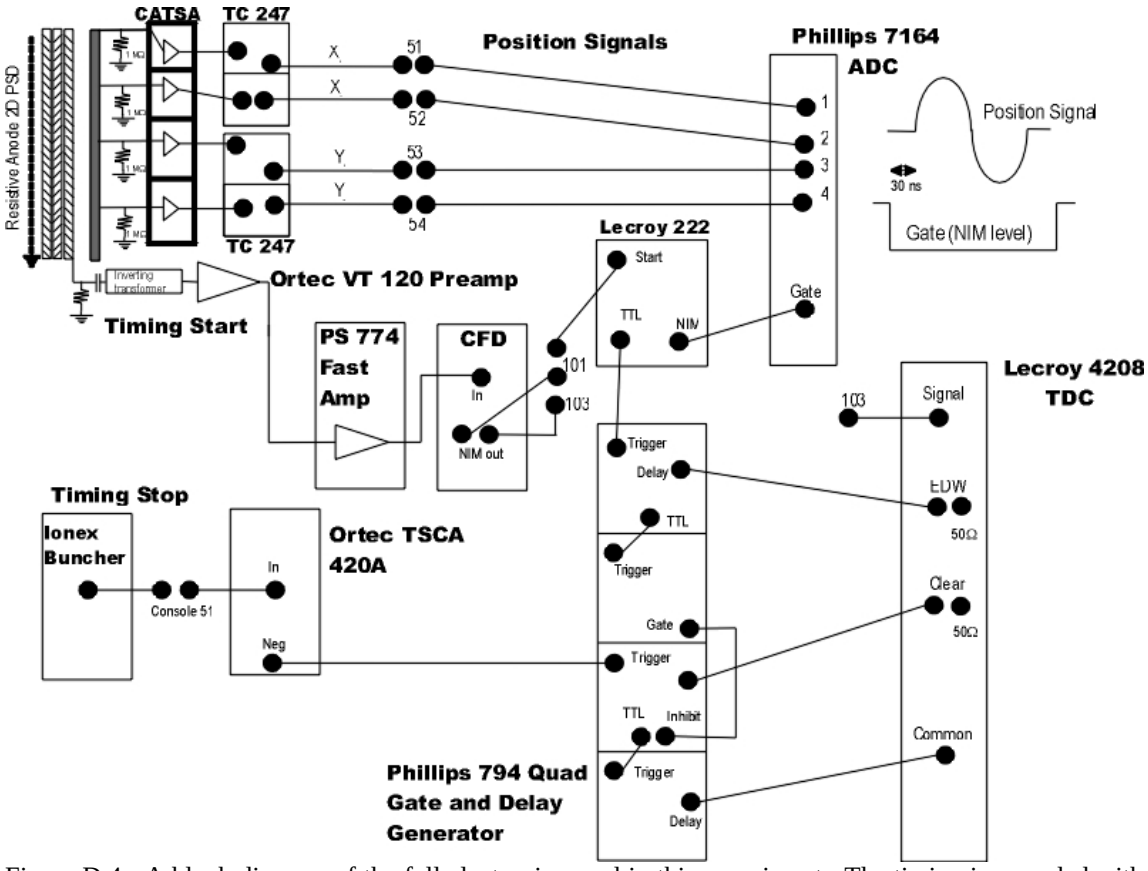

Figure D.4: A block diagram of the full electronics used in this experiment. The timing is recorded with the TDC, the position signals are sent to the Phillips ADC. The PS 774 fast amplifier on the timing signal is optional, and usually is not needed.

The TC-247 amplifiers shape the position signals and produce a unipolar output that is several μs wide and ranges in amplitude from 0 to 5 volts. These signals are sent to a Phillips 7164 ADC with a 0 – 10 volt input range. The Phillips 7164 ADC is a 12-bit ADC, and is therefore superior to the Ortec 811 ADC. Furthermore, the 0 – 10 volt input range is larger than the 0-2 volt input range of the Ortec 811, so it is not necessary to attenuate the output of the TC-247. A gate signal is needed to activate the ADC, which will then send a LAM signal to the front end of the computer. This gate signal is a NIM level signal that opens at least 30 ns before the position signals reach the ADC. The gate signal is generated from the timing signal. One of the NIM signals from the CFD is sent to a LeCroy 222 Dual Gate Generator. The TTL output from that unit is used to trigger

the first unit of the Phillips 794 quad gate and delay generator. The Phillips 794 quad gate and delay generator is used to produce the signals for the TDC. The NIM gate from the LeCroy 222 is used to gate the Phillips 7164 ADC. A block diagram of the full electronics (timing + position) used in this experiment is shown in figure D.4.

Appendix E: Spectrometers

Two spectrometer designs were used in this experiment; the first design was for the time-of-flight measurement, the second design was used for the three-dimensional momentum imaging experiment. This appendix contains details of the spectrometer dimensions and the methods used to determine their focusing properties.

The spectrometer used to measure only the time-of-flight of the recoil ions was a two stage Wiley-McLaren [E.1] design. A diagram of this design is shown in figure E.1, and details of the design and operation are given in references [E.2] and [E.3]. Ions produced in the collision region between the two center meshes are accelerated first by the extraction field ($\vec{E}_{extraction}$) and then by the acceleration field ($\vec{E}_{acceleration}$). After traversing the two acceleration stages, the ions enter a drift region, which extends to the mesh on the front of the micro-channel plate detector. The ratio of $k = \frac{V_1}{V_2}$ between the time-of-flight spectrometer voltages was set to give the best time focusing following the Wiley-McLaren condition [E.1]. In this context, time focusing means that ions produced at rest anywhere in the collision region will have the same time-of-flight. In practice, this is necessary because of the finite width of the projectile ion beam (usually about 1 mm), which introduces some spread into the time-of-flight [E.4]. This is sometimes called

space focusing, but we will use that term later to describe the focusing in the *y* and *z* directions with the momentum imaging spectrometer. The advantage of the two-stage design is that is allows time focusing for any length drift region (for some value of *k*). In resolution tests using Ne^+ ions, which typically have thermal energies (~ 0.04 eV), $\frac{\Delta t}{t}$ was measured to be 2.5 x 10^{-3} and independent of V_2 [E.2].

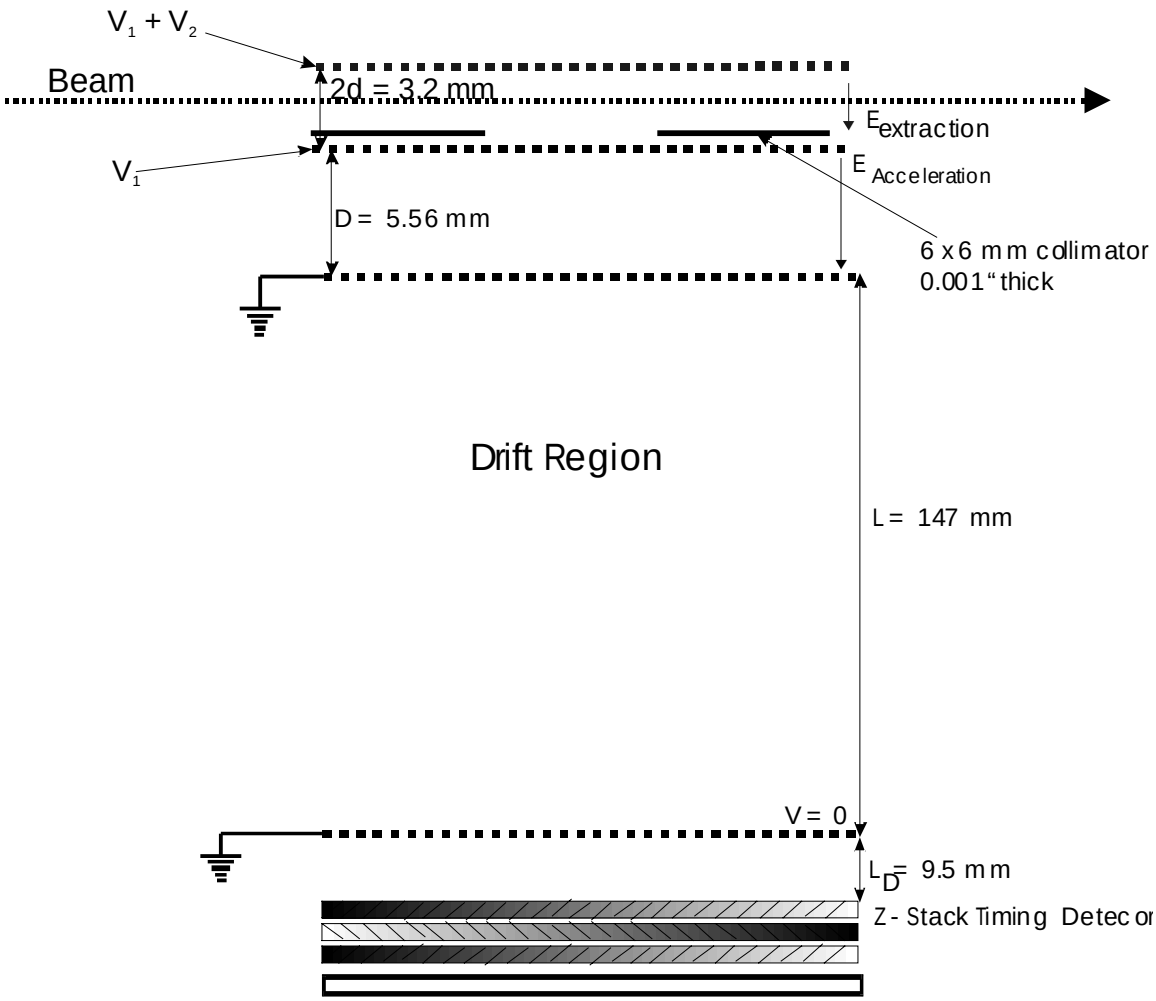

Figure E.1: A schematic picture of the time-of-flight spectrometer used to make the integrated measurements described in chapter 6.1. The dimensions shown were used for one set of measurements, and were frequently varied. The spectrometer stages are defined by 70 lines/inch copper electroform mesh.

To measure the momentum of the GSD fragments in all three dimensions we have designed a spectrometer similar to the ones used in many of the COLTRIMS experiments recently conducted in the Macdonald Laboratory [E.4-E.6]. The recoil ions are accelerated by an electric field defined by the series of rings described in Chapter 5.4 and shown in figure E.2. Spatial focusing (in the *y* and *z* directions, see figure 6.1 for a description of the coordinate system) is accomplished using a weak electrostatic lens formed by applying voltages to the pusher and one other electrode. The spectrometer is shown in figures E.2 and E.3.

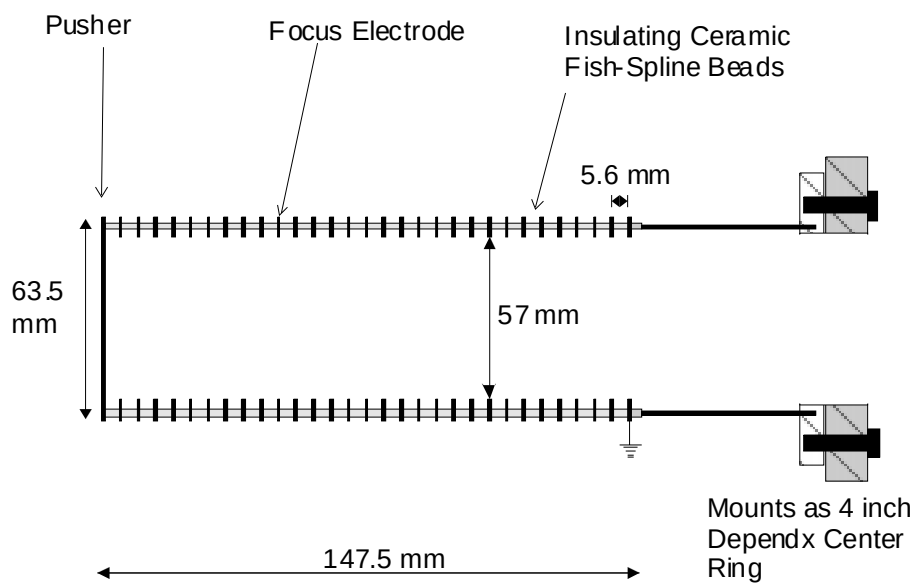

Figure E.2: A side view of the spectrometer. The spacing from the front of one electrode to the front of the next electrode is 5.6 mm. The total spectrometer length is 147.5 mm. Voltages are applied to the pusher and the focus electrode, while the last electrode is grounded. The electrodes are connected by 980 kΩ resistors. Theε spectrometer mounts to a special 4 inch Dependx center ring. The beam travels between the pusher and the first electrode.

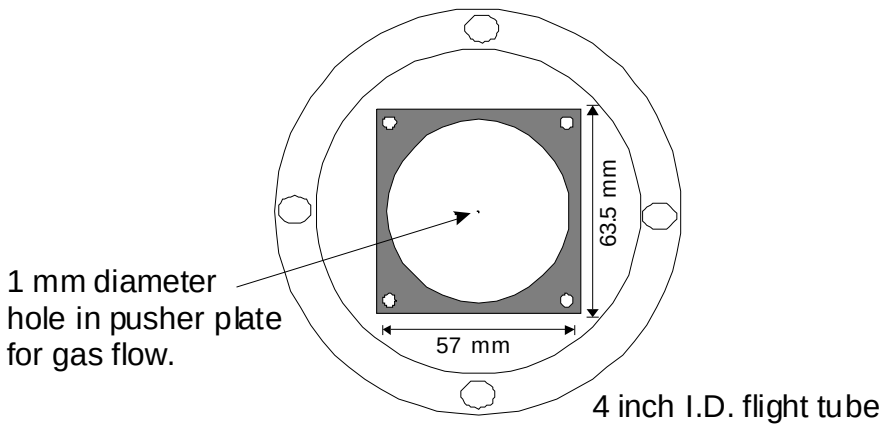

Figure E.3: An end view of the spectrometer. The pusher has a 1 mm hole in the center that allows the target gas to flow into the collision region. The circular I.D. of the spectrometer is 57 mm, the outside of the electrodes are 2.5-inch squares, which have enough clearance to fit in the 4-inch beamline we use as a flight tube.

The goal of the spectrometer focusing is to exclude the initial target size as a factor in the momentum measurement, or in other words, to make the target be a point source. We have used SIMION [E.7] simulations to determine the correct focusing conditions for the spectrometer. The equi-potential curves, generated with SIMION, for the spectrometer under focusing conditions are shown in figure E.4. Unlike the Wiley-McLaren design [E.2, E.3], the momentum spectrometer does not use copper electroform mesh to define the end of the extraction region. Therefore, as can be seen in figure E.4, the electric field extends into the drift region. If the voltage of the focus electrode is chosen so the electric field is uniform along the entire length of the spectrometer, the transition to zero field outside the spectrometer will act as a diverging lens for the recoil ions. This situation is illustrated in figure E.5. We did not use a mesh to define the end of the extraction region since under certain conditions the individual wires of the mesh can distort the data. In fact, early attempts at measuring the position of the recoil ions with a Wiley-McLaren type spectrometer succeeded only in imaging the mesh. As a

result, spatial focusing of the recoil ions is needed not only to compensate for the extended target length in the *y*- and *z*- directions, but also to overcome the built-in diverging lens at the exit of our spectrometer.

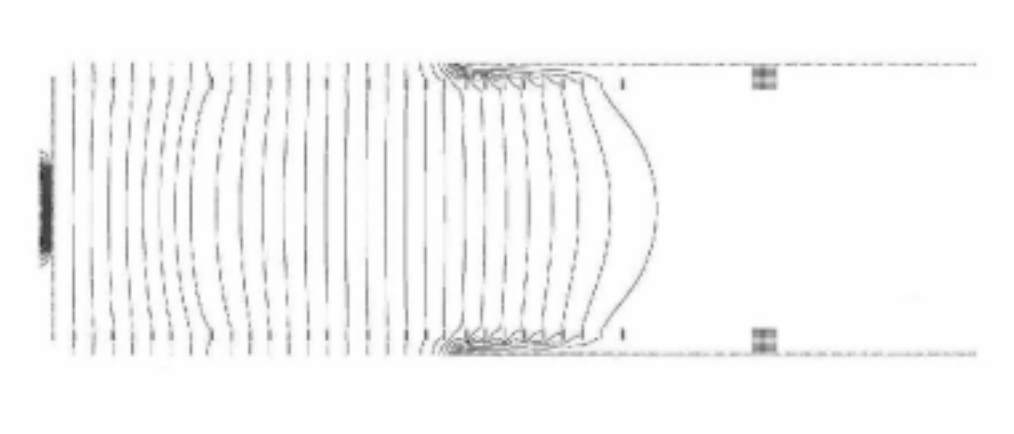

Figure E.4: The equi-potential lines of our spectrometer under focusing conditions.

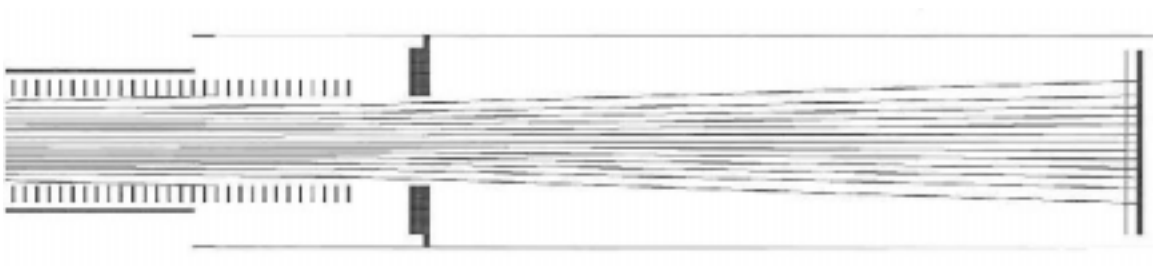

Figure E.5: Flight paths of recoil ions starting with zero kinetic energy from different points along the y-axis of the spectrometer. The spectrometer is in a uniform field operating mode, but the diverging lens at the spectrometer exit spreads the ions.

Mergal [E.8] gives a good description of the spectrometer as an electrostatic lens, and we followed that example for determining to correct voltages. If time focusing (compensating for the beam width in the *x*-direction) is not a concern, it is a simple matter to choose the correct focus voltage by trial and error with a few SIMION simulations. Getting a focus in all three dimensions, however, is slightly more complex.

It is well known [E.1, E.4, E.8-E.10] that a spectrometer with a homogeneous extraction field has first order focusing in the time-of-flight direction if the drift region is twice as long as the acceleration region. Qualitatively, this is because recoil ions created

farther from the detector have a higher potential energy, and therefore have a slightly higher velocity when exiting the spectrometer. By the time the recoil ions reach the detector, the faster ions have "caught up" with the slower ions. Using the focus electrode to create a lens for spatial focusing has the effect of making the electric field in the collision region smaller than it would be for uniform field conditions. As a result, it takes the recoil ions created further from the detector longer to "catch up" with the ions created closer to the detector, therefore the drift length will be longer than twice the length of the extraction field.

The first consideration when designing a spectrometer is usually the flight time of the recoil ion of interest. In our case, we need a flight time of several microseconds so the slow GSD fragments have enough time to spread out over the face of the detector, and we will be able to measure v_y and v_z with some reasonable precision. This determines a starting point for the length of our drift region. From that point, as a first approximation, the length of the spectrometer should be half the length of the drift region to take advantage of the time-focusing condition [E.1, E.4, E.8-E-10]. Additionally, the focus electrode should be far enough away from the collision region that the fields in the collision region are "flat" to a good approximation. From this rough starting point, SIMION simulations are used to find the plane where the detector can be placed to give three-dimensional focusing. For a fixed pusher voltage, reducing the strength of the lens has the effect of increasing the electric field in the collision region, and making the distance to the time-focusing plane smaller. Of course, reducing the strength of the lens also lengthens the distance to the spatial focusing plane. It takes some trial and error to arrive at conditions that are satisfactory in three dimensions, as well as having the correct overall time-of-flight for the recoil ions of interest.

We have defined "satisfactory" focusing conditions as follows: In the *y*- and *z*-directions, a 2 mm target must be focused to a spot on the detector less than our detector resolution (~0.15 mm). In the *x*-direction, a 1 mm wide beam must be time-focused at the detector plane so $\Delta t < 1.0$ ns, the resolution we hope to achieve with the bunched beam. These conditions were fulfilled for the dimensions listed in table E.1 and a focusing voltage of $\frac{V_{focus}}{V_{pusher}} = 0.83 \pm 0.005$. Once this ratio is determined, the pusher voltage may be scaled without damaging the focusing properties, a fact that was also verified with a SIMION simulation. An example (from SIMION) of our spectrometer focusing several groups of ions starting from an extended target is shown in figure E.6.

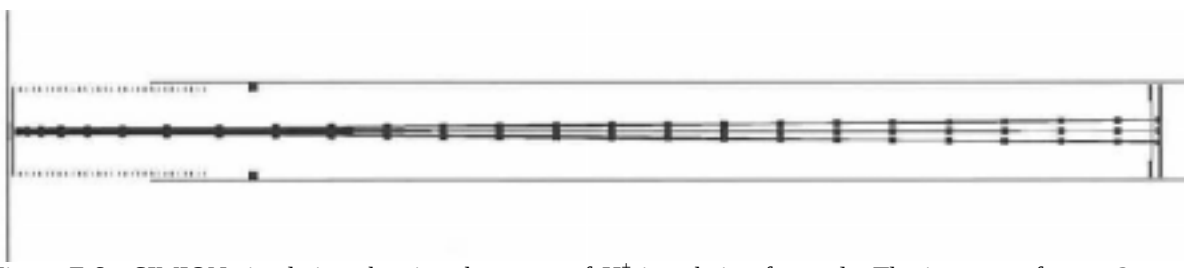

Figure E.6: SIMION simulation showing three sets of H^+ ions being focused. The ions start from a 2 mm diameter circular target. One set of ions has an initial velocity "up", one set of ions has an initial velocity "down" and the third set has an initial velocity toward the detector. This simulation starts the ions with 150 meV of initial energy. The focusing in the *y*- and *z*- directions is determined by the spot size on the detector, and in the *x*-direction by the spread in the time-of-flight of the simulated ions.

Spectrometer Region	**Length (mm)**
Extraction Region	147.5
Drift Region	698.6
Detector Mesh to Front Micro-Channel Plate	5.5

Table E.1: Spectrometer dimensions. The drift region was approximately measured, and then the drift length was slightly adjusted in SIMION so the simulated time-of-flights for several species of recoil ions (m/q = 1-4, 14,16,18,28,32) matched the measured time-of-flights for the same ions.

During the experiment, the spatial focusing voltage determined using SIMION can be verified by changing the ratio of $\frac{V_{focus}}{V_{pusher}}$ and examining the size of a (for example) He^+ peak, which has typically thermal energies. Translating the slits defining the beam position in the *x*-direction checks the time-focusing properties of the spectrometer. If the time-of-flight peak does not shift when the beam is moved, the spectrometer is correctly time focusing. We found the SIMION values to be in good agreement with the measured values, although the SIMION values can be determined more accurately as they are free of other experimental factors, such as detector resolution and the bunch width. One error that can be made in the SIMION calculation is not defining enough points in the potential array to accurately reflect the geometry of the spectrometer. The advances in computer technology in the last five years have virtually eliminated the problems experienced by Frohne [E.9] related to potential array grid size and computer memory considerations. Our array is defined so that there are 10 grid units for every 5.6 mm gap between spectrometer electrodes.

In addition to determining the correct focusing voltage, we used SIMION simulations to investigate the effect of the 1 mm hole in the pusher needed to allow gas flow from the pre-cooled effusive jet to reach the collision region. Equi-potential lines near the skimmer hole are shown in figure E.7. As long as the beam is 1 or 2 mm away

from the pusher, the distortions caused by the hole were judged not to be a problem. Recoil ions with a sizable initial velocity toward the pusher may be distorted, however, and will be discussed later.

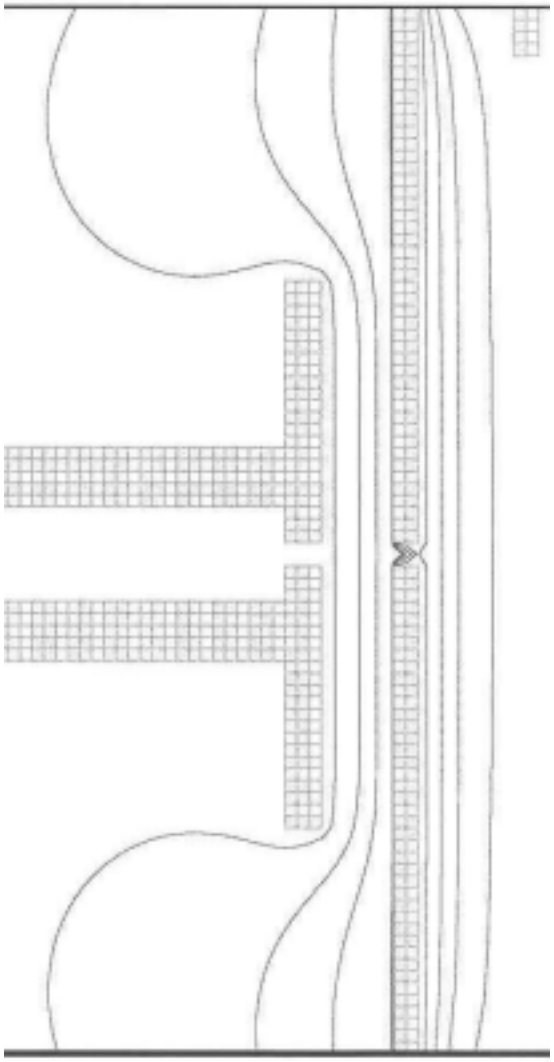

Figure E.7: The end of the pre-cooled effusive gas cell is shown on the left, and the middle of the pusher plate is shown on the right. The 1 mm diameter skimmer hole in the pusher produces distortions in the equi-potential lines only very close to the pusher surface, and if the beam is sufficiently far away, most of the recoil ions should no be affected.

The diverging lens created by the spectrometer exit and the converging lens used to spatially focus the recoil ions result in a non-uniform field, which makes a conversion

from the time-of-flight (TOF) of the recoil ions to the x-component of the momentum (P_x) of the recoil ions difficult to derive from first principles. If a uniform field was used, the conversion could be approximated with the aid of the impulse equation as

$$P_x = Eq(t - t_0)\,, \qquad \text{(E.1)}$$

where E is the electric field, q is the charge of the recoil ion, t is the time-of-flight, and t_0 is the time-of-flight of an ion with $P_x = 0$ (the centroid of the time-of-flight peak). This equation is not valid for two reasons. First, the impulse equation cannot be easily applied since the ratio of $\frac{t - t_0}{t_0}$ can approach 0.1 for some of the fields used in our experiment. Second, as stated before, the electric fields in the spectrometer are non-uniform. To determine the correct conversion of TOF to P_x, we again use SIMION simulations.

For each pusher voltage used, trajectories are calculated for 140 recoil ions with P_x values ranging from (plus or minus) the highest value of P_x expected for the most energetic dissociation process of the hydrogen molecule, double ionization. For H^+ ions, this ranges from -45 a.u. $\leq P_x \leq 45$ a.u. Most of the simulated ions are concentrated near $P_x = 0$, in the range of interest for the GSD process. For each value of P_x, the TOF of the ion is recorded, and then this data is fit to a second order polynomial of the form,

$$P_x = a_1(t - t_0) + a_2(t - t_0)^2\,. \qquad \text{(E.2)}$$

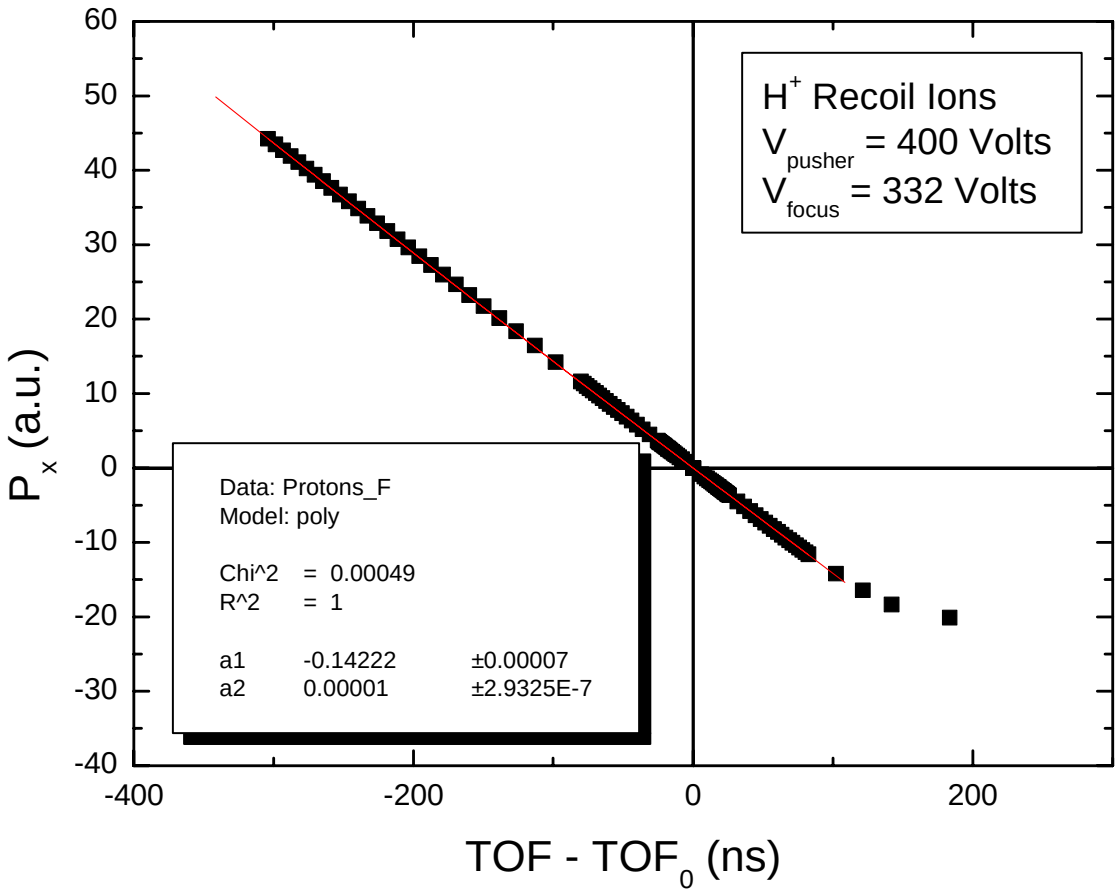

Figure E.8: Ion flight times as a function of P_x simulated with SIMION. A curve of the form of equation (E.2) is then fit to the simulation, which is then used to determine P_x from the measured recoil ion time-of-flight. The asymmetry for positive values of $(t - t_0)$ is the effect of ions flying too close to the pusher and the time-of-flight becoming distorted.

A typical fit is shown in figure E.8. The a_2 term is usually quite small in comparison to the a_1 term ($\frac{a_2}{a_1} \approx 0.0001$) as expected, since we do not expect equation (E.1), which predicts a linear relationship, to be completely wrong. Some distortions appear in figure E.8 for recoil ions that have trajectories that pass close to the pusher. We exclude these ions from our fit and from our data analysis. To exclude these recoil ions from our analysis, we can sort our data off-line in two ways: The first way is to exclude

all recoil ions with an initial velocity away from the detector. The second way is to exclude recoil ions with $(t - t_0) > t_{pusher}$, where t_{pusher} is some cutoff value indicating the range of the pusher influence and is determined from SIMION.

Appendix F: Effusive Jet

Since the beginning of the century researchers have used slow beams of neutral atoms and molecules to study low velocity atomic and molecular processes. An in-depth discussion of the subject may be found in references [F.1-F.3]. By using differential pumping, a pressure difference between two regions produces a flow of gas from the higher pressure region to the lower pressure region. If the overall pressure is low enough, the atoms or molecules can escape through the aperture between the high pressure and the low pressure region without any change in their spatial or velocity distributions. This limiting case is called a molecular, or effusive, flow.

Given a container (or source) with a single circular aperture of diameter d and thickness l, as l approaches 0, the gas flow is considered effusive if

$$d << \lambda \quad , \tag{F.1}$$

where λ is the mean free path of the atoms in the container. Using the kinetic theory for an ideal gas, λ is calculated as a function of the pressure (P) and temperature (T) of the gas in the source, and the collision cross section of the atoms in the source (σ_k). Approximating the cross section as a solid sphere gives

$$\sigma_k = \pi \left(\frac{\delta}{2} \right)^2 , \tag{F.2}$$

where δ is the atomic diameter. λ is then

$$\lambda = \frac{kT}{\sqrt{2}\,\sigma_k P}, \tag{F.3}$$

where k is the Boltzmann constant.

Within the solid angle, $d\Omega$, defined by the angle θ, the number of atoms flowing per unit time is

$$dN = \frac{d\Omega}{4\pi} n\bar{v} A_s \cos(\theta), \tag{F.4}$$

where n is the number of atoms per unit volume in the source and $\bar{v}$ is the mean particle velocity. A_s is the aperture area,

$$A_s = \pi \left(\frac{d}{2} \right)^2. \tag{F.5}$$

If m is the particle mass, the mean particle velocity, $\bar{v}$, is

$$\bar{v} = \sqrt{\frac{8kT}{m\pi}}. \tag{F.6}$$

The total number of particles effusing in all directions per unit time is found by integrating equation (F.4) over all angles, which results in

$$N = \frac{1}{4} n\bar{v} A_s. \tag{F.7}$$

The flow from such an aperture is basically in all directions, with more probability in the forward direction, as can be seen from the cosine in equation (F.4). By increasing the ratio of l/d, (giving the aperture some thickness) the directionality of the effusive flow can be increased. If $l >> d$, equation (F.7) is modified by a reduction factor, ξ,

$$\xi = \frac{4d}{3l}. \tag{F.8}$$

The derivation of equation (F.8) is found in Reference [F.1]. Equation F.7 then simplifies to

$$N = \frac{\pi d^3}{12l} n\bar{v}\,. \qquad \text{(F.9)}$$

For an effusive aperture with a non-zero length, the intensity as a function of angle (θ) can be derived from geometric considerations [F.1, F.4, F.5] but it is not simple, and only the result will be presented here. Defining $\beta = \frac{d}{l}$, and $q = \frac{1}{\beta}\tan(\theta)$, the result is

$$I(\theta) = \frac{n\bar{v}}{4}\left(\frac{d}{2}\right)^2 j(\theta) \qquad \text{(F.10)}$$

where for $q \le 1$,

$$j(\theta) = \alpha\cos(\theta) + \frac{2}{\pi}\cos(\theta)\left[(1-\alpha)R(q) + \frac{2}{3q}(1-2\alpha)\left\{1-(1-q^2)^{\frac{3}{2}}\right\}\right], \qquad \text{(F.11)}$$

and for $q \ge 1$,

$$j(\theta) = \alpha\cos(\theta) + \frac{4}{3\pi q}(1-2\alpha)\cos(\theta)\,. \qquad \text{(F.12)}$$

In equation (F.11), *R(q)* is defined as

$$R(q) = \cos^{-1}(q) - q(1-q^2)^{\frac{1}{2}}, \qquad \text{(F.13)}$$

and in equations (F.10) and (F.11), α is defined as

$$\alpha = \frac{1}{2} - \frac{1}{3\beta^2}\left[\frac{1-2\beta^3+(2\beta^2-1)(1+\beta^2)^{\frac{1}{2}}}{(1+\beta^2)^{\frac{1}{2}} - \beta^2 \sinh^{-1}\left(\frac{1}{\beta}\right)}\right]. \qquad \text{(F.14)}$$

In our system, the length to diameter ratio is 9:1 (β = 0.11); therefore the effusive jet does have some directional flow. The values of $j(\theta)$ for several values of β are shown in figure F.1. We use two other factors to limit the size of our target. First, the effusive flow not only passes through a single channel aperture, it must pass through a skimmer of 1 mm diameter located about 2.5 mm away from the exit of the pre-cooled gas cell. Second, the ion beam intersects the effusive flow within 3-4 mm of the skimmer. The combination of these two factors provides some limited beam collimation. The size of the extended target formed by the intersection of the beam and the jet can be compensated for using the three-dimensional focusing properties of the spectrometer.

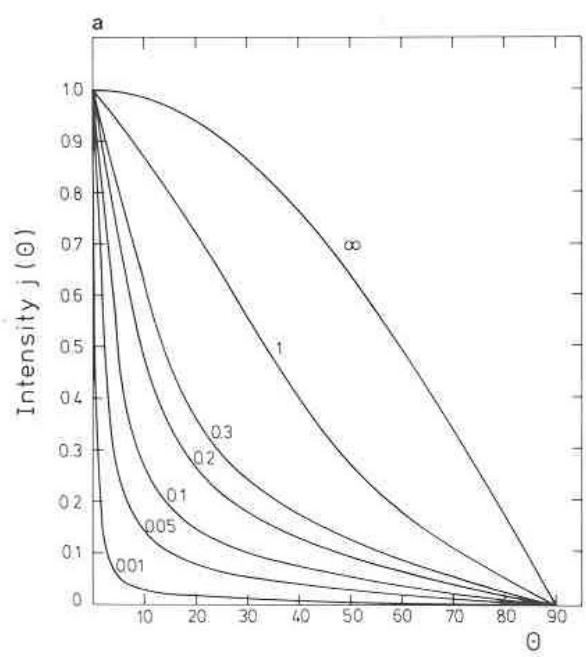

Figure F.1: A plot of $j(\theta)$ calculated using equations (F.11) and (F.12) for several values of β. This figure is from reference [F.1].

Larger target densities could be achieved by replacing our single aperture with a capillary array. Typical arrays of this type are made of glass and have diameters of around 30 μm to 1 mm and lengths of 300 μm to 10 mm. Since each capillary collimates the flow, and many capillaries are combined to allow a larger volume of gas to flow through the aperture, the target density is increased by

$$N = N_{ch} \frac{\pi d^3}{12l} n\bar{v}, \qquad \text{(F.15)}$$

where N_{ch} is the total number of capillaries in the array.

If the pressure difference between the source and the target area is too large, the result is a supersonic flow [F.6]. The condition for this type of flow is d >> λ, resulting in many particle-particle and particle-wall collisions before the gas can escape the aperture. The collisional cooling, and the shock wave of the expanding gas, when combined with a skimmer to select only the core of the elliptical expansion of gas, provides a highly directional flow and a dense target, which is extremely useful in many applications. In our situation, however, it is a situation to be avoided, since the cold, dense, supersonic expansion is an ideal breeding ground for clusters. If a cluster is formed, it is conceivable that ionizing one of the electrons of the cluster would result in some process that could produce low energy H^+ or D^+ fragments that would be indistinguishable from the GSD fragments of interest in this study. To avoid this, we keep the source pressure low enough that the mean free path is similar to (or smaller than) the diameter of the aperture. The source pressure is monitored by a vacuum gauge located on the source side of the needle valve used to control the gas flow into the source.

We have been unable to directly measure the velocity the particles in our effusive jet. Because the source pressure is so low, the effusive flow conditions should be valid

and we estimate the mean velocity using equation (F.6). Taking the measured temperature of the HD^+ distribution (14.4 K), the calculated mean velocity is 114 m/s, or 0.11 mm/μs, which is near the limit of our detection ability.

Appendix G: Resolution and Error Analysis

For the integrated measurement, depending on time-of-flight only, the resolution is simply a matter of being able to identify the ground state dissociation (GSD) fragments from fragments from other processes. Since the timing resolution is quite sufficient to differentiate a H^+ ion from a D^+ ion, we only need be concerned with higher energy fragments from ionization-excitation and double-ionization processes. This contribution is subtracted from the low energy GSD peaks using the method described in chapter 5.3. The error in the integrated GSD measurement is evaluated as follows.

The H^+ GSD yield is:

$$H^+ (GSD) = H^+_{HD} - H^+_{H2O} - H^+_{H2} - H^+_{random} \qquad (G.1)$$

In this expression, all of the terms represent the yield of the low energy part of the spectra. The subscript indicates the origin of the fragments. The uncertainty in the H^+ GSD yield is then:

$$\sigma_{H^+(GSD)} = \sqrt{\sigma^2_{H^+_{HD}} + \sigma^2_{H^+_{H2O}} + \sigma^2_{H^+_{H2}} + \sigma^2_{H^+_{random}}} \qquad (G.2)$$

The individual uncertainties have different components. The error in evaluating the H_2O^+ peaks in the background and HD runs (and therefore the error in the normalization of the background run) gives the uncertainty in $H^+_{H2O.}$ The error in determining the H_2 contamination in the HD bottle leads to the uncertainty in H^+_{H2}, which is arrived at by

$$H^{+}{}_{H2} = \left(HD^{+}\right)\left(\frac{H_2{}^{+}}{HD^{+}}\right)\left[GSD\left(\frac{H^{+}}{H_2{}^{+}}\right)\right], \qquad \text{(G.3)}$$

where (HD^+) is the yield of HD^+ fragments, $\frac{H_2{}^{+}}{HD^{+}}$ is the relative amount of H_2 contamination in the HD bottle (which is determined using the methods described in appendix B) and GSD$\left(\frac{H^{+}}{H_2{}^{+}}\right)$ is the theoretical GSD fraction for H_2 (see chapter 3).

The random correction is the flat background in the TOF spectra that still remains after subtracting the H_2O background. Estimating the error in evaluating the areas of the different peaks gives the values of σ. For example, the error in the H^+_{H2O} yield was determined by using the error in the areas of the H_2O^+ peaks to estimate the largest (and smallest) reasonable value of $H^+_{H2O.}$

The goal of the analysis is to obtain a value for the ratio between the yield of H^+ from ground state dissociation and the yield of HD^+.

$$R_H = \frac{H^{+}(GSD)}{HD^{+}}. \qquad \text{(G.4)}$$

Since the relative error in the measurement of the HD^+ yield is very small, it is a good approximation to treat that value as a constant when determining the uncertainty in the ratio. Thus,

$$\sigma_{R_H} = \frac{\sigma_{H^{+}(GSD)}}{HD^{+}} \qquad \text{(G.5)}$$

Using runs GSD3P183 (HD 3kV) and GSD3P184 (BG 3kV) as an example, the following yields were measured:

$H^+_{HD} = 83257 \pm 700$
$H^+_{H2O} = 18379 \pm 900$
$H^+_{H2} = 951 \pm 48$
$H^+_{random} = 63 \pm 12$
$HD^+ = 1.215352 \times 10^7 \pm 3740$.

The H^+ (GSD) yield is then 63864 ± 1141, and $R_H = 0.525\% \pm 0.009\%$**.**

The other channel of interest is the D^+ channel, which has the additional complication of having the same mass to charge ratio as the H_2^+ peak, which is present because of the impurities in the HD bottle. The D^+ GSD yield is:

$$D^+ (GSD) = D^+_{HD} - H_2^+{}_{H2O} - H_2^+{}_{HD} - D^+_{D2} - D^+_{random}. \qquad (G.6)$$

The notation in equation (G.6) is similar to equation (G.1) with the subscripts indicating the origin of the fragments.

The error analysis is similar to the H^+ analysis, although equation (G.6) does have one more term then equation (G.1), which is the dominant contribution to the error of this channel.

$$\sigma_{D^+(GSD)} = \sqrt{\sigma^2_{D^+_{HD}} + \sigma^2_{H_2^+{}_{H2O}} + \sigma^2_{H_2^+{}_{HD}} + \sigma^2_{D^+_{D2}} + \sigma^2_{D^+_{random}}} \qquad (G.7)$$

The ratio between the yield of D^+ from ground state dissociation and the yield of HD^+ is called

$$R_D = \frac{D^+(GSD)}{HD^+}. \qquad (G.8)$$

The error in R_D is given by

$$\sigma_{R_D} = \frac{\sigma_{D^+(GSD)}}{HD^+} \qquad (G.9)$$

Using runs GSD3P183 (HD 3kV) and GSD3P184 (BG 3kV) as an example, the following yields were measured:

$D^+_{HD} = 123861 \pm 600$
$H_2{}^+_{H2O} = 2224 \pm 51$
$H_2{}^+_{HD} = 64413 \pm 2430$
$D^+_{D2} = 302 \pm 35$
$D^+_{random} = 77 \pm 15$
$HD^+ = 1.215352 \times 10^7 \pm 3740$.

The D^+ (GSD) yield is then 55628 ± 2503, and R_D = 0.464% ± 0.021%. The largest single source of error is clearly the uncertainty in the amount of H_2 contamination in the HD target.

The vertical error bars in the differential measurement depend on the same factors, and are evaluated in the same manner, except that the evaluation must be done on a bin-by-bin basis, i.e., for each kinetic energy release.

The energy resolution of the differential measurement depends on factors that may be divided into two categories. First are the inherent uncertainties in the process we are measuring, such as the center-of-mass (thermal) motion of the molecular ion and the momentum transfer to the molecular ion in the collision. The other category is uncertainties in our measurement of the energy of the dissociating fragments. These uncertainties are caused by technical factors, such as the position resolution of the detector. The measurement uncertainty can be calculated from the contributions of the individual uncertainties in the measurement. The measured energy is given by,

$$E_{measured} = \frac{P^2}{2m}, \qquad \text{(G.10)}$$

where

$$P = \sqrt{P_x{}^2 + P_y{}^2 + P_z{}^2}\ . \qquad \text{(G.11)}$$

In equation (G.11), P_x is defined from the TOF to P_x conversion factor derived in Appendix E,

$$P_x = a_1 t + a_2 t^2, \tag{G.12}$$

with $t = t' - t_0$ being the difference between the measured time-of-flight for that event (t'), and the centroid of the time-of-flight peak (t_0). δt includes uncertainties from the buncher width and the timing electronics, $\delta t = \sqrt{\delta t_{bunch}^2 + \delta t_{electronics}^2}$, which is typically about 1.6 ns (1.05 ns electronics, 1.2 ns buncher). P_y and P_z are measured from the position information, and are similar to each other,

$$P_y = \frac{m v_y}{2.18847}, \tag{G.13}$$

and

$$P_z = \frac{m v_z}{2.18847}, \tag{G.14}$$

where the number in the denominator is a conversion from atomic units to eV that will be useful later. The velocities in equations (G.13) and (G.14) are measured using the position and the time-of-flight,

$$v_y = \frac{y' - y_0}{t'}, \tag{G.15}$$

and

$$v_z = \frac{z' - z_0}{t'}. \tag{G.16}$$

The measured energy, calculated in eV (where the time is measured in ns and the position in mm), is given by:

$$E_{measured} = \frac{27.2116}{2m}\left[P_x{}^2 + P_y{}^2 + P_z{}^2\right]$$

$$E_{measured} = \frac{27.2116}{2m}\left[\left(a_1 t + a_2 t^2\right)^2 + \frac{m^2}{(2.18847)^2}\left(\frac{(y' - y_0)^2}{t'^2} + \frac{(z' - z_0)^2}{t'^2}\right)\right]. \quad \text{(G.17)}$$

Neglecting the very small error in y_0 and z_0, ($\delta y_0 << y_0$) we can calculate, from equation (G.17), the quantity $\delta E_{measured}$:

$$\begin{aligned}\delta E^2_{measured} = &\left[\frac{27.2116}{2(2.18847)^2}\frac{2m(y' - y_0)\delta y'}{t'}\right]^2 + \left[\frac{27.2116}{2(2.18847)^2}\frac{2m(z' - z_0)\delta z'}{t'}\right]^2 \\ &+ \left[\frac{(27.2116}{2m}2\left(a_1 t + a_2 t^2\right)\left(a_1 + 2a_2 t\right)\delta t\right]^2 \\ &+ \left[\frac{27.2116m}{2(2.18847)}\left((y' - y_0)^2 + (z' - z_0)^2\right)\left(\frac{-2\delta t'}{t'^3}\right)\right]^2 \\ &+ \left[\frac{27.2116}{2m}2\left(a_1 t + a_2 t^2\right)\left(t\delta a_1\right)\right]^2 \\ &+ \left[\frac{27.2116}{2m}2\left(a_1 t + a_2 t^2\right)\left(t^2\delta a_2\right)\right]^2\end{aligned} . \quad \text{(G.18)}$$

We use a simulation to generate a distribution of values of y, z, and t, and calculate the error using equation (G.18). The results of this simulation are shown in figure G.1. From the resulting values we see that $\delta E_{measured}$ scales with $\sqrt{E_{measured}}$, and we can fit the curve to obtain a value for the coefficient. To convert the measured kinetic energy in the lab frame to kinetic energy release in the center of mass frame, the uncertainty in the measured energy must also be multiplied by a factor, ε, where $\varepsilon = 3$ for D^+ particles and $\varepsilon = \frac{3}{2}$ for H^+ particles. For the molecular ion peaks in our experiment, $\varepsilon = 1$, since there is no dissociation. The uncertainty in the measurement of the energy of the dissociating fragments can then be expressed as

$$\delta E_{measured}\left(E_k\right) = \alpha\varepsilon\sqrt{E_{measured}} , \quad \text{(G.19)}$$

where ε is defined above, and α is determined from the fit of figure G.1. For the particular case of V_{pusher} = 400 volts, V_{focus} = 332 volts shown in figure G.1, α = 0.485 meV.

Table G.1 summarizes the various factors influencing the resolution of our energy measurement.

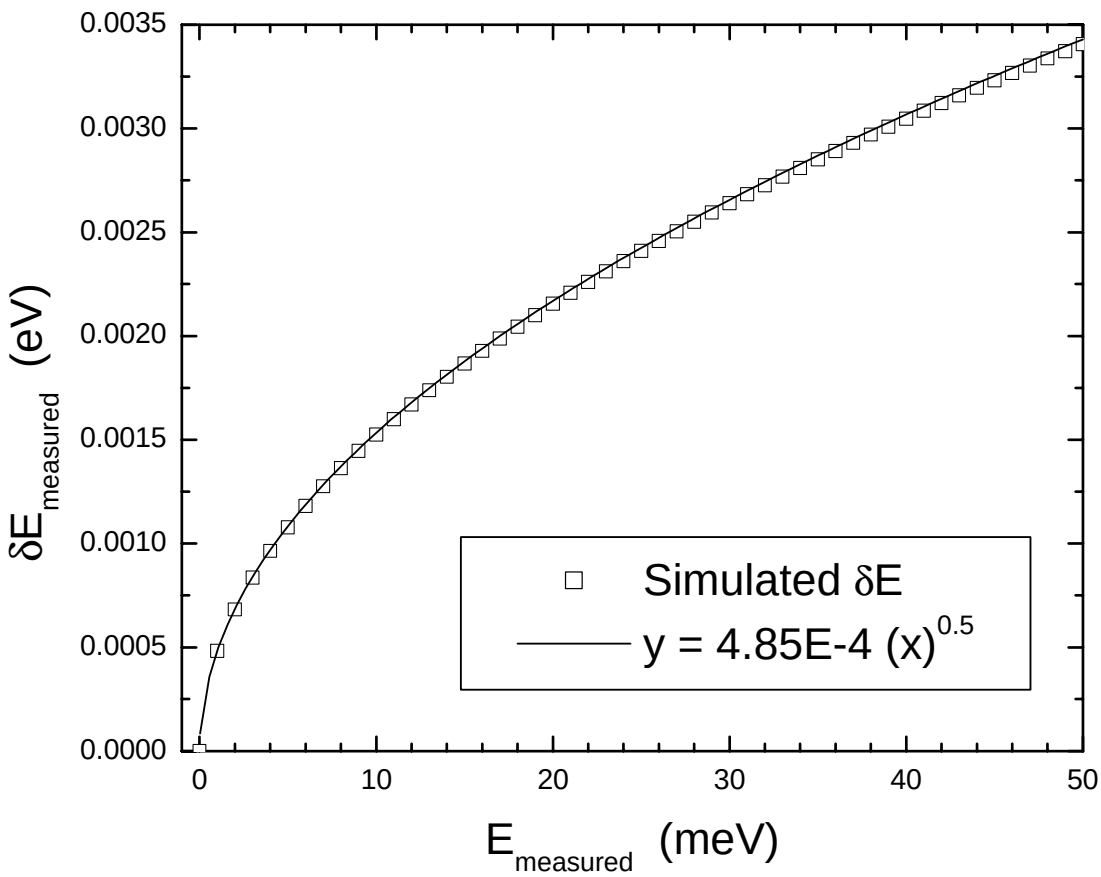

Figure G.1: Calculated δE using equation (G.18) for D^+ recoil ions and a simulated distribution of *y*, *z*, and *t*. This figure is for the case V_{pusher} = 400 volts, V_{focus} = 332 volts

Uncertainty	Size	Source	Possibility for Improvement
δy, δz	0.21 ± 0.03 mm	Detector position resolution	Fix I_3 signal. Should be able to obtain 0.15 mm resolution.
δy_0, δz_0	< 0.05 mm	Locating centroid of peak in analysis	Patience in sorting. Lower residual B-field
δt	1.62 ns	Buncher width = 1.2 ns Resolution of timing electronics = 1.1 ns	Bunching: Use LINAC? Timing: sub-ns TDC
δa_1	$\frac{\delta a_1}{a_1} \cong 10^{-4}$	Fitting error	-
$\delta t a_2$	$\frac{\delta a_2}{a_2} \cong 10^{-2}$	Fitting error	-
Thermal	14.4 K ≈ 1.2 meV	Gas temperature	Use a skimmer for geometrical cooling.
$P_{longitudinal}$	Included in δy_0	Q-value of reaction	Smaller Q-value with protons than C^{3+}
P_{recoil}	≤ 0.6 meV	Electron	Measure the electron momentum.

Table G.1: A summary of the factors influencing our experimental resolution and some possibilities for future improvement.

Appendix H: Beamline L2

This experiment was carried out on beamline L2, located in the square room of the J.R. Macdonald Laboratory (see figure H.1). This beamline is on the left 30-degree port of the Tandem switching magnet.

The first part of this experiment, the identification of the H^+ and D^+ recoil ions by their time-of-flight only, was conducted on the apparatus used for coincidence time-of-flight (CTOF) studies of molecular dissociation [H.1, H.2]. A diagram of L2 during that period is shown in figure H.2.

Several improvements were made to L2 during the development of the momentum imaging experimental method. First, the beamline was re-aligned and the cylinder (see figure H.2) used for the CTOF experiments was removed. The L2 telescope stand was moved from the carpeted area of the square room to the more stable cement floor, and aligned on the benchmarks. A set of *x* and *y* magnetic steerers were added to the beamline downstream of the quadrapole magnet. A beam profile monitor was added after the target region. Two additional sets of four-jaw slits were added to provide better beam collimation. An updated diagram of the beamline, including distances, is shown in figure H.3.

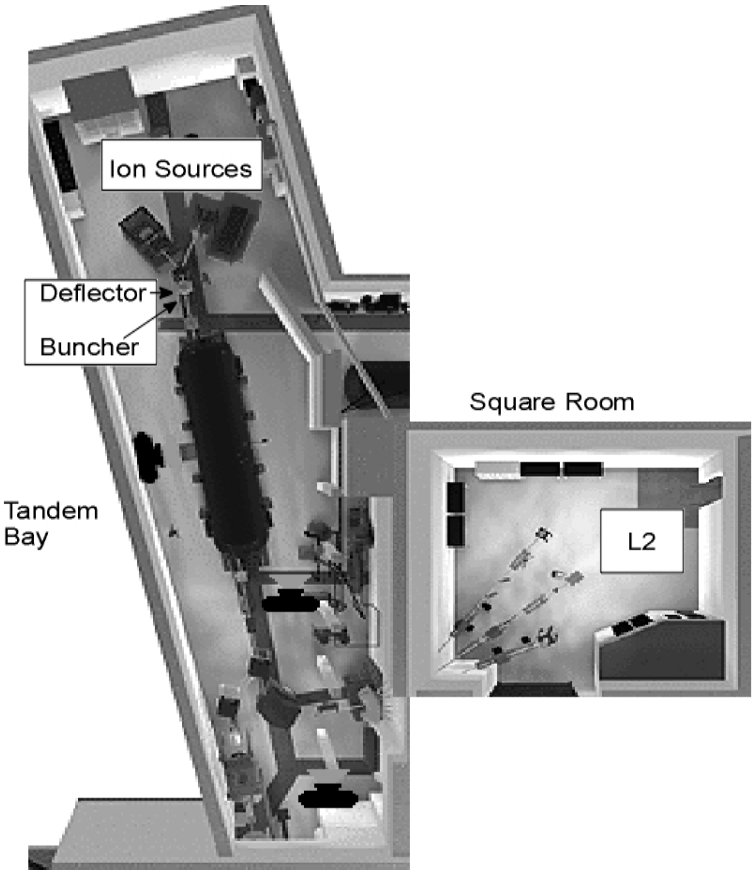

Figure H.1: An overview of the JRM floor plan. Beamline L2 is located in the square room, off the left 30-degree port on the Tandem accelerator.

The momentum imaging spectrometer and cold head are housed in a 7 5/8” x 7 5/8” x 11” target chamber, with six 4” ports and four 2” ports on the corners. This serves as the primary target location on the beamline. There is, however, an additional cube downstream of this target that can be used for another experiment. The target chamber has a liquid nitrogen trap to limit the amount of residual water vapor present in the chamber. The liquid nitrogen trap contains sufficient nitrogen to stay cold for over eight hours without re-filling. For a diagram of the target chamber, refer to figure H.4.

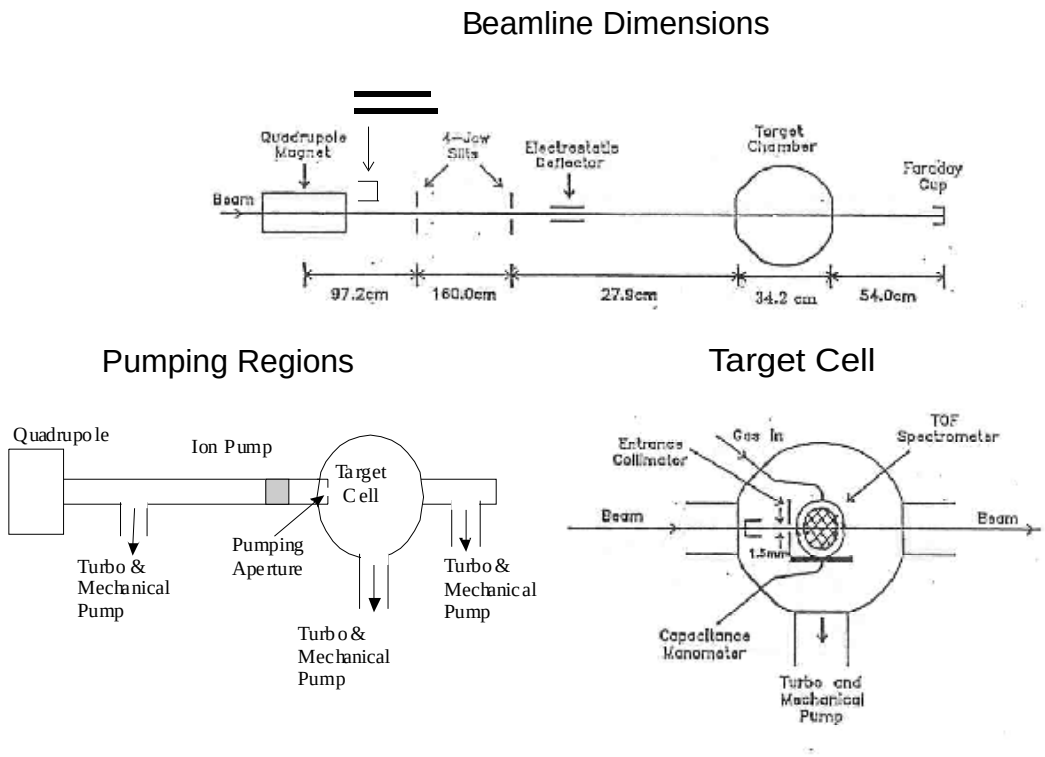

Figure H.2: Beamline L2 during the time period it was configured for CTOF measurements. Parts of this figure are adapted from reference [H.1].

In order to perform measurements of the bunch quality, a diagnostic cube containing a retractable gold foil and a surface barrier detector was added just after the quadrupole. The bunch width can then be determined without transferring the beam to the diagnostic cube before LCM1 (see Appendix A). The foil is 240 cm before the target region. The difference in the time-focusing properties of the buncher, however, is not expected to vary significantly over this region (see Appendix A).

Two ion pumps and a turbo-molecular pump provide pumping upstream of the target. A 3 mm diameter differential pumping aperture is located on the entrance to the target chamber. One turbo-molecular pump pumps the target region itself, another on the drift tube. A third turbo-molecular pump is located on the beamline just downstream of the target chamber. Typical baseline pressure readings in the target region during an

experiment with the cryo-head on and the liquid nitrogen trap full ranged from low 10^{-7} torr to mid 10^{-8} torr. Most of the beamline contains O-ring vacuum seals. For a major vacuum improvement, switching to Con-flat® type seals is probably required.

Figures H.5 and H.6 show recent photographs of L2.

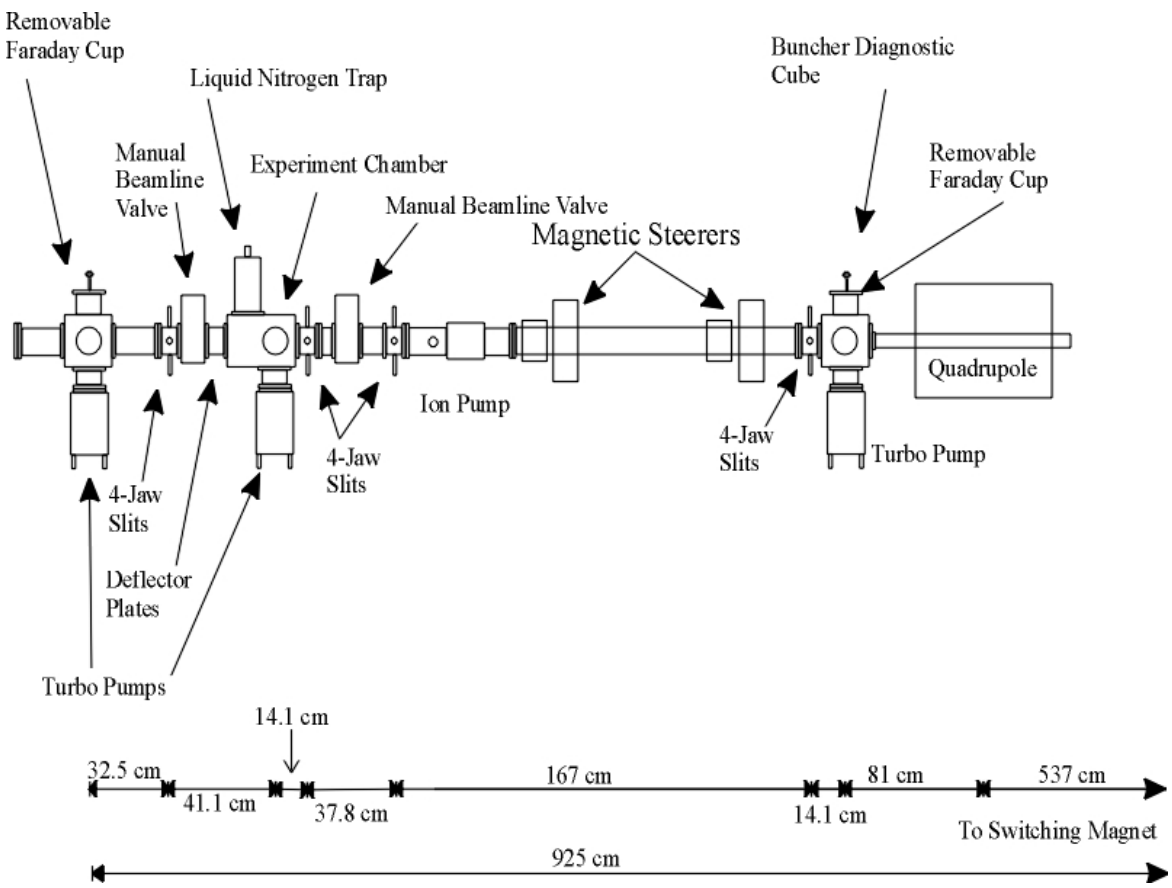

Figure H.3: A diagram of the current configuration of L2.

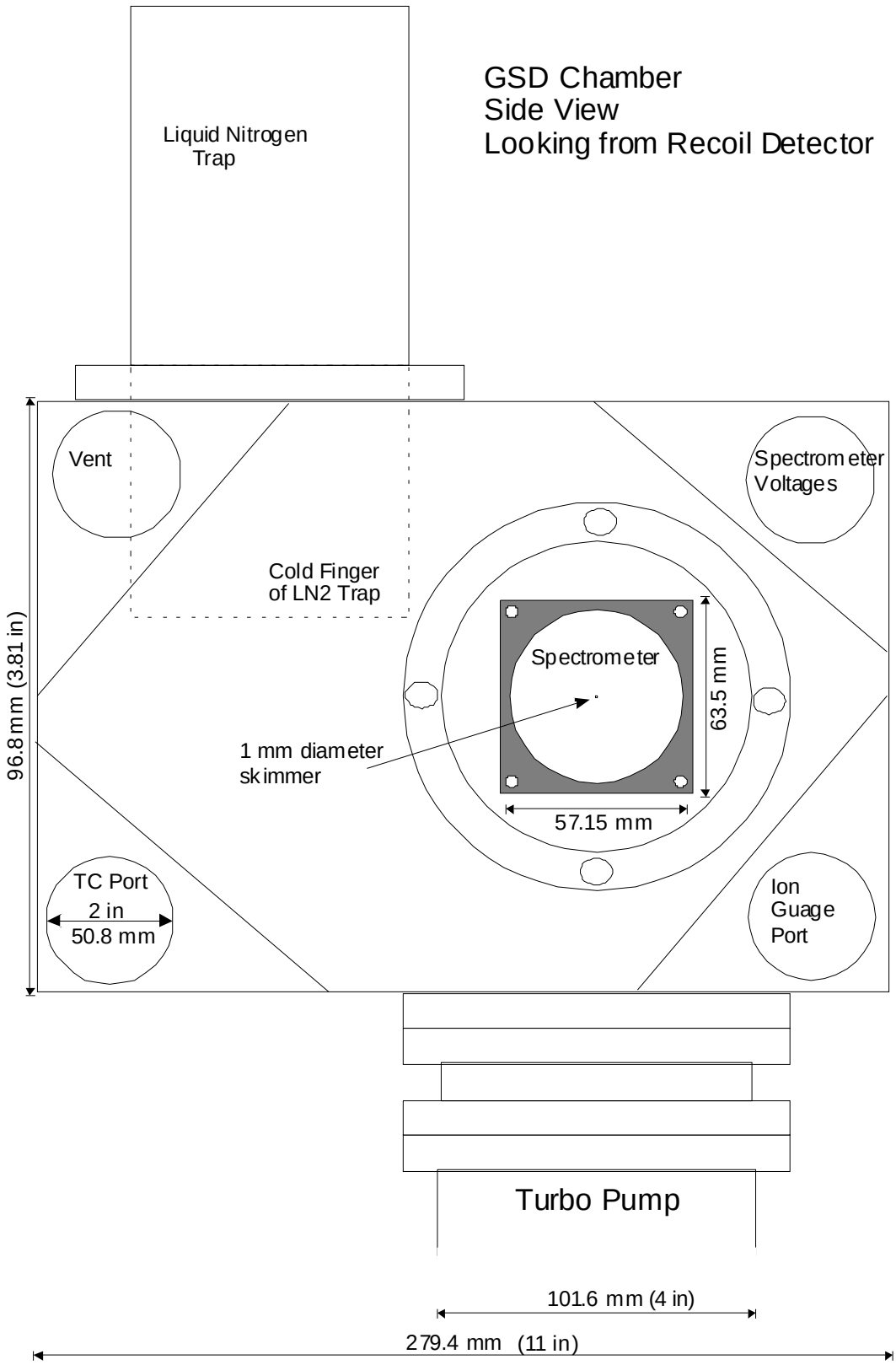

Figure H.4: A diagram of the experimental chamber used for these measurements.

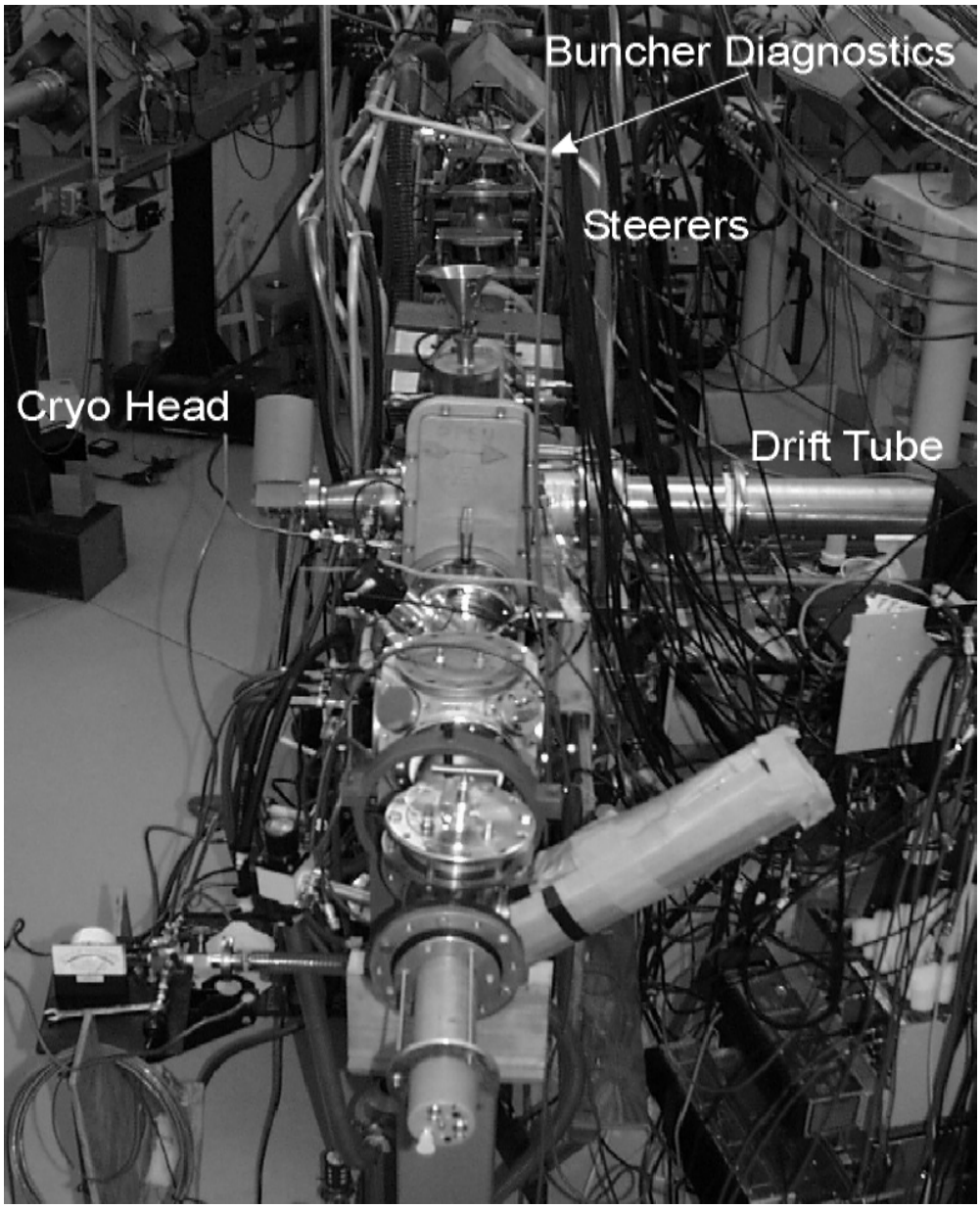

Figure H.5: An end view of L2.

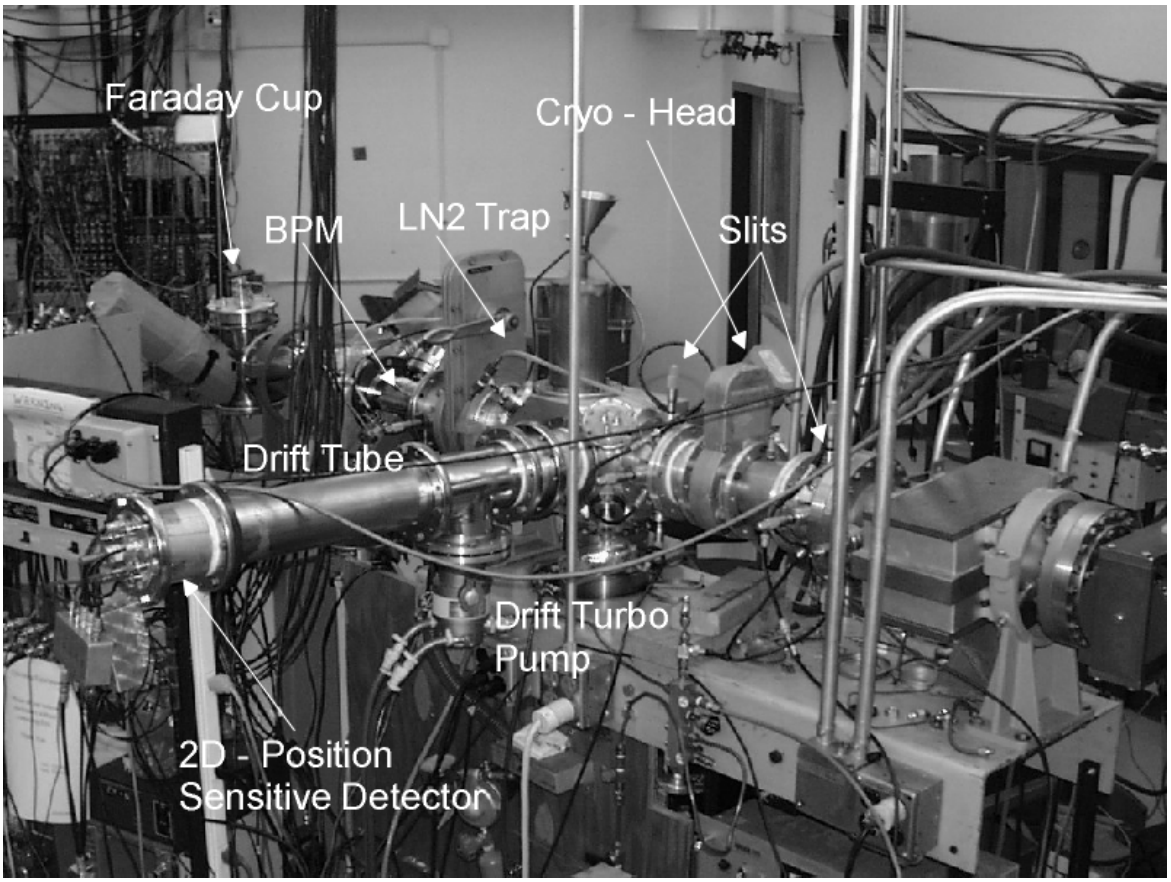

Figure H.6: A closer view of the experiment region on L2. The drift tube and recoil ion detector are in the foreground. The cryo-head is on the opposite side of the beamline.

Appendix I: Data Analysis Code

The XSYS data acquisition system [I.1] is used to process and record the signals sent to the CAMAC electronics (see Appendices C and D). The data is read and stored in a list mode. With this type of storage the experiment can be rerun "offline" with different parameters and sorting conditions since all of the information for each event is stored separately. This appendix includes the XSYS code used to sort the events.

Two files are used for the XSYS sorting. The first file (.com) specifies the histograms and two-dimensional density plots that can be created to store the analyzed data. The second file (.evl) contains the sorting code, specifying the operations to be carried out. The EVAL language used in XSYS is similar to an assembly language, and does operations only on the single variable in the accumulator. The sorting code increments each memory area allocated with the .com file on an event-by-event basis.

The first program, for a coincidence-time-of-flight experiment, is relatively simple. The second program, used for the differential measurements, is more complex. It contains separate blocks for the energy and momentum calculations for each recoil ion species. Doing these calculations in XSYS is somewhat tedious, since XSYS does not support, for example, histograms with negative numbers on the x-axis. This results in lots of shifts to put the zero point of a momentum spectrum, for instance, at the midpoint of the histogram. It would certainly be more elegant to write this part of the program as a

FORTRAN subroutine, and have the XSYS block just be a series of CALL statements. Making a CALL is a slow process, however, and would increase our computational time. The other consideration in keeping the entire program in the XSYS EVAL language is that the sorting program evolved over time, and it was frequently easier to add a block to the XSYS code than it would have been to convert to external sub-routines. If starting from scratch, however, using external subroutines would probably be the best choice.

For the momentum-imaging sorting program, there is a quite lengthy list of parameters that needs to be entered for each voltage. To expedite this process, a file (also a .com file) is created that contains a list of parameters to be used in the sorting program.

Finally, there are three other files that are needed to collect data with the XSYS data acquisition system: USERCONFIG.H, USEREVENTS.H, and USERBEGIN.H. These files are not included and are specific to the electronics and CAMAC crate used for a particular experiment.

The four files included are only examples, and are included as illustrations. The sorting programs were changed many times in the course of the offline analysis to examine particular issues.

The following programs, HDTDC.COM and HDTDC.EVL are for a coincidence-time-of-flight experiment using the LeCroy 4208 TDC.

```
$! HDTDC.COM
$!COM FILE FOR TDC timing
$!'Fragmentation of HD including test for H2 contamination'
$dmem all global file
$amem new 4000 pages
$amem 1  TOF1    16384
$amem 2  TOF2    16384
$amem 5  T21all   2048
$amem 6  COMP  16384
$amem 7  BG       16384
$amem 8  SNG_BG  16384
$amem 9  SINGLES 16384
$amem 10 HDfast              8192
$amem 50 T2T1 256 256
$amem 51 projT1 256
$amem 52 projT2 256
$tdg alloc 11 G2DHD  spec 50
$gate
 new 64
 1 3
 2 3
 5 3
 9 3
$clear flags
$clear all
```

```
C hd.EVL
C EVL FOR TDC (IN TWO-FOLD MULTIHIT MODE)
C And recoil position using Ortec 811.
C includes test for H2 contamination level.
C **************ONLINE DATA ************
C IBI June 1996
C
C          Last updated EW, September 1996
C
OPTION TAPE
!                    Parameters to be set for each run!
!
INTEGER Icomp=2                    ! 2D data compression factor
INTEGER I0=0              ! TOF shift for the compressed 2D spectrum
REAL T3                            ! H2(+) Time-of-Flight
REAL T4                            ! H2O(+) Time-of-Flight
!
INTEGER T21max=900   ! max Tdiff, any event above is truly a single.
!                      it has to be smaller than Tdif to the Edw.
!
REAL a                       ! TOF = a (m/q)**0.5 + T0
REAL T0                            !
INTEGER TF1                  ! Time-of-Flight First ion
INTEGER TF2                  ! Time-of-Flight Second ion
INTEGER ILIM=16384   ! Length of Singles spectrum
INTEGER HILIM=255    ! Length of position spectrum
INTEGER I1                   ! compressed and shifted TOF1
INTEGER I2                   ! compressed and shifted TOF2
INTEGER I2I1                 !for 2D index
INTEGER TF21          ! TF21   = T2 - T1   time difference
INTEGER TF12          ! TF12   = T1 + T2   time sum
!
OPTION ALLSPEC                     ! define all spectra and 2D gates
!
GATE G1D1 Singles 1
GATE G1D2 Singles 2
!
FORMAT ST1 1 16 1
FORMAT ST2 2 16 1
!
EVENT BEGIN
!
TAPE                 !RECORDs Begin
!
LDA T4
SUB T3
DIV 2.82843
STA a
MUL 0.41421
SUB 255
FIX
STA T21s                     ! Time difference shift for H(+) + D(+)
!
LDA T4
MUL 1.41421
STA T0
LDA T3
```

```
MUL 4.2426
SUB T0
DIV 2.82843
STA T0
!
EVENT 1
!
TAPE                !RECORDs all events
!
GET ST1
STA TF1
IF GT ILIM SET TF1=ILIM
INC TF1 TOF1
!
GET ST2
STA TF2
IF GT ILIM SET TF2=ILIM
INC TF2 TOF2
!
IF TF2 EQ 0          ! "singles"
INC TF1 SINGLES                 ! increment single's TOF1 IF TF2=0
GOTO LX                             ! goto next event
ENDIF
!
!          Beyond this point TF2>0 ion-pair events.
!
!TAPE               !RECORD ONLY COINCIDENCE DATA ON TAPE
!
LDA TF2
SUB TF1          !TF21 = tof difference >0
STA TF21
TINC TF21 T21all
IF TF21 GT T21max        ! correction of Edw to singles
INC TF1 SINGLES                 ! increment single's TOF1 IF TF2=0
GOTO LX                             ! goto next event
ENDIF
!
! creating 2D spectra
!
LDA TF1                      !LOAD Y WITH THE 16384 RANGE TIME SIGNAL
SUB I0        ! shift I0
DIV Icomp         ! compress data
STA I1
IF LE 0 GOTO LX
IF GE 255 GOTO LX
LDA TF2                      !LOAD X WITH THE 16384 RANGE TIME SIGNAL
SUB I0        ! shift I0
DIV Icomp         ! compress data
STA I2
IF LE 0 GOTO LX
IF GE 255 GOTO LX
INC I2 I1 T2T1   !INCREMENT COINCIDENCE SPECTRUM  [ 256 X 256 2D spectra ]
STA I2I1
!                            H(+) + D(+) coincidences
IF I2I1 G2DHD
INC TF1 HDfast
INC TF2 HDfast
```

```
ENDIF
!
LX:             ! end of ion-pair analysis
!
EVENT 4                 !QCNT EVENT
HALT            !HALT RUN WHEN PRESET COUNTDOWN TO 0 OCCURS
END
```

The next three programs, RGSD3P.COM, RGSD3P.EVL, and VAR400.COM are the sorting programs for the momentum and energy analysis. The VAR400.COM file is the file containing the variables for the .evl file for an extraction field of 400 volts.

```
$! RGSD3P.COM
$! COM FILE FOR HD GSD experiments - Recoil PSD (resistive anode)
$ DMEM ALL GLOBAL FILE
$ AMEM NEW 35000 PAGES*
$ AMEM  1    TAC1          32768
$ AMEM  2    TAC2          32768
!$ AMEM  3    TAC3         4096
$ AMEM  5    T21all        32768
$ AMEM  7    TAC1H1       32768
$ AMEM  8    RclRate    8192
$ AMEM  9    SINGLES      32768
$ AMEM  11   HETAC        32768
$ AMEM  12   DETAC       32768
$ AMEM  13   HDETAC      32768
$ AMEM  30   RX1        4096
$ AMEM  31   RX2          4096
$ AMEM  32   RY1          4096
$ AMEM  33   RY2          4096
$ AMEM  34   RQSUM       16384
$ AMEM  40   XY       256 256
$ AMEM  41   PROJX    256
$ AMEM  42   PROJY    256
$ AMEM  43   XYGH     256 256
$ AMEM  44   XYGD     256 256
$ AMEM  45   XYGHD    256 256
$ AMEM  46   XYGD2    256 256
$ AMEM  47   XYGBG    256 256
$ AMEM  50   T2T1     256 256
$ AMEM  51   PROJT1   256
$ AMEM  52   PROJT2   256
$ AMEM  60   PXT1     256 256
$ AMEM  61   T1       256
$ AMEM  62   PX       256
$ AMEM  101  HRPZ     256
$ AMEM  102  HRPY     256
$ AMEM  103  HRPX     1024
$ AMEM  104  HRPYZ    256 256
$ AMEM  105  HRPXZ    256 1024
$ AMEM  106  HRPXY    256 1024
$ AMEM  107  PROJPX   1024
$ AMEM  108  PROJPZ   256
$ AMEM  109  PROJPY   256
$ AMEM  110  ENERH    8192
$ AMEM  111  HRPXYvZ  256 256
$ AMEM  112  PHTRAN   128
$ AMEM  113  HEGATE   8192
$ AMEM  120  EHK      8192
```

```
$ AMEM  161  HPZCUT   256
$ AMEM  162  HPYCUT   256
$ AMEM  163  HPXCUT   1024
$ AMEM  201  DRPZ     256
$ AMEM  202  DRPY     256
$ AMEM  203  DRPX     1024
$ AMEM  204  DRPYZ    256 256
$ AMEM  205  DRPXZ    256 1024
$ AMEM  206  DRPXY    256 1024
$ AMEM  210  ENERD    8192
$ AMEM  211  DRPXYvZ  256 256
$ AMEM  212  PDTRAN   128
$ AMEM  213  DEGATE   8192
$ AMEM  220  EDK      8192
$ AMEM  230  EDKshft  8192
$ AMEM  261  DPZCUT   256
$ AMEM  262  DPYCUT   256
$ AMEM  263  DPXCUT   1024
$ AMEM  301  HDRPZ    256
$ AMEM  302  HDRPY    256
$ AMEM  303  HDRPX    1024
$ AMEM  304  HDRPYZ   256 256
$ AMEM  305  HDRPXZ   256 1024
$ AMEM  306  HDRPXY   256 1024
$ AMEM  310  ENERHD   8192
$ AMEM  311  HDRPXYvZ  256 256
$ AMEM  312  PHDTRAN   128
$ AMEM  313  HDEGATE   8192
$ AMEM  320  HDscale   8192
$ AMEM  330  HDshft    8192
$ AMEM  361  HDPZCUT   256
$ AMEM  362  HDPYCUT   256
$ AMEM  363  HDPXCUT   1024
$ AMEM  401  D2RPZ    256
$ AMEM  402  D2RPY    225
$ AMEM  403  D2RPX    1024
$ AMEM  404  D2RPYZ   256 256
$ AMEM  405  D2RPXZ   256 1024
$ AMEM  406  D2RPXY   256 1024
$ AMEM  410  ENERD2   8192
$ AMEM  411  D2RPXYvZ  256 256
$ AMEM  412  PD2TRAN   128
$ AMEM  413  D2EGATE   8192
$ AMEM  451  HDZ      4095
$ AMEM  452  HDY      4095
$ AMEM  461  D2PZCUT   256
$ AMEM  462  D2PYCUT   256
$ AMEM  463  D2PXCUT   1024
$ AMEM  520  hplusd    8192
$ AMEM  901  SCRATCHE  8192
$ AMEM  902  SCRATCH2  8192
$ AMEM  1001 WORK1     256
$ AMEM  1002 WORK2     8192
$ AMEM  1003 WORK3     32768
$ TDG ALLOC 1 RXYgate SPEC 40
$ TDG ALLOC 2 T2T1gate SPEC 50
$ TDG ALLOC 3 center SPEC 45
```

```
$ TDG ALLOC 11 hpz SPEC 104
$ TDG ALLOC 12 hpy SPEC 104
$ TDG ALLOC 13 hpx SPEC 106
$ TDG ALLOC 21 dpz SPEC 204
$ TDG ALLOC 22 dpy SPEC 204
$ TDG ALLOC 23 dpx SPEC 206
$ TDG ALLOC 31 hdpz SPEC 304
$ TDG ALLOC 32 hdpy SPEC 304
$ TDG ALLOC 33 hdpx SPEC 306
$ TDG ALLOC 41 d2pz SPEC 404
$ TDG ALLOC 42 d2py SPEC 404
$ TDG ALLOC 43 d2px SPEC 406
$ GATE
   new 64
 1 5
      2 5
 9 5
 11 5
 12 5
 13 5
 110 1
 210 1
 310 1
 410 1
$ scal new 2
$ scal head 1 "projectile" "recoil"
$ scal box 1 1 2
$ scal clear all
$ CLEAR FLAGS
$ CLEAR ALL
```

```
! RGSD3P.EVL
! .EVL file for HD ground state dissociation experiments with resistive
! anode PSD as the recoil detector.  This program is for use with the
! Phillips ADC, i.e. channels are 2**11 = 4096.  TOF is 2**15 = 32768
! long, to accommodate the possibility of going to a 42-microsecond rep
! rate on the deflector.
!
! NOTE:  Whenever the LeCroy 4208 TDC is used, we must read all 24 bits
! of time data and use software limits to throw away data outside of our
! range of interest.  Reading only the bottom 16 bits allows negative times
! to wrap around and give spurious results.
!
! The program calculates the x y and z momentum of H+, D+, D2+ and HD+ recoils
! and converts this momentum to energy.  The z and y components of the
! velocity are calculated using the full 4096 channel range of the Phillips
! ADC rather than calculating them after the conversion to 256 channel areas.
!
! For the momentum distributions we are adopting the Cocke group axis
! conventions.  X is the TOF direction, Y is the vertical direction, and
! Z is the beam direction.  In the block of the program that reads the position
! we will retain our original notation.  X = beam axis, Y = vertical axis.
!
! Pz and Py are plotted in 256 channel areas.  Px is plotted in 1024 since
! the detector is larger in Px than in Py or Pz.
!
! Ptran refers to the 1d plots of (Pz^2 + Py^2)^.5 These plots are in areas
! 112, 212, 312.  The P(Ek) plots are 110, 210, 310, and 410.
!
! The center gate on the HD recoils (area 45, gate 3) produces full 12-bit
! z and y position distribution on the HD recoils for determining the center
! of the recoil distribution.
!
! Parameters are stored in the var(Vpush).com files. (e.g. var1400.com)
!
!           ************************************
!           *   Last modified: 1/11/2000 ew     *
!           ************************************
!
!                              GENERAL PURPOSE PARAMETERS
!
OPTION TAPE
INTEGER HILIM=65355 ! Overflow limit (2**14)
INTEGER LOLIM=50      ! for defining singles
INTEGER PHILIM=4096 ! Overflow limit (2**12)
INTEGER I255=255         ! length of Position spectra
INTEGER I128 = 128       ! Half of position spectra (for shift)
INTEGER I4096 = 4096    ! 11 bit limit
INTEGER I2048 = 2047   ! Transverse momentum limit
INTEGER I1024 = 1024   ! Z momentum limit
INTEGER I512 = 512       ! half of I1024 (for shift)
INTEGER I8192 = 8192    ! Energy limit
INTEGER Seed=8723645 ! random number seed
INTEGER Seed1=2532
INTEGER Seed2=65756
INTEGER Seed3=919178
REAL dChannel
INTEGER RunTime                    ! Create spectrum of scaler (projectile) counts vs time
```

```
INTEGER Cnts
!
!                                   TIMING PARAMETERS
!
INTEGER TOF1
INTEGER TOF2
INTEGER TOF2raw
INTEGER T1x
INTEGER I1
INTEGER I2
INTEGER I0=2600
INTEGER Icomp=4
INTEGER TXcomp=4
INTEGER ISINGLE=1
INTEGER CNT
INTEGER TOF1OFF=0   ! Offset for Phillips ADC
INTEGER TOF2OFF=0   ! Offset for Phillips ADC
INTEGER TOF3OFF=0   ! Offset for Phillips ADC
INTEGER T1thresh=0      ! T1 threshold
INTEGER T2thresh=0      ! T2 threshold
INTEGER T3thresh=0      ! T3 threshold
INTEGER PRHZ
INTEGER PRDZ
INTEGER PRHDZ
INTEGER PRD2Z
INTEGER PRHX
INTEGER PRDX
INTEGER PRHDX
INTEGER PRD2X
INTEGER PRHY
INTEGER PRDY
INTEGER PRHDY
INTEGER PRD2Y
REAL R2 = 1.0200
REAL T20 = -101.52
REAL TDCH=255.0
REAL dt
REAL dx
REAL dy
REAL dz
REAL dEX
REAL dEY
REAL dEZ
!
!                           RECOIL PSD PARAMETERS
!
REAL X1                             ! X1
REAL X2                             ! X2
REAL Y1                             ! Y1
REAL Y2                             ! Y2
INTEGER Y2D             ! (Y1+Y2)/QSUM
REAL QSUM               ! Recoil sum of all signals
REAL NSUM               ! Normalized sum
REAL ZX1=1.18634        ! X1 offset for Phillips ADC
REAL ZX2=1.41967        ! X2 offset for Phillips ADC
REAL ZY1=1.0985                     ! Y1 offset for Phillips ADC
REAL ZY2=1.75555        ! Y2 offset for Phillips ADC
```

```
REAL GX1=1.01370        ! X1 Gain
REAL GX2=1.02343        ! X2 Gain
REAL GY1=1.0246                 ! Y1 Gain
REAL GY2=1.0            ! Y2 Gain
REAL THRESHX1 = -100            ! X1 Lower THRESHOLD
REAL THRESHX2 = -100            ! X2 Lower THRESHOLD
REAL THRESHY1 = -100            ! Y1 Lower THRESHOLD
REAL THRESHY2 = -100            ! Y2 Lower THRESHOLD
REAL THRESHsm = 150  ! Projectile sum Lower THRESHOLD
REAL X1big = 4095
REAL X2big = 4095
REAL Y1big = 4095
REAL Y2big = 4095
REAL X2DFULL                    ! 12 bit spectra
REAL Y2DFULL                    ! 12 bit spectra


!
!                    Variables for Energy and Momentum Conversion
REAL T0 = -570.529              ! Offset for TOF
REAL TEZY               ! TOF - T0
REAL ZHcen = 1892.8     ! Z (x) Center of recoils on the detector 11 bit
!                       ! (120.1/256)*4096
REAL YHcen = 2128.0     ! Y Center of recoils on the detector 11 bit
REAL ZDcen = 1865.6
REAL YDcen = 2116.9
REAL ZHDcen = 1896.4
REAL YHDcen = 2154.0
REAL ZD2cen = 1926.5
REAL YD2cen = 2185.3
REAL HTMID = 1030.8   ! Middle of H+ TOF peak
REAL HPUSH = 1030.8   ! TOF cutoff for pusher plate
REAL DTMID = 1698.4
REAL DPUSH = 1870.0
REAL HDTMID = 2207.1
REAL HDPUSH = 2304.0
REAL D2TMID = 2645.9
REAL D2PUSH = 3000.0
REAL CONZY = 5.3423e-3          ! = (ch/ns)*(mm/ch)*(0.45710 a.u./(mm/ns))  mm/ch 11 bit
!
!                       ********************************
!                 *  Conversion factors to a.u.  *
!                       *  1 mm/ns = 0.457103 a.u.     *
!                       *  1 a.u. = 2.18769 mm/ns      *
!                       *  1 a.u. = 2.41889 x 10^-17 s *
!                       *  1 a.u. = 5.1 x 10^9 V/cm    *
!                       *  1 a.u. = 27.2116 eV             *
!                       ********************************
!
!
REAL Velx
REAL Vely
REAL Velz
REAL Escale = 27.2116           ! convert to meV from a.u.
REAL MBscale3 = 1.00
REAL MBscale4 = 1.00
REAL MBscale = 1.00
```

```
REAL EKSCALE = 3.00
REAL GAP = 0.0037
REAL GAPchan
REAL EH
REAL ED
REAL EHD
REAL ED2
REAL PHZYMAX = 45.53
REAL PDZYMAX = 64.48
REAL PHDZYMAX = 78.93
REAL PD2ZYMAX = 84.0
REAL PXSQ
REAL PYSQ
REAL PZSQ
REAL PRHZ2
REAL PRDZ2
REAL PRHDZ2
REAL PRD2Z2
REAL Px_min1 = 0.0
REAL Px_min
REAL aprhx                      !H+ x momentum in a.u.
REAL aprhy
REAL aprhz
REAL aprdx
REAL aprdy
REAL aprdz
REAL aprhdx
REAL aprhdy
REAL aprhdz
REAL aprd2x
REAL aprd2y
REAL aprd2z
REAL scaleph = 256.0
REAL phlim = 30.0               ! Max Pz, Py for H+ ions (detector edge/TOF)*M
REAL phlimx = 119.886           ! Max Px for H+ ions       defined by TOF gate
REAL pdlim = 38.0               ! Max Pz, Py for D+ ions
REAL pdlimx = 151.99232                 ! Max Px for D+ ions
REAL phdlim = 50.0              ! Max Pz, Py for HD+ ions
REAL phdlimx = 199.98           ! Max Px for HD+ ions
REAL pd2limx
REAL pd2lim
REAL MassH = 1836.0     ! Mass of recoil ion in a.u.
REAL MassD = 3672.3     ! Mass of recoil ion in a.u.
REAL MassHD = 5509.3  ! Mass of recoil ion in a.u.
REAL MassD2 = 7344.0   ! Mass of recoil ion in a.u.
REAL T_t0
!
!                               SIMION CONVERSION TOF to P FACTORS
REAL hlinterm = -0.23944
REAL linhalf
REAL hsqterm = 1.28756e-4
REAL dlinterm = 0.23951
REAL dsqterm = 9.01903e-5
REAL hdlterm = -0.23918
REAL hdsqterm = 7.60234e-5
REAL d2lterm = -0.23
REAL d2sqterm = 7.0e-5
```

```
!                    Energy factors
REAL EHLIM = 5.238
REAL EDLIM = 5.238
REAL EHDLIM = 5.238
REAL ED2LIM
!
!                    Scaling for troubleshooting.  Should be 1.0 on real sorting
REAL SCALPZ = 1.0
REAL SCALEPY = 1.0
! SORTING

OPTION ALLSPEC                    ! this defines the spectra and 2-d gates
                                  !REAL DATA IS 12 BITS.
FORMAT SX1 1 12 1
FORMAT SX2 2 12 1
FORMAT SY1 3 12 1
FORMAT SY2 4 12 1
!FORMAT ST1 5 24 1 $LONG
FORMAT ST1 5 16 1
FORMAT ST2 6 16 1
!FORMAT ST2 6 24 1 $LONG
!FORMAT RATEp1 1 24 1 $LONG
!FORMAT RATEr1 2 24 1 $LONG
!
Gate TOF1G TAC1 1
Gate TOF2G TAC1 2
Gate TOF3G TAC1 3
Gate TOF4G TAC1 4
Gate TOF5G TAC1 5
Gate EH1G  ENERH 1
Gate ED1G  ENERD 1
Gate EHD1G ENERHD 1
Gate ED21G ENERD2 1
!
EVENT BEGIN
TAPE
SET CNT=ISINGLE
SET RunTime=0
!
EVENT 2
!
!                    ****************************************
!                    *                Timing                *
!                    ****************************************
!
GET ST1                           ! Get TAC1 signal
STA TOF1
TINC TAC1                 ! Increment the time amplitude spectrum
TAPE                      ! record all events with valid TOF1
!
GET ST2                           ! Get TAC2 signal
SUB TOF2OFF               ! Subtract offset for Phillips ADC
!IF LE T2thresh GOTO L2           ! Skip Ion-Pair if Less than threshold
STA TOF2raw
IF LT LOLIM               ! Singles are defined as TOF2=0
INC TOF1 SINGLES
!IF LE T2thresh GOTO L2  ! Skip Ion-Pair if Less than threshold
```

```
!DEC CNT
!IF CNT EQ 0
!TAPE
!SET CNT=ISINGLE
!ENDIF
GOTO L2:
ENDIF
!
!                    ************************************
!                    *                Ion-Pairs         *
!                    ************************************
!
RAN(Seed)
ADD TOF2raw
!SUB HILIM
!CHS
MUL R2
ADD T20
FIX
STA TOF2
TINC TAC2                ! Increment the time amplitude spectrum
!
SUB TOF1
STA TF21                 ! Time-of-flight difference
TINC TF21 T21all         ! unconditional time difference spectrum
!
!
!          Creating ion-pair 2D spectra
!
LDA TOF1
SUB I0
DIV Icomp
STA I1
IF LE 0 GOTO L2:
IF GE I255 GOTO L2:
!
LDA TOF2
SUB I0
DIV Icomp
STA I2
IF LE 0 GOTO L2:
IF GE I255 GOTO L2:
TINC I2 I1 T2T1
STA I2I1
!
L2:                  ! end of ion-pair analysis
!
!                         ************************************
!                         *       Recoil Position            *
!                 *     Resistive Anode PSD       *
!                         ************************************
RAN (Seed)
STA dX
GET SX1                  ! Get X1 PSD signal
FLOAT
ADD dX
SUB ZX1
```

```
MUL GX1
IF GE PHILIM EXIT       ! Exit if it is an overflow
IF GE X1big GOTO L3     ! Exit if above upper threshold
IF LE THRESHX1 GOTO L3        ! Exit if less than lower threshold
STA X1
FIX                     ! Store as real variable
TINC RX1                ! Increment raw X1 spectrum
!
RAN (Seed)
STA dX
GET SX2                 ! Get X2 PSD signal
FLOAT
ADD dX
SUB ZX2
MUL GX2
IF GE PHILIM EXIT       ! Exit if it is an overflow
IF GE X2big GOTO L3     ! Exit if above upper limit
IF LE THRESHX2 GOTO L3        ! Exit if less than lower threshold
STA X2                  ! Store as real variable
FIX
TINC RX2                ! Increment raw X2 spectrum
!
RAN (Seed)
STA dX
GET SY1                 ! Get Y1 PSD signal
FLOAT
ADD dX
SUB ZY1
MUL GY1
IF GE PHILIM EXIT       ! Exit if it is an overflow
IF GE Y1big GOTO L3     ! Exit if above upper threshold
IF LE THRESHY1 GOTO L3        ! Exit if less than lower threshold
STA Y1                  ! Store as real variable
FIX
TINC RY1                ! Increment raw Y1 spectrum
!
RAN (Seed)
STA dX
GET SY2                 ! Get Y2 PSD signal
FLOAT
ADD dX
SUB ZY2
MUL GY2
IF GE PHILIM EXIT       ! Exit if it is an overflow
IF GE Y2big GOTO L3     ! Exit if above upper threshold
IF LE THRESHY2 GOTO L3        ! Exit if less than lower threshold
STA Y2                  ! Store as integer variable
FIX
TINC RY2                ! Increment raw Y2 spectrum
!
LDA X1
ADD X2
ADD Y1
ADD Y2
STA QSUM                ! Resistive anode PSD charge signal
FIX
TINC RQSUM
```

```
IF LE THRESHsm GOTO L3          ! Exit if less than lower threshold
IF QSUM EQ 0. EXIT       ! prevent divide by zero
!
LDA Y1
ADD X2
DIV QSUM
STA Y2Dfull              ! Store for 11 bit position later
MUL I255
FIX
STA Y2D                          ! Projectile Y coordinate
!
LDA Y1
ADD X1
DIV QSUM
STA X2Dfull              ! Store for 11 bit position later
MUL I255
FIX
STA X2D                          ! Projectile X coordinate
!
TINC X2D Y2D XY          ! Increment 2D Recoil position spectrum
!
!                        *  End of Unconditional Position Spectrum *
!-----------------------------------------------------------------------
!                        *  Create Position gated on TOF      *
STA PXPY
!                        Gated 2D Position Spectra
IF TOF1 TOF1G TINC X2D Y2D XYGH    ! recoil 2D for gate 1 (H+) TOF1
IF TOF1 TOF2G TINC X2D Y2D XYGD    ! recoil 2D for gate 2 (D+) TOF1
IF TOF1 TOF3G TINC X2D Y2D XYGHD   ! recoil 2D for gate 3 (HD+) TOF1
IF TOF1 TOF4G TINC X2D Y2D XYGD2   ! recoil 2D for gate 4 (D2+) TOF1
IF TOF1 TOF5G TINC X2D Y2D XYGBG   ! recoil 2D for gate 5 (BG) TOF1
!
!-----------------------------------------------------------------------
IF PXPY RXYgate TINC TOF1 TAC1H1  ! TOF of first recoil in coinc with Gate
!                          in XY
!-----------------------------------------------------------------------
!
!
!                        Creating Proj_X-TOF1 2D spectra
!
LDA TOF1
SUB I0
DIV TXcomp
FIX
STA T1x
TINC X2D T1x PXT1
STA PX2DI1
!
L3:
IF PXPY RXYgate          !  If recoil is in big gate in area 40 (excludes
!                           detector edge)
!-----------------------------------------------------------------------
!
!              ********************************************
!              *  Creating Momentum Spectra of fragments  *
!              ********************************************
!
```

```
!----------------------Proton Block-------------Proton Block---------------
!
IF TOF1 TOF1G           ! IF particle is H+ fragment
        Ran(seed)       ! Random number to prevent beats
        STA dt
        ADD TOF1        ! Get time of flight
        SUB T0          ! Subtract t0
        STA TEZY        ! Store TOF for Vx and Vy calculation
!
!                       Find Vz (beam)

        LDA X2Dfull     ! Get x position (changing to z notation)
        MUL I4096       ! Convert to 11 bit
        STA Zbig        ! STA 11 bit z position
        RAN(seed1)      ! Random number to prevent beats
        STA dx
        ADD Zbig        !Load X position in accumulator
        SUB ZHcen       !Calculate distance from center of recoils
        DIV TEZY        ! divide by TOF to get velocity
        MUL CONZY       ! multiply by a conversion factor
        STA Velz        ! Store X component of recoil velocity squared
        MUL MassH       ! Multiply by H mass
        MUL SCALPZ
        DIV phlim     ! divide by hilim
        STA aprhz       ! store momentum in a.u. as real variable (% of phlim)
        MUL I255        ! Scale
        ADD I128
        FIX
        STA PRHZ
        TINC HRPZ

!
!                       Find Vy (vertical)

        LDA Y2Dfull     ! Get x position (changing to z notation)
        MUL I4096       ! Convert to 11 bit
        STA Ybig        ! STA 11 bit z position
        RAN(seed2)      ! Random number to prevent beats
        STA dy
        ADD Ybig                ! Load Y position in accumulator
        SUB YHcen       ! Calculate distance from center of recoils
        DIV TEZY        ! divide by TOF to get velocity
        MUL CONZY       ! multiply by a conversion factor
        STA Vely        ! Store Y component of recoil velocity squared
        MUL massH       ! Multiply by mass of H to get momentum
        MUL SCALEPY
        DIV phlim
        STA aprhy
        MUL I255        ! Scale to fit 256 area
        ADD I128        ! shift center to 128
        FIX
        STA PRHY
        TINC HRPY       ! Incriment Py 1-d spectrum
!
!               Calculating Transverse momentum for H+
        LDA aPRHZ       ! Get Pz
        MUL phlim
```

```
        MUL             ! Square
        STA PRHZ2       ! Store Pz
        LDA aPRHY       ! Get Py
        MUL phlim
        MUL             ! Square
        ADD PRHZ2       ! Add Pz^2
        SQRT            ! Square root
        DIV PHZYMAX ! divide by max (in a.u.)
        MUL I128        ! Scale
        FIX
        STA HPTRAN
        TINC PHTRAN
!
!
!                       Find Vx  (TOF)
        IF TOF1 LE HPUSH        ! Only take particles toward the detector
         RAN(seed3)     ! Random fraction to prevent beats
         ADD TOF1       ! Load TOF1 in accumulator
         SUB HTMID      ! Find difference between TOF1 and center of TOF peak
         STA T_t0
         MUL hlinterm   ! Multiply by SIMION conversion factor
         STA linhalf    ! Store
         LDA T_t0       ! Get differnce between TEXY and Pz = 0
         MUL            ! Square
         MUL hsqterm    ! Multiply by SIMION conversion factor
         ADD linhalf    ! Add linear part of 2nd order polynomial
         DIV phlimx     ! Divide by momentum limit
         STA aprhx
         MUL I1024      ! Scale
         ADD I512       ! SHIFT 0 to channel 512
         FIX
         STA PRHX       ! Store
         TINC PRHX HRPX         ! Incriment Pz 1-d spectrum
!
!               Create 2D Momentum spectra
!
                TINC PRHZ PRHY HRPYZ            ! Pxy 2-d
                STA HRPZY
                TINC PRHZ PRHX          HRPXZ ! Pxz 2-d
                STA HRPZX
                TINC PRHY PRHX HRPXY            ! Pyz 2-d
                STA HRPYX
!
!               Create Momentum slices from 2D gates
                IF HRPZY HPZ TINC PRHZ HPZCUT
                IF HRPZY HPY TINC PRHY HPYCUT
                IF HRPYX HPX TINC PRHX HPXCUT
!
!               Create pzpy vs. px
!
                LDA PRHZ
                SUB I128
                MUL
                STA PRHZsq
                LDA PRHY
                SUB I128
                MUL
```

```
                ADD PRHZsq
                SQRT
                FIX
                STA PHdet
                LDA PRHX
                DIV 4.0
                FIX
                STA PHtof
                TINC PHdet PHtof HRPXYvZ
                STA HRPYXvZ
!
!           ****************************
!           *     Create Energy Spectrum *
!           ****************************
!
        IF aPRHx GE Px_min1
                LDA aPRHZ
                MUL phlim
                MUL
                STA PZSQ
!
                LDA aPRHY
                MUL phlim
                MUL
                STA PYSQ
!
                LDA aPRHX
                MUL phlimx
                MUL
                STA PXSQ
!
                LDA PXSQ
                ADD PYSQ
                ADD PZSQ
                DIV 2.0
                DIV MassH
                MUL ESCALE
                DIV EHLIM
                MUL I8192
                STA EH
                FIX
                TINC ENERH
                LDA EH
                MUL 1.5
                FIX
                TINC EHK
                TINC hplusd
          ENDIF
        ENDIF
        IF EH EH1G TINC TOF1 HETAC
ENDIF
!
!----------------End Proton Block------------End Proton Block--------------
!
!----------------Begin D+ Block--------------Begin D+ Block----------------
!
IF TOF1 TOF2G           ! IF particle is H+ fragment
```

```
        Ran(seed)       ! Random number to prevent beats
        STA dt
        ADD TOF1        ! Get time of flight
        SUB T0          ! Subtract t0
        STA TEZY        ! Store TOF for Vx and Vy calculation
!
!                       Find Vz  (BEAM)
!
        LDA X2Dfull     ! Get x position (changing to z notation)
        MUL I4096       ! Convert to 11 bit
        STA Zbig        ! STA 11 bit z position
        RAN(seed1)      ! Random number to prevent beats
        STA dx
        ADD Zbig        !Load X position in accumulator
        SUB ZDcen       !Calculate distance from center of recoils
        DIV TEZY        ! divide by TOF to get velocity
        MUL CONZY       ! multiply by a conversion factor
        STA Velz        ! Store X component of recoil velocity squared
        MUL MassD       ! Multiply by D mass
        MUL SCALPZ
        DIV pdlim     ! divide by hilim
        STA aPRDZ
        MUL I255        ! Scale
        ADD I128
        FIX
        STA PRDZ
        TINC DRPZ

!
!                       Find Vy (vertical)

        LDA Y2Dfull     ! Get x position (changing to z notation)
        MUL I4096       ! Convert to 11 bit
        STA Ybig        ! STA 11 bit z position
        RAN(seed2)      ! Random number to prevent beats
        STA dy
        ADD Ybig                ! Load Y position in accumulator
        SUB YDcen       ! Calculate distance from center of recoils
        DIV TEZY        ! divide by TOF to get velocity
        MUL CONZY       ! multiply by a conversion factor
        STA Vely        ! Store Y component of recoil velocity squared
        MUL massD       ! Multiply by mass of D to get momentum
        MUL SCALEPY
        DIV pdlim
        STA aPRDY
        MUL I255        ! Scale to fit 256 area
        ADD I128        ! shift center to 128
        FIX
        STA PRDY
        TINC DRPY       ! Incriment Py 1-d spectrum
!
!
!               Calculating Transverse momentum for D+
        LDA aPRDZ       ! Get Pz
        MUL pdlim       ! get in a.u.
        MUL             ! Square
        STA PRDZ2       ! Store Pz
```

```
        LDA aPRDY       ! Get Py
        FLOAT
        MUL pdlim       ! get in a.u.
        MUL             ! Square
        ADD PRDZ2       ! Add Pz^2
        SQRT            ! Square root
        DIV PDZYMAX ! divide by max (in a.u.)
        MUL I128        ! Scale
        FIX
        STA DPTRAN
        TINC PDTRAN
!
!                       Find Vx  (TOF)
        IF TOF1 LE DPUSH        ! Only take particles toward the detector
         RAN(seed3)
         ADD TOF1       ! Load TOF1 in accumulator
         SUB DTMID      ! Find difference between TOF1 and center of TOF peak
         STA T_t0
         MUL dlinterm   ! Multiply by SIMION conversion factor
         STA linhalf    ! Store
         LDA T_t0       ! Get differnce between TEXY and Pz = 0
         MUL            ! Square
         MUL dsqterm    ! Multiply by SIMION conversion factor
         ADD linhalf    ! Add linear part of 2nd order polynomial
         DIV pdlimx     ! Divide by momentum limit
         STA aPRDX
         MUL I1024      ! Scale
         ADD I512       ! SHIFT 0 to channel 512
         FIX
         STA PRDX       ! Store
         TINC PRDX DRPX         ! Incriment Pz 1-d spectrum
!
!               Create 2D Momentum spectra
!
                TINC PRDZ PRDY DRPYZ            ! Pxy 2-d
                STA DRPZY
                TINC PRDZ PRDX          DRPXZ ! Pxz 2-d
                STA DRPZX
                TINC PRDY PRDX DRPXY            ! Pyz 2-d
                STA DRPYX
!
!               Create Momentum slices from 2D gates
                IF DRPZY DPZ TINC PRDZ DPZCUT
                IF DRPZY DPY TINC PRDY DPYCUT
                IF DRPYX DPX TINC PRDX DPXCUT
!
!               Create pzpy vs. px
!
                LDA PRDZ
                SUB I128
                MUL
                STA PRDZsq
                LDA PRDY
                SUB I128
                MUL
                ADD PRDZsq
                SQRT
```

```
                FIX
                STA PDdet
                LDA PRDX
                DIV 4.0
                FIX
                STA PDtof
                TINC PDdet PDtof DRPXYvZ
                STA DRPYXvZ
!
!           ****************************
!           *     Create Energy Spectrum *
!           ****************************
!
        LDA Px_min1
        Mul 1.4142              ! scaling minimum momentum by mass ratio
        STA Px_min
        IF aPRDx GE Px_min
                LDA aPRDZ
                MUL pdlim
                MUL
                STA PZSQ
!
                LDA aPRDY
                MUL pdlim
                MUL
                STA PYSQ
!
                LDA aPRDX
                MUL pdlimx
                MUL
                STA PXSQ
!
                LDA PXSQ
                ADD PYSQ
                ADD PZSQ
                DIV 2.0
                DIV MassD
                MUL ESCALE
                DIV EDLIM
                MUL I8192
                STA ED
                FIX
                TINC ENERD
                LDA ED                          ! Scaling to Ek
                MUL 3.0
                FIX
                TINC EDK
!
                LDA GAP                         ! = 0.0037 eV
                DIV EDLIM
                MUL I8192               ! getting 3.7 meV into channels
                STA GAPchan
                LDA ED                          ! Get ED
                MUL 3.0                         ! scale to Ek
                ADD GAPchan             ! add 3.7 meV in channels
                STA shiftED
                FIX
```

```
                TINC EDKshft
                TINC hplusd                 ! add to total P(Ek)
          ENDIF
        ENDIF
        IF ED ED1G TINC TOF1 DETAC
ENDIF
!
!-------------------------End D+ Block-------------End D+ Block--------------
!
!---------------------Begin HD+ block-----------Begin HD+ block--------------
!
IF TOF1 TOF3G           ! IF particle is H+ fragment
        Ran(seed)       ! Random number to prevent beats
        STA dt
        ADD TOF1        ! Get time of flight
        SUB T0          ! Subtract t0
        STA TEZY        ! Store TOF for Vx and Vy calculation
!
!
!               Find Vz  (BEAM)
!
        LDA X2Dfull     ! Get x position (changing to z notation)
        MUL I4096       ! Convert to 11 bit
        STA Zbig        ! STA 11 bit z position
        RAN(seed1)      ! Random number to prevent beats
        STA dx
        ADD Zbig        !Load X position in accumulator
        SUB ZHDcen      !Calculate distance from center of recoils
        DIV TEZY        ! divide by TOF to get velocity
        MUL CONZY       ! multiply by a conversion factor
        STA Velz        ! Store X component of recoil velocity squared
        MUL MassHD      ! Multiply by HD mass
        MUL SCALPZ
        DIV phdlim      ! divide by hilim
        STA aPRHDZ
        MUL MBscale3    ! scale by (mh2/mhd)^.5 for H2 subtraction
!                       ! SET MBscale32 = 1.0 for energy analysis
        MUL I255        ! Scale
        ADD I128
        FIX
        STA PRHDZ
        TINC HDRPZ

!
!                       Find Vy (vertical)

        LDA Y2Dfull     ! Get x position (changing to z notation)
        MUL I4096       ! Convert to 11 bit
        STA Ybig        ! STA 11 bit z position
        RAN(seed2)      ! Random number to prevent beats
        STA dy
        ADD Ybig                ! Load Y position in accumulator
        SUB YHDcen      ! Calculate distance from center of recoils
        DIV TEZY        ! divide by TOF to get velocity
        MUL CONZY       ! multiply by a conversion factor
        STA Vely        ! Store Y component of recoil velocity squared
        MUL massHD      ! Multiply by mass of HD to get momentum
```

```
        MUL SCALEPY
        DIV phdlim
        STA aPRHDY
        MUL MBscale3  ! multiply by (mh2/mhd)^.5 for h2 subtraction
!                     ! SET MBscale32 = 1.0 for energy analysis
        MUL I255      ! Scale to fit 256 area
        ADD I128      ! shift center to 128
        FIX
        STA PRHDY
        TINC HDRPY    ! Incriment Py 1-d spectrum
!
!!
!               Calculating Transverse momentum for HD+
        LDA aPRHDZ    ! Get Pz
        MUL phdlim    ! get in a.u.
        MUL           ! Square
        STA PRHDZ2    ! Store Pz
        LDA aPRHDY    ! Get Py
        FLOAT
        MUL phdlim    ! get in a.u.
        MUL           ! Square
        ADD PRHDZ2    ! Add Pz^2
        SQRT          ! Square root
        DIV PHDZYMAX          ! divide by max (in a.u.)
        MUL I128      ! Scale
        FIX
        STA HDPTRAN
        TINC PHDTRAN
!
!
!                     Find Vx  (TOF)
        IF TOF1 LE HDPUSH     ! Only take particles toward the detector
         RAN(seed3)
         ADD TOF1     ! Load TOF1 in accumulator
         SUB HDTMID   ! Find difference between TOF1 and center of TOF peak
         STA T_t0
         MUL hdlterm  ! Multiply by SIMION conversion factor
         STA linhalf  ! Store
         LDA T_t0     ! Get differnce between TEXY and Pz = 0
         MUL          ! Square
         MUL hdsqterm ! Multiply by SIMION conversion factor
         ADD linhalf  ! Add linear part of 2nd order polynomial
         DIV phdlimx  ! Divide by momentum limit
         STA aPRHDX
         MUL I1024    ! Scale
         ADD I512     ! SHIFT 0 to channel 512
         FIX
         STA PRHDX    ! Store
         TINC PRHDX HDRPX   ! Incriment Pz 1-d spectrum
!
!               Create 2D Momentum spectra
!
                TINC PRHDZ PRHDY HDRPYZ   ! Pxy 2-d
                STA HDRPZY
                TINC PRHDZ PRHDX HDRPXZ   ! Pxz 2-d
                STA HDRPZX
                TINC PRHDY PRHDX HDRPXY   ! Pyz 2-d
```

```
                STA HDRPYX
!
!               Create Momentum slices from 2D gates
                IF HDRPZY HDPZ TINC PRHDZ HDPZCUT
                IF HDRPZY HDPY TINC PRHDY HDPYCUT
                IF HDRPYX HDPX TINC PRHDX HDPXCUT
!
!               Create pzpy vs. px
!
                LDA PRHDZ
                SUB I128
                MUL
                STA PRHDZsq
                LDA PRHDY
                SUB I128
                MUL
                ADD PRHDZsq
                SQRT
                FIX
                STA PHDdet
                LDA PRHDX
                DIV 4.0
                FIX
                STA PHDtof
                TINC PHDdet PHDtof HDRPXYvZ
                STA HDRPYXvZ
!
!           ****************************
!           *   Create Energy Spectrum *
!           ****************************
!
        LDA Px_min1
        Mul 1.7321              ! scaling minimum momentum by mass ratio
        STA Px_min
        IF aPRHDx GE Px_min
                LDA aPRHDZ
                MUL phdlim
                MUL
                STA PZSQ
!
                LDA aPRHDY
                MUL phdlim
                MUL
                STA PYSQ
!
                LDA aPRHDX
                MUL phdlimx
                MUL
                STA PXSQ
!
                LDA PXSQ
                ADD PYSQ
                ADD PZSQ
                DIV 2.0
                DIV MassHD
                MUL ESCALE
                DIV EHDLIM
```

```
                MUL I8192
                STA EHD
                FIX
                TINC ENERHD
!
                LDA EHD                 ! Creating scaled HD for use for
                MUL Ekscale     ! subtracting the H2 from m/q=2 P(Ek)
                FIX             ! i.e. Spectrum EDK - SCRATCHE = D+ P(Ek)
                TINC HDscale
!
                LDA GAP                 ! shifting HD to use as H2 subtraction
                DIV EHDlim
                MUL I8192       ! create 3.7 meV in channels
                STA GAPchan
                LDA EHD
                MUL Ekscale
                ADD GAPchan
                FIX
                TINC HDshft     ! shifted, scaled HD for use as H2 subtraction
        ENDIF
      ENDIF
      IF EHD EHD1G TINC TOF1 HETAC
!
      LDA TOF1
      IF TOF1 TOF3G
                IF PXPY center
                        LDA Zbig
                        TINC HDZ
                        LDA Ybig
                        TINC HDY
                ENDIF
      ENDIF
ENDIF
!
!----------------------------End HD+ Block---------------End HD+ Block-------
!
!---------------------------Begin D2+ Block---------------------------------
!
IF TOF1 TOF4G           ! IF particle is D2+ fragment
      Ran(seed)         ! Random number to prevent beats
      STA dt
      ADD TOF1          ! Get time of flight
      SUB T0            ! Subtract t0
      STA TEZY          ! Store TOF for Vx and Vy calculation
!
!
!               Find Vz  (BEAM)
!
      LDA X2Dfull       ! Get x position (changing to z notation)
      MUL I4096         ! Convert to 12 bit
      STA Zbig          ! STA 12 bit z position
      RAN(seed1)        ! Random number to prevent beats
      STA dx
      ADD Zbig          !Load X position in accumulator
      SUB ZD2cen        !Calculate distance from center of recoils
      DIV TEZY          ! divide by TOF to get velocity
      MUL CONZY         ! multiply by a conversion factor
```

```
        STA Velz        ! Store X component of recoil velocity squared
        MUL MassD2      ! Multiply by D2 mass
        MUL SCALPZ
        DIV pd2lim      ! divide by hilim
        STA aPRD2Z
        MUL MBscale4    ! Scale check, set MBscale42 = 1.0 for energy analysis
        MUL I255        ! Scale
        ADD I128
        FIX
        STA PRD2Z
        TINC D2RPZ

!
!                       Find Vy (vertical)

        LDA Y2Dfull     ! Get x position (changing to z notation)
        MUL I4096       ! Convert to 11 bit
        STA Ybig        ! STA 11 bit z position
        RAN(seed2)      ! Random number to prevent beats
        STA dy
        ADD Ybig                ! Load Y position in accumulator
        SUB YD2cen      ! Calculate distance from center of recoils
        DIV TEZY        ! divide by TOF to get velocity
        MUL CONZY       ! multiply by a conversion factor
        STA Vely        ! Store Y component of recoil velocity squared
        MUL massD2      ! Multiply by mass of HD to get momentum
        MUL SCALEPY
        DIV pd2lim
        STA aPRD2Y
        MUL MBscale4    ! scale check, set MBscale42 = 1.0 for energy analysis
        MUL I255        ! Scale to fit 256 area
        ADD I128        ! shift center to 128
        FIX
        STA PRD2Y
        TINC D2RPY      ! Incriment Py 1-d spectrum
!
!!
!               Calculating Transverse momentum for D2+
        LDA aPRD2Z      ! Get Pz
        MUL pd2lim      ! get in a.u.
        MUL             ! Square
        STA PRd2Z2      ! Store Pz
        LDA aPRD2Y      ! Get Py
        FLOAT
        MUL pd2lim      ! get in a.u.
        MUL             ! Square
        ADD PRD2Z2      ! Add Pz^2
        SQRT            ! Square root
        DIV PD2ZYMAX            ! divide by max (in a.u.)
        MUL I128        ! Scale
        FIX
        STA D2PTRAN
        TINC PD2TRAN
!
!
!                       Find Vx  (TOF)
        IF TOF1 LE D2PUSH       ! Only take particles toward the detector
```

```
        RAN(seed3)
        ADD TOF1       ! Load TOF1 in accumulator
        SUB D2TMID     ! Find difference between TOF1 and center of TOF peak
        STA T_t0
        MUL d2lterm    ! Multiply by SIMION conversion factor
        STA linhalf    ! Store
        LDA T_t0       ! Get differnce between TEXY and Pz = 0
        MUL            ! Square
        MUL d2sqterm   ! Multiply by SIMION conversion factor
        ADD linhalf    ! Add linear part of 2nd order polynomial
        DIV pd2limx    ! Divide by momentum limit
        STA aPRD2X
        MUL I1024      ! Scale
        ADD I512       ! SHIFT 0 to channel 512
        FIX
        STA PRD2X      ! Store
        TINC PRD2X D2RPX    ! Incriment Pz 1-d spectrum
!
!               Create 2D Momentum spectra
!
                TINC PRD2Z PRD2Y D2RPYZ     ! Pxy 2-d
                STA D2RPZY
                TINC PRD2Z PRD2X D2RPXZ     ! Pxz 2-d
                STA D2RPZX
                TINC PRD2Y PRD2X D2RPXY     ! Pyz 2-d
                STA D2RPYX
!
!               Create Momentum slices from 2D gates
                IF D2RPZY D2PZ TINC PRD2Z D2PZCUT
                IF D2RPZY D2PY TINC PRD2Y D2PYCUT
                IF D2RPYX D2PX TINC PRD2X D2PXCUT
!
!               Create pzpy vs. px
!
                LDA PRD2Z
                SUB I128
                MUL
                STA PRD2Zsq
                LDA PRD2Y
                SUB I128
                MUL
                ADD PRD2Zsq
                SQRT
                FIX
                STA PD2det
                LDA PRD2X
                DIV 4.0
                FIX
                STA PD2tof
                TINC PD2det PD2tof D2RPXYvZ
                STA D2RPYXvZ
!
!           ****************************
!           *     Create Energy Spectrum *
!           ****************************
!
        LDA Px_min1
```

```
        Mul 2.0          ! scaling minimum momentum by mass ratio
        STA Px_min
        IF aPRD2x GE Px_min
                LDA aPRD2Z
                MUL pd2lim
                MUL
                STA PZSQ
!
                LDA aPRD2Y
                MUL pD2lim
                MUL
                STA PYSQ
!
                LDA aPRD2X
                MUL pd2limx
                MUL
                STA PXSQ
!
                LDA PXSQ
                ADD PYSQ
                ADD PZSQ
                DIV 2.0
                DIV MassD2
                MUL ESCALE
                DIV ED2LIM
                MUL I8192
                STA ED2
                FIX
                TINC ENERD2
          ENDIF
        ENDIF
ENDIF
!-------------------------------END D2+ Block-----------------------------
!
ENDIF
END
```

```
! var400.com
!  .COM file for RGSD3PC.EVL variables
! This file contains TOF --> Px parameters for
! Vpush = 400 volts, Vfocus = 332 volts
!
! Last modified EW 1-22-00
!
$param R2 = 1.0200
$param T20 = 522.3
$param Icomp = 10
$param I0 = 3800.0
$param threshsm = 150                ! Position thresholds
$param threshx1 = -1
$param threshx2 = -1
$param threshy1 = -1
$param threshy2 = -1
$param x1big = 3380.0
$param x2big = 3373.0
$param y1big = 4094.0
$param y2big = 4020.0
$param zx1 = 1.18634                 ! ADC offsets for position signals
$param zx2 = 1.41967
$param zy1 = 1.0985
$param zy2 = 1.7555
$param gx1 = 1.00            ! Position gain calibration
$param gx2 = 1.00
$param gy1 = 1.12
$param gy2 = 1.0
$param T0 = -231.45
! a = 3760.43
$param ZHCen = 1873.37               ! H+ 12 bit jet center
$param YHcen = 2131.6096             ! H+ 12 bit jet center
$param ZDcen = 1866.345              ! D+/H2+
$param YDcen = 2122.86               ! D+/H2+
$param ZHDcen = 1896.1107            ! HD+
$param YHDcen = 2172.12096           ! HD+
$param ZD2cen = 1931.1848            ! D2+
$param YD2cen = 2182.9686            ! D2+
$param HTMID = 3517.967                      ! middle of H+ TOF peak (channels)
$param HPUSH =          3674.0               ! upper limit for H+ peak (pusher wall)
$param DTMID =          5076.46              ! middle of D+ TOF peak
$param DPUSH =          5212.0               ! upper limit for D+ peak
$param HDTMID =         6274.728             ! middle of HD+ TOF peak
$param HDPUSH =         6542.0               ! upper limit for HD+ peak
$param D2TMID = 7284.757             ! middle of D2+ peak
$param D2PUSH = 7419.0
$param CONZY = 5.571e-3              !converts channels to a.u. momentum zy direction
$param Escale = 27211.6              ! scales energy to meV
$param scaleph = 256.0               ! division factor for momentum plots
$param phlim =   16.0                ! zy limit of momentum for H+ fragments
$param phlimx =  28.0                ! x limit of momentum for H+ fragments
$param pdlim =   16.0                ! zy limit of momentum for D+ fragments
$param pdlimx =  28.0                ! x limit of momentum for D+ fragments
$param phdlim =  16.0                ! zy limit of momentum for HD+ fragments
$param phdlimx = 28.0
$param pd2lim = 16.0
```

```
$param pd2limx = 28.0                ! x limit of momentum for HD+ fragments
$param PHZYMAX = 22.6274             ! transverse momentum limit for H+
$param PDZYMAX = 22.6274             ! transverse momentum limit for D+
$param PHDZYMAX = 22.6274            ! transverse momentum limit for HD+
$param PD2ZYMAX = 22.6274
$param Px_min1 = 0.0                 ! minimum momentum for energy evaluation <0
!                    The following factors are for Vpush = 400 volts
!                                                  Vfocus = 332 volts
!                    Calculated using SIMION on 1/11/00
!
$param hlinterm = -0.1422! TOF to Px conversion factors (H+)
$param hsqterm = 1.01262e-5
$param dlinterm = -0.1422! TOF to Px conversion factors (D+)
$param dsqterm = 1.27617e-5
$param hdlterm = -0.1422 ! TOF to Px conversion factors (HD+)
$param hdsqterm = 6.34e-6
$param d2lterm = -0.1422 ! TOF to Px conversion factors (D2+)
$param d2sqterm = 6.34e-6
$param ehlim = 0.8192
$param edlim = 0.8192
$param ehdlim = 0.8192
$param ed2lim = 0.8192
$param escale = 27.2116
$param MBscale = 1.0
$param MBscale3 = 1.0
$param MBscale4 = 1.0
$param EKScale = 3.0
```